Towards Direct Frequency Comb Spectroscopy Using Quantum Logic

Von der Fakultät für Mathematik und Physik
der Gottfried Wilhelm Leibniz Universität Hannover

zur Erlangung des Grades

Doktor der Naturwissenschaften
Dr. rer. nat.

genehmigte Dissertation

von

Dipl.-Phys. Börge Hemmerling
geboren am 15. April 1981 in Saarlouis

2011

Referent: Prof. Dr. Piet O. Schmidt
Korreferent: Prof. Dr. Christian Ospelkaus
Tag der Promotion: 1. Juli 2011

Abstract

The possibility of variations of fundamental constants is highly debated and investigations have not yet reached a final conclusion. In the case of the fine-structure constant, the latest terrestrial experiments that employ ultra-precise spectroscopy on the timescales of a few years are consistent with no variation, whereas recent studies of quasar absorption spectra indicate a positive finding on both temporal and spatial variations of the fine-structure constant on astronomical scales.

The astrophysical investigations strongly depend on accurate laboratory wavelength of a number of transitions of various complex ions, such as Ti^+ and Fe^+, which, up to present, have resisted precision laser spectroscopy. In this thesis, a versatile setup that lays the basis to study such ions with a frequency comb as a spectroscopy source and theoretical calculations on the expected spectroscopy signal are presented. In this approach, the ions of interest (*spectroscopy ions*) are sympathetically cooled by well-controlled magnesium ions (*logic ions*) which are simultaneously stored in a Paul trap. Quantum logic techniques are employed to detect the spectroscopy signal from the spectroscopy ion on the logic ion. In contrast to previously implemented experiments that obtained precision data on such ions, the described apparatus is based on a single or a few ions and will therefore allow for isotope-selective spectroscopy.

As an initial stage of the proposed spectroscopy scheme, a single $^{25}\mathrm{Mg}^+$ ion is cooled to the motional ground state of the trap confinement. The presented setup is a major simplification over previously used setups, since a single solid-state laser system is employed to cool, manipulate, repump and detect the logic ion. The cooling performance is studied by driving Raman-stimulated Rabi oscillations on the motional sidebands. An average motional population number of $\bar{n} = 0.03 \pm 0.01$ is achieved.

Additionally, this work explores different detection schemes for $^{25}\mathrm{Mg}^+$ ions with potential application to other ions with hyperfine ground states. In contrast to the commonly implemented electron-shelving technique, the combination of electron-shelving with well-controllable radio-frequency induced spin-flips allows for post-selection of the observed statistics by filtering uncorrelated detection events. The achievable fidelity and the robustness of different detection strategies are studied.

Future applications of the developed apparatus include deterministic state preparation and detection of molecular ions, highly charged ions and other exotic species for which laser cooling is not available.

keywords: ground state cooling, ion trap, frequency comb spectroscopy

Zusammenfassung

Eine mögliche Variation fundamentaler Konstanten ist ein viel debattiertes Thema und Untersuchungen hierzu haben zurzeit noch kein abschließendes Ergebnis erbracht. Im Falle der Feintstrukturkonstanten sind die neuesten terrestrischen Experimente, welche Präzisionsspektroskopie auf einer Zeitskala von mehreren Jahren einsetzen, konsistent mit einem Nullresultat. Andererseits liefern kürzliche Studien von Quasarabsorptionsspektren ein Indiz dafür, dass sich die Feinstrukturkonstante sowohl zeitlich als auch räumlich auf astronomischen Skalen ändert.

Die astrophysikalischen Untersuchen hängen sehr stark von exakten Laborwellenlängen einiger Übergänge in verschiedenen komplexen Ionen, wie Ti^{+} und Fe^{+}, ab, die bis zum heutigen Zeitpunkt kein Gegenstand von Präzisionslaserspektroskopie waren. In dieser Arbeit werden sowohl ein vielseitiger Aufbau, welcher die Basis bildet, um derartige Ionen mit einem Frequenzkamm als Spektroskopiequelle zu untersuchen, als auch theoretische Berechnungen zum erwarteten Spektroskopiesignal präsentiert. Der hier diskutierte Ansatz verwendet gut kontrollierbare Magnesium-Ionen (Logik-Ionen) zum mitfühlenden Kühlen der zu untersuchenden Ionen (Spektroskopie-Ionen), welche simultan in einer Paul-Falle gespeichert sind. Quantenlogikmethoden werden eingesetzt, um das Spektroskopiesignal des Spektroskopie-Ions auf dem Logik-Ion zu detektieren. Im Gegensatz zu bisherigen Experimenten, welche Präzisionsdaten solcher Ionen erzielten, arbeitet der beschriebene Messplatz mit einem einzelnen Ion oder mit mehreren Ionen. Dies ermöglicht die Implementierung von isotopenselektiver Spektroskopie.

In einem ersten Schritt des beabsichtigten Spektroskopieschemas wird ein einzelnes $^{25}\mathrm{Mg}^{+}$-Ion in den absoluten Bewegungsgrundzustand des Falleneinschlusses gekühlt. Der beschriebene Aufbau ist eine bedeutende Vereinfachung gegenüber bisher verwendeten Aufbauten, da ein einzelnes Festkörperlasersystem für Kühlung, Manipulation, Recycling und Detektion des Logik-Ions eingesetzt wird. Die Effizienz des Kühlverfahrens wird anhand von ramanstimulierten Rabi-Oszillationen der Bewegungsseitenbänder untersucht, wobei eine mittlere Bewegungspopulation von $\bar{n} = 0.03 \pm 0.01$ erreicht wird.

Zusätzlich untersucht diese Arbeit verschiedene Detektionsverfahren für $^{25}\mathrm{Mg}^{+}$ mit potentiellen Anwendungen für andere Ionen mit Hyperfeingrundzuständen. Im Gegensatz zu der üblicherweise genutzten "electron-shelving"-Methode erlaubt die Kombination aus "electron-shelving" und gut kontrollierbaren radiofrequenzinduzierten Spinflips eine Postselektion der Messergebnisse durch Filterung unkorrelierter Detektionsereignisse. Die erwartete Genauigkeit und die Robustheit verschiedener Detektionsstrategien wird untersucht.

Zukünftige Anwendungen des entwickelten Messaufbaus umfassen deterministische Zustandspräparation und Detektion von Molekül-Ionen, hochgeladenen Ionen und anderen ausgefallenen Spezies, für die Laserkühlung nicht möglich ist.

Schlagworte: Grundzustandskühlen, Ionenfalle, Frequenzkammspektroskopie

Contents

List of Figures **v**

Fundamental Constants **viii**

1 Introduction **1**

2 Ions in a Linear Paul Trap **7**

2.1 Operation Principle of Ion Traps . . . 7
  2.1.1 Trapping Potential . . . 8
  2.1.2 Equations of Motion . . . 9
  2.1.3 Excess Micromotion . . . 10
2.2 Magnesium as a Qubit . . . 11
  2.2.1 Magnesium Level Scheme . . . 12
  2.2.2 Interaction of Light with Trapped Magnesium Ions . . . 14
  2.2.3 Coherent Manipulation . . . 19

3 Theoretical Description of Direct Frequency Comb Spectroscopy **23**

3.1 Spectrum of a Phase-Stabilized Pulsed Laser . . . 24
3.2 Time Evolution of the Atomic System . . . 26
  3.2.1 Definition of the Ion-Laser-Trap System . . . 27
  3.2.2 Optical Bloch Equations with a Pulsed Laser . . . 29

4 Simulation Results **37**

4.1 Three-Level Raman System . . . 37
4.2 The 5-Level System of $^{40}\mathrm{Ca}^{+}$ . . . 38
4.3 Calcium Raman Resonances with a Frequency Comb . . . 40
4.4 Calcium Single-Photon Resonances with a Frequency-Doubled Comb . . . 41
  4.4.1 393 nm and 397 nm Transitions . . . 43
  4.4.2 Laser-Induced Fluorescence Spectroscopy . . . 45
  4.4.3 Photon-Recoil Spectroscopy . . . 45
  4.4.4 Line Shapes and AC-Stark Shifts . . . 47

4.4.5 866 nm, 854 nm and 850 nm Transitions . . . 49
4.5 Comb Engineering . . . 49

5 Experimental Setup 54
5.1 Magnesium Laser System . . . 54
5.1.1 Photoionization Laser . . . 54
5.1.2 Magnesium Ion Laser System . . . 55
5.2 Doppler Cooling and Raman Beam Configuration . . . 60
5.2.1 Optical Setup . . . 60
5.2.2 Double-Pass Configuration Avoiding UV damage . . . 61
5.3 Microwave Antenna Setup . . . 63
5.4 Laboratory Frequency-Reference . . . 64
5.5 Vacuum Chamber . . . 64
5.6 Paul Trap and Atom Ovens . . . 65
5.7 Radio-Frequency Drive of the Paul Trap . . . 68
5.8 Magnetic Field Coils . . . 69
5.9 Fluorescence Detection of the Ion . . . 69
5.9.1 UV Objective . . . 70
5.9.2 Parabolic Mirror . . . 70
5.10 Laser Beam Configuration . . . 71
5.11 Experimental Control . . . 73

6 Experimental Prerequisites 74
6.1 Axial Trap Frequencies . . . 74
6.2 Radial Trap Frequencies . . . 75
6.3 Magnetic Field . . . 75
6.4 Compensation of Micromotion . . . 76
6.4.1 Camera . . . 77
6.4.2 Photon-Correlation Measurements . . . 78
6.4.3 Micromotion Sideband Spectroscopy . . . 78

7 Quantum State Detection Schemes 81
7.1 Offresonant Depumping of the Bright State . . . 81
7.2 Discrete Threshold Detection . . . 84
7.3 Distribution-Fit-Detection . . . 86
7.4 π-Pulse Detection . . . 88
7.5 Radio-Frequency Driven Rabi Flops . . . 91
7.6 Comparison and Robustness of Detection Methods . . . 93
7.7 Coherence Time Measurements . . . 96

8 Experimental Results **99**
8.1 Limit for Laser Cooling of Trapped Ions 99
8.1.1 Doppler Cooling 100
8.1.2 Pulsed Sideband Cooling 102
8.2 Measurement Principle and Doppler Cooling 106
8.3 Ground State Cooling of a Single Magnesium Ion 108
8.3.1 Sideband Cooling Results 110
8.3.2 Off-Resonant Depumping 113
8.3.3 Heating Rates 115

9 Summary and Outlook **117**

A Wigner Symbols and Normalizations **122**

B Polarization and Radiation Pattern **128**

C Population Distribution and Sideband Ratios **131**

D Comb Structure and Unitary Phase Transformation **133**
D.1 Comb Structure 133
D.2 Unitary Transformation for the Phase Dependence 133

E UV objective **137**

Bibliography **154**

List of Figures

2.1 Schematics of a Linear Paul Trap 8
2.2 Level Scheme of ^{25}Mg^{+} 13
2.3 Scaling of Rabi Frequencies in a Harmonic Potential 18
2.4 Coherent Manipulation of ^{25}Mg^{+} with a Raman Transition 20

3.1 Power Spectrum of an Ideal Phase-Stabilized Pulsed Laser 26
3.2 Time Scales of the Laser-Ion Interaction for a Frequency Comb 27
3.3 Energy Levels for the Ion-Comb-Trap System 28

4.1 Three-Level System Interacting with a Frequency Comb 38
4.2 Level Scheme of ^{40}Ca^{+} 39
4.3 Scheme of the Interaction of a Frequency Comb with Calcium Ions in a Raman Configuration 40
4.4 Simulation of Direct Frequency Comb Spectroscopy with ^{40}Ca^{+} in a Raman Configuration 41
4.5 Scheme of the Interaction of a Frequency Comb with Calcium Ions 42
4.6 Simulation of Direct Frequency Comb Spectroscopy of ^{40}Ca^{+} in the S State 44
4.7 Photon-Recoil Spectroscopy with ^{40}Ca^{+} in the S State 46
4.8 Symmetry of Transition Resonances and AC Stark-Shifts for Direct Frequency Comb Spectroscopy 48
4.9 Simulation of Direct Frequency Comb Spectroscopy with ^{40}Ca^{+} in the D State 50
4.10 Photon-Recoil Comb Spectroscopy with ^{40}Ca^{+}in the D State 51
4.11 Engineering of the Frequency Comb 52
4.12 Raman Resonance with a Frequency Comb 52
4.13 Raman Resonance with a Frequency Comb (Time Evolution) 53

5.1 Photoionization Laser Setup for Magnesium 56
5.2 Overview of Main Laser Setup 57
5.3 Sideband Generation with EOM 59

5.4 Overview of the Laser-Beam Configuration and the AOM Setup 61
5.5 Schematics of the Retro-Reflecting Double-Pass AOM setup 63
5.6 Setup for Radio-Frequency Generation 63
5.7 Frequency Reference Distribution 64
5.8 Schematics of the Vacuum Chamber 66
5.9 Schematics of the Paul Trap and the Atom Ovens 67
5.10 Vapor Pressure of Magnesium, Calcium, Titan and Iron 68
5.11 Calibration of the Helical Resonator 69
5.12 CCD-Camera Picture of a String of Magnesium Ions Imaged by the UV Objective 70
5.13 CCD-Camera Picture of the Ion Imaged by the Parabolic Mirror 71
5.14 Geometry of the Laser Beams and Magnetic Field 72

6.1 Axial Trap Frequencies for Different Isotopes in the Paul Trap 75
6.2 Radial Trap Frequencies in the Paul Trap and Schematics of the Photon-Correlation Setup 76
6.3 Magnetic Field Calibration 77
6.4 Photon-Correlation Measurements for Micromotion Compensation 79
6.5 Resolved-Sideband Spectroscopy for Micromotion Compensation 80

7.1 Optical Depumping of the Dark State in $^{25}\mathrm{Mg}^+$ 83
7.2 Error of Threshold Detection Method 85
7.3 Photon Distributions of Both Hyperfine Ground States in $^{25}\mathrm{Mg}^+$ 87
7.4 Error of the Distribution Fit Detection Method 88
7.5 Sequence for the π-Detection Method 89
7.6 Decision Tree for the π-Detection Method for the Bright State 90
7.7 Decision Tree for the π-Detection Method for the Dark State 91
7.8 Error of the π-Detection Method 92
7.9 Radio-Frequency Driven Rabi Oscillation 93
7.10 Comparison of Detection Methods via Rabi-Frequency Driven Rabi Oscillations 94
7.11 Robustness of Detection Methods 95
7.12 Measured Coherence Time of a Single $^{25}\mathrm{Mg}^+$ Ion 97

8.1 Heating and Cooling Processes in a Pulsed Sideband Cooling Scheme . . 103
8.2 Limit on the Lowest Achievable Average Population for Pulsed Sideband Cooling 106
8.3 Cooling and Manipulation Schemes of $^{25}\mathrm{Mg}^+$ 108
8.4 Sideband Cooling Sequence 110

8.5 Sideband Spectroscopy of a Single $^{25}\mathrm{Mg}^{+}$ Ion 111
8.6 Rabi Oscillations of a Single $^{25}\mathrm{Mg}^{+}$ Ion on Carrier and Motional Sidebands 113
8.7 Off-Resonant Excitation by the Raman Lasers 114
8.8 Heating Rates of a Single $^{25}\mathrm{Mg}^{+}$ Ion 116

A.1 Transition Strength $S_{1/2}(F=2,m_F)\to P_{1/2}(F',m_{F'})$ 124
A.2 Transition Strength $S_{1/2}(F=3,m_F)\to P_{1/2}(F',m_{F'})$ 125
A.3 Transition Strength $S_{1/2}(F=2,m_F)\to P_{3/2}(F',m_{F'})$ 126
A.4 Transition Strength $S_{1/2}(F=3,m_F)\to P_{3/2}(F',m_{F'})$ 127

E.1 Estimated Resolution of the UV Objective 138

Fundamental Constants[1]

Quantity	Symbol	Value	Unit
Fine-structure constant	α	$7.297352537(50) \times 10^{-3}$	
Speed of light	c	2.99792458×10^{8}	m s^{-1}
Boltzmann Constant	k_B	$1.3806504(24) \times 10^{-23}$	J K^{-1}
Elementary Charge	e	$1.60217648(40) \times 10^{-19}$	C
Planck Constant	h	$6.62606896(33) \times 10^{-34}$	J s
	$h/2\pi$	$1.054571628(82) \times 10^{-34}$	J s
Bohr Magneton	μ_B	$927.400915(23) \times 10^{-26}$	J T^{-1}
Vacuum Permittivity	ϵ_0	$8.854187817 \times 10^{-12}$	A s V^{-1} m^{-1}
Atomic Mass Unit	amu	$1.660538782(83) \times 10^{-27}$	kg

---

[1] CODATA recommended values [1]

Chapter 1

Introduction

> *"The constancy of the [fundamental] constants is merely an experimental fact"*
> *Savely G. Karshenboim* [2]

When Kepler presented his laws governing the motion of the planets, he introduced a quantity in the third law which was believed to be constant and universal. Only years later did Newton prove that this property actually depends on the particular stellar system and can be expressed by the mass of the host star and the gravitational constant. This historical example demonstrates the importance of a critical view and a deep understanding of what is commonly accepted as being correct regarding fundamental principles.

At present, there is no known way to derive the fundamental constants from axiomatic principles and there is no theoretical reason whatsoever why they should be constant at all. Paul Dirac was one of the first physicists to bring forward the idea of their temporal variation in his *large numbers hypothesis* [3]. He realized that the ratio of the electrostatic and gravitational forces between a proton and an electron is on the same order of magnitude as the age of the universe in atomic units. Based on this observation, he proposed that the gravitational constant change with the age of the universe.

The general idea of replacing the constants by varying quantities has over time been extended to allow for their possible spatial variation and culminates in modern field theories which strive to describe the unification of all fundamental forces in an expanding universe. These theories include additional spatial dimensions which might have detectable effects in our universe. For instance, it is proposed in the high-energy Kaluza-Klein model that the extra dimensions might expand or contract, which could reflect itself in a temporal change of the fundamental constants that are projected onto our three dimensions [4]. Thus, experiments that indicate a variation of a fundamental constant could either rule out or corroborate certain theories.

From a practical point of view, natural questions that arise in this scope are: a) on which scales we expect to observe possible variations; and b) which of the constants are optimal for an investigation. Usually dimensionless constants are preferred since they do not have the additional complication of deliberating whether the unit or the value itself varies[1]. A detailed description of theoretical and experimental constraints of all constants and the consequences for modern theories is found in [6, 7]. From all dimensionless constants, the present observational status of variations of the fine-structure constant is discussed here in more detail.

The fine-structure constant $\alpha = e^2/4\pi\epsilon_0\hbar c \sim 1/137$ governs the strength of the electro-magnetic interaction. Thus, it is quite natural to search for changes in atomic absorption spectra[2]. The comparison of atomic transition frequencies ω at different times gives a hint at possible variations of α. While the energy of atomic levels is proportional to α^2, the fine- and hyperfine interaction corrections scale with α^4. The corresponding shifts in frequency $\Delta(t)$ due to a change in α are usually written in the form

$$\Delta(t) := \omega(t) - \omega(0) = q_1\left(\frac{\alpha^2(t)}{\alpha^2} - 1\right) + q_2\left(\frac{\alpha^4(t)}{\alpha^4} - 1\right) \approx \left(\frac{\dot{\alpha}}{\alpha}\right) t\,(2q_1 + 4q_2) \quad ,$$

where α is the present value of the fine-structure constant and $\alpha(t) = \dot{\alpha}t + \alpha$. The introduced properties $q_{1,2}$ are determined by varying α in *ab initio* relativistic Hartree-Fock calculations of the energy levels [8, 9]. Their values span a broad range, including positive and negative numbers, and strongly depend on the atom and transition under consideration. For instance, the 282 nm transition from the ground state $^2\mathrm{S}_{1/2}$ to the excited state $^2\mathrm{D}_{5/2}$ in Hg^+ is expected to vary with $q_1 = -36785\,\mathrm{cm}^{-1}$ and $q_2 = -9943\,\mathrm{cm}^{-1}$ [10]. This corresponds to a frequency shift of $\sim 0.4\,\mathrm{Hz}$ over the course of one year assuming a linear change[3] in the fine-structure constant with a rate $\dot{\alpha}/\alpha \sim 10^{-16}\,\mathrm{a}^{-1}$. Clearly, the expected shifts are rather small and, consequently, the investigation of possible α variations requires precision spectroscopy measurements.

Current investigations are divided in two major branches: In a first approach, changes in a particular transition are observed very accurately in repetitive measurements during a period of a few years. The latest and currently most accurate finding puts an upper limit of $\dot{\alpha}/\alpha = (-1.6 \pm 2.3) \times 10^{-17}\,\mathrm{a}^{-1}$ by comparing the Al^+ and the Hg^+ single-ion optical clock frequencies over the course of one year [12]. There are a number of other atomic neutral and charged species which are used to pursue this endeavour. Among them we find Hg^+ [13], Yb^+ [14, 15, 16], Rb [17], H [18], Sr [19] and Dy [10, 20]. Apart from atomic species, it is worth mentioning that recent investigations yielded enhanced sensitivities to a variation of α for more complex systems, e.g. diatomic molecules [21, 22, 23], highly-charged ions [24] or nuclear transitions [25, 26, 27].

---

[1] An investigation that studied a non-dimensionless constant which is worth mentioning is the Michelson-Morley experiment carried out in 1887 with the goal of measuring the isotropy of the speed of light [5].

[2] For a detailed analysis on other methods to determine a variation of α, the reader is referred to [6, 7].

[3] It is worth mentioning that the assumption of a linear change is the simplest one, but not necessarily correct [11].

The second branch of experiments compares spectra of various elements on cosmological timescales. The light emitted by far-distant quasars which travels through interstellar clouds carries the imprinted spectral information of the particular cloud constituents and is matched to todays laboratory data. This is commonly referred to as *quasar absorption spectroscopy* (QSO) [11, 28]. The advantage of this method is that spectra are compared at large time differences of $\sim 10^{10}$ years, thus making the expected small shifts more accessible. However, apart from the need for a model of the α variation, QSO is affected by several systematic effects which need to be taken into account for the analysis [29, 30]. A quite recent observation, which so far cannot be explained by any systematic error, suggests that the fine-structure constant varies temporally as well as spatially [31]. This study analyses data from two different telescopes, namely the Very Large Telescope (VLT) in Chile and the Keck telescope in Hawaii. The combined analysis using many transitions lines in a so-called many-multiplet method [9, 10, 32] yields different values for α for different directions in the universe [31]. However, in order to intensify this study and to further exclude possible systematic errors, more accurate knowledge of laboratory reference spectra[4] is required [36]. At present, most laboratory data has been obtained by Fourier transform spectroscopy in combination with hollow-cathode discharge lamps (see e.g. [37]). A compilation of the obtained data with typical accuracy values ranging from 5×10^{-3} nm to 5×10^{-4} nm is found in [38, 39, 40]. While the desired accuracy of 10^{-5} nm is not yet reached for many lines [36], a more intriguing issue is the inability to resolve the isotope shifts. Since the heated cathode consists of the natural abundances of the various materials under study, usually isotope shifts are not resolved in the Doppler-broadened spectrum [41].

In the quasar spectra analysis, the isotope abundances were assumed to have terrestrial ratios. Since a cosmic evolution of such abundances cannot be unambiguously distinguished from a variation of α, one could argue that the isotope ratios were different at the time when the quasar light was absorbed and α had no other value than today's [42, 43]. Therefore it is highly desirable to obtain a precise knowledge and accurate spectroscopy data, in particular the isotope shifts of the used species. It should further be noted that an additional complication is that the expected isotope shifts are on the same order of magnitude as the expected line shifts given the present constraints on $\dot{\alpha}/\alpha$.

---

[4] Yet another concern, not further detailed here, is the calibration of the used Echelle spectrographs. Currently, the spectra of Thorium-Argon hollow-cathode lamps often serve as a reference for calibration. These lamps, however, suffer problems such as aging which makes reproducibility harder. Also, the available line density is rather low over the required spectral bandwidth. Effects of different line choices on the α analysis have been studied [33]. The recent development of astro-combs will eventually overcome these problems and provide for more accurate calibration [34, 35].

Overcoming this obstacle and providing more accurate spectroscopy data for the quasar absorption analysis with an independent method to confirm previous measurements is the basic motivation of the experiments described in this thesis. Among the broad range of elements which are of relevance for improving the described QSO analysis are singly-charged metal ions, such as Ti^+. A compilation of all species of interest with their particular transitions is found in [36]. At present, most of these species have resisted precision laser spectroscopy due to their complex level structure. Their lack of a closed cycling transition inhibits laser cooling and renders state detection via fluorescence measurement impossible. Setting up lasers to repump the ion back to the cycling transition for every decaying channel is impractical due to the required broad spectral coverage of several nm and the number of laser systems. These obstacles are commonly overcome by employing a large ion crystal or a beam of ions in combination with a broadband spectral source, such as the mentioned hollow-cathode discharge lamps. In general these methods are affected, nevertheless, by the finite temperature in the system and not precisely known local gas pressure, leading to e.g. transition line broadening and shifting effects.

In a different approach, while using only a single or a few ions, such difficulties disappear. In contrast to neutral atoms, the strong long-range Coulomb interaction between ions makes it possible to sympathetically cool the ion of interest *(spectroscopy ion)* with a different ion species *(logic ion)* which is easily accessible [44]. This approach is highly flexible, since the cooling performance does not depend on the internal level structure of the spectroscopy ion. In addition to the cooling feature, the coupling between the ions is used as a readout channel for the spectroscopy information from the ion, which cannot be directly accessed. This strategy is called *quantum logic spectroscopy* and has been successfully implemented in the group of D. Wineland in the year 2005 [45]. In that experiment, an Al^+ ion has been sympathetically cooled with a Be^+ ion. The technique, which originates in the field of quantum computing, enabled for the first time precision laser spectroscopy of the previously inaccessible Al^+ ion by mapping the state information of the Al^+ ion onto the Be^+ ion for state readout.

In order to implement a similar spectroscopy method for an ion with a more complex level structure, e.g. a heavy metal ion like Ti^+, a broadband and narrow linewidth spectroscopy source is required. It should be emphasized that a single cw laser which is tunable over the spectral range, e.g. a Dye laser, is not suitable since the ion will eventually decay into a dark state after a few photon scattering events. In contrast to that, an optical frequency comb [46, 47] serves as an ideal source, since it provides the necessary bandwidth to drive the desired transition and, at the same time, can act as a repumper to keep the ion in the spectroscopy cycle. This type of spectroscopy is commonly referred to as *direct frequency comb spectroscopy* [48] and has been successfully implemented with neutral atoms [49, 50] and recently with trapped ions [51, 52, 53].

This work lays out the path towards isotope-selective direct frequency comb spectroscopy, in a linear Paul trap [54], of several species which are interesting for the astrophysical investigations, namely Ca^+, Ti^+ and Fe^+ ions. Due to its rather simple level structure, Ca^+ will initially serve as a testbed for the experimental setup and technique, while confirming the previously acquired results with cw laser sources [55, 56, 57] and comb spectroscopy [51, 52, 53]. Ti^+ and Fe^+ have been chosen for investigation in the same setup since the Ti:Sapphire frequency comb, which will be used as a spectroscopy source, provides the desired spectral coverage in the ultra-violet after its output is accordingly upconverted. It is worth mentioning that, also from a purely spectroscopic point of view, a better understanding of the electronic structure of heavy metal ions is desirable since accurate theoretical predictions for complex multi-level systems are difficult and can only be given approximately.

Carrying out these experiments requires the following steps: The realization of ground state cooling of the trapped two-ion crystal, a theoretical understanding of the interaction of the frequency comb with the ion and the implementation of the quantum logic scheme to readout the spectroscopy signal. This work focuses on the first two steps and their implementation.

For all investigations, $^{25}\mathrm{Mg}^+$ has been chosen for the logic ion since the requirements of the laser system for state manipulation are rather simple. In the scope of this thesis, a single solid-state laser setup was developed to implement ground state cooling, state preparation and readout. This is a major simplification over previously operated setups [58] which usually require up to three separate laser systems. The performance of the setup is determined by observing the temporal evolution of Raman-stimulated sideband transitions between two hyperfine ground states of a single $^{25}\mathrm{Mg}^+$ ion. The setup has promising applications in the ongoing challenge of cooling molecules to their ro-vibrational ground state. Furthermore, given the measured performance results, operations that require high fidelities, such as quantum gates, can be implemented with the same setup.

The spectroscopy signal will be acquired by measuring the vibrational state of the initially cooled ion crystal as a function of the comb repetition rate or the respective offset frequency. Since every photon scattering event involves a photon recoil momentum, any comb line resonant to an electronic transition leads to heating of the ion crystal. The heating excites the shared mode of both ions in the trap. This excitation can be read out via the simultaneously confined $^{25}\mathrm{Mg}^+$ ion with almost unity fidelity. The exact transition frequencies are then determined by measuring the vibrational state for varying comb parameters and comparing the results with density matrix simulations that include the electronic and motional excitation levels of the combined ion and trap system.

In a similar fashion, this method of *photon-recoil spectroscopy* has been successfully implemented for a cloud of Doppler-cooled ions [59]. In contrast to that, we expect higher sensitivities for ground state cooled ions, which are available in our setup.

This thesis is organized as follows: In Chapter 2, a theoretical overview of the basics of Paul traps, along with a quantum mechanical description of the ion-laser interaction, are given. Chapter 3 discusses in detail the numerical simulations of the interaction of a phase-stabilized pulsed laser with a multi-level system in the framework of the semi-classical optical Bloch equations. The simulation results of different spectroscopy strategies are presented in Chapter 4. The experimental setup, including the laser systems, the ion trap and the vacuum chamber, is described in Chapter 5. The ion trap is characterized by means of standard calibration measurements presented in Chapter 6. Different detection schemes to perform quantum state detection on $^{25}\mathrm{Mg}^{+}$, as well as their estimated fidelity and robustness, are discussed in Chapter 7. In Chapter 8, the experimental results on ground state cooling of a single $^{25}\mathrm{Mg}^{+}$ ion and the expected theoretical limits on the cooling performance are presented. A summary and outlook for future prospects and possible experiments conclude this work. Furthermore, several appendices are attached to present details on various calculations used in the thesis.

Chapter 2

Ions in a Linear Paul Trap

In this chapter, the motion of a trapped ion in a linear Paul trap, as well as its interaction with light, are described. The discussion includes the state preparation and the coherent manipulation of a magnesium ion. The discussed methods are employed to cool an ion to the absolute ground state of its confining potential as experimentally realized and described in Chapter 8. Ground state cooling is a necessity for the described and proposed experiments within this thesis. For a more detailed analysis on ion trap dynamics, the reader is referred to textbooks [60, 61, 62, 63].

2.1 Operation Principle of Ion Traps

A charged particle can easily be trapped in one dimension by being subjected to a static confining potential. Extending the confinement to three dimensions is not possible for the following reason: Assuming a static potential of the form

$$\Phi(\vec{r}) = ax^2 + by^2 + cz^2 \quad , \tag{2.1}$$

where $\vec{r} = (x, y, z)$ is a vector of the spatial coordinates x, y, z and a, b, c are real-valued constants, Laplace's equation $\Delta\phi = 0$ reads $a + b + c = 0$. Given that two directions act as a confining potential (e.g. $a > 0, b > 0$), the third one has to be repulsive, since $c = -(a + b)$. Thus, a complete three-dimensional confinement is impossible using a three-dimensional static potential (*Theorem of Earnshaw*).

The problem is overcome by replacing the potential in the radial directions (x, y) by a time-dependent oscillating electric potential Φ_{rf} while leaving a static potential Φ_{dc} for the axial direction (z). A trap based on this principle is called a *Paul trap* [54]. While the original design was meant to act as a two-dimensional mass filter only, in modern designs the static potential for a complete confinement is added. In the trap that is used for the experiments described in this thesis, the oscillating field is applied to a pair of opposing electrodes, while a second pair is grounded (see Fig. 2.1). The total electric field can substantially be understood as a saddle potential which changes the sign of the slopes in x and y-direction with the oscillation period. If the oscillation is fast enough, this configuration provides a confinement for the ion in radial direction since it gets pushed back (on average over time) as soon as it moves away from the center. Additionally, a static field is applied to two opposing tip electrodes. The charged particles are then harmonically trapped in an effective three-dimensional confinement. In the following, the relation among the confining potential, the trap geometry and parameters is briefly derived. For an extended description the reader is referred to [54, 62, 63, 64, 65].

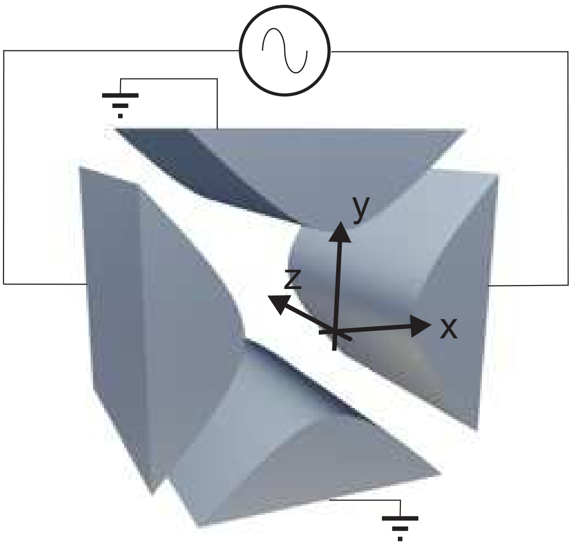

Figure 2.1: Linear Paul trap with two pairs of electrodes. The oscillating field for radial (x, y) confinement is applied to one opposing blade pair, while the other pair is grounded. At the same time, a static field is applied to an opposing pair of tip electrodes (not shown in the picture) to provide the confinement in axial direction (z) of the trap.

2.1.1 Trapping Potential

In a linear Paul trap of the type described in the previous section, a charged particle experiences to a good approximation a potential of the form

$$\Phi(\vec{r}, t) = \underbrace{\frac{x^2 - y^2}{2r_0^2} U_{\text{rf}}}_{\Phi_{\text{rf}}} \cos(\Omega_{\text{rf}} t) + \underbrace{\frac{\kappa U_{\text{dc}}}{r_0^2} \left(z^2 - \frac{1}{2}(x^2 + y^2) \right)}_{\Phi_{\text{dc}}} \quad , \tag{2.2}$$

where $U_{\text{rf}} \cos(\Omega_{\text{rf}} t)$ is the time-varying potential with an oscillation frequency Ω_{rf}, r_0 the distance between opposite blades and κ a constant geometrical factor. Using the following ansatz for the radial part of Schrödinger's equation

$$\psi(x,y,t) = \varphi(x,y,t)\exp\left(-\mathrm{i}e\Phi_{\mathrm{rf}}(x,y,t)\sin(\Omega_{\mathrm{rf}}t)/\hbar\Omega_{\mathrm{rf}}\right) \quad , \tag{2.3}$$

and averaging over one oscillation period of the radio-frequency yields [66]

$$\mathrm{i}\hbar\frac{\partial}{\partial t}\varphi = -\frac{\hbar^2}{2m}\nabla^2\varphi + e\Phi_{\mathrm{eff}}(x,y)\varphi \quad . \tag{2.4}$$

In the above equation m is the mass of the particle and an effective time-independent potential was introduced:

$$\Phi_{\mathrm{eff}} \approx e\frac{\vec{\nabla}\Phi_{\mathrm{rf}}\cdot\vec{\nabla}\Phi_{\mathrm{rf}}}{4m\Omega_{\mathrm{rf}}^2} = \frac{eU_{\mathrm{rf}}^2}{4m\Omega_{\mathrm{rf}}^2 r_0^4}\left(x^2+y^2\right) \quad . \tag{2.5}$$

If the static potential in z-direction is included in the consideration, the time-average shows that the particle is subject to a static harmonic potential in all three dimensions. However, this approximation is only valid within a certain parameter range. Parameters exceeding certain limits lead to resonances in the amplitude of motion and consequently to an unstable trap. The parameters for achieving a stable confinement are described in the following section by developing the equations of motion.

2.1.2 Equations of Motion

For simplicity, a classical treatment is considered here[1]. The equations of motion are derived by comparing the inertial and the electro-magnetic forces acting on a particle which carries one elementary charge e:

$$m\frac{d^2}{dt^2}\vec{r} \quad = \quad -e\nabla\Phi(\vec{r},t) \quad . \tag{2.6}$$

In dimensionless coordinates, the equations take the form of the Matthieu equation

$$\frac{d^2}{d\tau^2}x_i + \left[a_i + 2q_i\cos(2\tau)\right]x_i \quad = \quad 0 \quad ; \quad x_i \in \{x,y,z\} \quad , \tag{2.7}$$

---

[1] For this case, the full quantum mechanical treatment yields the same stability parameters as the classical discussion. This is attributed to the fact that the equation of motion of the Wigner function of this problem is equal to the classical Liouville equation. The reader is referred to [66] for a detailed discussion.

with a scaled time variable $\tau = \Omega_{\mathrm{rf}} t/2$ and the following parameter definitions:

$$\begin{aligned} a_x &= a_y = -\frac{1}{2} a_z = -\frac{4e\kappa U_{\mathrm{dc}}}{m r_0^2 \Omega_{\mathrm{rf}}^2} \quad ; \\ q_x &= -q_y = \frac{2eU_{\mathrm{rf}}}{m r_0^2 \Omega_{\mathrm{rf}}^2} \quad ; \\ q_z &= 0 \quad . \end{aligned} \tag{2.8}$$

This equation has stable solutions only if $a, q \ll 1$ [63]. To first order in q these read

$$x_i(t) \approx x_{0i} \cos(\omega_i t + \phi_i) \cdot \left(1 + \frac{q_i}{2} \cos(\Omega_{\mathrm{rf}} t)\right) \quad , \tag{2.9}$$

with the secular frequencies ω_i defined as

$$\begin{aligned} \omega_z &= \sqrt{\frac{e\kappa U_{\mathrm{dc}}}{2 m r_0^2}} \quad ; \\ \omega_{x,y} &= \frac{1}{2} \Omega_{\mathrm{rf}} \sqrt{a_{x,y} + \frac{q_{x,y}^2}{2}} \quad . \end{aligned} \tag{2.10}$$

The particle undergoes an oscillating motion with two different frequencies: the first corresponds to a three-dimensional harmonic oscillation in the effective trapping potential and is called *secular motion*. The second and faster oscillation originates from the high-frequency driving field (Ω_{rf}) and is called *micromotion*. In an ideal trap, it only occurs in the radial direction in an ideal potential.

2.1.3 Excess Micromotion

Since the amplitude of the micromotion is only a factor of $q_i/2$ of that of the secular motion, it is usually neglected. However, if the charged particle is subject to an additional static electric field $\vec{E}_{\mathrm{dc}}$, this situation changes dramatically. The equations of motion become

$$\frac{d^2}{d\tau^2} x_i + \left[a_i + 2q_i \cos(2\tau)\right] x_i = \frac{e\vec{E}_{\mathrm{dc}} \cdot \hat{x}_i}{m} \quad , \tag{2.11}$$

and the solution changes accordingly to

$$\begin{aligned} x_i(t) &\approx (x_{Ei} + x_{0i} \cos(\omega_i t + \phi_i)) \cdot \left(1 + \frac{q_i}{2} \cos(\Omega_{\mathrm{rf}} t)\right) \quad ; \\ x_{Ei} &\approx \frac{e\vec{E}_{\mathrm{dc}} \cdot \hat{x}_i}{m \omega_i^2} \quad . \end{aligned} \tag{2.12}$$

where $\hat{x}_i$ is a dimensionless unit vector in direction x_i. The additional static field thus shifts the particle away from the line of vanishing radio-frequency potential. The high-frequency field at that position generates micromotion, but with an increased amplitude $x_{Ei}q_i/2$. This effect is called *excess micromotion*. The same type of micromotion occurs if a phase shift between opposite blades of the high-frequency field exists. In this case the line of vanishing radio-frequency potential oscillates in position. Both effects have to be avoided in the experiment, since this type of motion is driven, thus it can not be cooled by means of lasers, and its existence can introduce heating effects which decrease the efficiency of laser cooling the motion of the ion. Since the experiments presented in this thesis rely on ground state cooling of the external motion of the ion, care has to be taken to minimize the micromotion amplitude as much as possible. This situation becomes even more critical for the case of a Coulomb crystal of several ions. There the kinetic energy is dominated by the micromotion since the equilibrium position of the ion crystal is not at the center of the trap. In a later stage of the experiment, when $^{25}\mathrm{Mg}^+$ is used for sympathetic cooling of spectroscopy ions, this effect will introduce additional limits on the cooling performance and has to be considered. For an extensive discussion on the influence of micromotion on laser cooling and other related effects in an experimental and theoretical context see [67, 68, 69].

2.2 Magnesium as a Qubit

For the experimental work presented in this thesis, the ion $^{25}\mathrm{Mg}^+$ was used. The main motivation for choosing this species lies in the requirements for the necessary laser system. In other employed species often several individual laser setups are necessary to provide cooling, coherent manipulation, repumping and state detection of the ion. For instance in the case of $^{40}\mathrm{Ca}^+$, the used electronic states are coupled by optical transitions which are largely separated: 397 nm for Doppler cooling, 854 nm and 866 nm for repumping and 729 nm for coherent manipulation (see also Fig. 4.2 for a $^{40}\mathrm{Ca}^+$ level scheme). In contrast to that, a two-level system in ions with hyperfine structure, like $^{9}\mathrm{Be}^+$ or $^{25}\mathrm{Mg}^+$, can be implemented by using two long-lived ground states. Since the separation of these states is on the order of $\sim$GHz, coherent manipulation can be achieved in a Raman configuration derived from a single laser by means of acousto-optic modulators. In addition to that one or two laser systems for repumping and detecting purposes are commonly used. With the incorporation of an additional electro-optic modulator in the setup this configuration can be even more simplified to just a single laser system for cooling, detecting, repumping and manipulating the ions. The experiments presented in this thesis have been carried out using such a single laser system (see Section 5.1 for details). The particular $^{25}\mathrm{Mg}^+$ isotope was chosen because of its hyperfine structure.

However, some of the calibration and laser alignment experiments have been performed with the $^{24}\mathrm{Mg}^+$ isotope.

Throughout this section, the atomic structure of magnesium ions, as well as its interaction with laser fields, are discussed. The description follows [70, 71] and was adapted to magnesium ions.

2.2.1 Magnesium Level Scheme

Magnesium is an alkaline earth metal with atomic number Z=12. The most common isotope is $^{24}\mathrm{Mg}$, with a natural abundance of 79%. The second most common are $^{25}\mathrm{Mg}$ and $^{26}\mathrm{Mg}$, with 10% and 11% percent, respectively. The corresponding singly-charged ions have one electron in their valence shell and their three lowest electron configurations are the hydrogen-like $\mathrm{S}_{1/2}$, $\mathrm{P}_{1/2}$ and $\mathrm{P}_{3/2}$ shells with inter-shell transitions at 279.6 nm and 280.3 nm and a common linewidth of $\Gamma \sim 2\pi \times 41.4\,\mathrm{MHz}$ [72]. The transition frequencies of $^{24}\mathrm{Mg}^+$ and $^{26}\mathrm{Mg}^+$ have been determined by precision spectroscopy experiments [72, 73]:

Transition	Frequency ν (MHz)
$^{24}\mathrm{Mg}^+$ $3s^2\mathrm{S}_{1/2}$ - $3p^2\mathrm{P}_{1/2}$	1 069 338 342.56 (16)
$^{24}\mathrm{Mg}^+$ $3s^2\mathrm{S}_{1/2}$ - $3p^2\mathrm{P}_{3/2}$	1 072 082 934.33 (16)
$^{26}\mathrm{Mg}^+$ $3s^2\mathrm{S}_{1/2}$ - $4p^2\mathrm{P}_{1/2}$	1 069 341 427.47 (16)
$^{26}\mathrm{Mg}^+$ $3s^2\mathrm{S}_{1/2}$ - $4p^2\mathrm{P}_{3/2}$	1 072 086 021.89 (16)

Of the different isotopes, $^{25}\mathrm{Mg}^+$ is the only one with a nuclear spin. As a consequence, the energy levels are split into the so-called hyperfine structure. These energy shifts arise from a coupling of the nuclear momentum with the electric field of the electrons. Their quantity can be expressed in terms of the nuclear spin I, the total electronic spin $J = L + S$, where L corresponds to the orbital angular momentum and S to the intrinsic spin, and the total angular spin $F = J + I$ as follows [74]

$$\Delta E_{\mathrm{HFS}} = \frac{K}{2} \cdot A + \frac{\frac{3}{2}K(K+1) - 2I(I+1)J(J+1)}{2I(2I-1)2J(2J-1)} \cdot B \quad , \tag{2.13}$$

where $K = F(F+1) - I(I+1) - J(J+1)$. The first term results from the energy of the nuclear dipole moment in the magnetic field produced by the electrons, whereas the second one accounts for the energy of the electric quadrupole moment of the nucleus in the electric field gradient. For $I = 0, 1/2$ the quadrupole moment vanishes ($B = 0$) [75]. The combined total spin F fulfills the condition $|I - J| \leq F \leq I + J$.

The resulting level scheme for $^{25}\mathrm{Mg}^+$ with its nuclear spin $I = 5/2$, as well as the corresponding hyperfine constants, A and B, have been either calculated or measured [76, 77] and are listed in Fig. 2.2. In accordance with the predicted isotope shifts and hyperfine splittings, we observe for the $^{25}\mathrm{Mg}^+$ transition $3s^2\mathrm{S}_{1/2}$ $|3,3\rangle$ to $3p^2\mathrm{P}_{3/2}$ $|4,4\rangle$ with a calibrated wavelength meter a resonance frequency of 1 072.085 265 (60) THz.

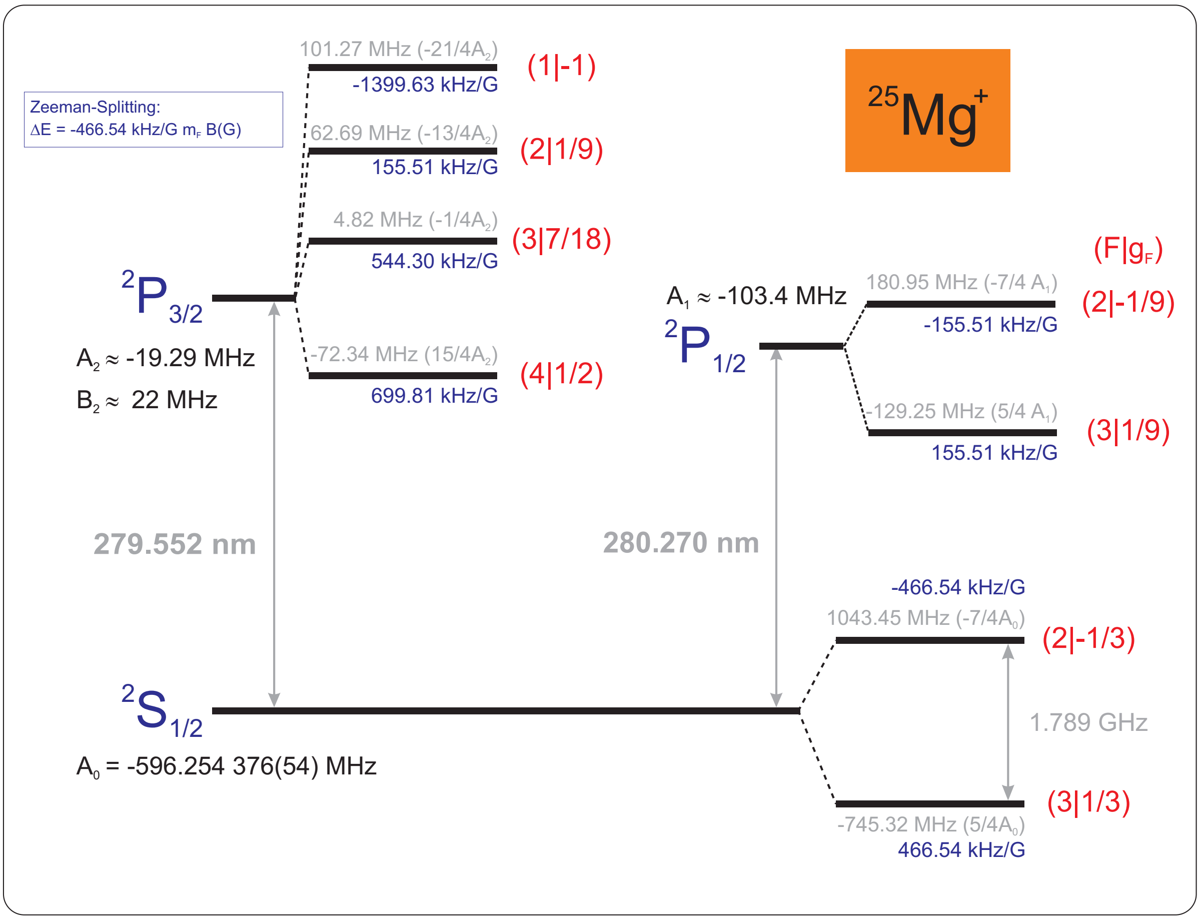
Zeeman-Splitting:
ΔE = -466.54 kHz/G m$_F$ B(G)
101.27 MHz (-21/4A$_2$)
-1399.63 kHz/G
(1|-1)
62.69 MHz (-13/4A$_2$)
155.51 kHz/G
(2|1/9)
4.82 MHz (-1/4A$_2$)
544.30 kHz/G
(3|7/18)
^{2}P$_{3/2}$
A$_2$ ≈ -19.29 MHz
B$_2$ ≈ 22 MHz
-72.34 MHz (15/4A$_2$)
699.81 kHz/G
(4|1/2)
^{25}Mg$^+$
(F|g$_F$)
A$_1$ ≈ -103.4 MHz
^{2}P$_{1/2}$
180.95 MHz (-7/4 A$_1$)
-155.51 kHz/G
(2|-1/9)
-129.25 MHz (5/4 A$_1$)
155.51 kHz/G
(3|1/9)
279.552 nm
280.270 nm
-466.54 kHz/G
1043.45 MHz (-7/4A$_0$)
(2|-1/3)
1.789 GHz
^{2}S$_{1/2}$
A$_0$ = -596.254 376(54) MHz
(3|1/3)
-745.32 MHz (5/4A$_0$)
466.54 kHz/G

Figure 2.2: Level scheme of $^{25}\mathrm{Mg}^+$ including hyperfine structure. Only the levels of relevance to the experiments are shown. The quadrupole fraction of the hyperfine-splitting for the $\mathrm{P}_{3/2}$ is included in the frequency shift values but not mentioned in the energy levels.

The hyperfine states are further split into magnetic sub-states which are denoted by the magnetic quantum number m_F, where $m_F \in \{-F, -F+1, \ldots, F\}$. Without any external magnetic field, these levels are degenerate. Such degeneracy is lifted in the experiments by applying an external field of typically $B_z \sim 6\,\mathrm{mT}$. Within the limit of weak fields, the levels experience a Zeeman-shift in energy according to[2]

$$\Delta E_{\mathrm{ZM}} \quad = \quad \mu_{\mathrm{B}} g_F m_F B_z \quad , \tag{2.14}$$

---

[2] Derivation of the Zeeman effects and the Landé factors can be found in textbooks [78].

where the Landé factors are approximately given in terms of the electronic spin S and orbital spin L by

$$\begin{aligned} g_J &\approx 1 + \frac{J(J+1) - L(L+1) + S(S+1)}{2J(J+1)} \quad ; \\ g_F &\approx g_J \frac{F(F+1) - I(I+1) + J(J+1)}{2F(F+1)} \quad . \end{aligned} \tag{2.15}$$

The corresponding values for g_F are shown in Fig. 2.2.

Of particular interest for the experiments in this thesis is the ground state splitting of 1.789 GHz of the $\mathrm{S}_{1/2}$ state. The magnetic sub-states $|\downarrow\rangle := |\mathrm{F} = 3, \mathrm{m_F} = 3\rangle$ and $|\uparrow\rangle := |2,2\rangle$ are used to encode the required two-level system. Both manifolds can be coupled via a magnetic dipole transition (M1) and are consequently long-lived states. In contrast to the electric dipole transitions, the decay rate is much smaller. The $^2\mathrm{S}_{1/2}$ F=2 state of $^{25}\mathrm{Mg}^+$ has a decay rate [79, 80]

$$\Gamma_{\mathrm{HF}} = \frac{4\alpha\omega^3\hbar^2 I}{27 m_e^2 c^4 (2I+1)} (\sqrt{2}\sqrt{1+\kappa} + 1)^2 \sim 10^{-14}\frac{1}{s} \quad , \tag{2.16}$$

where $\kappa = \sqrt{1 - Z^2\alpha^2}$, α is the fine-structure constant, m_e the electron mass, I the nuclear spin of $^{25}\mathrm{Mg}^+$ and $\omega = 2\pi \times 1.789$ GHz the hyperfine-splitting. This corresponds to a lifetime of $> 10^6$ years and thus spontaneous decay is neglected in what follows.

It should be further noted that the extremal magnetic sub-state $|4,4\rangle$ of the $\mathrm{P}_{3/2}$ manifold has only a single decay channel, namely to the $|\downarrow\rangle$ state. Thus, by coupling the $\mathrm{S}_{1/2}$ and $\mathrm{P}_{3/2}$ states with a laser field and choosing the correct polarization ($\sigma^\pm$), this optical cycling transition can be employed for Doppler cooling the ion and initializing its internal state via optical pumping, where the ion is successively transferred into the $|\downarrow\rangle$ state independently of its initial state distribution in the $\mathrm{S}_{1/2}$ $F = 3$ manifold. At the same time, an additional repumper which couples the $\mathrm{S}_{1/2}$ $F = 2$ state to the $\mathrm{P}_{3/2}$ state is used to address the population in the $F = 2$ manifold.

2.2.2 Interaction of Light with Trapped Magnesium Ions

In this section, the interaction of a laser field with an ion confined in a harmonic trapping potential is described. The ion is assumed to be in a state distribution

$$\psi \;=\; (a\,|\uparrow\rangle + b\,|\downarrow\rangle) \otimes \sum_{n=0}^{\infty} c_n\,|n\rangle \quad , \tag{2.17}$$

where $|n\rangle$ represents the oscillator levels and the following normalization condition applies for the complex constants a, b and c_n:

$$|a|^2 + |b|^2 = 1 \quad ; \quad \sum_n |c_n|^2 = 1 \quad . \tag{2.18}$$

The combined system essentially shows two new types of resonances in addition to the resonance of the isolated two-level system. These allow for coupling the internal electronic and external motional degrees of motion and are used e.g. in ion trap quantum computing as a quantum bus between different ions [81]. An extensive study of such systems is found in [63, 64, 65].

Hamiltonian

The Hamiltonian of a two-level system trapped in a harmonic oscillator with frequency ω_T and interacting with a running electro-magnetic wave $E(t) = E_0 \cos(\vec{k}\hat{\vec{x}} - \omega_L t)$ reads[3] [65]

$$\begin{aligned}
\hat{H} &= \hat{H}_0 + \hat{H}_1 \quad ; \\
\hat{H}_0 &= \frac{\hat{p}^2}{2m} + \frac{1}{2} m \omega_T^2 \hat{x}^2 + \frac{1}{2}\hbar\omega_0\hat{\sigma}_z \quad ; \\
\hat{H}_1 &= \frac{1}{2}\hbar\Omega\left(\hat{\sigma}^+ + \hat{\sigma}^-\right)\left(e^{\mathrm{i}(\vec{k}\hat{\vec{x}} - \omega_L t + \phi)} + e^{-\mathrm{i}(\vec{k}\hat{\vec{x}} - \omega_L t + \phi)}\right) \quad ,
\end{aligned} \tag{2.19}$$

where $\hat{\sigma}_z^{+,-}$ represent the Pauli spin matrices, Ω the Rabi frequency, ω_0 the atomic transition frequency, ω_L the electro-magnetic wave frequency with a phase ϕ and wave vector $\vec{k}$ with $|\vec{k}| = k$. The Rabi frequency depends on the amplitude E_0 of the electric field and on the dipolar matrix element between the electronic states as follows

$$\hbar\Omega = E_0 \cdot \langle\uparrow|\hat{\vec{d}}|\downarrow\rangle \quad , \tag{2.20}$$

where $\hat{\vec{d}}$ is the dipole operator. The Hamiltonian consists of two parts: $\hat{H}_0$ describes the energy levels of the ion whereas $\hat{H}_1$ couples the internal (electronic) to the external (motional) states of the ion. This becomes clearer by expressing the Hamiltonian in terms of creation and annihilation operators

$$\begin{aligned}
\hat{a}\,|n\rangle &= \sqrt{n}\,|n-1\rangle \quad ; \quad \hat{x} = x_0(\hat{a} + \hat{a}^\dagger) \quad ; \\
\hat{a}^\dagger\,|n\rangle &= \sqrt{n+1}\,|n+1\rangle \quad ; \quad \hat{p} = \tfrac{\mathrm{i}}{x_0}(\hat{a}^\dagger - \hat{a}) \quad ,
\end{aligned} \tag{2.21}$$

---

[3] For simplicity, only the 1D Hamiltonian is considered here.

where $n = 0, 1, 2, \ldots$ and $x_0 = \sqrt{\frac{\hbar}{2m\omega_T}}$. The Hamiltonian (Eq. (2.19)) now reads

$$\begin{aligned} \hat{H}_0 &= \hbar\omega_T \left(\hat{a}\hat{a}^\dagger + \frac{1}{2} \right) + \frac{1}{2}\hbar\omega_0\hat{\sigma}_z \quad ; \\ \hat{H}_1 &= \frac{1}{2}\hbar\Omega \left(e^{\mathrm{i}\eta\left(\hat{a}+\hat{a}^\dagger\right)}\hat{\sigma}^+ e^{-\mathrm{i}\omega_L t} + e^{-\mathrm{i}\eta\left(\hat{a}+\hat{a}^\dagger\right)}\hat{\sigma}^- e^{\mathrm{i}\omega_L t} \right) \quad . \end{aligned} \tag{2.22}$$

Here, the Lamb-Dicke parameter $\eta = kx_0$ was introduced. Its square defines the ratio between the photon recoil energy and the energy level spacing in the harmonic oscillator

$$\eta^2 = \frac{(\hbar k \cos\theta)^2}{2m} / \hbar\omega_T \quad \rightarrow \quad \eta = k\cos\theta \sqrt{\frac{\hbar}{2m\omega_T}} \quad , \tag{2.23}$$

where θ is the angle between the wave vector and the trap axis $\cos(\theta) = \vec{k}\hat{x}$.

The Hamiltonian can be further simplified in the rotating frame of the interaction picture with the unitary transformation $\hat{U} = e^{\mathrm{i}\hat{H}_0 t\hbar}$

$$\hat{H}_I = \hat{U}^\dagger \hat{H} \hat{U} = \frac{1}{2}\hbar\Omega \left(e^{\mathrm{i}\eta(\tilde{a}+\tilde{a}^\dagger)}\hat{\sigma}^+ e^{-\mathrm{i}\Delta t} + e^{-\mathrm{i}\eta(\tilde{a}+\tilde{a}^\dagger)}\hat{\sigma}^- e^{\mathrm{i}\Delta t} \right) \tag{2.24}$$

and the co-rotating operators $\tilde{a} = \hat{a}e^{\mathrm{i}\omega t}$ and the atom-laser detuning $\Delta = \omega_L - \omega_0$.

Allowed Transitions

The interaction Hamiltonian in Eq. (2.24) allows for transitions between internal (electronic) and external (vibrational) states. Their amplitudes are given by the matrix elements of the interaction Hamiltonian. While the diagonal elements are zero, the off-diagonal are calculated as follows[4]

$$\begin{aligned} \langle\psi'| \hat{H}_I |\psi\rangle &= \langle\uparrow, n'| \hat{H}_I |\downarrow, n\rangle \\ &= \frac{1}{2}\hbar\Omega \langle\uparrow, n'| e^{\mathrm{i}\eta(\tilde{a}+\tilde{a}^\dagger)}\hat{\sigma}^+ e^{-\mathrm{i}\Delta t} + e^{-\mathrm{i}\eta(\tilde{a}+\tilde{a}^\dagger)}\hat{\sigma}^- e^{\mathrm{i}\Delta t} |\downarrow, n\rangle \\ &= \frac{1}{2}\hbar e^{-\mathrm{i}\Delta t} \cdot \underbrace{\Omega \langle n'| e^{\mathrm{i}\eta(\tilde{a}+\tilde{a}^\dagger)} |n\rangle}_{\text{Scaled Rabi Frequency } \Omega_{n'n}} \quad . \end{aligned} \tag{2.25}$$

The transition amplitudes depend on the overall Rabi frequency Ω and on the occupation level n in the harmonic oscillator. These matrix elements can be expressed in terms of the associated Laguerre polynomials [65]

---

[4] Only Fock states are considered here since the generalization to an arbitrary state distribution is straightforward. Furthermore, the amplitudes for $\langle\downarrow, n'| \rightarrow |\uparrow, n\rangle$ are omitted here, since the derivation is the same.

$$\begin{aligned} \langle n'|\, e^{\mathrm{i}\eta(\tilde{a}+\tilde{a}^\dagger)}\, |n\rangle &= e^{-\eta^2/2}\sqrt{\frac{n_<!}{n_>!}}\eta^{|n'-n|}L_{n_<}^{|n'-n|}(\eta^2) \quad ; \\ L_n^\alpha(x) &= \sum_{k=0}^{n}(-1)^k \binom{n+\alpha}{n-k}\frac{x^k}{k!} \quad , \end{aligned} \tag{2.26}$$

where $n_<(n_>)$ is the lesser (greater) of n' and n. There are three categories of transitions:

- *carrier transition*, in which only the electronic spin is flipped while the vibrational quantum number stays unchanged; For instance, its scaled Rabi frequency for the $|{\downarrow}\rangle\,|0\rangle$ to $|{\uparrow}\rangle\,|0\rangle$ transition reads

$$\Omega_{00} = \Omega\,\langle 0|\, e^{\mathrm{i}\eta(\tilde{a}+\tilde{a}^\dagger)}\, |0\rangle = \Omega e^{-\eta^2/2} \quad . \tag{2.27}$$

- *red sideband transition*, in which the electronic spin is flipped along with a decrease of the vibrational quantum number; For instance, its scaled Rabi frequency for the $|{\downarrow}\rangle\,|1\rangle$ to $|{\uparrow}\rangle\,|0\rangle$ transition reads

$$\Omega_{10} = \Omega\,\langle 1|\, e^{\mathrm{i}\eta(\tilde{a}+\tilde{a}^\dagger)}\, |0\rangle = \Omega\eta e^{-\eta^2/2} \quad . \tag{2.28}$$

- *blue sideband transition*, in which the electronic spin is flipped along with an increase of the vibrational quantum number. The scaled Rabi frequency for the $|{\downarrow}\rangle\,|0\rangle$ to $|{\uparrow}\rangle\,|1\rangle$ is the same as the same as for the red sideband, i.e. $\Omega_{10} = \Omega_{01}$.

The blue and red sideband transitions can add or subtract multiple motional quanta at a time which is determined by the order of the transition.

Lamb-Dicke Approximation

In the limit of a very small Lamb-Dicke parameter and/or low average vibrational occupation, the wave packet is confined to a region much smaller than the transition wavelength. This is called the *Lamb-Dicke regime*. Under this condition the expression for the transition amplitudes can be expanded in a Taylor series

$$\eta^2(2n+1) \ll 1 \quad \rightarrow \quad e^{\mathrm{i}\eta(\tilde{a}+\tilde{a}^\dagger)} \approx 1 + \mathrm{i}\eta(\tilde{a}+\tilde{a}^\dagger) - \frac{\eta^2}{2}(\tilde{a}+\tilde{a}^\dagger)^2 + \cdots \tag{2.29}$$

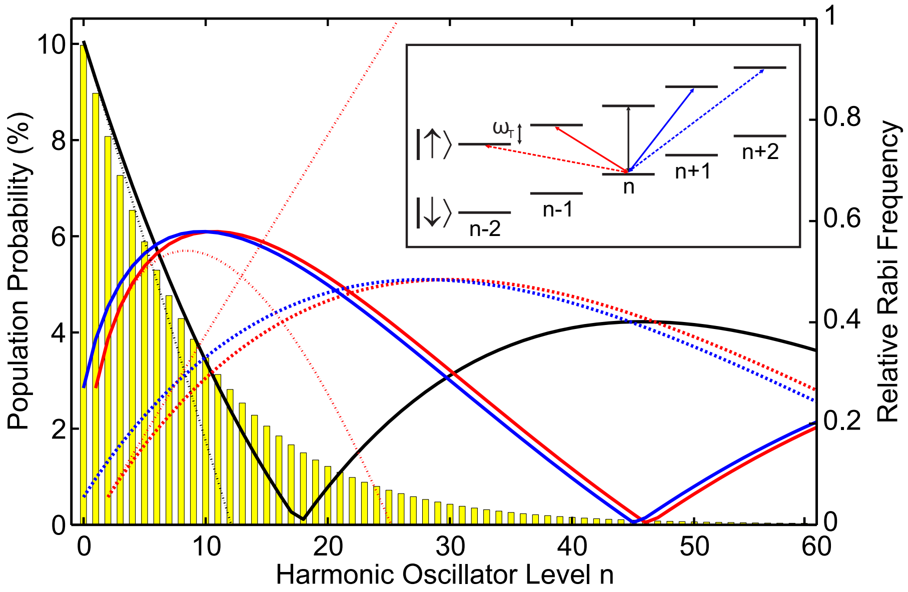

Figure 2.3: Transition amplitudes as a function of the trap level. The scaling of the Rabi frequencies (right ordinate) with the harmonic oscillator level is shown for the different types of transitions: carrier transitions (black solid line), 1st blue/red sideband (blue/red solid line), 2nd blue/red sideband (blue/red dashed line). The approximations in the Lamb-Dicke regime are depicted by the thin dot-dashed lines for the carrier and the red sidebands, only. Furthermore, the population distribution for a thermal state at the Doppler cooling temperature is plotted (yellow bars, left ordinate). The inset depicts the different types of transitions between the two hyperfine states in the same color coding. For this graph, the Lamb-Dicke parameter was chosen to be $\eta = 0.28$ and the trap frequency $\omega_T = 2\pi \times 2.2\,\mathrm{MHz}$.

The transition amplitudes take the following form up to third order in η

$$\begin{aligned} \langle n'|\, e^{\mathrm{i}\eta(\tilde{a}+\tilde{a}^\dagger)}\, |n\rangle \approx \quad & \delta_{n',n} \cdot \left\{1 - \frac{\eta^2}{2}(2n+1)\right\} \\ & + \delta_{n'-1,n} \cdot \left\{\mathrm{i}\eta\sqrt{n} - \mathrm{i}\frac{\eta^3}{2}\left(\sqrt{n}\right)^3\right\} \\ & + \delta_{n'+1,n} \cdot \left\{\mathrm{i}\eta\sqrt{n+1} - \mathrm{i}\frac{\eta^3}{2}\left(\sqrt{n+1}\right)^3\right\} \\ & + \delta_{n'-2,n} \cdot \left\{-\frac{\eta^2}{2}\sqrt{(n-1)n}\right\} \\ & + \delta_{n'+2,n} \cdot \left\{-\frac{\eta^2}{2}\sqrt{(n+1)(n+2)}\right\} \quad , \end{aligned} \tag{2.30}$$

where $\delta_{n',n}$ represents the Kronecker-Delta. The amplitudes are sorted by the different transition forms: $\langle n'|n\rangle$ corresponds to a carrier transition, whereas $\langle n' \pm 1|n\rangle$ ($\langle n' \pm 2|n\rangle$) correspond to 1st (2nd) order sideband transitions. The transition amplitudes along with their approximate results (Eq. (2.30)) are plotted in Fig. 2.3.

2.2.3 Coherent Manipulation

In the following two sections a description of the coherent coupling of the two hyperfine states, noted $|\uparrow\rangle$ ($\left|F_\uparrow, m_{F_\uparrow}\right\rangle = |2, 2\rangle$) and $|\downarrow\rangle$ ($\left|F_\downarrow, m_{F_\downarrow}\right\rangle = |3, 3\rangle$), is given. The coupling is employed either by using two-photon stimulated Raman transitions or by a direct application of radio-frequency fields. The discussion is restricted to the coupling between the qubit states via the $\mathrm{P}_{3/2}$ state. For a more detailed analysis on Raman-induced Rabi oscillations, the reader is referred to [82, 83].

Raman Transitions

Coherent transitions between the hyperfine ground states ($|\downarrow\rangle$ and $|\uparrow\rangle$) are achieved by applying two phase-coherent laser fields[5] $\vec{E} = \hat{\epsilon}_1 E_1 \cos(\omega_1 t + \vec{k}_1 \vec{r}) + \hat{\epsilon}_2 E_2 \cos(\omega_2 t + \vec{k}_2 \vec{r})$ to the ion, where $E_{1,2}$ are the laser field amplitudes, $\vec{k}_{1,2}$ correspond to the wave vectors and $\hat{\epsilon}_{1,2}$ represent the unit polarization vectors of each laser field.

Under the assumption that both lasers couple off-resonantly to intermediate states $|i\rangle$ whose detunings are large compared to their individual decay rates, $\Delta_i \gg \Gamma_i$, the auxiliary states are not significantly populated. If the difference of the laser field energies furthermore corresponds to the energy difference of the hyperfine states, i.e. $\omega_1 - \omega_2 \sim \omega_\uparrow - \omega_\downarrow$, the states undergo sinusoidal Rabi-type oscillations. The 2-level Rabi frequency is replaced by an effective Rabi frequency which reads

$$\Omega_{\mathrm{eff}} = \frac{E_1 E_2}{4\hbar^2} \sum_i \frac{\langle \uparrow | \hat{\vec{d}} \cdot \hat{\epsilon}_1 | J_i F_i m_{F_i} \rangle \langle J_i F_i m_{F_i} | \hat{\vec{d}} \cdot \hat{\epsilon}_2 | \downarrow \rangle}{\Delta_i} \quad , \tag{2.31}$$

where $\hat{\vec{d}}$ represents the dipole operator. It is convenient to rewrite this operator in spherical components as follows [84]:

$$\begin{aligned} \hat{d}_{\sigma^\pm} &= \frac{1}{\sqrt{2}}(\mp \hat{d}_x - \mathrm{i}\hat{d}_y) \quad ; \\ \hat{d}_\pi &= \hat{d}_z \quad . \end{aligned} \tag{2.32}$$

The indices represent the different transition types, π corresponding to a transition which does not change the magnetic quantum number, whereas $\sigma^\pm$ changes it by ± 1.

Here, a Raman transition, comprised of a combination of σ- and π-polarized laser beams, is considered to couple the hyperfine states (see Fig. 2.4). Using the Wigner-

---

[5] One way to realize such laser fields is to split one laser beam into two branches and shift each branch using acousto-optic modulators to bridge the frequency difference of the two long-lived ground states. This way laser phase fluctuations are common mode rejected, since both branches originate from the same local oscillator, while the frequency difference is in the radio-frequency regime and thus easily controlled with high precision.

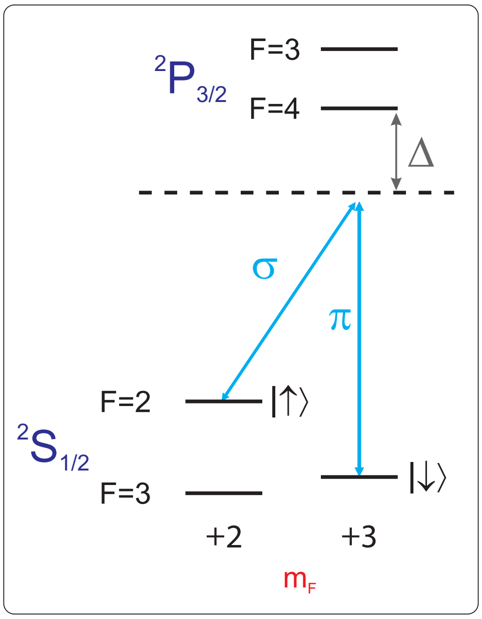

Figure 2.4: Coherent manipulation of the ion. The Raman transition between the two hyperfine ground states driven by a π-polarized and a phase-coherent σ-polarized beam is shown. Both lasers are resonant to a virtual level which is detuned by $\Delta = 2\pi \times 9.2\,\mathrm{GHz}$ with respect to the $\mathrm{P}_{3/2}$-state.

Eckart theorem, the effective Rabi frequency simplifies to [78, 85]

$$\begin{aligned}
\sum_i \frac{1}{\Delta_i}\langle\uparrow|\hat{d}_{\sigma_+}\cdot\hat{\epsilon}_{1,\sigma_+}|J_iF_im_{F_i}\rangle\langle J_iF_im_{F_i}|\hat{d}_\pi\cdot\hat{\epsilon}_{2,\pi}|\downarrow\rangle &= \\
\sum_i \frac{1}{\Delta_i}\langle\uparrow||\hat{d}||J_iF_i\rangle\langle\uparrow|F_im_{F_i}J_{ph}q_1\rangle\cdot\langle J_iF_i||\hat{d}||\downarrow\rangle\langle F_im_{F_i}|\downarrow J_{ph}q_2\rangle &= \\
\sum_i \frac{1}{\Delta_i}\langle\uparrow||\hat{d}||J_iF_i\rangle(-1)^{F_i-1+m_\uparrow}\sqrt{2F_\uparrow+1}\begin{pmatrix} F_i & J_{\mathrm{ph}} & F_\uparrow \\ m_{F_i} & q_1 & -m_{F_\uparrow}\end{pmatrix}_{3j} &\cdot \\
\langle J_iF_i||\hat{d}||\downarrow\rangle(-1)^{F_\downarrow-1+m_{F_i}}\sqrt{2F_i+1}\begin{pmatrix} F_\downarrow & J_{\mathrm{ph}} & F_i \\ m_{F_\downarrow} & q_2 & -m_{F_i}\end{pmatrix}_{3j} &,
\end{aligned} \tag{2.33}$$

where the photon angular momentum is given by $J_{\mathrm{ph}} = 1$ and the polarizations are defined by $q_1 = -1$ and $q_2 = 0$. In this sum, the Wigner 3-j symbols are non-zero only if the following selection-rules are fulfilled:

$$\begin{aligned}
m_{F_i} + q_1 = m_{F_\uparrow} \quad &; \\
m_{F_\downarrow} + q_2 = m_{F_i} \quad &.
\end{aligned} \tag{2.34}$$

This relation represents the conservation of angular momentum of the photon-electron system.

The reduced matrix elements $\langle\cdot||\cdot||\cdot\rangle$ can be further simplified in terms of the Wigner 6-j symbols

$$\begin{aligned}\langle\uparrow||\hat{d}||J_iF_i\rangle &= (-1)^{J_\uparrow+I+F_i+1}\sqrt{(2J_\uparrow+1)(2F_i+1)}\begin{Bmatrix} J_\uparrow & F_\uparrow & I \\ F_i & J_i & 1\end{Bmatrix}_{6j}\langle J_\uparrow||\hat{d}||J_i\rangle \quad ; \\ \langle J_iF_i||\hat{d}||\downarrow\rangle &= (-1)^{J_i+I+F_\downarrow+1}\sqrt{(2J_i+1)(2F_\downarrow+1)}\begin{Bmatrix} J_i & F_i & I \\ F_\downarrow & J_\downarrow & 1\end{Bmatrix}_{6j}\langle J_i||\hat{d}||J_\downarrow\rangle \quad .\end{aligned} \tag{2.35}$$

It should be noted that different normalizations are used in the literature. This issue is discussed in Appendix A.

Using the fact that the Wigner 3-j symbols are non-vanishing for $F_i = 3$ and $m_{F_i} = 3$ only, the final expression for the effective Rabi frequency reads

$$|\Omega_{\text{eff}}| = \frac{E_1E_2}{4\hbar^2\Delta}\left(\frac{\sqrt{5}}{3\sqrt{6}}\cdot|\langle J=1/2||d||J=3/2\rangle|^2\right) \quad . \tag{2.36}$$

Taking the motion of the ion in the trap into account, this Rabi frequency is to be scaled with the transition amplitudes in Eq. (2.26) to obtain the Rabi frequencies as a function of the harmonic oscillator level for the specific transition type: For instance, the scaled Rabi frequency for the carrier transition of the ground state reads $\Omega_{0,0} = \Omega_{\text{eff}}e^{-\eta^2/2}$. The Lamb-Dicke parameter η is determined by the k-vector difference of the Raman beams, i.e. $k = |\vec{k}_1 - \vec{k}_2|$ in Eq. (2.23). It has a typical value of $\eta \sim 0.3$ in our experiments.

Besides the coherent coupling between the qubit levels, the interaction of the laser field shifts the energy levels according to [83]

$$\delta_\uparrow = \sum_i \frac{E_1^2}{4\hbar^2\Delta_i}|\langle\uparrow|d\vec{\epsilon}|i\rangle|^2 \quad \text{and} \quad \delta_\downarrow = \sum_i \frac{E_2^2}{4\hbar^2\Delta_i}|\langle\downarrow|d\vec{\epsilon}|i\rangle|^2 \quad , \tag{2.37}$$

where the detuning Δ_i is large compared to the decay rate $\Delta_i \gg \Gamma_i$ of state $|i\rangle$. This effect is called *AC-Stark shift*. The sum includes coupling to all excites states.

Consequently, the transition frequency between the $|\downarrow\rangle$ and $|\uparrow\rangle$ states is changed by the difference of the individual shifts $\delta_\downarrow - \delta_\uparrow$. In contrast to the Rabi frequency calculation presented before, the $\mathrm{P}_{3/2}$ $|4,3\rangle$ level has to be taken into account, since it couples to the π-polarized Raman beam. The differential shift of the states reads

$$\begin{aligned}\delta_\uparrow - \delta_\downarrow &= g_2^2\frac{2}{9}\frac{1}{\Delta} - g_1^2\left(\frac{5}{24}\frac{1}{\Delta} + \frac{1}{8}\frac{1}{\Delta+\omega_{\text{HF}}}\right) \\ &\approx \frac{2g_2^2 - 3g_1^2}{9\Delta} \quad ,\end{aligned} \tag{2.38}$$

where the hyperfine splitting of the excited states was neglected, since $\Delta \gg \omega_{\mathrm{HF}}$, and the constants g_i are defined as $g_i = \frac{E_i^2}{4\hbar^2\Delta}| \langle J = 1/2||d||J = 3/2\rangle |^2$. In principle the Stark shift can be compensated for by choosing the relative beam intensities as $g_1^2 = \frac{2}{3}g_2^2$. However, for practical reasons, this is commonly done in a different way by choosing different polarizations for each individual beam. An example for this type of compensation for the case of $^9\mathrm{Be}^+$ can be found in [82].

Radio-Frequency Transitions

The second possibility for a coherent coupling between the two hyperfine ground states in $^{25}\mathrm{Mg}^+$ is by directly exciting the magnetic dipole (M1) transition with a radio-frequency field at 1.789 GHz.

The transition amplitudes between the different Zeeman sub-states are calculated in the same way as above using the Wigner-Eckart theorem with the magnetic dipole operator $M = \vec{\mu}_{\mathrm{M}}\vec{B}$

$$\langle F m_{\mathrm{F}}|M|F' m_{\mathrm{F'}}\rangle = (-1)^{F-m_{\mathrm{F}}-1}\sqrt{2F'+1}\begin{pmatrix} F & 1 & F' \\ m_{\mathrm{F}} & q & -m_{\mathrm{F'}} \end{pmatrix}\langle F||M||F'\rangle \quad , \tag{2.39}$$

where q corresponds to the polarization of the oscillating field and $\vec{\mu}_{\mathrm{M}}$ represents the magnetic dipole moment. Similar to the electric dipole transition, the same selection rules apply. The matrix elements are non-zero, if $m_{\mathrm{F}} + q - m_{\mathrm{F'}} = 0$, where $q = 0$ corresponds to π-transitions and $q = \pm 1$ represents $\sigma^{\pm}$-transitions between the Zeeman states.

The Lamb-Dicke parameter for radio-frequency transitions is extremely small, namely $\eta \sim 10^{-7}$ for a harmonic trapping frequency of 2 MHz. As a result, sideband transitions can only be driven with very high field amplitudes since their Rabi frequency is reduced by the factor η (see Section 2.2.2). This is not possible in our experiment and consequently only carrier transitions are driven by application of radio-frequency fields. It is worth mentioning that in a recent experiment that employs a surface-electrode trap high radio-frequency field gradients could be achieved to overcome this limit and drive carrier and sideband transitions in the ion [86].

Chapter 3

Theoretical Description of Direct Frequency Comb Spectroscopy

In usual fluorescence spectroscopy, a cw-laser is used to excite an atomic transition and fluorescence due to spontaneous emission is then recorded as a spectroscopy signal. Measuring the fluorescence spectrum as a function of the laser detuning with respect to the atomic resonance frequency yields the desired frequency information about the transition under investigation. This situation is rather different when a frequency comb is used as a spectroscopic probe instead. In the frequency domain, this situation can be understood as if a large number of very low-power cw-lasers (> 100000) excited the atomic transition. For a multi-level system, this means that many transitions are excited simultaneously and multi-photon processes also become relevant, since photons from different parts of the comb spectrum can participate in the excitation. Those processes occurring concomitantly, it cannot be unambiguously identified which photon (or comb tooth) excited a certain transition only by measuring fluorescence photons; the interpretation of the acquired signals is thus rendered accordingly difficult.

Looking at the interaction in the time domain is equally challenging. Since a frequency comb is generated by a train of phase-stabilized femtosecond laser pulses with repetition periods typically from 100 MHz up to 1 GHz, each pulse interferes with the coherence built-up in the ion, i.e. the ion acts as an interferometer for the cascading pulses. Each of the pulses containing many frequency components, again, it cannot be unambiguously decided only by measuring the fluorescence which component excited a specific transition after the interaction with a single laser pulse.

It is also worthwhile mentioning that it is the pulsed nature of this spectroscopy probe that imposes a fundamental limitation on the types of transitions that can be investigated. If the lifetime of the excited states is much smaller than the repetition period of the frequency comb, no significant population can be transferred to the excited states since they decay completely via spontaneous emission before the arrival of the consecutive laser pulse. Thus, in practise the ion will not experience a frequency comb spectrum since the interference with the following pulses is suppressed and the frequency resolution of the spectroscopy is restricted to that of a single laser pulse.

For these reasons, it is important to have a good understanding of the underlying dynamics of the ion-comb interaction in order to interpret the acquired complex spectra. In this chapter, these dynamics are theoretically developed yielding the expected population evolution as a function of the exact comb parameters. In the first part, the frequency comb structure is derived from a train of phase-stabilized laser pulses. In the second part, the semi-classical optical Bloch equations are solved to determine the time-evolution of the atomic states.

3.1 Spectrum of a Phase-Stabilized Pulsed Laser

In this section, the spectrum of a phase-stabilized pulsed laser is derived in the time-domain. In this picture, the interference of consecutive laser pulses leads to the emergence of a frequency comb structure. In an equivalent alternative way, this derivation can be done in the frequency-domain (see e.g. [47]).

Let $E_k(t)$ be the electric field of a single laser pulse

$$E_k(t) \quad = \quad \sigma(t) \cdot \left(e^{\mathrm{i}\omega_c t + \mathrm{i}\phi_k} + c.c.\right) \quad , \tag{3.1}$$

where $\sigma(t)$ is a real-valued envelope function. This function is usually assumed to be a Gaussian or a hyperbolic secant, i.e. for example $\sigma(t) = e_0 \cdot \mathrm{sech}(t/\sigma)$ with a field amplitude e_0. The laser carrier frequency is denoted by ω_c and ϕ_k represents the carrier-envelope phase.

A phase-stable train of p pulses is then given by

$$E_T(t) = \sum_{k=0}^{p} E_k(t - t_k) = \sum_{k=0}^{p} \sigma(t - t_k) \cdot e^{\mathrm{i}\omega_c(t-t_k)+\mathrm{i}\phi_k} \quad , \tag{3.2}$$

where the following definitions are used:

$$\begin{aligned} t_k &= \frac{k}{\nu_R} = k\tau_R \quad ; \\ \phi_k &= \phi_0 + k \cdot \delta\phi \quad ; \\ \delta\phi &= 2\pi \cdot \frac{\nu_0}{\nu_R} = \omega_0 \tau_R \quad . \end{aligned} \tag{3.3}$$

Here, $\nu_R = \tau_R^{-1}$ is the repetition rate of the train of pulses, $\omega_0 = 2\pi\nu_0$ the offset frequency,

ϕ_0 an initial offset-phase and $\delta\phi$ a constant pulse-to-pulse phase shift. The reasons for these designations will become clear in the frequency domain, which is considered in what follows.

The Fourier spectrum of the train of pulses $E_T(t)$ reads

$$\mathrm{FT}\left\{E_T(t)\right\} = \sum_{k=0}^{p}\left\{e^{-\mathrm{i}\omega t_k+\mathrm{i}\phi_k}\sigma_F\left(\omega-\omega_c\right)+e^{-\mathrm{i}\omega t_k-\mathrm{i}\phi_k}\sigma_F\left(\omega+\omega_c\right)\right\} \quad , \tag{3.4}$$

where $\sigma_F(\omega)$ is the Fourier transform of the envelope function. The second term will be left out henceforth since it only represents the (symmetric) negative frequencies.

$$\begin{aligned}\mathrm{FT}\left\{E_T(t)\right\} &= \sigma_F\left(\omega-\omega_c\right)\cdot\sum_{k=0}^{p}e^{-\mathrm{i}\omega t_k+\mathrm{i}\phi_k}\\ &= \underbrace{\sigma_F\left(\omega-\omega_c\right)}_{\text{envelope}}\cdot e^{\mathrm{i}\phi_0}\cdot\underbrace{\sum_{k=0}^{p}e^{-\mathrm{i}(\omega-\omega_0)k\tau_R}}_{\text{comb structure}} \quad .\end{aligned} \tag{3.5}$$

The sum is simplified as (see Appendix D)

$$\mathrm{FT}\left\{E_T(t)\right\} = \sigma_F\left(\omega-\omega_c\right)\cdot e^{-\mathrm{i}(\omega-\omega_0)\frac{p}{2}\tau_R+\mathrm{i}\phi_0}\cdot\left\{\frac{\sin\left(\frac{1}{2}(\omega-\omega_0)(p+1)\tau_R\right)}{\sin\left(\frac{1}{2}(\omega-\omega_0)\tau_R\right)}\right\} . \tag{3.6}$$

The extrema of this function are found when $(\omega-\omega_0)\cdot\tau_R/2=\pi\cdot n$, yielding

$$\boxed{\omega=\omega_0+\omega_R\cdot n} \quad \text{with } n\in\{0,1,2,\ldots\}$$

This periodic structure corresponds to a frequency comb in the Fourier domain. The offset frequency ω_0 results from the constant pulse-to-pulse phase shift. The repetition rate of the laser pulses is reflected in the equidistant structure of the comb teeth.

The power spectrum of the frequency comb is given by the square of the Fourier transform of the electric field

$$\begin{aligned}P(\omega) &= \left|\mathrm{FT}\left\{E_T(t)\right\}\right|^2\\ &= \left|\sigma_F\left(\omega-\omega_c\right)\right|^2\cdot\left\{\frac{\cos\left((\omega-\omega_0)\cdot(p+1)\cdot\tau_R\right)-1}{\cos\left((\omega-\omega_0)\cdot\tau_R\right)-1}\right\} \quad .\end{aligned} \tag{3.7}$$

Using the rule of L'Hôpital, the power value at the position of the comb teeth is given by

$$P(\omega_0+\omega_R\cdot n)=\left|\sigma_F\left(\omega_0+\omega_R\cdot n-\omega_c\right)\right|^2\cdot(p+1)^2 \quad . \tag{3.8}$$

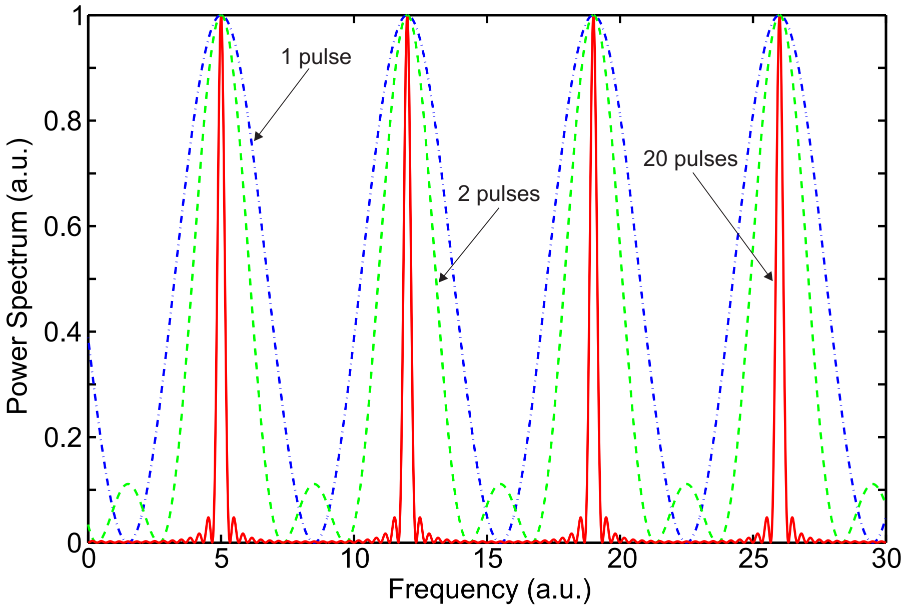

Figure 3.1: The normalized power comb spectrum $P(\omega)/|\sigma_F(\omega-\omega_c)|^2(p+1)^2$ is depicted. The difference in the curves is the number of total pulses (blue dot-dashed line: 1 pulse, green dashed line: 2 pulses, red solid line: 20 pulses). The emergence of the comb structure after the interference of even a small number of pulses is clearly observed.

The divergence in the power spectrum for an infinite number of pulses is explained by the fact that the comb teeth transform into peak-like delta-distributions which are Fourier limited in width. In Fig. 3.1, the comb spectrum for a different number of pulses p is shown. Even after only a few pulses, the emergence of the comb structure is clearly visible.

3.2 Time Evolution of the Atomic System

In this section, the interaction of the phase-locked pulsed laser with a multi-level atom is described in the framework of the semi-classical optical Bloch equations. An efficient numerical algorithm is developed with which the temporal evolution of the population in the different energy states of the multi-level atom can be obtained as a function of the comb parameters.

Numerically[1], one major challenge is the existence of very different timescales (see Fig. 3.2): the pulse length (typically $\sim 10-100\,\mathrm{fs}$), the repetition rate (typically $\sim 1\,\mathrm{ns}$) and the spontaneous decay (typically $\sim$ 10th of ns). As a consequence, during the interaction of the laser pulse with the ion, spontaneous decay can be neglected. After the interaction took place, a period of free evolution that is only governed by spontaneous emission events follows and consequently laser interaction is neglected. These approximations are used in the following considerations.

---

[1] An analytical result for a two-level system interacting with a pulse train is found in [87].

The algorithm discussed here is based and adapted from the work of D. Felinto [88, 89, 90] and A. Marian [91]. In contrast to these references, the interaction Hamiltonian is not expanded and approximated in a Dyson series, instead solved numerically. This introduces more flexibility in the application. For instance, in the case of $^{40}\mathrm{Ca}^+$, the existence of clock transitions (from the S to the D states), along with dipole transitions (from the S to the P states), introduces transition matrix elements which differ by orders of magnitude, preventing the Dyson series to converge. This problem is overcome in the approach presented here.

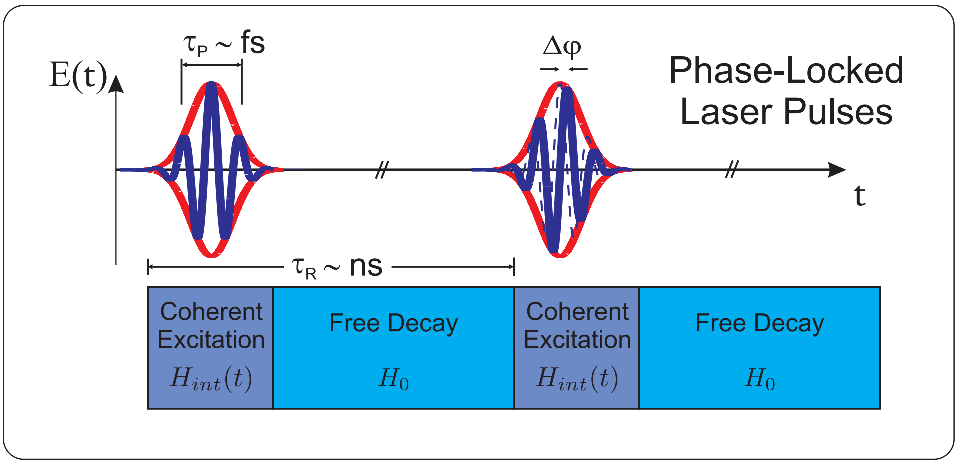

Figure 3.2: Time scales in the comb theory. The comb is comprised of phase-locked laser pulses with a width on the femto-second scale, while the repetition period is typically in the nano-second regime. As a consequence, the laser-atom interaction only needs to be taken into account during the shorter timescale, while a process of (trivial) free decay governs the longer periods between the pulses.

3.2.1 Definition of the Ion-Laser-Trap System

The atomic system confined in an ion trap is represented by a set of N electronic energy states $\{|r\rangle\}$ and a set of N_{trap} harmonic oscillator levels $\{|n\rangle\}$. As shown in Fig. 3.3, the energy of the states of the combined system are sorted $\epsilon_1 \leq \epsilon_2 \leq \cdots \leq \epsilon_{N \cdot N_{\text{trap}}}$. They read[2]

$$\epsilon_i := \epsilon_{r,n} = \epsilon'_r + \hbar\omega_T \cdot \left(n + \frac{1}{2}\right) \quad , \tag{3.9}$$

---

[2] For simplicity, an additional magnetic field is not considered in the simulation here. This is, however, easily added by shifting the energies correspondingly as $m^r_{F/J} \cdot g^r_{F/J} \cdot \mu_{\mathrm{B}} B_z$, where $m^r_{F/J}$ is the magnetic quantum number, $g^r_{F/J}$ the Landé-factor of the rth electronic level (including magnetic sub-states).

where r denotes the electronic levels with $r = 1, \ldots, N$, ω_T the trap frequency, n the trap excitation quantum number with $n = 1, \ldots, N_\mathrm{trap}$ and $i = n + N_\mathrm{trap}(r-1)$.

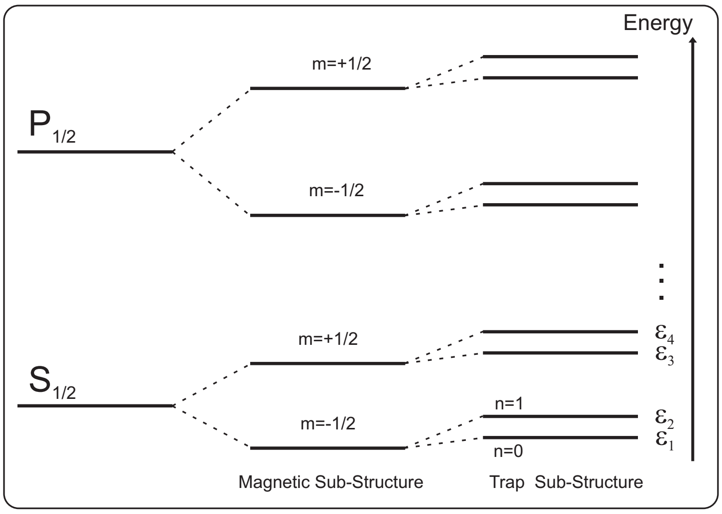

Figure 3.3: Energy level nomenclature for the ion-comb-trap system. The energies are sorted $\epsilon_1 \leq \epsilon_2 \leq \cdots \leq \epsilon_{N \cdot N_\mathrm{trap}}$. This is an example for an S-P level system including magnetic sub-structure and two harmonic trap levels.

In the same way, we define the set of energy states as $|i\rangle := |r\rangle\,|n\rangle$.

The dipole matrix elements μ_{ij} between energy levels i and j are determined by the Einstein A_{ij} coefficients and the laser polarization (see Section 2.2.2 and Appendix B),

$$\mu_{ij} \quad = \quad \langle i|\hat{\epsilon}\vec{r}|j\rangle = C_{ij} \cdot \sqrt{\frac{3\epsilon_0 \hbar A_{ij} \lambda_{ij}^3}{8\pi^2}} \quad , \tag{3.10}$$

where $\hat{\epsilon}$ is the polarization vector, C_{ij} the Clebsch-Gordan coefficient and λ_{ij} the wavelength of the corresponding transition. In order to take the effect of the harmonic confinement into account, the Einstein coefficients need to be replaced by scaled coefficients which are a function of the trap level and the Lamb-Dicke parameter of the particular transition[3]

$$A_{ij} = A_{ij}(\eta_{ij}) \quad \text{with} \quad \eta_{ij} = \frac{2\pi}{\lambda_{ij}} \cdot \sqrt{\frac{\hbar}{2m\omega_T}} \quad . \tag{3.11}$$

With the above designated quantities, the total Hamiltonian of the atomic system interacting with a train of p laser pulses in the dipole approximation reads

---

[3] This introduces the different strength of the carrier and the sideband transitions in the system. See Section 2.2.2 for their functional behavior. The Einstein coefficients have to be multiplied by the square of the corresponding transition amplitudes between different trap levels.

$$\begin{aligned}
H &= H_0 + H_{int} \quad ; \\
H_0 &= \sum_{i=1}^{N} \epsilon_i |i\rangle\langle i| \quad ; \\
H_{\text{int}} &= -E_T(t) \sum_{i,j} \mu_{ij} |i\rangle\langle j| + c.c. \quad ; \\
E_T(t) &= \sum_{k=0}^{p} \sigma(t-t_k) e^{\mathrm{i}\omega_c(t-t_k)+\mathrm{i}\phi_k} + c.c. \quad ,
\end{aligned} \tag{3.12}$$

where $\hbar\omega_{ij} = \epsilon_j - \epsilon_i$. It should be noted that the Hamiltonian is periodic with a change in the carrier-envelope phase $\phi_k = \phi_0 + k\omega_0\tau_R$ from pulse-to-pulse. This feature is used in the following derivation.

3.2.2 Optical Bloch Equations with a Pulsed Laser

In the following, the approximations mentioned in the introduction that make use of the different timescales in the system are used develop an iterative algorithm which outputs the state of the system after the interaction with a single laser pulse and a period of spontaneous decay. The final state serves again as an input of the algorithm to interact with the consecutive laser pulse. Following this protocol, the density matrix after a certain number of pulses is determined.

The time-evolution of the atom-laser system is modelled by the semi-classical optical Bloch equation. In the density matrix formalism, they read

$$\dot{\rho}_{ij} \quad = \quad -\frac{\mathrm{i}}{\hbar} [H, \rho]_{ij} - \Gamma_{ij}\rho_{ij} + \delta_{ij} \sum_r \gamma_{ir}\rho_{rr} \quad . \tag{3.13}$$

Here, Γ_{ij} represent the decay rates of the matrix elements and γ_{ij} the population 'feeding' terms, i.e. γ_{ij} is the rate with which the jth level decays into the ith level. The Kronecker-Delta guarantees that these terms only occur on the diagonal. The parameters follow the properties

$$\begin{aligned}
\gamma_{ij} &= C_{ij}^2 \cdot \tilde{A}_{ij}(\tilde{\eta}_{ij}) \quad ; \\
\Gamma_{jj} &= \sum_i \gamma_{ij} \quad ; \\
\Gamma_{ij} &= \frac{1}{2} (\Gamma_{ii} + \Gamma_{jj}) \quad .
\end{aligned} \tag{3.14}$$

It should be noted that the Einstein coefficients $\tilde{A}_{ij}(\tilde{\eta})$ used here, differ from the previous one used in the calculation of the matrix elements in Eq. (3.10). In contrast to the laser excitation, which is determined by the direction of the wave vector $\vec{k}$, the spontaneous decay can emit photons into the full solid angle. This effect reduces the Lamb-Dicke parameter for the decay. It is assumed in the simulations here, that the emission occurs with equal probability in each direction and the Lamb-Dicke parameter is assumed to be an average over all three direction, thus $\tilde{\eta}_{ij} \approx \frac{1}{3}\sum_{k\in\{x,y,z\}} \eta_{ij}(\omega_k)$. For typical experimental parameters for an axial trapping frequency $\omega_z = 2\pi \times 2\,\mathrm{MHz}$ and radial trapping frequencies $\omega_{x,y} = 2\pi \times 5\,\mathrm{MHz}$ we find $\tilde{\eta}_{ij} \sim 0.8 \cdot \eta_{ij}(\omega_z)$.

For simplification, the Bloch equations are transformed into the rotating frame of the interaction picture (denoted I), i.e.

$$\dot{\rho}^I_{ij} \quad = \quad -\frac{\mathrm{i}}{\hbar}\left[H^I_{\mathrm{int}}, \rho^I\right]_{ij} - \Gamma_{ij}\rho^I_{ij} + \delta_{ij}\sum_r \gamma_{ir}\rho^I_{rr} \quad . \tag{3.15}$$

After applying the rotating wave approximation where fast-oscillating terms are neglected [92], the quantities in the interaction picture are of the form

$$\begin{aligned} H^I_{\mathrm{int}} &= U_0^\dagger H_{\mathrm{int}} U_0 = -\sum_{k=0}^{p}\sum_{i,j}\sigma(t-t_k)e^{-\mathrm{i}\Delta^I_{ij}(t-t_k)+\mathrm{i}(\phi_k-\omega_{ij}t_k)}\mu_{ij}|i\rangle\langle j| + c.c. \\ \rho^I &= U_0^\dagger \rho U_0 \quad \rightarrow \quad \rho^I_{ij} = e^{-\mathrm{i}\omega_{ij}t}\rho_{ij} \quad , \end{aligned} \tag{3.16}$$

where $U_0 = e^{-i\frac{H_0}{\hbar}t}$ and $\hbar\Delta^I_{ij} = \omega_{ij} - \omega_c$.

It is now convenient to integrate the optical Bloch equations in order to use the mentioned approximations regarding the timescales of the system. The goal is to seek the density matrix after the interaction of the system with the kth laser pulse. For this, the Bloch equations are integrated over one repetition period $(t_1, t_2) := (k\tau_R, (k+1)\tau_R)$. The integral form of the optical Bloch equations reads[4]

$$\boxed{\begin{aligned} \rho^I_{ij}(t_2) = e^{-\Gamma_{ij}\cdot(t_2-t_1)}\Bigg(&\rho^I_{ij}(t_1) - \frac{\mathrm{i}}{\hbar}\int_{t_1}^{t_2} dt' e^{\Gamma_{ij}\cdot(t'-t_1)}\left[H^I_{\mathrm{int}}, \rho^I\right]_{ij} \\ &+\delta_{ij}\sum_r \gamma_{ir}\int_{t_1}^{t_2} dt' e^{\Gamma_{ii}\cdot(t'-t_1)}\rho^I_{rr}(t')\Bigg) \end{aligned}} \tag{3.19}$$

---

[4] Here, the following trivial relation was used:

$$\dot{\rho}(t) \quad = \quad \alpha\rho(t) + f(t) \qquad \Bigg| \cdot \int_{t_1}^{t_2} dt' e^{-\alpha t'} \tag{3.17}$$

$$\rightarrow \rho(t_2) \quad = \quad e^{\alpha(t_2-t_1)}\left(\rho(t_1) + \int_{t_1}^{t_2} dt' e^{\alpha(t_1-t')} f(t')\right) \tag{3.18}$$

Here, $\rho^I(t_2)$ corresponds to the density matrix after the pulse, whereas $\rho^I(t_1)$ represents the density matrix prior to the kth laser pulse.

These equations are further simplified by using the fact that the interaction of the laser pulse with the atom is short compared to all other timescales in the system.

Approximations and Iterative Method

Since the electric field in the interaction Hamiltonian H^I_{int} is only present for a short time on the order of femto-seconds, the exponential term is approximately unity for both diagonal and off-diagonal elements, i.e. $\Gamma_{ij} \cdot (t_2' - t_1) \approx 0$ for $t_2' = t_1 + \epsilon$ where $\epsilon \sim 10^{-13} s$ denotes the length of the pulse and $\Gamma \sim 10^8 s^{-1}$ is the typical atomic relaxation rate. The integral is simplified as

$$\int_{t_1}^{t_2'} dt' e^{\Gamma_{ij} \cdot (t' - t_1)} \left[H^I_{\text{int}}, \rho^I\right]_{ij} \approx \int_{t_1}^{t_2'} dt' \left[H^I_{\text{int}}, \rho^I\right]_{ij} \quad . \tag{3.20}$$

In the same way, the feeding terms are neglected during the laser pulse excitation

$$\int_{t_1}^{t_2'} dt' e^{\Gamma_{ii} \cdot (t' - t_1)} \rho^I_{rr} \approx \epsilon \cdot \rho^I_{rr} \approx 0 \quad . \tag{3.21}$$

This leads to the following expressions for the density matrix

$$\begin{aligned} \rho^I_{ij}(t_2) &= e^{-\Gamma_{ij} \cdot (t_2 - t_1)} \cdot \left(\rho^{I,c}_{ij}(t_2') + \delta_{ij} \sum_r \gamma_{ir} \int_{t_2'}^{t_2} dt' e^{\Gamma_{ii} \cdot (t' - t_1)} \rho^I_{rr} \right) \quad ; \\ \text{with} \quad \rho^{I,c}_{ij}(t_2') &= \rho^I_{ij}(t_1) - \frac{\mathrm{i}}{\hbar} \int_{t_1}^{t_2'} dt' \left[H^I_{\text{int}}, \rho^I\right]_{ij}(t') \quad , \end{aligned} \tag{3.22}$$

where $\rho^{I,c}_{ij}$ is the coherently excited density matrix. It only takes the unitary interaction of the laser with the atomic system into account.

The algorithm to solve for the time-evolution works in the following way:

1. Given the initial conditions for the density matrix and the frequency comb, namely population distribution, offset frequency and repetition rate, the Hamiltonian H^I_{int} is determined and the coherently excited density matrix Eq. (3.22) is solved. This yields the time evolution of the density matrix during a single laser pulse on a femtosecond timescale.

2. After the laser pulse excited the system, Eq. (3.22) is applied to the density matrix, which corresponds to a free evolution of the system since no laser field is present for the rest of the repetition period.

3. Repeat steps 1 and 2 while using the resulting density matrix of step 2 as new initial condition to apply the next pulse to the system. It should be noted that the Hamiltonian H_{int}^I has to be adjusted for each pulse due to the pulse-to-pulse change of the carrier-envelope phase.

This algorithm is applied up to the number of desired pulses. In the following, the solution to the different parts of Eq. (3.22) and Eq. (3.22) are presented.

Coherently Excited Density Matrix

The coherently excited density matrix is best determined using the time propagation formalism. First, Eq. (3.22) is rewritten in differential form

$$\dot{\rho}_{ij}^{I,c} = -\frac{\mathrm{i}}{\hbar}\left[H_{\text{int}}^I, \rho^I\right]_{ij} \quad , \tag{3.23}$$

The formal solution of this differential equation is given by

$$\rho^{I,c}(t_2) = U_I(t_2, t_1) \cdot \rho^{I,c}(t_1) \cdot U_I^\dagger(t_1, t_2) \quad , \tag{3.24}$$

where $U_I(t)$ denotes the time-propagation operator. It is determined by the Schrödinger equation $\mathrm{i}\hbar\dot{U}_I(t) = H_{\text{int}}^I(t)U_I(t)$. In order to solve for the time propagation operator that yields the time evolution between consecutive pulses k and $k+1$, the time variable is shifted $t = t' + k\tau_R$ and the Schrödinger equation is integrated over one repetition period:

$$\begin{aligned}
&\mathrm{i}\hbar\dot{U}_I(t' + k\tau_R, \varphi_k) \\
= \;& H_{\text{int}}^I(t' + k\tau_R)U_I(t' + k\tau_R, \varphi_k) \\
= \;& \left(-\sum_{m=0}^{p}\sum_{i,j}\sigma(t' + (k-m)\tau_R)e^{-\mathrm{i}\Delta_{ij}^I(t'+(k-m)\tau_R)+\mathrm{i}\varphi_m}\mu_{ij}|i\rangle\langle j|\right)U_I(t' + k\tau_R, \varphi_k) \\
\approx \;& \underbrace{\left(-\sum_{i,j}\sigma(t')e^{-\mathrm{i}\Delta_{ij}^I t'+\mathrm{i}\varphi_k}\mu_{ij}|i\rangle\langle j|\right)}_{=:H_{k,\text{int}}^I(t'+k\tau_R)}U_I(t' + k\tau_R, \varphi_k) \\
= \;& H_{k,\text{int}}^I(t' + k\tau_R)U_I(t' + k\tau_R, \varphi_k) \qquad \left| \int_0^{\tau_R} dt' \right. \quad .
\end{aligned} \tag{3.25}$$

Since the integration only takes place over the duration of the kth laser pulse, only the kth term in the sum remains and all other terms can be neglected.

The solution of Eq. (3.25) yields the time-propagation operator $U_I(t' + k\tau_R, \varphi_k)$ as a function of the phase $\varphi_k := \phi_k - \omega_{ij}t_k = k(\omega_0 - \omega_{ij})\tau_R$ during the kth laser pulse[5]. This phase dependence can be factored out by a unitary transformation ($K \cdot K^\dagger = 1$) [93]

---

[5] The first term corresponds to the phase shift between consecutive laser pulses and equals $\delta\phi = \omega_0\tau_R$,

$$K^\dagger(\varphi_k) H^I_{k,\mathrm{int}}(t' + k\tau_R) K(\varphi_k) = -\sigma(t') \sum_{i,j} \mu_{ij} e^{-\mathrm{i}\Delta^I_{ij} t'} |i\rangle\langle j| + c.c. \tag{3.26}$$

The time-propagation operator containing the full phase dependence is then given by

$$U_I(t' + k\tau_R, \varphi_k) \quad = \quad K(\varphi_k) U_I(t' + k\tau_R) K^\dagger(\varphi_k) \quad . \tag{3.27}$$

It should be emphasized that the full phase dependence is obtained by solving the differential equation Eq. (3.25) for $\varphi_k = 0$ and applying the unitary transformation $K(\varphi_k)$ to the resulting U_I. Some examples and explicit expressions for K are given in Appendix D.

Direct Integration of the Time Propagation Operator

In order to integrate Eq. (3.25), standard numerical functions, like `ode45` in Matlab [94] are employed. As a numerical precision check, it is convenient to observe the unitarity of the time propagation operator, which is typically $U_I \cdot U_I^\dagger - 1 \approx 10^{-12\ldots-15}$ in our algorithm[6].

In principle, the method of directly integrating the differential equation Eq. (3.25) can be used in general and has no restrictions regarding the atomic system. In an alternative way, the time-propagation operator can be expanded in a Dyson series as

$$U_I(t') = 1 + \sum_{m=1}^{\infty} \left(-\frac{\mathrm{i}}{\hbar}\right)^m \int_0^{t'} dt_1 \int_0^{t_1} dt_2 \cdots \int_0^{t_m} dt_m \prod_{\kappa=1}^{m} H^I_{\mathrm{int}}(t_\kappa) \quad . \tag{3.28}$$

As before, this operator determines the time evolution of the density matrix. Here, only the nested integrals have to be calculated. They represent the different orders of photon absorption processes, e.g. the term $m = 2$ represents two-photon processes. This method was applied in other experiments taking up to fourth-order processes into account [91]. However, the Dyson expansion does not always converge very fast and yields a much rougher approximation, its advantage coming uniquely from the relatively short computing times. In particular, the convergence of the Dyson series breaks down for the calcium ion level scheme due to the matrix elements of the clock transition (S – D state) and the dipolar transitions (S – P state) which are different by orders of magnitudes. This was the main reason why this approach was not followed in the description given here.

---

whereas the second term is an effect of the sampling with the repetition frequency in the rotating frame.

[6] Before the unitary transformation was implemented, Eq. (3.25) was solved directly for many different phases and the result was interpolated with a spline or a sinusoidal function. Apart from much more computer time which was required, it turned out that the unitarity condition was only given to a level of 10^{-8} per pulse.

Additional Frequency-Doubled Comb

In order to achieve a better coverage of the atomic transition lines, an additional frequency-doubled comb derived from the original comb can be employed. This is for instance of relevance for the case of calcium ions (see Section 4.2), where the main comb at 800 nm covers the P-D (repumping) transition at ~ 860 nm while the Doppler cooling transition at ~ 400 nm is covered by the frequency-doubled part.

The interaction Hamiltonian is then split into two separate parts $H^I_{\text{int}} = H^I_{1,\text{int}} + H^I_{2,\text{int}}$, each of which describes an individual comb part. Since the wavelengths differ by a factor of two, the cross terms in the interaction are neglected and the rotating wave approximation is applied by assuming that the 400 nm transition is not affected by the 800 nm part of the comb and vice-versa. It should be noted that the phase evolution of the frequency-doubled comb is twice as fast, i.e. the second part of the Hamiltonian is of the form

$$H^I_{2,\text{int}} = -\sum_{k=0}^{p} \sum_{i,j} \sigma_2(t-t_k) e^{-\mathrm{i}(\omega_{ij}-2\omega_c)(t-t_k)+\mathrm{i}(2\phi_k-\omega_{ij}t_k)} \mu_{ij} |i\rangle\langle j| + c.c. \tag{3.29}$$

Similarly to the case of a single frequency comb, a unitary transformation K is applied to the time-propagation operator of the complete system $\mathrm{i}\hbar\dot{U}_{I,\text{total}} = H^I_{\text{int}} U_{I,\text{total}}$ to factor out the phase dependence. The full solution and the phase dependence for the case of a $^{40}\text{Ca}^+$ ion is given in Appendix D.

Feeding Terms

The last missing elements in order to get the desired time evolution of the system are the feeding terms which govern the spontaneous decay of the diagonal elements (see Eq. (3.22)). Since only the diagonal elements of Γ and $\rho^{I,c}$ contribute, the convention $\Gamma_{ii} = \Gamma_i$ and $\rho^{I,c}_{ii} = \rho^{I,c}_i$ is used for clarity.

The time dependence of the diagonal elements in the integral of Eq. (3.22) is rewritten as follows[7]

$$\begin{aligned}\rho^I_{a_1}(t) &= e^{-\Gamma_{a_1}\cdot(t-t_1)} \cdot \left(\rho^{I,c}_{a_1}(t) + \sum_{a_2} \gamma_{a_1 a_2} \int_{t_1}^{t} dt' e^{\Gamma_{a_1}\cdot(t'-t_1)} \rho^I_{a_2}(t') \right) \\ &= e^{-\Gamma_{a_1}\cdot(t-t_1)} \cdot \left(\rho^{I,c}_{a_1}(t) + \sum_{a_2} \gamma_{a_1 a_2} \int_{0}^{t-t_1} dt'' e^{\Gamma_{a_1}\cdot t''} \rho^I_{a_2}(t''+t_1) \right) \quad .\end{aligned} \tag{3.30}$$

with $t_1 = k\tau_R \approx t'_2$ and $t_1 \leq t \leq t_1 + \tau_R$. The indices a_i represent the different energy levels $a_i \in \{1, 2, \ldots, N \cdot N_{\text{trap}}\}$ and $i \in \{1, 2, \ldots, N \cdots N_{\text{trap}}\}$. After inserting the relation for the density matrix elements recursively, the feeding terms are found to be

---

[7] Throughout this calculation, the starting point in time $t'_2 = k\tau_R + \epsilon$ is set to $t'_2 \approx t_1 = k\tau_R$ to simplify the time arguments.

$$\begin{aligned}
&\sum_{a_2} \gamma_{a_1 a_2} \int_0^{t-k\tau_R} dt_2 e^{\Gamma_{a_1} t_2} \rho^I_{a_2}(t_2 + k\tau_R) \\
&= \sum_{a_2} \gamma_{a_1 a_2} \rho^{I,c}_{a_2}(t) \int_0^{t-k\tau_R} dt_2 e^{\left(\Gamma_{a_1} - \Gamma_{a_2}\right) \cdot t_2} \\
&\quad + \sum_{a_2, a_3} \gamma_{a_1 a_2} \gamma_{a_2 a_3} \rho^{I,c}_{a_3}(t) \int_0^{t-k\tau_R} dt_2 \int_0^{t_2} dt_3 e^{\left(\Gamma_{a_1} - \Gamma_{a_2}\right) \cdot t_2 + \Gamma_{a_2} \cdot t_3} \rho^I_{a_3}(t_3 + k\tau_R) \\
&= \sum_{k=2}^{N} \sum_{a_2, \ldots, a_k} \left(\prod_{j=1}^{k-1} \gamma_{a_j a_{j+1}} \right) \rho^{I,c}_{a_k}(t) \int_0^{t-k\tau_R} dt_2 \cdots \int_0^{t_{k-1}} dt_k \exp\left(\sum_{l=1}^{k-1} \left(\Gamma_{a_l} - \Gamma_{a_{l+1}}\right) \cdot t_{l+1} \right) \quad .
\end{aligned} \tag{3.31}$$

Since the levels are sorted in ascending order of energy, the recursion stops at the highest level N since this level is not fed by any other levels via spontaneous emission:

$$\rho^I_N(t) = e^{-\Gamma_N \cdot (t - k\tau_R)} \rho^{I,c}_N \quad . \tag{3.32}$$

There is no general solution for this integral since it strongly depends on the given atomic system. Thus, in our implementation these feeding terms are integrated symbolically for the system of interest using either the Matlab [94] symbolic toolbox or the symbolic integration of Maxima [95].

The rather complicated expression Eq. (3.31) can be rewritten in a more intuitive and also practical way: As mentioned before, the upmost state is trivially given by Eq. (3.32). Every state with less energy has a possible feeding term which originates only in higher energy states since a spontaneous emission event will project the system into a state with lower energy. In that way, the population can be imagined to 'drip' down like water in a cascaded fountain where each level represents an energy level of the ion. Rewriting

Eq. (3.31) for each state leads to the following expressions:

$$\begin{aligned}
\rho^I_N(t) &= e^{-\Gamma_N\cdot(t-k\tau_R)}\rho^{I,c}_N \quad ; \\
\rho^I_{N-1}(t) &= e^{-\Gamma_{N-1}\cdot(t-k\tau_R)}\left(\rho^{I,c}_{N-1} + \gamma_{N-1,N}\int_0^{t-k\tau_R} dt' e^{\Gamma_{N-1}\cdot t'}\rho^I_N(t'+k\tau_R)\right) \quad ; \\
\rho^I_{N-2}(t) &= e^{-\Gamma_{N-2}\cdot(t-k\tau_R)}\left(\rho^{I,c}_{N-2} + \gamma_{N-2,N-1}\int_0^{t-k\tau_R} dt' e^{\Gamma_{N-2}\cdot t'}\rho^I_{N-1}(t'+k\tau_R)\right. \\
&\qquad \left. + \gamma_{N-2,N}\int_0^{t-k\tau_R} dt' e^{\Gamma_{N-2}\cdot t'}\rho^I_N(t'+k\tau_R)\right) \quad ; \\
&\vdots
\end{aligned}$$

It is maybe worthwhile mentioning that also from a practical point of view this form of the feeding terms is advantageous since the implementation in a computer code is simpler.

Chapter 4

Simulation Results

In this section, the results of the simulated interaction of a frequency comb with two different systems are presented. First, one- and two-photon transitions in a three-level system are discussed, aiming to provide an intuitive picture of the underlying dynamics. This serves as a basis to the second part of this chapter where numerical results and different strategies to map the full calcium level scheme are studied.

In all scans presented here, the offset frequency is only varied over one repetition rate, after which the spectrum repeats itself, which is due to the periodicity of the repetition rate in the spectrum.

4.1 Three-Level Raman System

Consider a three-level Raman system ($|1\rangle, |2\rangle, |3\rangle$), as depicted in Fig. 4.1 (a), interacting with a frequency comb with a repetition rate of 824 MHz[1]. Applying the frequency comb, centered at 800 nm, a Raman transition between the $|1\rangle$ and the $|3\rangle$ level via the $|2\rangle$ level is driven. In addition to that, a single-photon transition can be driven between the $|1\rangle$ and the $|2\rangle$ level. Since this system contains all types of transitions relevant for the 5-level system of $^{40}\mathrm{Ca}^{+}$, i.e. one- and two-photon transitions, it represents an ideal model for a basic understanding of the underlying dynamics and the spectroscopy signal.

A scan of the offset frequency over a full repetition period yields several resonances in the spectrum. In Fig. 4.1 the population in the second level (ρ_{22}) is shown after interacting with 10000 laser pulses (blue solid curve). The initial population was set to be $\rho_{11}(t=0) = 1$. The two different types of resonances occur in the following way: one-photon resonances occur if a comb tooth is resonant with the $|1\rangle$ to $|2\rangle$ transition and two-photon resonances occur if the combination of two comb teeth matches the frequency

---

[1] The relevant parameters for this simulation are: The frequency comb is defined by $\nu_{\mathrm{R}} = 824\,\mathrm{MHz}; t_P = 50\,\mathrm{fs}; E_0 = 151.08 \times 10^6\,\mathrm{V/m}; \omega_c = 12500\,\mathrm{/cm}$, whereas the energies and the decay rates are: $\epsilon_1 = 13650.19\,\mathrm{/cm}; \epsilon_2 = 25191.51\,\mathrm{/cm}; \Gamma_{1,2} = 1.01 \times 10^6\,\mathrm{1/s}; \Gamma_{2,3} = 1.00 \times 10^5\,\mathrm{1/s}$.

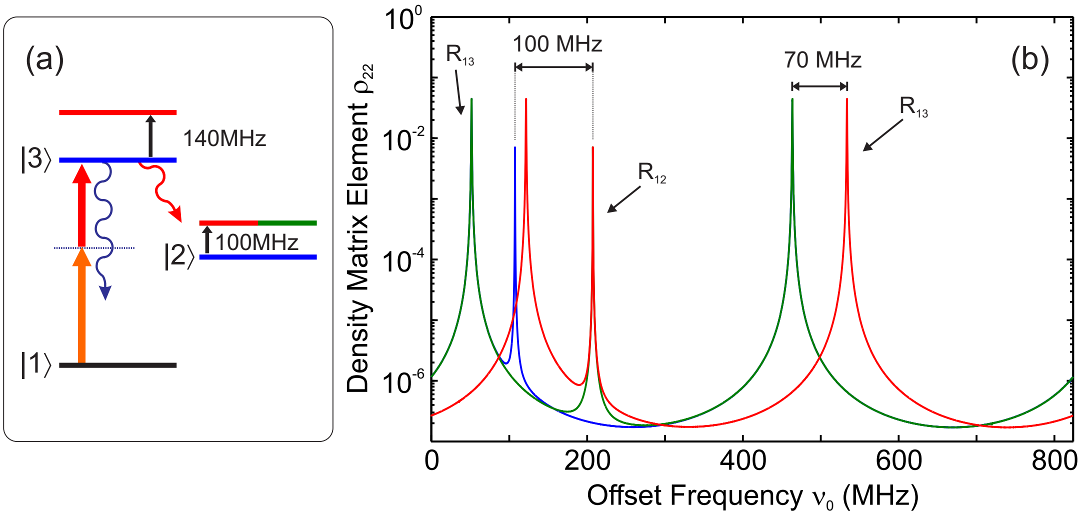

Figure 4.1: Three-level system interacting with a frequency comb. The population of the level $|2\rangle$ as a function of the offset frequency over one repetition rate is shown in picture (b). Additional shifts in each individual level move the corresponding one- (R_{12}) and two-photon resonances (R_{13}) at an offset frequency of $\sim 110\,\mathrm{MHz}$ and $\sim 50(450)\,\mathrm{MHz}$, respectively. The blue curve represents the non-shifted system, the green curve shows the result for the shift of the middle level and the red curve depicts the result of shifting both upper levels according to the picture (a).

difference between the $|1\rangle$ and $|3\rangle$ state. This is corroborated and easily understood by repeating the simulation for various shifted energy levels: A 100 MHz shift of the $|2\rangle$ level clearly shifts the single-photon resonance at $\sim$ 100 MHz to $\sim$ 200 MHz leaving the other resonances untouched (green curve). An additional shift of the $|3\rangle$ level by 140 MHz also moves the two-photon resonances at $\sim$ 50 and $\sim$ 450 MHz (red curve). The two-photon resonances occur twice during one scan over one repetition period since each photon provides half of the necessary energy. With the same argument, the additional shift of the upmost level only shifts the resonance by half of the amount.

Given this simple model, the simulations on the ^{40}Ca$^+$ 5-level system are discussed in the next section.

4.2 The 5-Level System of ^{40}Ca$^+$

Calcium is an alkaline earth metal with the atomic number 20. Its most common isotope is ^{40}Ca, with a natural abundance of 96.941% [96]. Singly-ionized calcium has a level structure similar to that of magnesium, but with the addition of two meta-stable D states which introduce two dipole-forbidden clock transitions from the ground state. The level scheme with the five lowest energy levels and relevant transitions, that are used in the simulations, are shown in Fig. 4.2. Some of these transitions have been investigated

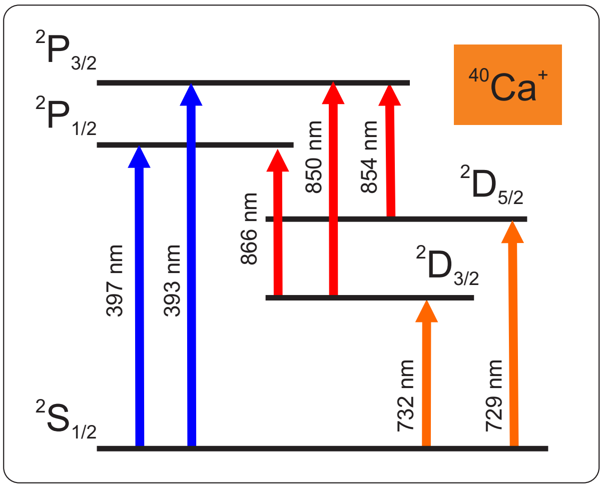

Figure 4.2: Level Scheme of $^{40}Ca^+$. Only the lowest five levels and their corresponding transitions used in the simulations are shown (the transition to the next higher S level is at ~ 374 nm and is not covered by the comb spectrum). While the S-P and P-D transitions are rather strong dipole transitions (see text), the S-D transitions are quadrupole clock transitions with a sub-Hz linewidth (see table for details).

using precision laser spectroscopy. Their characteristic values, including the Einstein A coefficients, are listed in the following table:[2]

Transition	Frequency ν	λ_{vac} (nm)	A_{ij} coeff. (s^{-1})	Ref.
$4s^2S_{1/2}$ - $3d^2D_{5/2}$	411 042 129 776 393.2 (1.0) Hz	729.347	1.3	[53, 56]
$4s^2S_{1/2}$ - $3d^2D_{3/2}$	Δ_{FS} = 1 819.599 021 504(37) MHz	732.591	1.3	[97]
$4s^2S_{1/2}$ - $4p^2P_{3/2}$	761 905 012.7 (0.5) MHz	393.477	$135.0(4) \times 10^6$	[51, 55]
$4s^2S_{1/2}$ - $4p^2P_{1/2}$	755 222 766.2 (1.7) MHz	396.959	1.4×10^8	[57]
$3d^2D_{3/2}$ - $4p^2P_{3/2}$	–	850.035	$0.955(6) \times 10^6$	[55]
$3d^2D_{5/2}$ - $4p^2P_{3/2}$	–	854.444	$8.48(4) \times 10^6$	[55]
$3d^2D_{3/2}$ - $4p^2P_{1/2}$	–	866.452	1.06×10^7	[96]

Given a calcium system initialized to the S state, the existence of the dipole-forbidden transitions hinders the excitation of the upper levels, especially if no comb tooth is resonant to the S-D transition. In the next section, this issue and different ways to overcome it are discussed.

---

[2] Values that are not referenced are taken from [96]. Δ_{FS} corresponds to the fine-structure splitting between both D levels.

4.3 Calcium Raman Resonances with a Frequency Comb

As a first approach, the interaction of a Ti:Saph frequency comb emitting at 800 nm with the 5-level ^{40}Ca^{+} ion is discussed. The different excitations that occur are similar to the case of the three-level system discussed in the previous section, i.e. a Raman two-photon excitation connects the $S_{1/2}$ with the $P_{1/2}$ and $P_{3/2}$ levels, whereas the $S_{1/2}$ to $D_{3/2}$ and $D_{5/2}$ transitions are single-photon excitations. In Fig. 4.3, the frequency spectrum assuming a pulse width of ∼50 fs of the comb is depicted along with all possible single-photon transitions.

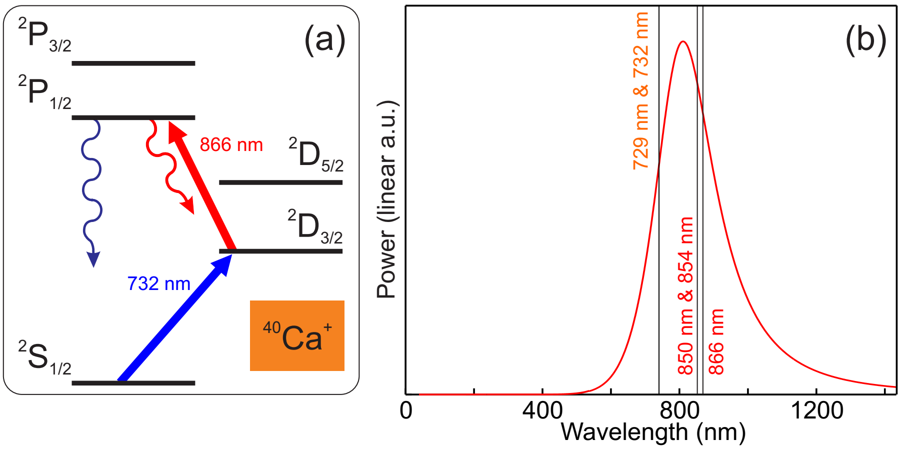

Figure 4.3: Frequency comb interacting with calcium ions in a Raman configuration and the assumed comb power spectrum. (a) The ^{40}Ca^{+} level scheme is shown with an example for a possible Raman excitation from the S to the P level via the D level. (b) The theoretical power spectrum of the comb. The spectrum was derived from a 50 fs laser pulse of hyperbolic secant form.

At first sight, it appears that all transitions are covered by the frequency comb spectrum and can be driven. The presence of the clock transition, however, strongly reduces the excitation of the upper levels. In Fig. 4.4, the population of the excited levels is plotted as a function of the offset frequency of the comb after the interaction of laser 5000 pulses. The comb parameters are the same as for the three-level example in the previous section. As is seen in the different plots, each of the P levels has two resonances. These correspond to the two-photon Raman resonances. The D states are populated by the finite branching ratio of the P states into the D states. In both D states resonances occur when either of the P states is excited. This is related to the existence of the 850 nm transition which is also excited and transfers population from the $D_{3/2}$ to the $P_{3/2}$ level. This population has two decay channels, namely back to the $D_{3/2}$ or to the $D_{5/2}$ state.

The population of the upper states is at a rather low level of $\sim 10^{-8} - 10^{-9}$. Taking the decay rates of the P states into account, the number of fluorescence photons at the wavelength 393 nm and 379 nm is on the order of ~ 10. These photons are emitted into the full solid angle, which imposes challenging requirements on the fluorescence detection optics. Though shining the comb laser for much longer times generates more scattering events, in a different approach using a partially frequency-doubled comb this problem can be circumvented. This is discussed in the next section.

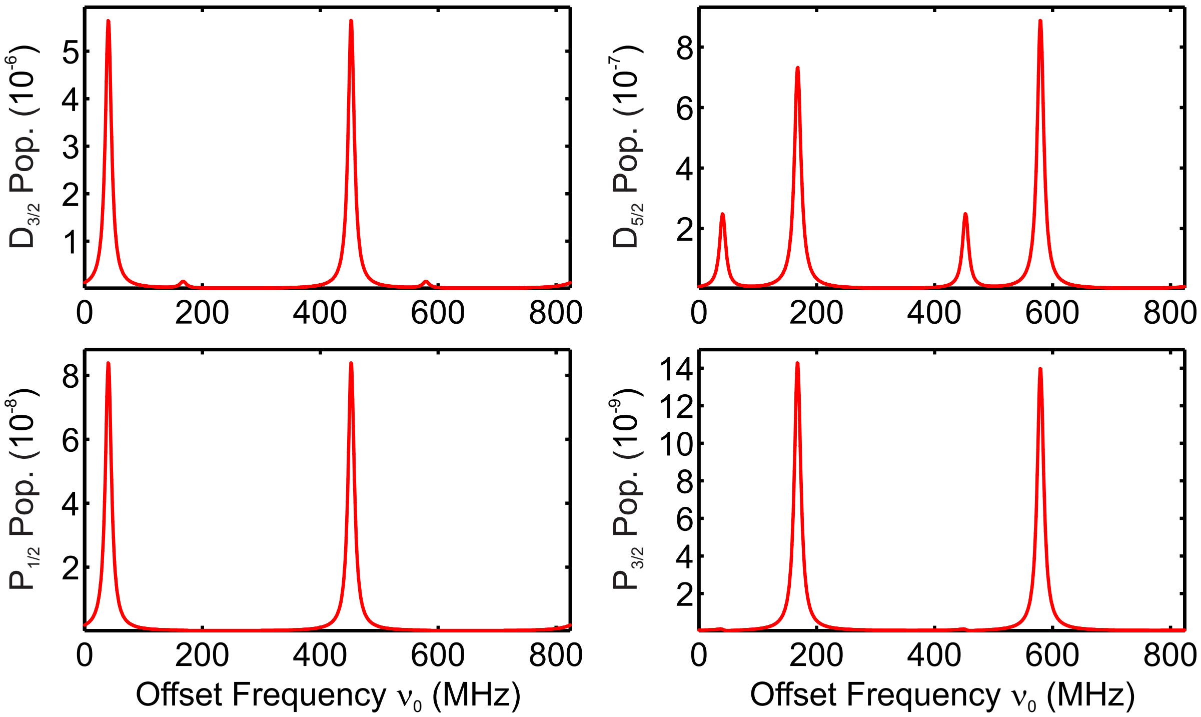

Figure 4.4: Direct frequency comb spectroscopy of $^{40}\mathrm{Ca}^+$ in a Raman configuration. The population distribution for the P and D states, summed over the trap levels, is shown as a function of the offset frequency of the frequency comb (see also Fig. 4.3). The scan is taken over a complete repetition rate of 824 MHz. For each scanning point, the population was initialized to the $S_{1/2}$ $n = 0$ state. The low excitation probability of $10^{-8} - 10^{-9}$ in the P levels only leads to a number of ~ 10 fluorescence photons on the S-P transitions at 393 nm and 397 nm. For this reason, a different approach is favorable, where the S-P transition is directly excited with a partially frequency-doubled comb.

4.4 Calcium Single-Photon Resonances with a Frequency-Doubled Comb

In order to circumvent the excitation of the clock transition, the frequency comb is partially frequency-doubled. In particular, given a Ti:Saph frequency comb laser which emits at ∼800 nm, the main comb covers the D-P transitions, while the frequency-doubled part encompasses the S-P transitions[3]. This situation is depicted in Fig. 4.5: In contrast to the three-level system described before, there are two single-photon resonances between the S level and both P levels at 397 nm and 393 nm. These resonances combine to a Raman resonance if the comb is simultaneously resonant with the corresponding D-P transition at e.g. 866 nm. In this case, the ion is continuously pumped between the S and D states. In a non-Raman configuration, i.e. if only the S-P transition is resonantly excited, the ion will eventually decay into the D states due to the finite branching ratio between the P and D states and remain there. It should be noted that the situation of a Raman configuration can be synthesized by correctly choosing the comb parameters. This is discussed in detail in Section 4.5.

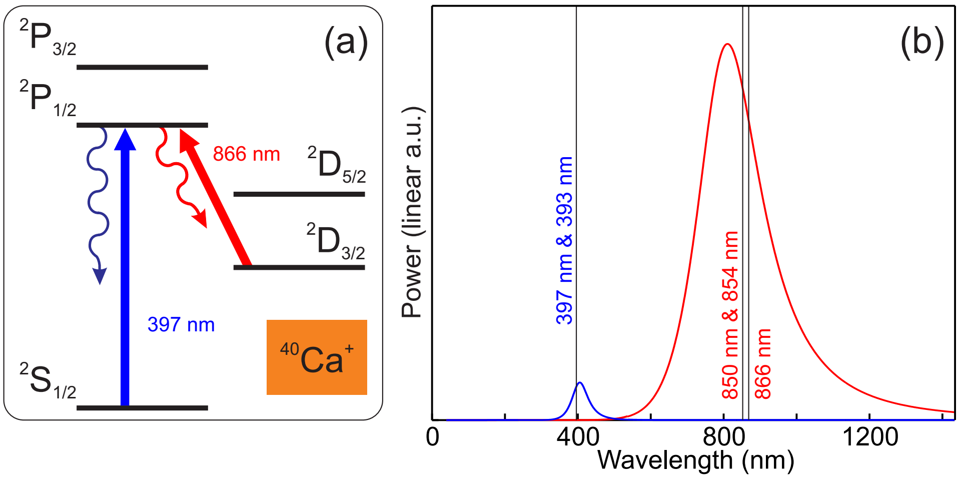

Figure 4.5: Frequency comb interacting with calcium ions and the assumed comb power spectra. (a) The $^{40}Ca^+$ level scheme is shown with an example for a possible excitation where the S-P transition is covered by the frequency-doubled comb (other combinations of transitions are omitted for clarity). (b) The theoretical power spectra of both parts of the comb, i.e. the main and the frequency-doubled part, are shown. Here, it was assumed that the doubled part has an electric field amplitude of 10% of the main comb. The spectrum was derived from a 50 fs laser pulse of hyperbolic secant form. For simplicity, the pulse width was assumed to be the same for the doubled part.

It should be noted that the resulting population distribution strongly depends on the exact frequency power spectrum of the applied comb. For simplicity, laser pulses of hyperbolic secant form are assumed in all simulations. However, in order to compare the numerical results with experimental data, the theoretical power spectrum, and thus the pulse shape, of the comb must be adapted to the experimental situation. Furthermore, the doubling efficiency as well as the phase-matching of the frequency-doubled part of the comb need to be taken into account.

---

[3] A detailed overview of frequency doubling strategies of a pulsed laser is given in [98].

In addition to that, the motion of the ion needs to be taken into account for two major reasons. While for a Doppler-cooled ion the observed spectroscopy line shapes follow a Cauchy-Lorentzian function to good approximation, this situation changes for a ground state cooled ion. There, the line shape is mainly determined by the carrier transition with additional components due to the motional sidebands. Since the linewidth of the S-P and P-D transitions are on the order of $\sim 10 - 20\,\mathrm{MHz}$, these sidebands are not resolved given typical trap frequencies of $\sim 1-2\,\mathrm{MHz}$ and, consequently, a distorted line shape is expected. In order to reproduce such line shapes, the motional trap levels and thus sideband transitions need to be taken into account in the simulations.

Apart from laser-induced fluorescence spectroscopy, a new spectroscopy technique is proposed in this context which is based on quantum logic spectroscopy [45], namely *photon-recoil spectroscopy*. The basic idea of this approach is to measure the motional excitation of a previously ground state cooled ion crystal consisting of a $^{25}\mathrm{Mg}^+$ and a $^{40}\mathrm{Ca}^+$ ion as a function of the comb parameters. Therefore it is also required to include the motional states in the simulation.

4.4.1 393 nm and 397 nm Transitions

In Fig. 4.6, the population distribution of all considered excited levels $^{40}\mathrm{Ca}^+$ are plotted for a scan of the offset frequency over one full repetition rate. For each scanning point, the system is initialized in the $\mathrm{S}_{1/2}$ state and in the absolute ground state of the harmonic oscillator ($n = 0$). In the simulation, three trap levels ($n = 0, 1, 2$) are taken into account, resulting in a total of 15 energy levels. The trap frequency is assumed to be $\omega_\mathrm{T} = 2\pi \times 2.2\,\mathrm{MHz}$. In Fig. 4.6, the trace is taken over the trap levels, whereas in Fig. 4.7 the trace over the electronic levels is shown.

All plotted populations are the result of the interaction of the ion with 1000 laser pulses. Several resonances are observed in the spectrum: at $\nu_0 \approx 50\,\mathrm{MHz}$ a comb tooth is resonant with the 397 nm transition, transferring the initial population in the S level to the $\mathrm{P}_{1/2}$ state, which in turn decays into the $\mathrm{D}_{3/2}$ state via spontaneous emission. The population in the $\mathrm{D}_{5/2}$ state at this frequency results from off-resonant coupling of the 850 nm laser between the $\mathrm{D}_{3/2}$ and the $\mathrm{P}_{3/2}$ levels. At $\nu_0 \approx 180\,\mathrm{MHz}$, the resonance of the 393 nm transition is retrieved. The additional wiggles on the resonance peak occur when a tooth of the main comb is resonant with one of the D-P transitions. Since the $\mathrm{P}_{3/2}$ state additionally decays into the $\mathrm{D}_{3/2}$ state, one would expect an additional peak in the lower D level at this offset frequency. Since the branching ratio of the spontaneous decay is 10 times smaller, this peak is on the level of 10^{-4} and is not visible at the particular scale.

It should be noted that even though the obtained spectra look similar to the ones

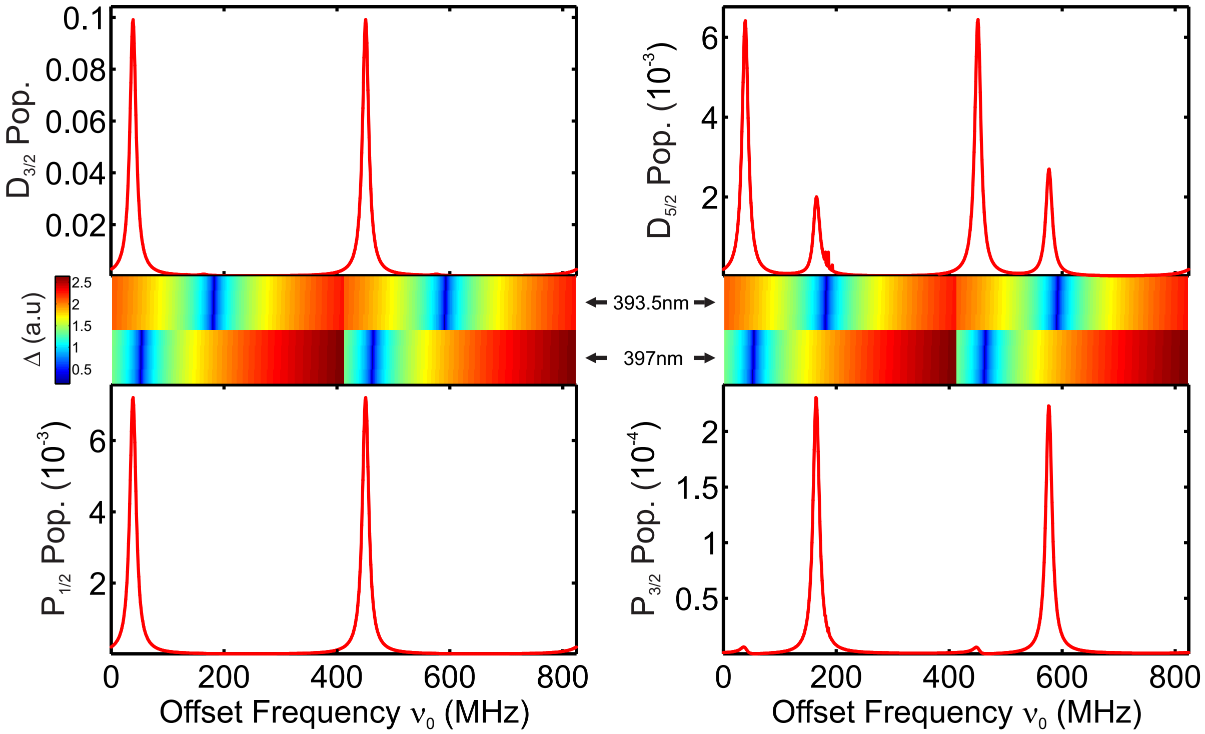

Figure 4.6: Direct frequency comb spectroscopy of $^{40}\mathrm{Ca}^+$. The population distribution for the P and D states, summed over the trap levels, is shown as a function of the offset frequency of the frequency comb (see also Fig. 4.5). The scan is taken over a complete repetition rate of 824 MHz. In between the graphs, the positions of the theoretically expected resonances at 393.5 nm and 393 nm are shown. The color coding (in arbitrary units) represents the detuning of a single comb tooth of the frequency-doubled comb to the theoretical atomic transition. The prediction does not include the expected stark shifts of the lines which explains the shift in each of the resonances (see Fig. 4.8). The spectrum repeats itself after half the repetition rate due to the phase evolution of the doubled-part of the comb. For each scanning point, the population was initialized to the $\mathrm{S}_{1/2}$ $n = 0$ state. The tiny wiggles at the resonance at ~ 200 MHz originate from the resonant repumping transitions at $\sim$850 nm (see Fig. 4.9).

of the previous comb configuration (see Fig. 4.3) that these resonances have a different origin. In this case, all resonances are single-photon excitations. Furthermore, the 397 nm and 393 nm resonances repeat themselves in the spectrum. This results from the carrier-envelope phase evolution of the frequency-doubled part of the comb, which is twice as fast.

Additionally to the expected population distributions, the theoretically expected positions of the resonances are shown in the pictures. These are determined by evaluating the comb tooth number in the vicinity of the resonance

$$n_{\mathrm{a}} = \left\lfloor \frac{\omega_{\mathrm{a}}}{\omega_{\mathrm{R}}} \right\rfloor \tag{4.1}$$

and plotting the detuning $\Delta = \omega_\mathrm{a} - (\omega_0 + n_\mathrm{a}\omega_\mathrm{R})$ as a function of the offset frequency ω_0. Since this method does not include the AC-stark shift, the predicted resonances are offset to the observed numerical calculations.

It is worth mentioning that the strong asymmetry in the excitation of the 397 nm and the 393.5 nm transitions is not a result of the (only slightly) different transition matrix elements. Instead, the asymmetry is due to the particular power in the comb at the individual wavelength and can be drastically changed by moving the central frequency of the comb by mere 5 nm, from 800 nm to 795 nm.

4.4.2 Laser-Induced Fluorescence Spectroscopy

The spectroscopy signal yielding the precision measurement of the desired transitions can be acquired in two different ways: In a direct way, fluorescence resulting from the spontaneous decay on the 397 nm and the 393.5 nm transitions is collected as a function of the offset frequency (*laser-induced fluorescence spectroscopy*). The photon scattering rate depends on the Einstein A coefficient $A_{ij} = \Gamma_\mathrm{a}$ of the particular transition and is proportional to the population ρ_a of the decaying state. The expected number of emitted photons after a time T is given by[4]

$$N_\mathrm{ph} = \int_0^T dt \Gamma_\mathrm{a} \rho_\mathrm{a}(t) \quad . \tag{4.2}$$

In the case of calcium, an instantaneous scattering rate $\Gamma_{397}\rho_{397}(t') \approx 910\,\mathrm{kHz}$ is expected on the 397 nm transition at the time of the 1000th laser pulse $t' = 1000\tau_R$. The collection of these fluorescence photons requires detection optics designed for that particular wavelength. In principle this can be achieved with an implemented wavelength independent parabolic mirror (see Chapter 5), but will be, nevertheless, limited by a large amount of stray light from the frequency comb which cannot be spectrally filtered sufficiently. These issues are overcome with a new spectroscopy method which will be explained in detail in the next paragraph.

4.4.3 Photon-Recoil Spectroscopy

In a different approach, a much more sensitive and wavelength-independent detection method is proposed here. First, two ions are loaded into the ion trap: a $^{25}\mathrm{Mg}^+$ ion (*logic ion*) and a $^{40}\mathrm{Ca}^+$ ion (*spectroscopy ion*). The logic ion is used to sympathetically cool the two-ion crystal to the absolute motional ground state. After that, the frequency comb is applied for exciting the spectroscopy ion. Every scattering event imposes a photon-recoil which is absorbed by the crystal. This effect is strongly enhanced as soon as a comb tooth is resonant with an electronic transition. Both ions are affected by this recoil due to their Coulomb interaction. Given that the system is initially in the absolute ground state, the photon-recoil induces a heating to higher harmonic oscillator states which can be read out with almost unity efficiency with the logic ion by observing the excitation on the motional red sideband. The probability that a photon-recoil excites a motional quantum scales with the square of the Lamb-Dicke parameters η^2, which equals the ratio of recoil energy to the trap energy spacing. For typical trap frequencies in the case of $^{40}\mathrm{Ca}^+$ only ~ 10 photons need to be scattered on the 397 nm transition to excite a motional quantum in the trap. Achieving similar detection efficiencies with regular optics is a formidable challenge. A further advantage of this method is that its principle does not strictly depend on the spectroscopy ion. As long as the laser probe covers the required transitions and sympathetic cooling is efficient with both species in the trap, only the logic ion needs to be well controlled and fluorescence detection optics is only required for the logic ion. In case of $^{25}\mathrm{Mg}^+$, complete control can be achieved by only a single laser system which provides cooling, state preparation and readout. Such a system is presented in Chapter 5 and its performance is characterized in Chapter 8.

---

[4] The actual number of collected photons differs from this number by the collection efficiency of the optics and the detection efficiency.

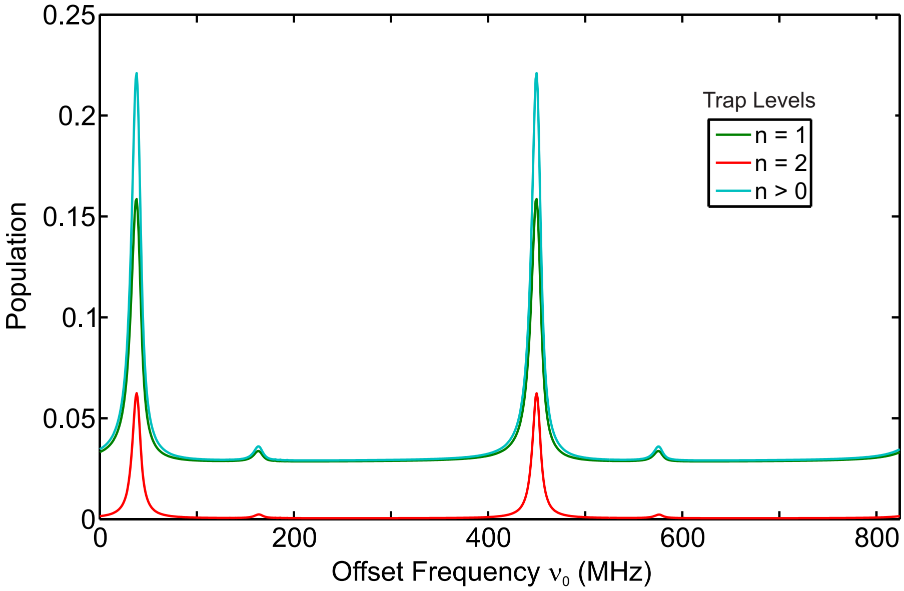

Figure 4.7: Photon-recoil spectroscopy with $^{40}\mathrm{Ca}^+$. The population distribution for the excited harmonic oscillator levels ($n = 1, 2$), summed over all electronic levels (S,P and D), is shown. The parameters are the same as in Fig. 4.6. Additionally, the sum over the first and the second trap level is shown ($n > 0$). This corresponds to the expected heating signal after scattering photons for 1000 laser pulses ($\sim 1\,\mu$s).

The fluorescence signal is then acquired by detecting the motional state of the, initially ground state cooled, ion crystal after the interaction with the frequency comb as a function of the offset frequency[5]. This is performed by measuring the red sideband excitation on the ^{25}Mg$^+$ ion. This way, the full spectrum can be inferred. It is worth mentioning that the inclusion of higher order red sidebands in the analysis should improve the detection efficiency even further.

In order to calculate the expected heating signal, the trace over the electronic states needs to be considered. This is shown in Fig. 4.7 for the different trap levels. The same resonances as for the case of fluorescence spectroscopy are observed. Given the same parameters as for the simulation in Fig. 4.6, a total population of 20% in the first and second motional state is expected when the 397 nm resonance is excited. At the offset frequency where the 393 nm transition is resonantly driven, the excitation is much smaller since the $P_{3/2}$ state is populated with a factor of 10 less compared to the $P_{1/2}$ state. As mentioned before, this is a result of the particular comb spectrum. The underlying broadband constant excitation of the first motional state is a result of offresonant excitation by the whole frequency comb.

4.4.4 Line Shapes and AC-Stark Shifts

A closer inspection of the particular line shapes in the resonance spectra yields asymmetries. These are the result of the introduction of the sideband transitions in the harmonic confinement and need to be taken into account if line centers are to be determined. A comparison of the line shapes is found in Fig. 4.8. A Cauchy-Lorentz function of the form

$$\rho(\omega) = a\frac{\gamma^2}{(\omega - \omega_{\text{center}})^2 + \gamma^2} \tag{4.3}$$

was fitted to the chosen transition. Here, a is the amplitude, 2γ the FWHM of the resonance and ω_{center} the center of the line. While in the case of no trap levels the line is found to be symmetric (seen in the residuals in Fig. 4.8 (a))[6], the presence of trap levels adds to the asymmetry (part (c)). This effect is amplified when the trace over the electronic levels is taken (shown in part (b)).

Given these effects, the fits reveal a systematic shift of the line center by almost one trap frequency. This issue can be tackled by a multi-component fit (also shown in part (b)), where a sum of Lorentzian with components shifted by multiples of the trap frequency is used. Such an approach resembles the observed line shape significantly better. All fitting results are summarized in the following table:

---

[5] A similar type of *heating spectroscopy* with much lower sensitivity has been implemented by the group of K. Brown for Doppler-cooled calcium ions [59].

[6] The remaining non-zero residuals are due to power broadening of the line.

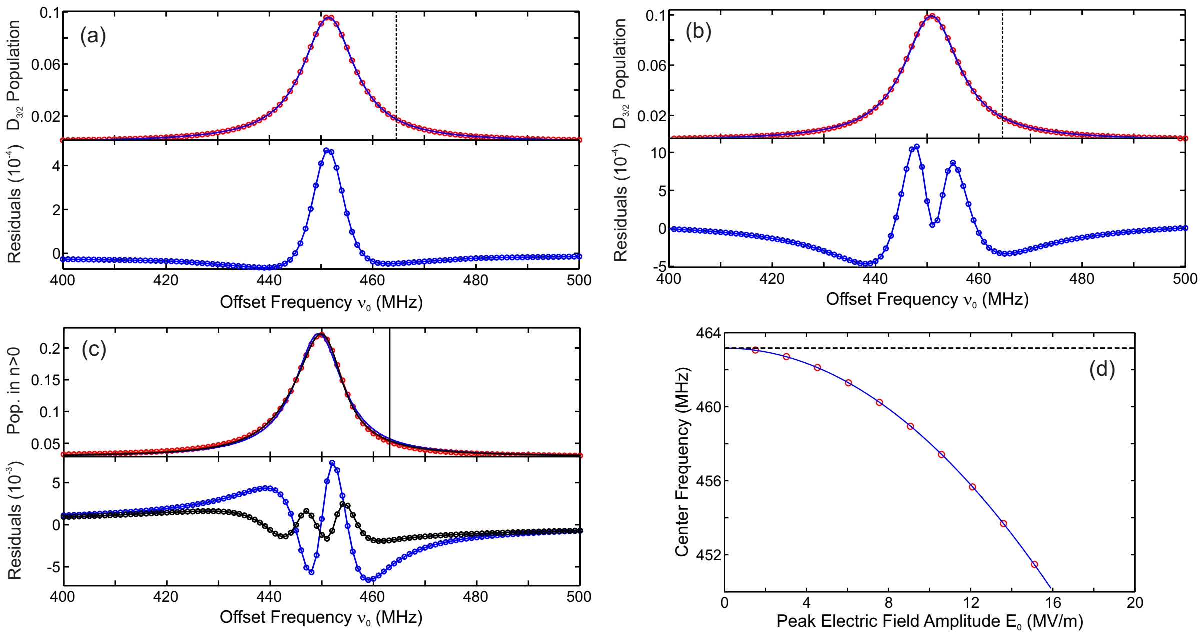

Figure 4.8: Symmetry of transition resonances and AC Stark-shifts. A zoom of the resonance at ∼450 MHz of Fig. 4.6 is shown. The red circles correspond to the simulated population distribution, the solid blue lines are fits to a Cauchy-Lorentz distribution (see text). In the lower part of the graphs, the residuals of the fit in each plot are shown. (a) shows the simulation without trap levels, whereas (b) depicts the population in the $D_{3/2}$ state while tracing over the trap levels. There, an asymmetry in the line shape is observed by introducing the trap levels. This is amplified if the trace is taken over the electronic levels instead (photon-recoil spectroscopy signal Fig. 4.7), as is shown in part (c). Also shown in (c) is a Lorentz fit with additional components shifted by the trap frequency (black line) which resembles the calculated absorption curve better. The dashed lines in all pictures show the theoretically expected position of the transition, omitting the AC stark-shift. In part (d), the center position of the resonance in (a) is plotted as a function of the peak electric field of the laser pulses (red circles). A quadratic fit yields a frequency shift of 492 MHz/mW for a spot size of 100 μm.

	ω_{center} (MHz)	Shift (MHz)
(a) No trap levels	451.48	-
(b) Trace over trap levels	450.86	0.62
(c) Trace over electronic levels	449.38	2.10
Multi-component fit	451.36	0.12

A further systematic effect is introduced by the presence of strong AC-stark shifts. In part (d) of Fig. 4.8, the fitted line center following from the simulations is shown as a function of the electric field of the interacting laser comb. The function follows a quadratic behavior with a Stark-shift coefficient of $\sim 492\,\mathrm{MHz/mW}$[7] for a spot size of $100\,\mu$m for this particular transition and needs to be carefully calibrated in the experiment.

4.4.5 866 nm, 854 nm and 850 nm Transitions

In the spectra shown before, no D-P transitions are observed due to the rather low D state occupation during the excitation process. This situation changes significantly if the calcium ion is initialized in the D state instead of the S state. One way to deterministically achieve this using the same laser system is to tune the comb to the right offset frequency (see above) and drive a S-P transition for a sufficiently long time to populate the D level via spontaneous decay. After that, a re-cooling step should be performed to cool the system again to the ground state of motion. Starting from there, the expected resonances after 1850 laser pulses are shown in Fig. 4.9. In these simulations the field amplitude of the frequency comb was reduced by a factor of two compared to Fig. 4.6. Nevertheless, the AC stark shifts are larger in this case since the ~850 nm transitions are driven by the main part of the comb.

Several resonances are observed in the spectrum. First, the excitation of the repumping D-P transitions are found at offset frequencies ~ 180 MHz and ~ 790 MHz. The additional peak at 200 MHz in the $D_{3/2}$ population is a result of the 850 nm excitation which effectively transfer part of the population to the $P_{3/2}$ state. This is seen in the distortion of the $P_{3/2}$ line shape. In addition to that, resonances at ~ 50 MHz and ~ 450 MHz occur in the $P_{1/2}$ population. These are a result of the 397 nm excitation which couples the $S_{1/2}$ with the $P_{1/2}$ state (see also Fig. 4.6). Photon-recoil spectroscopy is equally applicable to this case and the expected results are shown in Fig. 4.10.

It is worthwhile mentioning that all simulations here do not represent the steady-state of the system. Instead, only a few thousands laser pulses are applied. In the experiments, this can be achieved by switching the frequency comb with a KD*P Pockels cell[8] and has been successfully demonstrated in the group of J. Ye [99].

4.5 Comb Engineering

In what has been described, the repetition rate of the comb was assumed to be constant and at some (arbitrary) value while the offset frequency was used for scanning over the resonances. It is worth mentioning that by adjusting the repetition rate, the comb structure can be engineered to match certain frequency conditions. For instance, it is

---

[7] This coefficient is related to the time-averaged power of the comb.

[8] Conoptics Inc., Model 25D

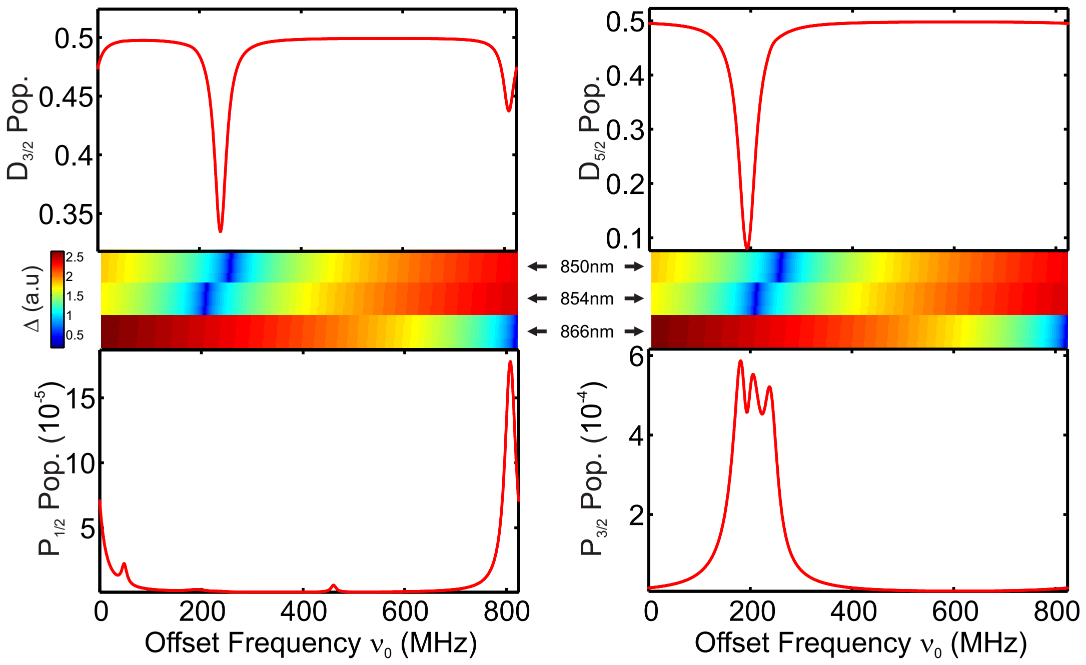

Figure 4.9: Direct frequency comb spectroscopy with ^{40}Ca$^+$. The population distribution for the P and D states, traced over the trap levels, are shown as a function of the offset frequency. The plots and parameters differ to that in Fig. 4.6 only by the laser power, which is reduced by a factor of two. Here, the population was initialized equally to both D states to observe the anti-resonances of the $\sim 850 - 866$ nm transitions in the D state population.

always possible to make two different atomic transitions, with $\omega_a \neq \omega_b$, resonant with two different comb teeth at one particular offset frequency. Since

$$\begin{aligned} \omega_a &= n_1\omega_\mathrm{R} + \omega_{0,a} \quad ; \\ \omega_b &= n_2\omega_\mathrm{R} + \omega_{0,b} \quad , \end{aligned} \tag{4.4}$$

both offset frequencies are equal $\omega_{0,a} = \omega_{0,b}$, if the repetition rate follows the equation

$$\omega_\mathrm{R} = \frac{\omega_a - \omega_b}{n_1 - n_2} \quad . \tag{4.5}$$

That means that by a particular choice of the repetition rate, the resonances of the S-P and the D-P transition can be overlapped. This process is shown in Fig. 4.11 by plotting the detuning of the individual atomic resonances as a function of the repetition rate and the offset frequency. Given the parameters at the crossing of the resonances (red circle in the plot) and correcting for the Stark shift, Raman transitions between the S-D levels with the intermediate P level are driven. The population distribution after 5000 pulses of the laser, with the population initially in the S state, is shown in Fig. 4.12.

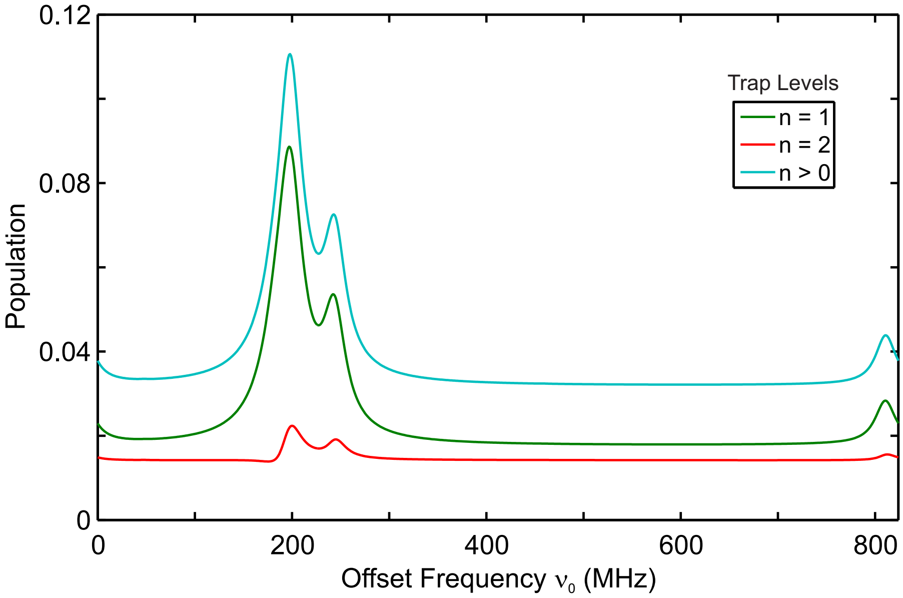

Figure 4.10: Photon-recoil comb spectroscopy with ^{40}Ca$^+$. The population distribution for the excited harmonic oscillator levels ($n = 1, 2$), traced over all electronic levels (S,P and D), is shown. The plots and parameters are the same as in Fig. 4.7, only here, the laser power is reduced by a factor of two and the population was initialized equally to both D states.

The overlap of the transitions introduces a Raman mechanism that populates the $D_{5/2}$ state at an offset frequency of $\sim 85\,\mathrm{MHz}$ with a peak shaped feature. This also reflects itself in a dark resonance in the excited state population in the $P_{3/2}$ level. At the same time, this population is missing in the $D_{3/2}$ state since it is pumped between the $D_{5/2}$ and the $S_{1/2}$ state. Furthermore, the complete time evolution of the system is shown in Fig. 4.13. Initially the excitation of the $P_{3/2}$ level pumps the population in both D states over the scanned frequency range. The creation of a narrow-linewidth Raman resonances is observed after $\sim 3 - 4\,\mu$s of temporal evolution.

In conclusion, such configurations can in principle be used to design the frequency comb in a way that the ion cycles between the S and D states. Furthermore, since the Raman excitation depends on the relative phase between different parts of the comb spectrum, also coherence phenomena among the comb teeth could be investigated by driving this transition with different comb parameter sets that resemble the same Raman configuration.

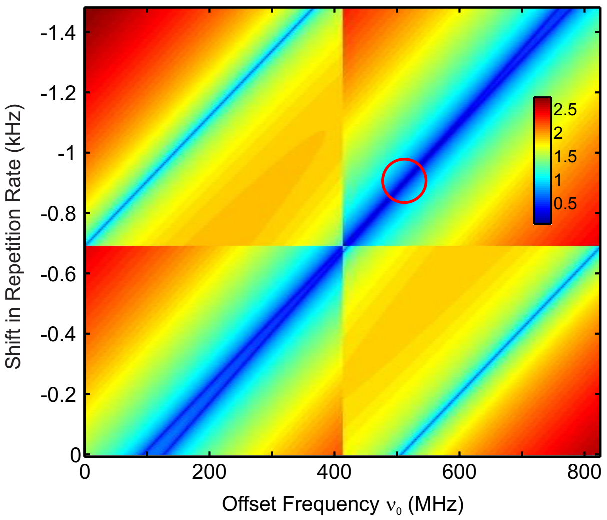

Figure 4.11: Engineering the frequency comb. The color coding (in arbitrary units) represents the detuning of the 393 nm and the 854 nm transition to a single comb tooth of the frequency-doubled and respectively the main comb. The detuning is shown as a function of the offset frequency and a shift in the repetition rate in units of MHz. At the position of the crossing blue lines (red circle), two different comb lines are resonant with the individual transitions. The simulation does not include the AC-Stark shift. (The horizontal and vertical lines are a sampling artefact of selecting the nearest comb tooth.)

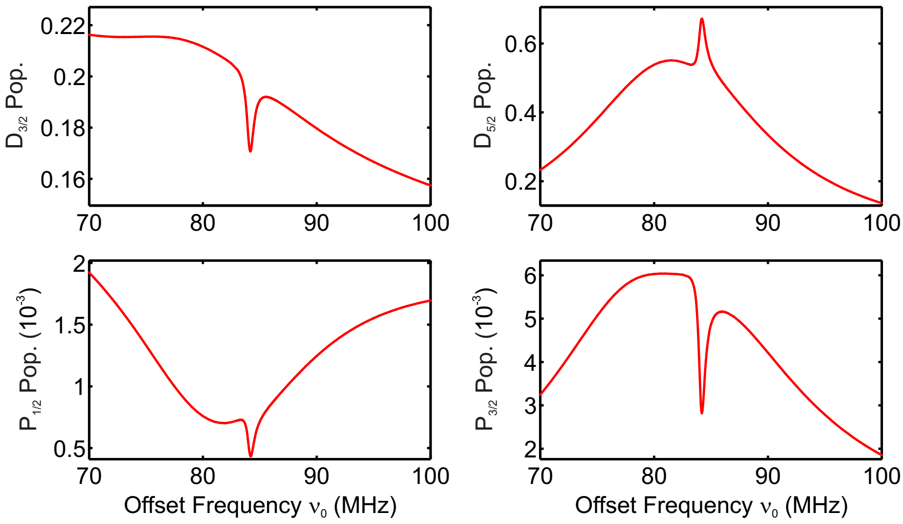

Figure 4.12: Raman resonance with a frequency comb. The population in the P and D levels as a function of the offset frequency after the interaction with 5000 pulses is shown. A shift of the repetition rate overlaps the resonances of the 393 nm and the 854 nm transition at a certain offset frequency (see Fig. 4.11). Given these parameters, a Raman resonance between the S and D levels is observed. No trap levels have been included in this simulation.

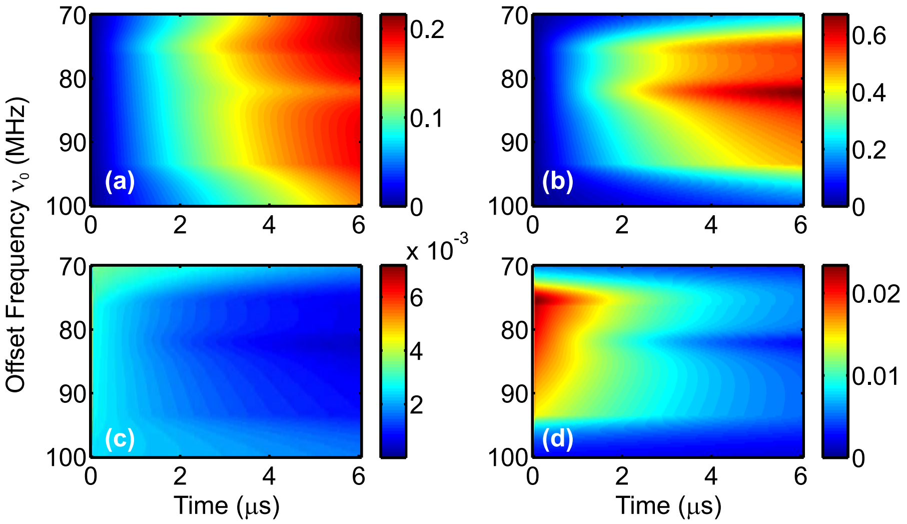

Figure 4.13: Raman resonance with a frequency comb (II). The time evolution for the system in Fig. 4.12 is shown. The individual pictures show: (a) $D_{3/2}$ state population, (b) $D_{5/2}$ state population, (c) $P_{1/2}$ state population and (d) $P_{3/2}$ state population. No trap levels have been included in this simulation.

Chapter 5

Experimental Setup

This chapter contains a detailed description of the experimental apparatus, including laser systems and the vacuum setup. With this setup, the ground state cooling of a single $^{25}\mathrm{Mg}^{+}$ ion, which is the initial step of the proposed frequency comb spectroscopy experiments using the photon-recoil technique has been implemented. The description encompasses the generation of magnesium ions with a photoionization laser system, the setup for cooling, manipulation and detection with a frequency-quadrupled fibre laser system, an overview of the operation of the Paul trap and of the detection optics.

During the experiments, it was observed that certain optical components suffered from damage induced by ultra-violet irradiation at the magnesium resonance wavelength of 280 nm. Such effects triggered a redesign of commonly used acousto-optic modulator configurations which provide the Raman laser beams to manipulate the ion qubit. Such a configuration, a description of which is found in this chapter, was successfully implemented.

5.1 Magnesium Laser System

5.1.1 Photoionization Laser

Magnesium ions are produced by photoionizing a thermal beam of neutral magnesium atoms. The beam is provided by resistive-heating of a stainless steel tube filled with magnesium powder (see Section 5.6). Photoionization takes place in a two-photon process [100]. In a first step, neutral magnesium is excited by laser light at a wavelength of 285 nm to the $^{1}\mathrm{P}_{1}$ state. This light is provided by a frequency-quadrupled diode laser[1]. The diode laser with an output power of $\sim$70 mW at 1140 nm and a specified linewidth of 100 kHz is frequency-doubled in a second-harmonic generation (SHG) bow-tie cavity using a 0.5 × 3 × 10 mm periodically-poled $LiNbO_3 \cdot MgO$ doped crystal[2] in a quasi-phase matching configuration at a temperature of $\sim 493\,K$. Typical output powers of 20 mW at 570 nm are achieved. The cavity is length-stabilized using the Pound-Drever-Hall (PDH) technique [101]. The required sidebands at ±20 MHz are generated by fast current modulation of the laser diode.

---

[1] Toptica DL Pro ECDL

A small fraction of the green light is fibre-coupled to a wavelength meter[3] for monitoring purposes. The main part of the light is frequency-doubled in a second SHG cavity using an anti-reflection coated 3 × 3 × 10 mm β-Barium-Borate (BBO) crystal[4] which is critically phase-matched. The cavity is also stabilized with the PDH technique[5]. Typical output powers of 300 μW at 285 nm are achieved for a non-optimized system. The whole setup is depicted in Fig. 5.1. A detailed study of this laser system and the characterization of the doubling-cavities is found in the diploma thesis of Daniel Nigg [102].

It is worth mentioning that in the initial stage of the experiment, an electron-emitter was used for ion production. However, since this method was not isotope-selective and resulted in difficulties for loading single magnesium ions, it was abandoned after successfully implementing the ionization laser system.

The second step of the ionization process is provided by the Doppler cooling laser (see below) at 280 nm which excites the magnesium atoms from the $^1P_1$ state to the continuum. Isotope-selective loading is provided by tuning the diode laser according to the corresponding isotope shifts of neutral magnesium. Due to its large specified tuning range of > 30 GHz, all three isotopes of magnesium are accessible in our setup.

5.1.2 Magnesium Ion Laser System

The laser light for Doppler cooling, detection and coherent manipulation is provided by a frequency-quadrupled fibre laser system, similar to the setup used in the group of Tobias Schätz [58]. A major simplification to their and other, similar setups is the introduction of an electro-optic modulator to provide a fast switch between an off-resonant coherent and a resonant laser configuration. This methods allows operating the ion trap system with one single laser source only, which will be described in this section. A general overview of this part of the laser setup is shown in Fig. 5.2.

---

[2] HG Photonics

[3] HighFinesse WS/7 Super Precision

[4] Castech Crystal Inc.

[5] It is worth mentioning that the current modulation of the diode laser is sufficient to produce an error signal for both cavities.

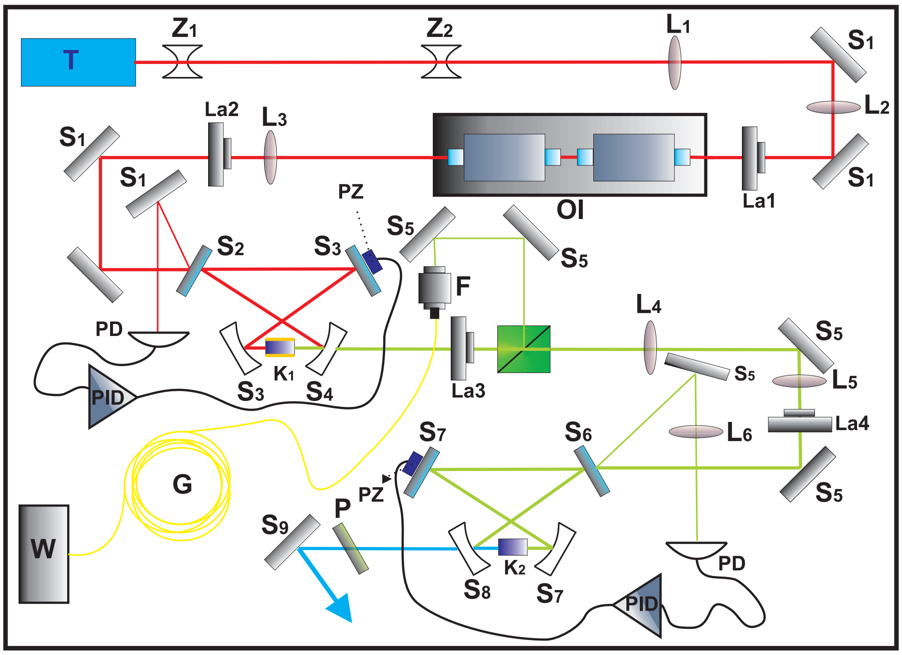

Figure 5.1: Photoionization laser setup. A diode laser at 1140 nm is frequency-quadrupled in two cascading doubling cavities. The first incorporates a PPLNb crystal, whereas the second an anti-reflection coated BBO crystal. Both cavities are length stabilized with the Pound-Drever Hall technique. A typical output power of $\sim 300\,\mu$W is achieved. Picture taken from [102]. Legend: S: mirror; Z,L: lenses; W: wavelength meter; K: crystal; PZ: piezo-actuated mirror; La: waveplate; PD: photodiode; OI: optical isolator.

Doubling Cavities

The ~ 1.2 W output power of the fiber laser[6] at 1118 nm is frequency-doubled in a first SHG cavity in a bow-tie configuration with a $4 \times 4 \times 18\,\mathrm{mm}^3$ Lithium Triborate (LBO) crystal[7] using 90° non-critical phase-matching of type I. The crystal is temperature-stabilized at ~ 370 K to provide the phase-matching. The cavity length is stabilized using the Hänsch-Couillaud technique [103] and has a typical output power of ~ 450 mW at 559 nm. The main part of this light is used in a second SHG cavity for frequency doubling to the UV. Here, a $3 \times 3 \times 10\,\mathrm{mm}^3$ BBO crystal[8] in critical phase-matching of type I is used. The cavity is stabilized in the same way as the first one in the setup and an output power of ~ 60 mW at 279.5 nm is achieved. A detailed characterization of the doubling-cavities and the locking-schemes is found in the diploma thesis of Lukas An der Lan [104].

---

[6] Koheras Boostik$^{\mathrm{TM}}$Y10/Menlo Systems GmbH orange one-1

[7] Castech Crystal Inc.

[8] Döhrer Elektrooptik

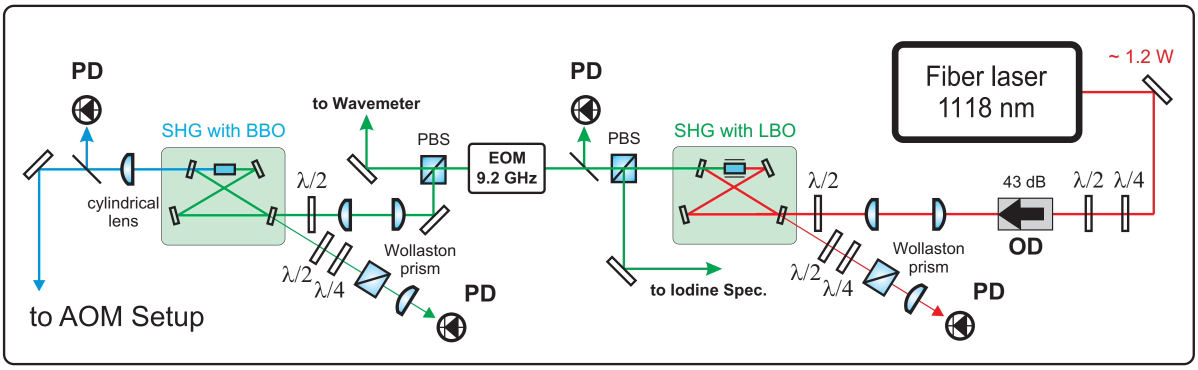
PD
SHG with BBO
to Wavemeter
PBS
EOM
9.2 GHz
PD
PBS
SHG with LBO
Fiber laser
1118 nm
~ 1.2 W
cylindrical
lens
λ/2
λ/2
43 dB
λ/2 λ/4
OD
Wollaston
prism
Wollaston
prism
λ/2
λ/4
PD
to Iodine Spec.
λ/2
λ/4
PD
to AOM Setup

Figure 5.2: Overview of main laser setup. A fibre laser at 1118 nm is frequency-quadrupled to 279.5 nm to provide light for Doppler cooling, detection and coherent manipulation. The doubling takes place in two cascaded SHG cavities with a LBO and a BBO crystal, respectively. The system has a typical output power of ∼60 mW in the UV. A fraction of the green light is used to frequency-stabilize the fibre laser with an iodine saturation spectroscopy and monitor the wavelength on a wavemeter. An EOM modulates sidebands at ±9.2 GHz onto the green light, which allows for switching between a resonant and off-resonant configuration, respectively. Legend: PD: photodiode; PBS: polarizing beam splitter; $\lambda/2, \lambda/4$: waveplates; OD: optical diode.

Iodine Spectroscopy

Approximately 15 mW of the green output power is fibre-coupled and guided to an iodine saturation spectroscopy setup [105] which incorporates a molecular $^{129}I_2$ cell[9] (see Fig. 5.2). The error signal of the spectroscopy is provided by a lock-in amplifier[10] and fed back to a proportional-integral controller loop (PI) connected to a piezo-electrical fiber stretcher of the fibre laser to lock its frequency to an iodine transition.

Electro-Optic Modulator

A resonant electro-optic modulator[11] (EOM) with an MgO-doped $\mathrm{LiNbO_3}$ crystal[12] is located in between the two cascaded SHG cavities. Driven with a sinusoidal electronic drive field, the EOM imprints sidebands on the spectrum of the laser field in the following way: Consider an incidenting field $E(t) = \frac{1}{2}E_0 \cdot e^{i\omega t} + c.c.$ The EOM, which is driven with a radio-frequency of $\Omega = 2\pi \times 9.2\,\mathrm{GHz}$, phase-modulates the signal leading to sidebands as follows

---

[9] The cell was provided by the group of Uwe Sterr, PTB.

[10] Scitec Instruments Model 410

[11] Laser 2000 GmbH NFO-4851-M

[12] This material is chosen due to its large electro-optic coefficient and its broadband optical transparency and low radio-frequency losses.

$$E(t) \;=\; \frac{1}{2}E_0 \cdot e^{\mathrm{i}\omega t+\mathrm{i}\beta\sin(\Omega t)} + c.c. = \frac{1}{2}E_0 \cdot e^{\mathrm{i}\omega t} \sum_{n=-\infty}^{\infty} J_n(\beta) e^{\mathrm{i}n\Omega t} + \mathrm{c.c.} \quad , \tag{5.1}$$

where J_n are the Bessel functions of order n and β is the modulation index which depends on the EOM π-voltage and the driving electric field amplitude. The particular EOM used in the setup has a specified π-voltage of $\sim 33\,\mathrm{V}$ at 560 nm and a modulation depth of $\sim 0.05\,\mathrm{rad/V}$.

After the sidebands are imprinted, the light is frequency-doubled in the second SHG cavity. It should be emphasized that this process does not change the frequency difference of the sidebands to the carrier [106]. Instead, the modulation index is doubled since the SHG process squares the field amplitude

$$\begin{aligned} E(t) \quad \xrightarrow{\text{SHG}} \quad E(t)^2 &= \frac{1}{2}E_0^2 + \frac{1}{4}E_0^2 \cdot e^{\mathrm{i}2\omega t+\mathrm{i}2\beta\sin(\Omega t)} + \mathrm{c.c.} \\ &= \frac{1}{2}E_0^2 + \frac{1}{4}E_0^2 \cdot e^{\mathrm{i}2\omega t} \sum_{n=-\infty}^{\infty} J_n(2\beta) e^{\mathrm{i}n\Omega t} + \mathrm{c.c.} \end{aligned} \tag{5.2}$$

However, the free-spectral range of the cavity needs to be adjusted to be a multiple of Ω in order to guarantee the transmission of the sidebands and the carrier simultaneously[13].

In Fig. 5.3, the theoretical power distribution in the different sidebands is shown as a function of the modulation index β before entering the BBO cavity. In the experiment, a typical modulation index of $\beta \approx 0.58$ is used. This yields a power of $\sim 24\%$ in the first sidebands after frequency doubling by the BBO cavity. This ratio was measured with the help of two separate Fabry-Perot cavities [107], one located before and one after the doubling cavity.

The driving electric field is provided by an amplified frequency-multiplier[14], as shown in the inset of Fig. 5.3. Here, the output of a frequency generator[15] is multiplied by 920 to $\sim 9.2\,\mathrm{GHz}$ and amplified up to 3 W. After the amplifier, a variable-gain attenuator allows adjusting the output power of the system. Furthermore, a TTL input channel is used to switch the frequency output on a timescale of $< 5\,\mu\mathrm{s}$. The output frequency is adjusted to match the resonance frequency of the EOM circuit.

Driving the EOM with radio-frequency powers higher than 1.3 W yields significant beam deflection probably through thermal effects in the EOM crystal. This leads to a decrease in the coupling efficiency to the BBO cavity. Furthermore, a change in the EOM's resonance frequency is observed. In order to avoid these effects, the EOM is

---

[13] This is done by changing the distance of the flat mirrors in the bow-tie cavity. This way, only the FSR changes without changing the waists in the cavity significantly.

[14] Kuhne electronic GmbH KULO092A;KUPA092X;KUATT092A

[15] Stanford Research Systems DS-345

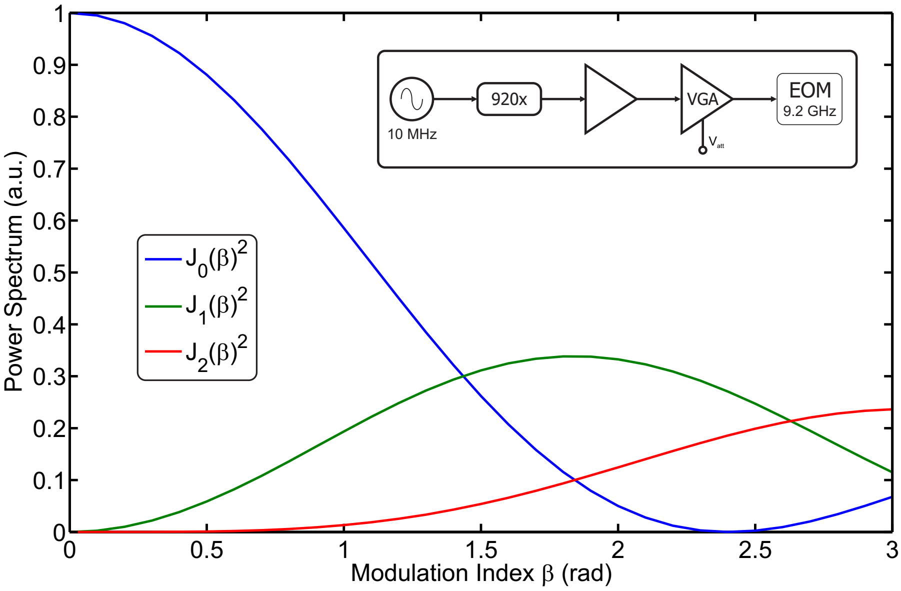

Figure 5.3: Sideband generation with the EOM before the BBO cavity. The power distribution in the carrier $J_0(\beta)^2$, the first and second sideband $J_{1,2}(\beta)^2$ is shown as a function of the modulation index β. Typical experimental parameters are $\beta \approx 0.58$. This corresponds to $\sim 8\%$ of the power in the first order sidebands and $\sim 25\%$ after frequency doubling. Effects of the second order sideband are neglected since that order only carries $\sim 2\%$ of the total power. The inset shows the electronic EOM setup. The 10 MHz reference is multiplied by 920 and amplified to provide the 9.2 GHz drive for the EOM.

driven with powers below 1.3 W.

The EOM is used to switch between a resonant configuration for Doppler cooling and detection of the ions and an off-resonant configuration for driving Raman transitions. The fiber laser is thereby adjusted to be 9.2 GHz detuned from the $P_{3/2}$ state of Mg^+. This way, one of the sidebands of the EOM is resonant with the $P_{3/2}$ when the EOM is switched on. The laser beams configuration are described later in Section 5.2.

A positive or a negative detuning for the Raman beams can be chosen. Both configurations work in principle, however, it turned out that the blue-detuned laser induced significant heating of the ions when loading multiple ions in the trap. For that reason, a red-detuned laser configuration was chosen later.

It is worth mentioning that the introduction of the EOM into the setup simplifies the requirements of the magnesium laser systems tremendously. In other setups [58], a second laser source resonant to the $S_{1/2}$ to $P_{1/2}$ transition is used to provide coherent manipulation while the first laser system is used for detection and Doppler cooling purposes. A third laser system is then used to generate Raman beams with several 10th of GHz detuning. The advantage of the EOM is the possibility to combine all requirements in one single laser system. However, the relatively small detuning of 9.2 GHz introduces off-resonant scattering which effectively limits the fidelity of coherent manipulation. This issue is discussed in Section 8.3. It is worth mentioning that this limit can be overcome by employing higher order sidebands with a larger detuning, e.g. 18.4 GHz detuning for the 2nd order sideband. Also, an increase of the resonance frequency of the EOM reduces this limitation further.

Wavemeter

During the operation of the experiment, all visible lasers are monitored by a precision wavemeter[16]. The wavemeter has a specified absolute accuracy of $\sim 60\,\mathrm{MHz}$ in the range of 370-1100 nm, while showing a much better reproducibility. However, due to temperature drifts and air fluctuations, the wavemeter needs to be re-calibrated to a known frequency to guarantee this precision. This is done by referencing the wavemeter to a temperature-stabilized Helium-Neon laser which is frequency-stabilized to the $^{127}\mathrm{I}_2$ R(127) 11-5 d-component at the frequency 473.612 379 828 THz [108, 109, 110]. This calibrated laser was provided by the group of U. Sterr, PTB.

5.2 Doppler Cooling and Raman Beam Configuration

The laser light for Doppler cooling, detection and coherent manipulation is produced by guiding the UV output of the frequency-quadrupled fibre laser system through a combination of acousto-optic modulators (AOM) to allow for frequency-adjusting and phase-coherent fast switching. An overview of the setup is given in Fig. 5.4 and is detailed in the following.

5.2.1 Optical Setup

The Raman laser beams are provided by splitting the beam into two branches, each of which passes through a single-pass AOM1/2[17] resonantly driven at 450 MHz and a double-pass AOM3/4[18] resonantly driven at 220 MHz. This way, the frequency difference of the beams matches the hyperfine splitting of $\sim 1.8\,\mathrm{GHz}$ in $^{25}\mathrm{Mg}^+$. The employed radio-frequencies are provided by several individual DDS circuit boards in combination with a pulse sequencer hardware (see Section 5.11).

The single-pass AOMs usually operate at a diffraction efficiency of $\sim 70\%$, whereas $\sim 50\%$ is achieved in the double-pass configurations. Throughout this thesis, the Raman

---

[16] HighFinesse WS/7 Super Precision

[17] Brimrose Corp. QZF-450-100-.280

[18] IntraAction Corp. ASM-2202B3

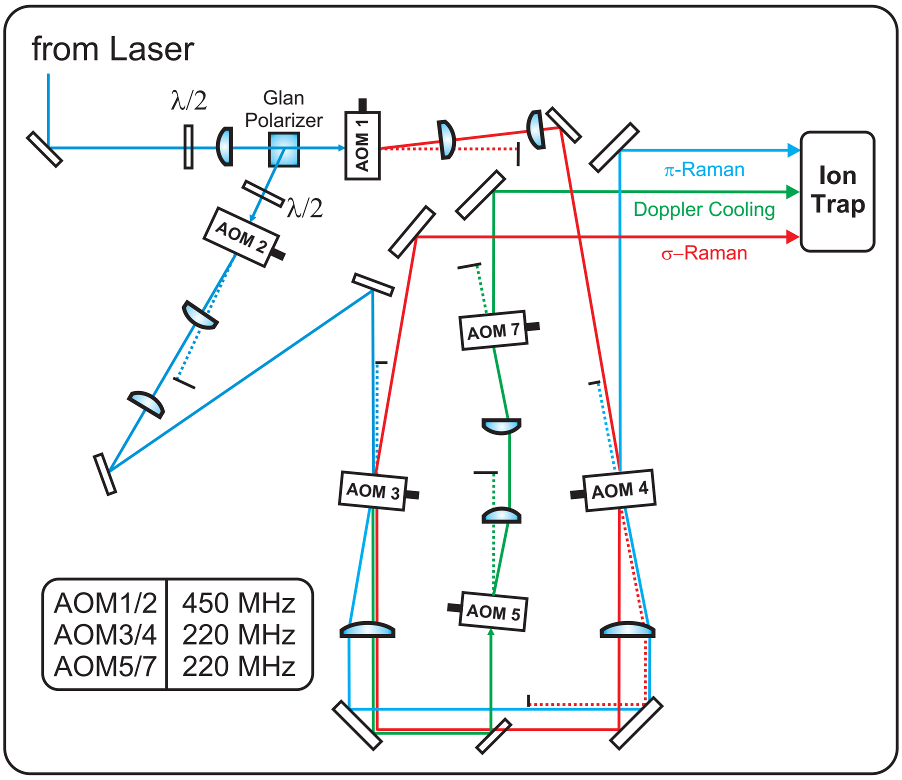
from Laser
λ/2
Glan Polarizer
AOM 1
λ/2
AOM 2
π-Raman
Doppler Cooling
σ–Raman
Ion Trap
AOM 7
AOM 3
AOM 4
AOM 5
AOM1/2 450 MHz
AOM3/4 220 MHz
AOM5/7 220 MHz

Figure 5.4: Laser-beam configuration. The output of the laser is split into two branches which produce both Raman beams (AOM1/2 and AOM3/4). The zeroth order of AOM3 is used for the Doppler cooling beam path. The setup is designed to avoid foci near any optical surfaces in order to avoid UV damage. The inset shows the different driving frequencies of each individual AOM.

beams are referred to as σ and π-beam, referring to their polarization entering the vacuum chamber (see Section 5.10).

The zeroth order of AOM3 is diverted into yet another double-pass AOM configuration (AOM5 and AOM7, both driven at 220 MHz) to provide the Doppler cooling and detection beam. Due to this configuration, this beam has the same frequency as the π-Raman beam. However, the Doppler cooling beam is σ-polarized to drive the cycling transition in $^{25}\mathrm{Mg}^{+}$.

Due to the 9.2 GHz detuning of the laser with respect to the $\mathrm{P}_{3/2}$ state, the Doppler cooling beam becomes resonant as soon as the EOM is switched on, whereas the Raman beams are applied when the EOM is switched off.

5.2.2 Double-Pass Configuration Avoiding UV damage

UV induced damage on the optical surfaces of miscellaneous components (mirrors, prisms, waveplates, ...) made a re-design of the double-pass AOM configuration, compared to commonly used setups [111, 112], necessary.

The major problem in double-pass AOM setups is the separation of the incoming and the outgoing beam. In the visible, AOM crystals are available whose diffraction efficiency is polarization independent. Here, the combination of a polarizing beam-splitter, AOM, quarter-waveplate and retro-reflector allows for the separation of the beams. This is not possible in the UV, since the efficiency drops significantly if the polarization is turned by 90° in the second passage. Commonly, the beams are separated geometrically by inclining the incoming collimated beam through the AOM crystal, shining the outgoing beam through a lens and retro-reflecting it with a vertical offset and reversed inclination angle by total internal reflection in a right-angle prism (see Fig. 5.5 (a) and (b)). For this setup to work, the AOM and the prism are required to be at the focal distance of the lens. This ensures that the first and zeroth order beams are parallel for all AOM driving frequencies. The AOMs we use contain a long crystal and require a near-collimated laser beam for optimum efficiency. The negative effect hereby is that the mentioned requirement at the prism-lens distance imposes an optical focus near the prism surface.

In such a configuration, visible optical damage was observed on the prism surface after operating the AOM setup for several hours. The incident beam typically had a power of 5 mW and was focused onto the prism yielding a waist of $\sim 50 - 70\,\mu$m which corresponds to an intensity of $320 - 640\,\mathrm{kW/m^2}$. The damage manifested itself in a distorted beam shape after passing through the prism and a significant degradation of the AOM efficiency. A parallel shift of the prism recovered the efficiency and the beam shape. Additionally, operating the setup at a decreased beam power shows no degradation at all. Both effects support the conclusion that the degradation originates from UV induced damage when the intensity overcomes a certain threshold [113].

This problem is eliminated by a novel double-pass configuration, as shown in Fig. 5.5 (c). In this setup, both Raman beams counter-propagate through the same AOMs. The principle is the same as in the conventional setup with the difference that all optical foci near surfaces are avoided. It should be noted that all beams are in a single plane. However, the beam separation is achieved by shifting the beams slightly in the plane of diffraction by a few $\sim$mm. This results in a small non-significant shift in the switching times of the Raman beams. It should be noted that both AOMs need to be driven by the same frequency to guarantee the Bragg condition for each beam. Thus, an individual frequency scan of each individual AOM is not possible. At the same time the shared optical path reduces phase noise between the Raman beams.

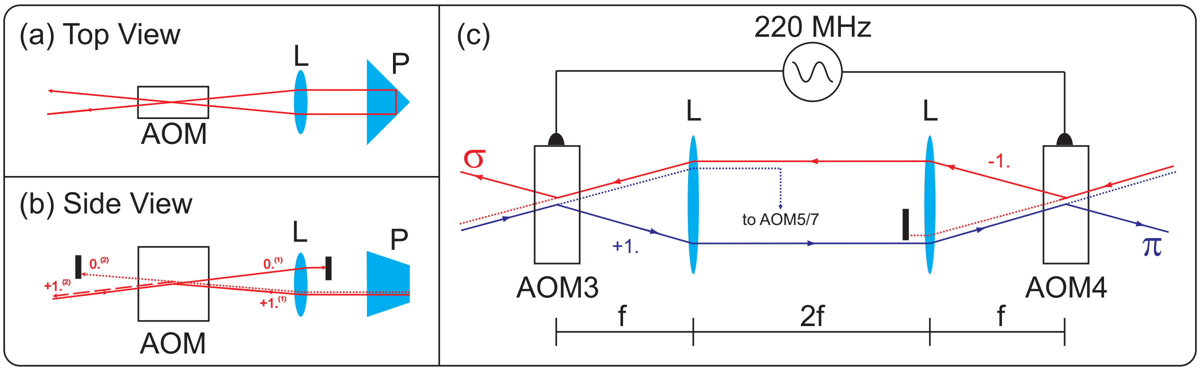
(a) Top View
L
P
AOM
(b) Side View
L
P
0.(2)
+1.(2)
0.(1)
+1.(1)
AOM
(c)
220 MHz
L
L
σ
-1.
to AOM5/7
+1.
π
AOM3
AOM4
f
2f
f

Figure 5.5: Schematics of the double-pass AOM setup. (a) and (b) show top and side views of commonly implemented AOM setups in a double-pass configuration, where polarization optics cannot be used for beam separation. The different diffraction orders are labeled, where the superscript represents the first and second pass. L: lens; P: prism. (c) This setup avoids foci near optical surfaces. Both Raman beams (σ and π) are produced with this configuration. While all beams are in the same plane, the beam separation takes place by shifting one of the beams in the plane of diffraction by a few mm. The zeroth order of AOM3 serves as an input for the double-pass of AOM5/7 for the Doppler cooling beam (not shown). Both AOMs are driven by the same frequency to fulfill the Bragg condition for both beams.

5.3 Microwave Antenna Setup

The radio-frequency to directly drive coherent Rabi oscillations between the $|\downarrow\rangle$ and the $|\uparrow\rangle$ states is provided by mixing a DDS output channel with a function generator[19] and amplifying[20] the resulting radio-frequency up to 4 W. The complete setup including filters is shown in Fig. 5.6.

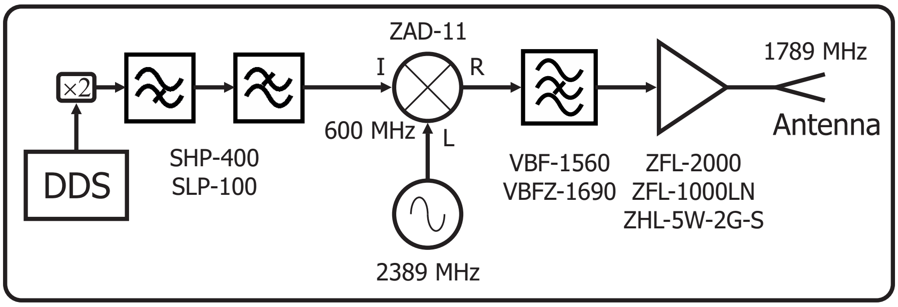
ZAD-11
×2
DDS
SHP-400
SLP-100
I
R
L
600 MHz
2389 MHz
VBF-1560
VBFZ-1690
ZFL-2000
ZFL-1000LN
ZHL-5W-2G-S
1789 MHz
Antenna

Figure 5.6: Radio-frequency setup. The radio-frequency for driving coherent oscillations is generated by mixing the output of a DDS board with a function generator and amplifying it to ~ 4 W. The antenna is comprised of a special coaxial cable (see text).

The amplified field is sent to an impedance-matched quarter-wave antenna made of a special coaxial cable[21] with a very low attenuation of 0.27 dB/m at 1.8 GHz. The production of sufficiently strong field amplitudes at the position of the ion is realized by mounting the antenna on top of the vacuum chamber at a distance of ∼12 cm from the center of the trap.

---

[19] Marconi Instruments 2024

[20] Mini-Circuits ZHL-5W-2G-S

5.4 Laboratory Frequency-Reference

All components providing radio-frequency fields that are phase-sensitive are referenced to a single 10 MHz frequency-reference[22] with an accuracy of ±5 ppm. The signal is distributed to all relevant components by a frequency-distribution amplifier[23]. The schematic of the distribution is shown in Fig. 5.7. In the near future, the common reference will be replaced by a direct connection to a hydrogen maser provided by PTB.

It is worthwhile mentioning that even though the AOMs and the function generator producing the Raman beams and the radio-frequency have a common reference, differential fluctuations in the optical path of the two Raman beams introduce phase fluctuations between the laser field and the radio-frequency field at the position of the ion.

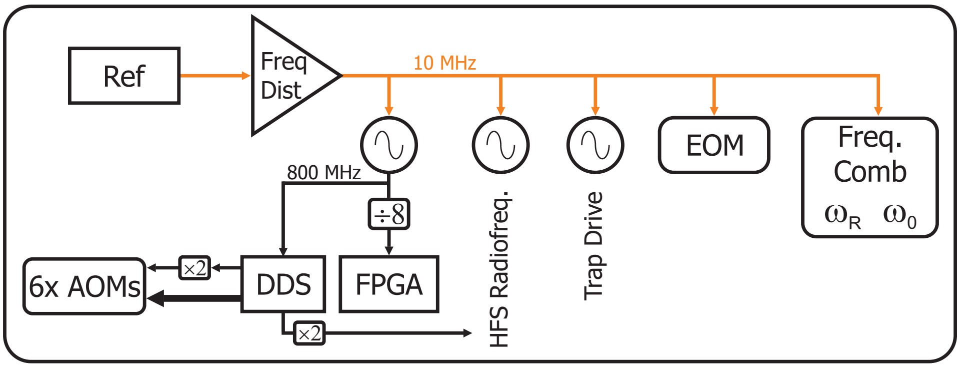

Figure 5.7: Reference frequency distribution. All components used in the experiment are referenced to a single timebase (SRS DS-345).

5.5 Vacuum Chamber

The vacuum setup comprises of a stainless-steel octagon chamber (size CF200), as shown in Fig. 5.8 in a cross-section. In the center of the chamber, the ion trap with the atomic ovens is placed. Close to the trap is a parabolic mirror and an inverted viewport[24] containing a self-build objective for fluorescence collection. A six-way cross is connected to the port behind the parabolic mirror[25] (P in picture) which holds the vacuum pumps (ion-getter pump[26] and Titanium sublimation pump[27], a vacuum gauge[28], a needle-valve[29] and a full-metal valve[30]). While the chamber has been pre-evacuated using a roughing pump connected to the metal-valve, the final vacuum of $< 10^{-11}\,\mathrm{mbar}$[31] is reached with the two remaining pumps[32] after several days of bake-out at 180°C.

---

[21] Andrew CommScope FSJ1-50A

[22] Stanford Research Systems DS-345 with Standard Timebase

[23] TimeTech, Frequency Distribution Amplifier 10219

[24] UKAEA, custom-made

Optical access is provided via six fused-silica viewports[33] (size CF63), connected to the ports of the main chamber and a single fused-silica viewport[34] (size CF100) on top of the chamber. The inverted viewport and the viewports have a $\mathrm{MgF_2}$ anti-reflection coating[35] centered at 280 nm.

The parabolic mirror is placed on a dynamical bellow[36] which is attached to a self-build translation stage and a self-build mirror holder outside the chamber. This allows for precision adjustments (via x, y, z-axes translation and 2-axis rotation) of the position of the parabolic mirror.

The needle-valve allows for a specified leak rate of $1.3 \times 10^{-10}\,\mathrm{mbar\ l/sec}$ and can be used for leaking hydrogen into the chamber to produce hydrid ions, such as $\mathrm{MgH^+}$. This is of relevance for a later stage of the experiment where molecular ions shall be prepared in the ro-vibrational ground state.

Two 8-pin electrical feedthroughs[37] serve as leads for all required DC voltage connections to the Paul trap, the atom ovens and two separate electronic emitters[38]. A third feedthrough on top of the chamber guides the radio-frequency to the blades of the trap.

5.6 Paul Trap and Atom Ovens

The Paul trap is shown in Fig. 5.9. It consists of four stainless-steel blades to which the radio-frequency is applied and two tip electrodes to which a DC voltage provided by a precision power supply[39] is applied. Typical operating values are 24.8 MHz for the

---

[25] KUGLER GmbH, custom-made
[26] Varian Star Cell 20l
[27] Varian TSP
[28] Varian UHV-24 Gauge
[29] Caburn MDC ULV-150
[30] VAT Deutschland GmbH
[31] The actual value is at the limit of the vacuum gauge.
[32] During the pre-evacuation, the chamber was baked for about two weeks to improve the vacuum.
[33] Caburn MDC
[34] Caburn MDC
[35] Torr Scientific LTD
[36] COMVAT, custom-made
[37] Caburn-MDC HV5-30C-8-C40
[38] Kimball Physics ES-015 on CB-104
[39] iseg Spezialelektronik GmbH DPR206052410

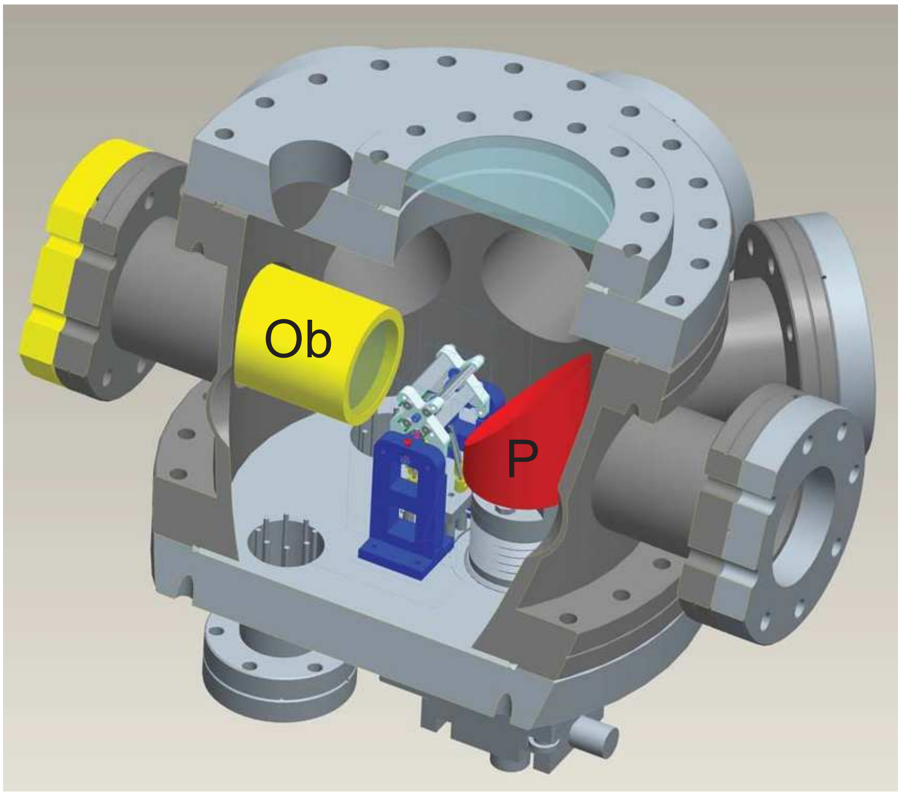

Figure 5.8: Main vacuum chamber. In the center of the chamber, the Paul trap is placed. Fluorescence detection is performed via a parabolic mirror (P) and an objective (Ob) which is located inside an inverted viewport. The atom ovens are placed below the trap. Optical access is provided by eight viewports connected to the hexagon.

radio-frequency drive at 3-5 W input power and DC voltages between 0 and 2000 V.

Furthermore, two pairs of compensation electrodes are available to shift the ion's radial position by applying DC voltages[40] between 0 and 500 V. In axial direction, a differential voltage of up to 130 V[41] between the endcaps allows for shifting the ion. All voltages are applied for compensation of micromotion.

Apart from the openings at the side of the trap, optical access is given on the trap axis via holes that are drilled into the trap electrodes. The whole construction is fixed by a macor piece on each side and pressed together with screws.

Below the trap, an array of six different ovens is placed (unless otherwise mentioned, the ovens contain the natural abundances): two magnesium ovens, one enriched ^{25}Mg[42], a calcium oven, a titanium oven and an iron oven. The complete construction is shown in Fig. 5.9. Apart from the case of titanium and iron, all ovens are resistively-heated steel tubes which contain a powder of the corresponding material. This doesn't work for

---

[40] iseg Spezialelektronik GmbH DPR05106245

[41] This is provided by self-build electronics.

[42] OAK Ridge National Laboratories

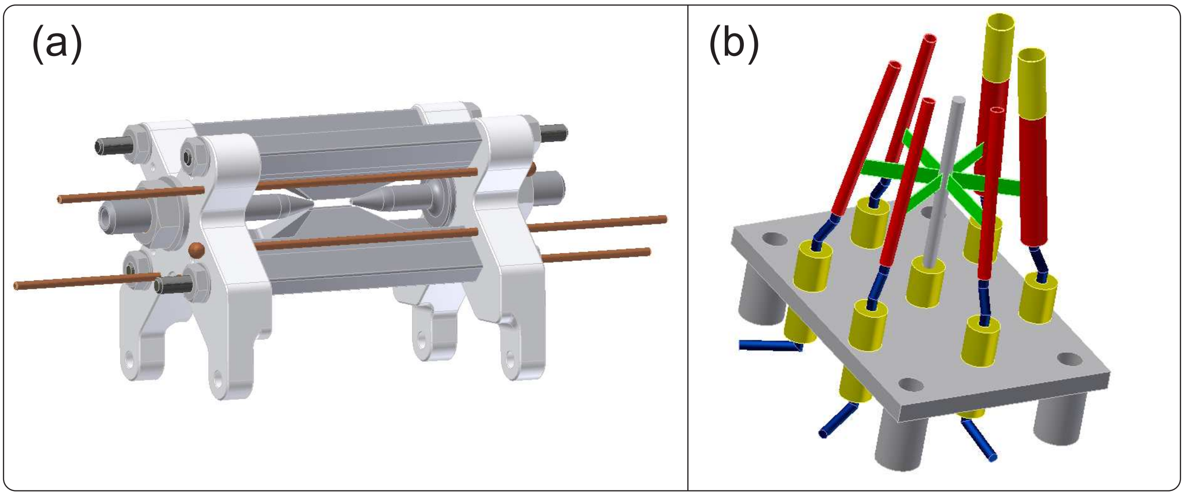

Figure 5.9: (a) Drawing of the linear Paul trap. The radio-frequency is applied to the stainless steel blades and the DC voltage is applied to the stainless steel tip electrodes. The whole construction is held together by two macor pieces, one on each side. The compensation electrodes (welding rods, colored brown in the picture) allow for shifting the ion in radial direction. (b) Oven setup. Six individual ovens supply thermal atomic beams by resistive heating. The stainless-steel tubes contain ^{24}Mg, enriched ^{25}Mg and ^{40}Ca. Additional two ovens comprise of a titanium and respectively an iron wire spooled around a tungsten wire. The ovens have a common ground and are placed below the ion trap and their outlets are directed towards its center.

titanium or iron since their melting point is too high (see Fig. 5.10). For this reason, these ovens consist of a tungsten wire with a wound up thin titanium/iron wire (similar to a light bulb). The tungsten wire is heated and the material in the surrounding of the wire starts evaporating.

All ovens are directed towards the center of the trap. Since the ionization laser shines through the trap axis, it is almost perpendicular to the thermal beam of the atoms and no significant Doppler shift is expected for the excitation frequencies. A single magnesium ion is loaded into the trap by heating the oven with typically $\sim 6\,\mathrm{W}$ for one or more minutes while shining the photoionization laser through the trap center. After photoionization took place, the laser is blocked with a mechanical shutter to stop the loading process.

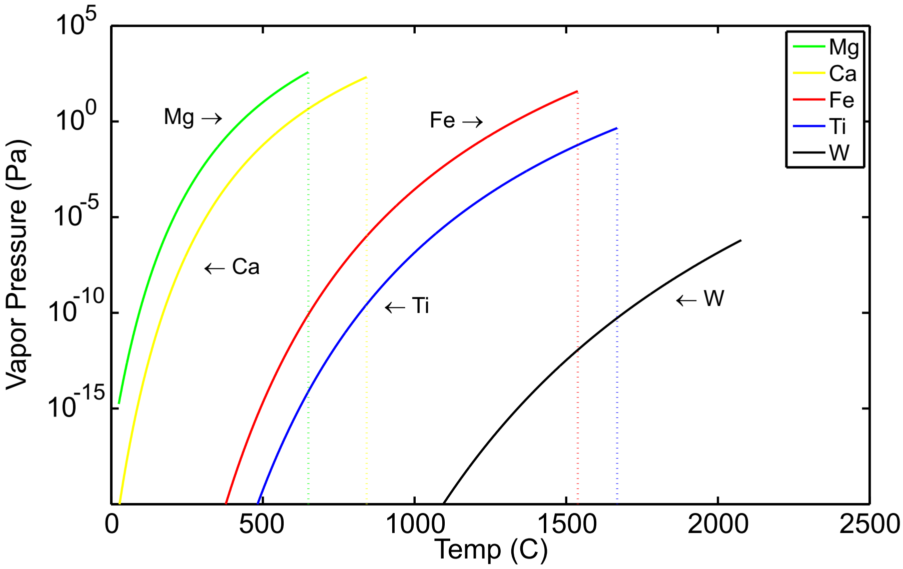

Figure 5.10: Vapor pressure for different elements. The vapor pressure is plotted as a function of the temperature up to the melting point. The functional behaviour is $a_1 + a_2/T + a_3 \log(T) + a_4/T^3$, where a_i are material constants (see [114]).

5.7 Radio-Frequency Drive of the Paul Trap

The oscillating potential for radial confinement in the Paul trap is provided by a function generator[43] whose output is amplified[44] and sent through a self-build helical resonator [115] for amplitude enhancement. One pair of opposing trap electrodes is connected to the output of the resonator, while the remaining pair is grounded to the vacuum chamber at the outside. The resonator shows an unloaded (without trap) resonance frequency of ~55 MHz. Its resonance frequency changes to ~25 MHz, if the trap is connected.

It is worthwhile mentioning that the resonator showed a rather low quality factor when the trap was connected for the first time ($Q \sim 60$). It turned out that the main reason for this low value was caused by capacitive coupling to components close to the blades of the trap. These components are connected to the electrical feedthroughs at the bottom of the chamber and supposedly act as antennas producing large radio-frequency noise in the laboratory. In the meantime, the radiation issue has been overcome by a direct capacitive[45] shunting - optimized for ~23 MHz - between the entry point of the feedthroughs and the chamber. No other low-pass filter is used in the setup. With the new configuration, a quality factor of $Q \sim 250$ is achieved and the radio-frequency noise in the lab is significantly reduced. The results of a S-parameter measurements to determine the quality factor is shown in Fig. 5.11.

---

[43] Marconi Instruments 2024

[44] Mini-Circuits ZHL-5W-1

[45] Vishay Draloric Ceramic AC Capacitors Class X1, 760 VAC

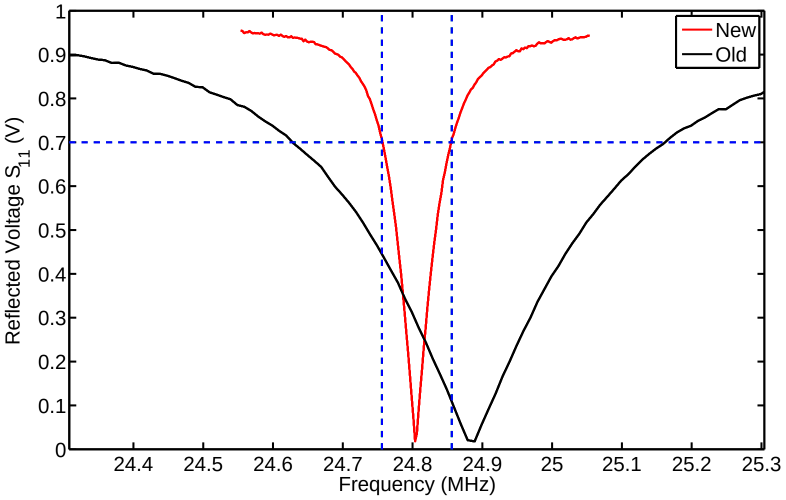

Figure 5.11: Quality factor of the helical resonator. The reflected voltage (S_{11}-Parameter) of the helical resonator (connected to the Paul trap) is shown as a function of the frequency. The measurement was done using the S-Parameter set of a Hewlett-Packard network analyzer. The quality factor of $Q \sim 60$ *(black curve)* has been improved to $Q \sim 250$ *(red curve)* by adding capacitive couplings to the feedthroughs at the chamber (see text for details).

5.8 Magnetic Field Coils

The magnetic quantization field to lift the degeneracy of the magnetic substates is provided by a pair of self-build coils in Helmholtz configuration. The coil axis is aligned to the Doppler cooling beam (see Section 5.10). Typically, a field of ~0.6 mT is achieved at the ions position with 6 A driving current. Additionally, two pairs of compensation coils are employed along the remaining two perpendicular directions. Both coils produce a compensation field of 0.18 mT and respectively 0.28 mT with 1 A driving current [102]. All coils are driven with individual precision current drivers[46].

5.9 Fluorescence Detection of the Ion

There are two channels to observe the ions fluorescence: a self-build UV objective and a parabolic mirror. Both channels are imaged onto either a photomultiplier tube (PMT)[47] with a specified quantum efficiency of ~30% or a charge-coupled device (CCD) camera[48] with a specified quantum efficiency of ~ 25% at 280 nm. While the PMT is used for quantitative analysis, the camera is mainly used for monitoring and alignment purposes due to the slow readout process. A computer controlled flipping mirror is installed in the beam path to either guide the fluorescence onto the PMT or the CCD camera.

---

[46] Agilent 3615A/3616A

[47] Hamamatsu H8259MOD w/ R7518P

[48] Andor iXon 885

5.9.1 UV Objective

The UV objective is a six-lens system, based on an existing design [116] which was adapted to be used at a wavelength of 280 nm. The objective was designed and optimized with the software Zemax [117]. Since our experiments do not require high spatial resolution images, the optimal lenses were replaced by commercial lenses for economic reasons. A detailed description of the lens parameters is given in Appendix E. Using this objective, the ion is imaged onto an iris for mode and stray light filtering. The intermediate image is in turn imaged by a two-lens objective onto either the CCD camera or the PMT. The estimated overall f-number of this configuration is approximately $\sim$1.24, for a full aperture of the objective. This corresponds to a solid angle of $\sim$3.6% for fluorescence collection.

In Fig. 5.12 an example image of an ion string in the Paul trap taken with the CCD camera is shown. Clearly, optical aberrations lead to a distortion of the ion images which act as point sources. This is due to the chosen non-optimal lens parameters and due to misalignments of the lenses with respect to each other inside the objective.

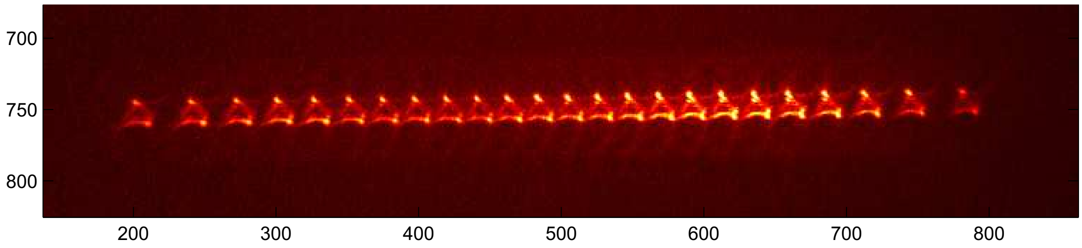

Figure 5.12: Picture of magnesium ions string. A picture of a string of $^{24}\mathrm{Mg}^{+}$ ions imaged by the self-build UV objective onto the CCD camera is shown. The pixel size of the camera is $8 \times 8\,\mu\mathrm{m}^2$. The deviation from point source images is due to optical aberrations which result from lens misalignment and the used non-optimal commercial lenses.

5.9.2 Parabolic Mirror

The parabolic mirror is custom-made and consists of aluminium. It does not contain any anti-reflective coating and has a specified reflectivity of $> 90\%$ at 280 nm. Theoretically, it covers a solid angle of $\sim 11\%$. In Fig. 5.13 a picture of a single ion simultaneously imaged with the parabolic mirror and the UV objective onto the CCD camera is shown. Strong aberrations are observed which are expected to result from coma for off-axis imaging. The typically observed photon counting histograms of the combined image onto the PMT is shown in Fig. 7.3. Even though the estimated solid angle which is covered by the parabolic mirror is much larger than that of the objective, we observe only roughly the same amount of light as with the objective. This is probably due to a non-optimum alignment. In addition to that, a much larger background due to stray light is observed. An explanation for that can be a reduced surface quality due to remaining grooves from the machining process of the mirror and the fact that the image of the parabolic mirror is not spatially filtered with an iris like the image of the UV objective.

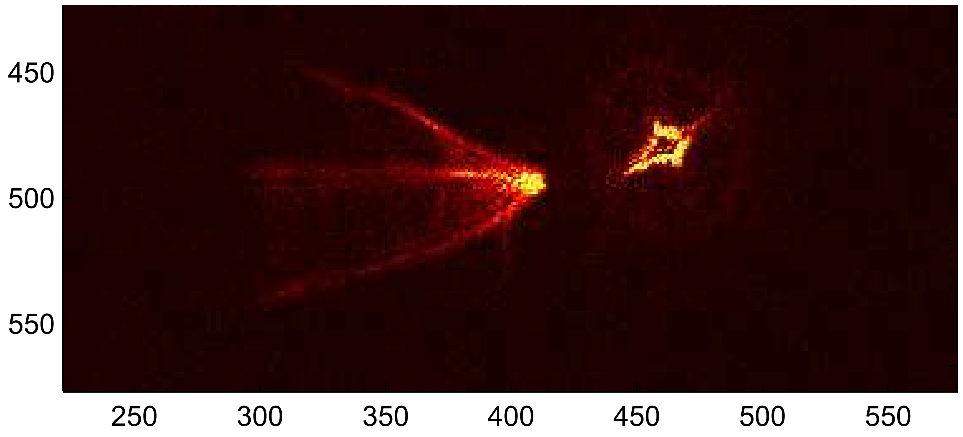

Figure 5.13: A single ^{24}Mg^{+} ion is simultaneously imaged onto the CCD camera by the UV objective (rhs) and the parabolic mirror (lhs). Strong aberrations of the parabolic mirror image result from coma, if the ion is misaligned from the focal point of the mirror.

5.10 Laser Beam Configuration

The polarization of each laser beam in the setup depends on its direction with respect to the quantization axis defined by the main magnetic field. It defines which transitions in the ion are driven and needs to be carefully adjusted in the experiments to avoid excitations to unwanted auxiliary states. Both Doppler cooling and σ-Raman beam are co-aligned with the magnetic field and thus circular polarized driving σ-transitions. The π-Raman beam is perpendicular to the magnetic field and drives pure π-transitions. All beams are in the horizontal plane and focused onto the ion using lenses of 200 or 300 mm focal length. The main magnetic field is tilted by 45° with respect to the trap axis. In Fig. 5.14 the geometry of all beams entering the vacuum chamber is shown. Before the beams enter the chamber, a beam pickup is used to monitor their individual intensity. The signals are fed back to a sample-and-hold proportional-integral controller loop to control the AOMs for intensity stabilization. The sample-and-hold configuration allows for intensity stabilized pulsed operation of the laser beams on a μs timescale.

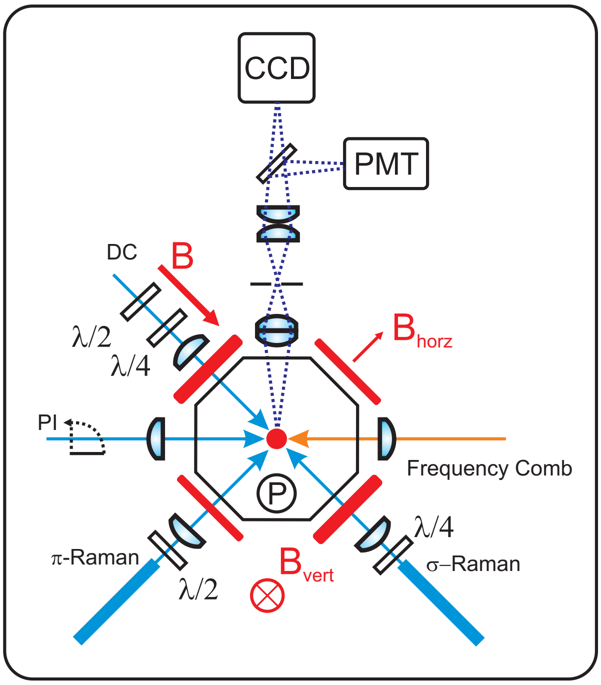

Figure 5.14: Top view of the geometry of the setup. The Doppler cooling (DC) beam is co-linear to the σ-Raman beam, whereas the π-Raman beam is perpendicular to both of these beams. All beams enter the chamber at an angle of 45° with respect to the trap axis. The photoionization beam (PI) is co-linear to the trap axis. The magnetic field is in direction of the Doppler cooling beam allowing for driving σ transitions with circular polarised light on that axis. Additional coils serve as compensation fields in horizontal B_{horz} and vertical direction B_{vert}. The Raman beams are guided to the center of the trap by fibres (see text for details). Each beam has an individual pickup in front of the chamber which is used as feedback for intensity stabilization (not shown). The fluorescence of the ion is collected with an objective (only two lenses are shown) and a parabolic mirror (P) and imaged onto a CCD camera or a PMT, respectively. In the objective path, the ion is imaged onto a pinhole (Thorlabs P100S) to reduce stray light.

Additionally, each Raman beam is coupled to a $\sim 10\,\mathrm{cm}$ hollow-core photonic-crystal fiber [118] to suppress beam pointing and for mode cleaning purposes. It should be noted though that this particular type of fiber exhibits multi-mode behaviour at 280 nm. However, it was kept in the setup as an alignment aide and for the purpose of decreasing beam pointing instabilities.

The power of each Raman beam is typically on the order of 1 mW with a beam diameter of $\sim 500\,\mu\mathrm{m}$ before the focusing lens. The Doppler cooling beam is adjusted to match the saturation intensity of the 280 nm transition by observing fluorescence counts on the PMT.

5.11 Experimental Control

All time-critical components are handled by a pulse sequencer hardware based on a field-programmable gate array[49] (FPGA) [119]. The user frontend is a Labview interface which communicates with the sequencer via an open-source Python server [120]. Furthermore, two data acquisition cards with various analogue and digital I/O channels are used for remote control of various components like power supplies, shutters, etc.

The pulse sequencer hardware has six direct-digital synthesizer (DDS) boards connected to it, each of which is equipped with an individual FPGA[50]. The DDS chip is clocked with 800 MHz so that a frequency output between ~ 10 and ~ 350 MHz is achieved. Since the present design does not allow for a sufficient (60dBc) radio-frequency output suppression when the DDS output is switched off, additional RF switches[51] are used for further suppression.

The complete setup allows for phase-coherent switching between the individual frequency output channels and amplitude modulation on a sub-μs timescale. A summary of important figures of merit are given in the following table [121]:

Figures of Merit	
Frequency Switching Time	< 150 ns
Phase Offset Accuracy	$2\pi \times 2.4 \times 10^{-4}$
Signal to Noise	50 dBc
Frequeny Resolution	0.18 Hz
Maximum Output Level	~ 1 dBm

For a detailed description of the complete sequencer system, the reader is referred to [119, 121].

---

[49] Altera Cyclone 1

[50] Altera Cyclone 2

[51] Mini-Circuits ZFSW-2-46

Chapter 6

Experimental Prerequisites

In this chapter, first experiments to characterize the Paul trap are discussed. In the first part, the calibration of the trap parameters is presented. This includes the measurement of the axial and radial trap frequencies and the calibration of the magnetic field strength. In the last part of this chapter, different ways to compensate for micromotion in the Paul trap, along with their experimental results, are presented.

6.1 Axial Trap Frequencies

There are two major ways to calibrate the axial trap frequency, i.e. the frequency of the ion's secular motion along the trap axis. In a first way, a direct excitation by applying a radio-frequency field to a component nearby the ion heats the ion crystal. This effectively decreases the fluorescence which is observed with the CCD camera. Since the axial trap frequency scales with the inverse square-root of the ion's mass, this method can be used to determine the loaded isotope. In Fig. 6.1, the measured axial trap frequencies as a function of the applied tip electrode voltage are shown. The radio-frequency exciting the ion has been applied to one of the electron emitters which is close to the ion. The corresponding fit yields a trap frequency dependence for $^{25}\mathrm{Mg}^+$ of

$$\omega_z = 2\pi \times 49.2(1) \cdot \sqrt{U_{\mathrm{dc}}} \quad . \tag{6.1}$$

Given the applied DC voltages of $0 - 2000\,\mathrm{V}$, axial trap frequencies up to $\sim 2.2\,\mathrm{MHz}$ are achieved. The different isotopes are clearly distinguished in their frequency ratios (see Fig. 6.1). Additionally, the geometric factor of the employed Paul trap (see Eq. (2.2)) is determined to be $\kappa \sim 0.08$ from a trap frequency measurement with a single $^{24}\mathrm{Mg}^+$ ion.

In a second way, the axial trap frequencies are determined by exciting Raman-stimulated sideband transitions. This method has a higher precision and is discussed in Section 8.

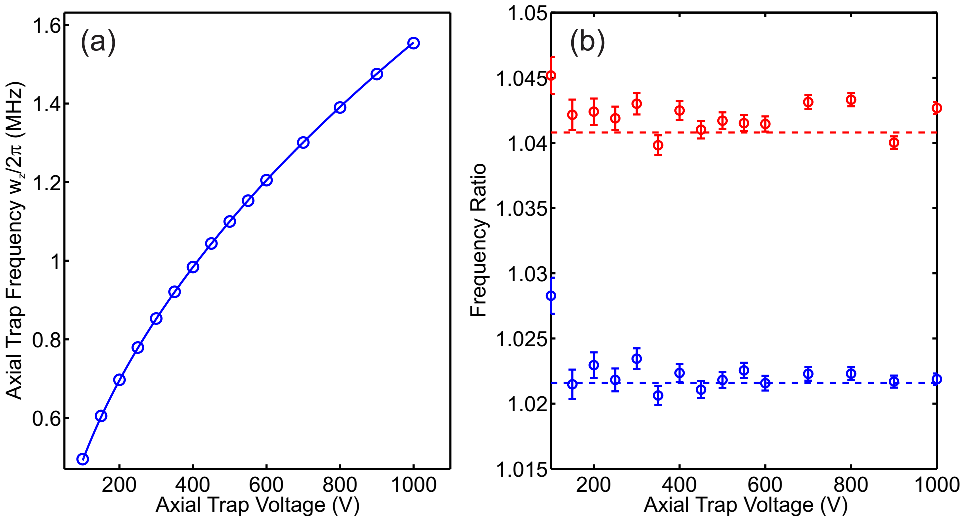

Figure 6.1: Axial trap frequency calibration. (a) The axial trap frequency is shown as a function of the endcap voltage for $^{24}\mathrm{Mg}^{+}$ ions. The error bars are on the order of 3 kHz and omitted for clarity. (b) The ratio of the axial trap frequency for $^{24}\mathrm{Mg}^{+}/^{25}\mathrm{Mg}^{+}$ (blue curve) and $^{24}\mathrm{Mg}^{+}/^{26}\mathrm{Mg}^{+}$ as a function of the endcap voltage is shown. The expected ratios are given by the dashed lines. The picture is taken and adapted from [102].

6.2 Radial Trap Frequencies

The radial trap frequencies are measured in a similar way as the axial ones. Only here, the radio-frequency excitation is mixed with the trap drive. The setup and the measurement results are shown in Fig. 6.2. With a tip electrode voltage of 1000 V and an incoupled radio-frequency power of 5 W, a radial trap frequency of ∼4.5 MHz is achieved.

Since the wave vector difference of the Raman beam configuration does not have a projection onto the radial directions, it is not possible to excite radial sidebands. However, one way to achieve this, is to send the π-Raman beam from the opposite side of the chamber onto the ion or irradiating it vertically by going through the upper viewport on top of the chamber. These configurations were used for compensating the micromotion in all three dimensions.

6.3 Magnetic Field

The magnetic field is calibrated by measuring the excitation frequency of the transition between the hyperfine ground states $|{\downarrow}\rangle$ and $|{\uparrow}\rangle$ as a function of the current through the coils producing the B-field. The result is shown in Fig. 6.3. A linear fit yields a magnetic field dependence of 0.089 ± 0.001 mT/A at the position of the ion. Additionally, magnetic field fluctuations have been characterized with a Hall probe[1]. After moving

---

[1] Stefan Mayer Instruments, FL3-100

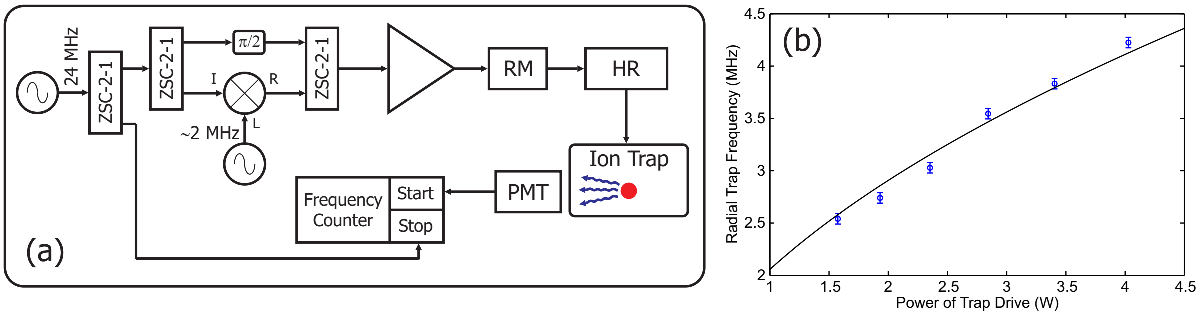

Figure 6.2: Radial trap excitation and photon-correlation setup. (a) To excite the ion radially, the trap drive is split and the excitation frequency is mixed to one line. The second line is phase-shifted by $\pi/2$ and both lines are combined again. This way, the amplitude modulation before going into the amplifier is reduced. In a saturated regime of the amplifier (though not desirable), where amplitude modulation is suppressed, this configuration can be helpful. The incoupled RF power is measured by a reflecto-meter (RM) and fed into the helical resonator (HR). Also shown is the photon correlation setup: The PMT signal is used as a start trigger and the second line of the trap drive is used as a stop trigger (see Section 6.4) to measure photon arrival times. (b) The measured radial trap frequencies as a function of the power which is incoupled to the trap are shown. The measurements were taken at a tip electrode voltage of 1000 V.

power supplies and other electronic equipment as far as possible from the trap, the fluctuations have been optimized to be on the order of $\sim 0.1 - 0.2\,\mu$T directly outside the vacuum chamber.

6.4 Compensation of Micromotion

The amount of excess micromotion in the ion trap is critical for the experiments. From a precision spectroscopic point of view it needs to be decreased as far as possible since it leads second order Doppler shifts and to a distortion of spectral lines due to the presence of micromotion sidebands. However, with respect to our work, since it is a driven motion, it is essential to cancel it since it can lead to heating of the secular motion of the ion. This is critical, if ground state cooling is to be achieved. A detailed discussion of such influences is found in [67, 68, 69].

There are different reasons for micromotion in Paul traps, among which one finds surface charges or relative phase-shifts between the radio-frequency lines. Surface charges, for instance, produce static electric fields which move the ion away from the center of the trap leading to excess micromotion (see Section 2.1.3). It is worth noting, that in the experiment, a direct illumination of the trap electrodes with UV laser light is therefore to be avoided since the photoeffect charges up the blades significantly, shifting the position of the ion. Relative phase-shifts originating from e.g. asymmetries in the cables guiding

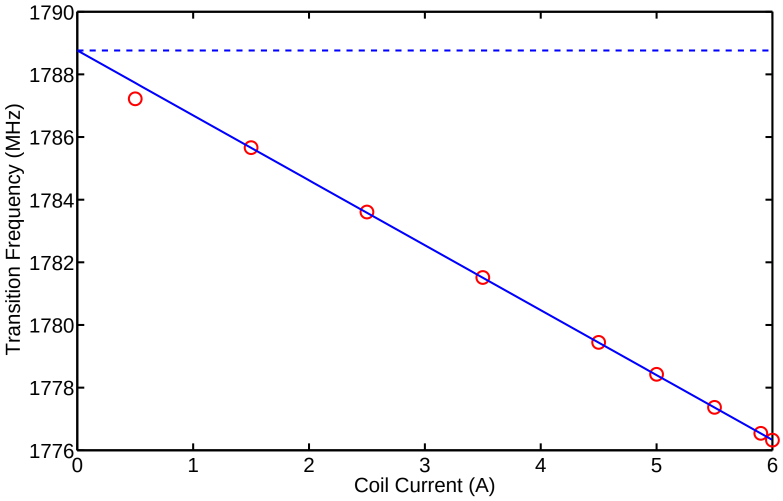

Figure 6.3: Magnetic field calibration. The frequency of the $S_{1/2}$ $|3,3\rangle$ to $|2,2\rangle$ transition is plotted as a function of the driving current of the magnetic field coils. At very low driving current of $< 1\,\mathrm{A}$, the field magnitude is so low that the earth's magnetic field becomes dominant leading to larger deviations from the linear behaviour. The dashed line corresponds to the expected zero-field transition frequency.

the radio-frequency to the trap, are to be avoided. Especially, since this type of shift can not be adjusted from outside the vacuum chamber.

There are several ways to compensate for micromotion three of which are explained in the following. A detailed overview including a complete theoretical description of the effects is found in [67].

6.4.1 Camera

An initial rough compensation is achieved by observing the position of the ion on the CCD camera for varying radio-frequency powers. At high powers, the position is determined only by the radio-frequency and stray fields are negligible. That means, that any shift of the ion while lowering the radio-frequency power needs to be compensated to arrive at the high-field position again. This way, the position of the ion can be made independent of the RF power and the ion is placed at the RF zero line of the Paul trap. In principle all directions can be roughly compensated with this technique. However, since a spatial shift in direction of the optical axis of the objective is difficult to observe, mainly the vertical and the axial compensation is performed in this way.

6.4.2 Photon-Correlation Measurements

In a second and more precise way, a correlation measurement between fluorescence photon arrival times and the phase of the trap frequency drive using a frequency counter[2] has been performed. For optimal performance, the laser is detuned off-resonantly to the slope of the Doppler cooling absorption line. Any movement of the ion will modulate the amount of fluorescence due to the corresponding frequency change of the Doppler effect. Since the excess micromotion is an oscillation driven by the trap drive, the number of measured fluorescence photons is correlated to the phase of the radio-frequency.

It should be noted that a vertical spatial offset of the ion from the trap center results in horizontal (micro)motion and vice versa. However, the Doppler shift is only sensitive to the projection of the k-vector of the exciting laser onto the direction of the motion. Consequently for a compensation in all directions, laser beams in all three spatial dimensions are needed. In the experiment, the horizontal direction is covered by the Doppler cooling beam, since it has one projection onto the trap axis and one in the direction of the objective. The vertical direction needs an additional laser beam which is guided through the viewport on top of the chamber onto the ion. The axial direction is covered by an additional beam which is guided through the trap axis.

In Fig. 6.4, the result of a measurement for the compensation of the axial micromotion is shown in form of the described photon arrival histograms. While shifting the ion on the trap axis, a clear minimum is observed in the contrast of the histogram function which is quantified by the standard deviation of the events. Additionally, while crossing the optimal point, the correlation experiences a 180° phase shift. This results from the sinusoidal drive of the trap blades.

6.4.3 Micromotion Sideband Spectroscopy

The third and most precise way to minimize excess micromotion is resolved sideband spectroscopy on micromotion sidebands. The (micromotion) sidebands are offset by a multiple of the radio-frequency of the trap drive Ω_{rf} from the carrier transition and their strength depends on the amount of excess micromotion. The ion can be excited on these transitions using the Raman lasers. In the limit of low saturation, the excitation rate on the nth order micromotion sideband is given by [67, 122]

$$\rho \approx \sum_{n=0,\pm1,\ldots} \frac{\Omega^2}{4} \frac{J_n^2(\beta)}{(\omega_{\mathrm{laser}} - \omega_{\mathrm{a}} - n\Omega_{\mathrm{rf}})^2 + (\Gamma/2)^2} \quad , \tag{6.2}$$

---

[2] Stanford Research Systems SR620

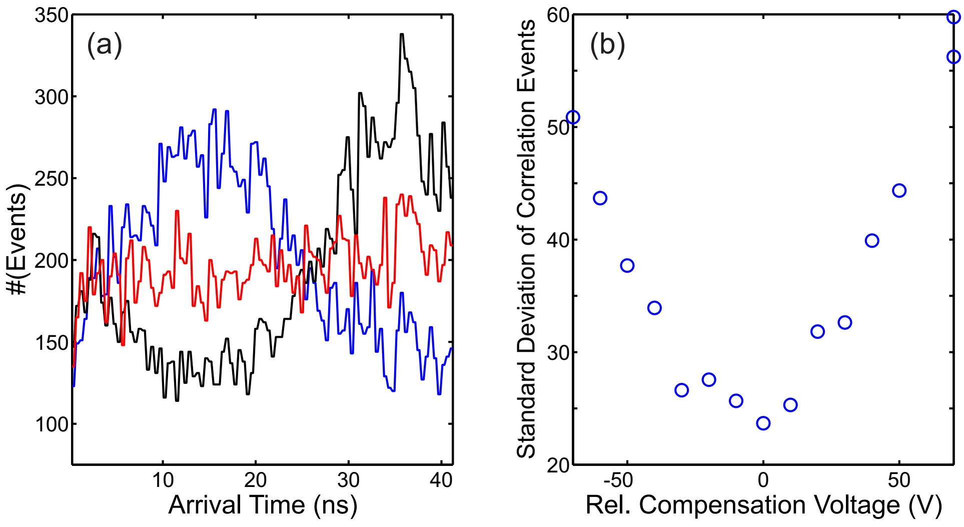

Figure 6.4: Photon-correlation measurements. (a) Histogram of the number of photons as a function of their arrival time with respect to the phase of the trap drive. The curves differ in the relative axial compensation voltage: -60 V (blue), 0 V (red), 60 V (black). (b) The standard deviation of the histograms in (a) is shown as a function of the axial compensation voltage.

where J_n are the Bessel functions of nth kind, $\omega_{\text{laser}} - \omega_{\text{a}}$ the laser detuning with respect to the atomic transition frequency, Γ the natural linewidth of the transition and Ω the carrier Rabi frequency. Thus, the modulation index β is determined experimentally by comparing the excitation on the carrier and a micromotion sideband, i.e. by comparing their respective Rabi frequencies

$$\frac{\Omega_s}{\Omega_c} = \frac{J_1(\beta)}{J_0(\beta)} \approx \frac{\beta}{2} + \frac{\beta^3}{16} + O(\beta^5) \quad . \tag{6.3}$$

In Fig. 6.5, this ratio is shown as a function of the differential tip electrode voltage for the 1st order axial micromotion sideband. A hyperbolic fit to the data yields a minimal modulation index of $\beta \sim 0.005$ which corresponds to an amplitude of the micromotion of $u_i = \beta/|\vec{k}| = \beta\lambda/2\pi\sqrt{2} \sim 0.2\,\text{nm}$[3]. This is in very good agreement with values observed in similar trap configurations, where β was found to be 0.004(1) [123].

Given the value of the modulation index, the second-order Doppler shift due to residual motion of the ion can be estimated [67]

$$\left(\frac{\Delta\nu}{\nu}\right)_{\text{Doppler}} \approx -\left(\frac{\Omega_{\text{rf}}}{ck} \cdot \frac{\beta}{2}\right)^2 \quad . \tag{6.4}$$

Inserting typical experimental parameters, we find an expected relative frequency shift of $< 10^{-19}$ which corresponds to $< 1\,\mathrm{mHz}$ for the transition at 280 nm. In other words, this shifts can be neglected in our experiments.

---

[3] The factor $\sqrt{2}$ is a result of the Raman beam configuration.

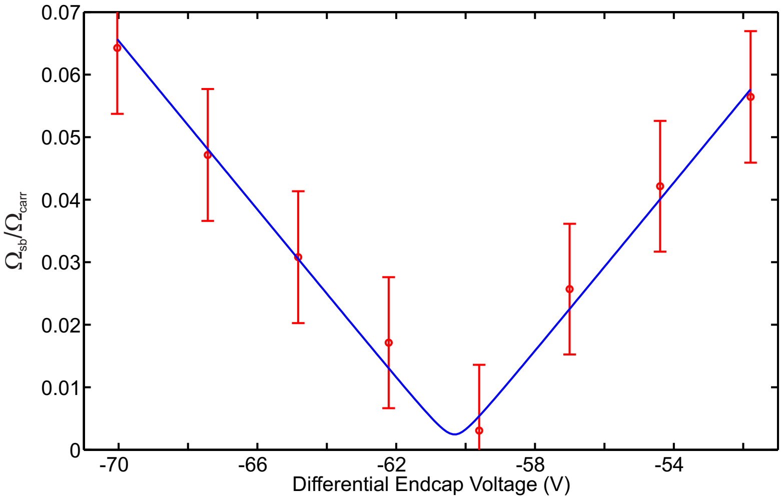

Figure 6.5: Micromotion sideband spectroscopy. The ratio of the Rabi frequency of the first micromotion sideband and the carrier transition is shown as a function of the differential voltage between the tip electrodes. The measurement was carried out with a ground state cooled $^{25}\mathrm{Mg}^{+}$ ion at a tip voltage of 1000 V and a RF trap power of 5 W. This corresponds to an axial trap frequency of $\sim 1.55\,\mathrm{MHz}$. The error bars represent the average fitting error. The solid line corresponds to a hyperbolic fit [70] yielding an estimate for the modulation index $\beta \sim 0.005$ at a differential voltage of -60.3 V.

Chapter 7

Quantum State Detection Schemes

When performing the spectroscopy schemes, the only information that results from each experiment is the quantum state of the logic ion. Here, one experiment is understood as consisting of a sequence of cooling, state preparation, state manipulation (with e.g. spectroscopy pulses) and readout. That means that, after exposing the ion to the resonant detection laser field, it is projected into either the $|\downarrow\rangle$ or the $|\uparrow\rangle$ state. These are distinguished by the *electron-shelving technique* [124]. The state discrimination is based on the fact that the fluorescence rate of one of the states is high (*bright state*), whereas the fluorescence of the other state is ideally negligible (*dark state*). In the case of hyperfine qubits, this technique is limited by the rather small frequency separation of the qubit states (1.789 GHz in the case of $^{25}\mathrm{Mg}^{+}$), which effectively introduces a finite scattering rate of the dark state because the ion can be depumped to the bright state during the detection pulse, thus yielding wrong state information.

In the scope of this thesis, different detection schemes have been investigated to both overcome this limitation and improve detection fidelity. In the following, the detection error and the optimal detection parameters for a single $^{25}\mathrm{Mg}^{+}$ ion are discussed. Similar treatments on limits of the achievable detection errors for a number of species, namely $^{40}\mathrm{Ca}^{+}$ [70], $^{111}\mathrm{Cd}^{+}$ [125], $^{9}\mathrm{Be}^{+}$ [126, 127] and $^{88}\mathrm{Sr}^{+}$ [128], are found in the literature.

In addition to the detection schemes, initial experiments on radio-frequency induced spin flips are presented. These are furthermore used as a tool to determine the coherence time of the ion confined in the Paul trap.

7.1 Offresonant Depumping of the Bright State

State discretization by electron-shelving in ions relies on the fact that the fluorescence rate largely differs between the states to be distinguished. For the case of $^{25}\mathrm{Mg}^{+}$, if the ion is in the $|\downarrow\rangle$ state, it resides in the cycling transition when the detection pulse is applied and scatters photons with a rate of $\Gamma/2 = 1.285 \times 10^8$ 1/s. On the other hand, being in the $|{\uparrow}\rangle$ state, the laser is detuned by $\Delta_{\mathrm{HF}} = 2\pi \times 1.789\,\mathrm{GHz}$ and the scattering rate is decreased as

$$\Gamma' = \Gamma \cdot \frac{s_0/2}{1 + s_0 + (2\Delta_{\mathrm{HF}}/\Gamma)^2} \sim \Gamma \cdot 0.26\% \quad (s_0 \sim 1) \quad . \tag{7.1}$$

The difference in scattering rates results in two distinguishable photon counting histograms. In Fig. 7.3, measured example histograms for a typical detection time of $\sim 12 - 15\,\mu$s are shown. Longer detection times are avoided in the experiment since the non-zero value of the scattering rate of the $|{\uparrow}\rangle$ state depopulates it with a finite probability and lets the ion eventually enter the cycling transition. Once in the cycling transition, the ion will scatter photons at a higher rate, thus yielding wrong state information.

A consequence of the limited detection time is a small number of detected photons. This results in overlapping photon distributions for the two states. For the particular example shown in Fig. 7.3, this overlap is approximately $\sim 1.4\,\%$. This percentage effectively imposes a limit on the single-shot state detection fidelity, since it cannot be decided in the overlapping region to which distribution a collected photon belongs.

It should be noted that this situation is rather different for optical qubits. There, the energy difference between the states is so large that readout fidelities of $> 99.99\%$ are achieved since the off-resonant scattering rate of the dark state is negligible [129, 130]. On the other hand, the finite life time of the metastable dark state also imposes a limitation on the maximum readout time, whereas the lifetime of a qubit encoded in two hyperfine states is practically infinite.

The off-resonant depumping effect is demonstrated in Fig. 7.1. In a first experiment, a single $^{25}\mathrm{Mg}^+$ ion is prepared in the $|{\downarrow}\rangle$ (bright) state and the average number of photons is measured as a function of the detection time (red circles). A linear slope is observed with increasing errors with higher average number of photons due to photon shot noise. In a second experiment, the ion is initialized in the $|{\uparrow}\rangle$ (dark) state by a radio-frequency induced spin-flip after Doppler cooling before the detection time is varied (black circles). The average number of photons is much lower than that of the first sequence in the beginning. Due to the discussed depumping effect, the photon scattering rate asymptotically approaches that of the ion being in the $|{\uparrow}\rangle$ state.

In order to model the depumping effect we assume that the dark state exponentially decays with a rate $1/T$ and the probability of having decayed is given by $W(t) = 1 - \exp(-t/T)$ or a respective rate $w(t) = dW/dt = 1/T \exp(-t/T)$. We further introduce the number of collected photons ξ. The probability of detecting k photons is given by a

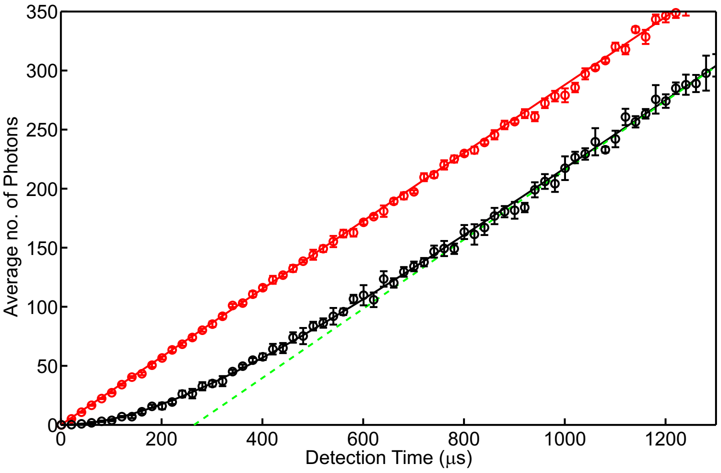

Figure 7.1: Optical depumping of the dark state. The average number of measured photons as a function of the detection time is shown for the bright (red) and dark (black) state. While the bright state fluorescence follows the expected linear curve, the dark state experiences a depumping due to its finite detuning to the bright state and its fluorescence rate asymptotically reaches the slope of the bright state. The black solid line is a fit to Eq. (7.4) with $\xi_\downarrow/\tau \sim 290\,\mathrm{kHz}$ and $\xi_\uparrow/\tau \sim 2.2\,\mathrm{kHz}$. The scattering rates in this measurement are slightly different to those of the simulations in this chapter, since only the UV objective was used here. This does, nevertheless, not affect the observed depumping time. The dashed line corresponds to the expected asymptotic behavior after the ion has been depumped to the bright state.

Poissonian distribution [92]

$$p(\xi = k) := p(k) = \frac{\bar{\xi}^k e^{\bar{\xi}}}{k!} \quad , \tag{7.2}$$

where $\bar{\xi} = \sum p(k)k$ denotes the average number of detected photons.

Let $\xi_\downarrow(\xi_\uparrow)$ be the number of photons scattered if the ion is in the $|\downarrow\rangle$ ($|\uparrow\rangle$) state. $\xi_\uparrow$ corresponds to the background count rate. Given a detection time τ, the amount of photons that is observed if the ion is depumped from the dark to the bright state at time $t < \tau$ reads

$$\xi_t \;=\; \frac{\xi_\uparrow}{\tau}t + \frac{\xi_\downarrow}{\tau}(\tau - t) \quad . \tag{7.3}$$

Here, the first term corresponds to the background counts while the ion is in the dark state and the second term covers the scattering rate during the remaining time of the detection interval when the ion is in the bright state.

The average number of photons is determined by weighting it with the decay rate and integrating it over time

$$\bar{\xi} \;=\; \underbrace{\int_0^\tau dt w(t)\bar{\xi}_t}_{\text{A}} + \underbrace{\int_\tau^\infty dt w(t)\bar{\xi}_\uparrow}_{\text{B}} = \bar{\xi}_\downarrow - \left(\bar{\xi}_\downarrow - \bar{\xi}_\uparrow\right)\frac{T}{\tau}\left(1 - e^{-\tau/T}\right) \quad . \tag{7.4}$$

Term A represents the number of photons that have been measured if the decay took place during the detection time, whereas B corresponds to the weighted average photon number if the decay took place at a later time, i.e. the event when only dark counts were measured. All averaged quantities are designated with a bar, e.g. $\bar{\xi}_t$. In Fig. 7.1, a measurement of the average number of photons as a function of the detection time is shown. The detection laser frequency was adjusted to the resonance and the laser power was calibrated to the saturation intensity[1]. The fit of Eq. (7.4) to the measured data in Fig. 7.1 yields a decay time of $T = 268 \pm 10\,\mu$s. The dark state is depumped for longer detection times and the scattering rate converges asymptotically to that of the bright state.

Based on this lifetime measurement, different detection strategies including their corresponding errors are presented and discussed in the following sections to improve the state detection fidelity for ^{25}Mg$^+$ ions.

7.2 Discrete Threshold Detection

The simplest detection method to distinguish the fluorescing from the non-fluorescing state is the *threshold detection*. Every event with a number of photons above a constant threshold σ is considered to belong to the bright state, whereas every other event is assigned to the dark state. This technique is commonly used for qubits encoded in hyperfine ground states, like ^{9}Be$^+$ [131], and optical qubits, like ^{40}Ca$^+$ [70].

Two different sources of errors yield wrong state information:

- The finite overlap of both photon distributions of the dark and bright state, makes it impossible to unambiguously determine the state in the overlap region (see below Fig. 7.3).
- Depumping from the dark into the bright state changes the ion state and yields wrong state information. The bright state is not affected by this type of error, resulting in a bias towards the bright state.

---

[1] Typically, in the experiments the frequency of the Doppler cooling laser is adjusted to the slope of the DC transition, whereas the detection pulse is performed with a resonant laser to increase the number of detected photons.

It should be noted that polarization misalignments also introduce state detection errors, since a wrong polarization distributes both of the states to other magnetic sub-states. During this discussion, this type of error is neglected. However, for this reason the polarization needs to be carefully adjusted in the experiments.

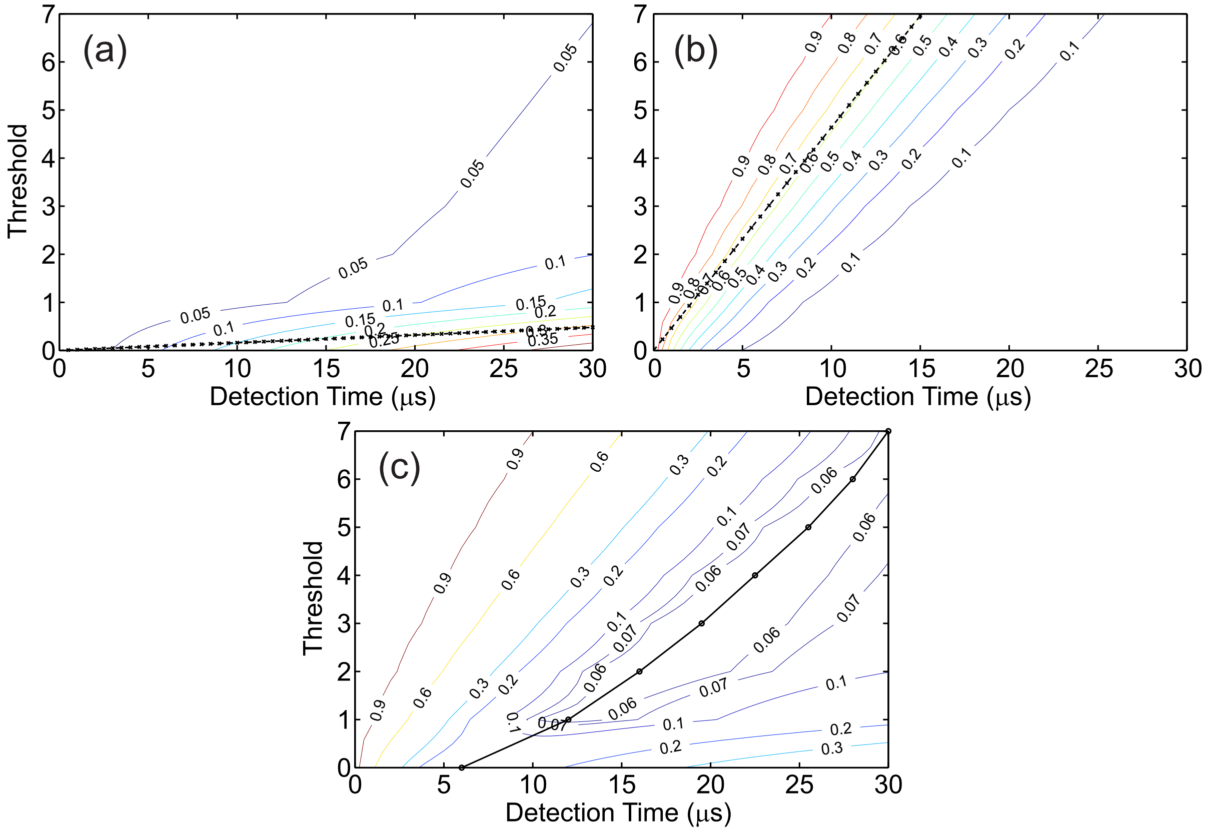

Figure 7.2: Threshold detection errors. The expected error of the (a) dark and (b) bright state as a function of the detection time and the chosen threshold is shown. The dash-dotted black lines depict the average number of photons following approximately the peak of the photon distribution. (c) corresponds to the average square of both errors. The solid line shows the optimal points of detection, i.e. the minimum error as a function of detection time and threshold. The parameters for the scattering rates in this simulation were $\xi_\downarrow/\tau = 464\,\text{kHz}$ and $\xi_\uparrow/\tau = 16\,\text{kHz}$.

Given a threshold σ, the probability with which the bright state is measured to be a dark state is given by

$$p^B(\xi_\downarrow \le \sigma) = \sum_{k=0}^{\sigma} \frac{\left(\bar{\xi}_\downarrow\right)^k e^{\bar{\xi}_\downarrow}}{k!} \quad . \tag{7.5}$$

The probability with which the dark state is mistaken to be a bright state needs to be weighted with the decay rate as in Eq. (7.4)

$$p^D(\xi_\uparrow > \sigma) = \int_0^\tau dt w(t) p(\xi_t > \sigma) + \int_\tau^\infty dt w(t) p(\xi_\uparrow > \sigma) \quad . \tag{7.6}$$

In Fig. 7.2 (a) and (b) both errors $p^B(\xi_\downarrow \leq \sigma)$ and $p^D(\xi_\uparrow > \sigma)$ are depicted as a function of the threshold and the detection time. The dark error $p^D(\xi_\uparrow > \sigma)$ gets worse when the detection time is increased due to a higher depumping probability. Whereas increasing the threshold barrier, decreases the error since all photon counting events, including the ones when the ion was depumped, are taken into account. In contrast to that, bright errors $p^B(\xi_\downarrow \leq \sigma)$ decrease if the detection time is higher since the part of the photon distribution which is below the threshold shrinks. For the same reason, the error increases if the threshold is set to higher values.

The question on the optimal detection point is not answerable in an unambiguous way since it depends on the requirements of the experiment. In our case, the lowest possible error value for both states is desired. In Fig. 7.2 (c) the squared average of both errors

$$p_{\text{total}} = \sqrt{p^B(\xi_\downarrow \leq \sigma)^2 + p^D(\xi_\uparrow > \sigma)^2} \tag{7.7}$$

is depicted. At the optimal detection parameters with the threshold method (depicted by the black solid line), the lowest error achievable in our setup is on the order of $\sim 5-6\,\%$ at $\sim 15-20\,\mu$s detection time and a chosen threshold of $\sigma \sim 2-3$.

7.3 Distribution-Fit-Detection

In a second approach, not only the information of the amount of detected photons is used. Instead, a fit to the histogram of the measured photon distribution yields the state information. A similar method, which takes the full histogram information into account by a maximum likehood estimate, for the case of ^{9}Be$^+$ is discussed in [126].

The fitting method requires two calibrated initial photon distributions, one for each state as a reference. These histograms are taken in the following way: After the ion is Doppler-cooled and optically pumped to the $|\downarrow\rangle$ state, a histogram of the measured number of photons $\xi_\downarrow$ for typically 250 experiments is taken with a certain detection time. The second histogram $\xi_\uparrow$ is measured by either switching off the EOM sidebands, yielding only off-resonant lasers, or releasing the ion from the trap, thus measuring only dark counts[2].

---

[2] That way, it is guaranteed, that the dark state is compared to a background count distribution. If instead the dark state was prepared e.g. by a radio-frequency pulse, one could argue that other states were populated due to pulse imperfections and the 'dark distribution' represents a mixture of different

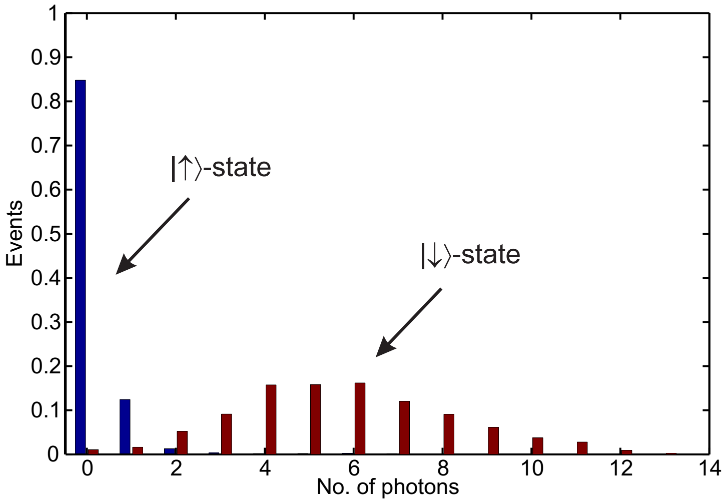

Figure 7.3: Measured photon distributions of the two hyperfine ground states $|\uparrow\rangle$ and $|\downarrow\rangle$ for detection times of $\sim 12.5\,\mu$s. The measured photon distribution is fitted to such calibrated histograms to determine the state of the ion. This reduces the error introduced by the finite overlap of the distributions. The measured scattering rates for the bright (dark) state are $\xi_\downarrow/\tau \sim 464\,$kHz ($\xi_\uparrow/\tau \sim 16\,$kHz).

In order to determine the expected error with this kind of *distribution-fit-detection* method, Monte-Carlo simulations have been performed with the following procedure: For each experiment, a dice is thrown. Its value is weighted with the sum of the Poissonian probability distribution of the bright and the dark state to determine the number of 'measured' photons. A number of k repetitions then yields a random histogram with k events. This histogram is fitted to the calibrated distributions with the function

$$\xi(a) = a \cdot \xi_\downarrow + (1-a) \cdot \xi_\uparrow \quad , \tag{7.8}$$

where a determines the state of the ion, described by $|\psi\rangle = \sqrt{a}\,|\downarrow\rangle + \sqrt{1-a}\,|\uparrow\rangle$. The simulation is iterated N times and the results are averaged $\bar{a} = \sum a_i/N$. The error is determined by the squared average as $\Delta\bar{a} = \sqrt{\sum(\Delta a_i)^2/N}$, where Δa_i corresponds to the fitting error to Eq. (7.8). The fitted value along with the fitting error of the simulated photon distribution is plotted in Fig. 7.4 as a function of repetitions and averages. It should be noted that no significant decrease of the fitting error is observed if the number of averages instead of the number of repetitions is increased.

In the experiments on the ground state cooling performance, the distribution fit detection method was used to determine the state of the ion. Most of the measurement have been performed with 100 repetitions and 3 averages and yielded a statistical error of $\sim 3\,\%$ in accordance with the simulation.

---

states.

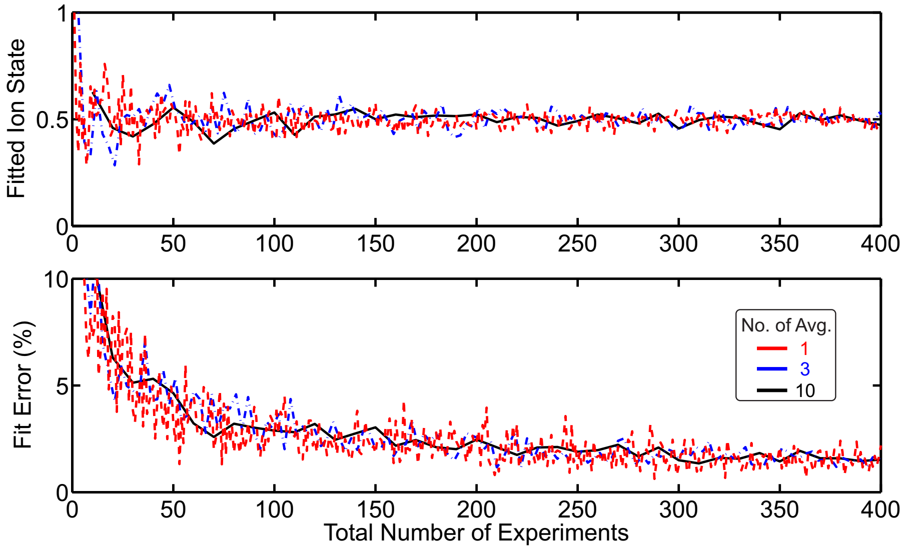

Figure 7.4: Monte-Carlo simulation of the distribution fit technique. The fit result (top graph) and fit error (bottom graph) is shown as a function of the number of total measurements (no. of repetitions × no. of averages) for a superposition state with $a = 1/2$ (see text). The simulated error of 2–3% at 3 × 100 repetitions corresponds well to the statistical error observed in the measured data.

7.4 π-Pulse Detection

The fact that coherent transitions between hyperfine states, as oppose to optical qubits, are easily driven by the application of a radio-frequency pulse, is used for yet another detection method: As shown in Fig. 7.5, in a first detection pulse, the fluorescence is measured and hereby the ion is projected into either of the $|\uparrow\rangle$ or $|\downarrow\rangle$ state. The threshold technique is used to determine the state. After that, the ion is coherently driven by a RF π-pulse to invert the state with high fidelity. This is followed by another detection pulse with state discrimination. Due to the inversion pulse, an anti-correlation between both detection events can be considered, i.e. only detection events which yield opposite states are kept. If both events result in the same state, the measurement is discarded. This way, the effective detection time is doubled.

The detection error of the π*-pulse detection* method is determined by a combination of errors arising from the threshold detection and the fidelity of the intermediate radio-frequency pulse $(1-\alpha)$. Again, we distinguish between errors of the dark and the bright state. In Fig. 7.6, a decision tree for the case when the ion is in the bright state is shown. Summing over all branches which yield a false measurement, the total bright state error

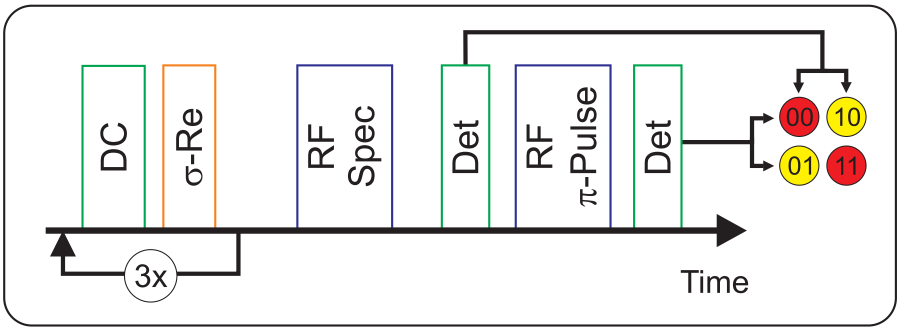

Figure 7.5: Sequence for the π-detection technique. After the ion is cooled and subjected to spectroscopy, the ion state is determined with a resonant detection pulse which is followed by a radio-frequency π-pulse and a second detection pulse. All events that yield the same result in both detection pulses are discarded (red circles).

probability reads

$$\begin{aligned} p_{\text{err}}^{B} &= p(\xi_\downarrow \le \sigma) \cdot \alpha \cdot p(\xi_\uparrow > \sigma) + \\ &\quad p(\xi_\downarrow \le \sigma) \cdot (1-\alpha) \cdot \left(\int_0^\tau dt w(t) p(\xi_t > \sigma) + \int_\tau^\infty dt w(t) p(\xi_\uparrow > \sigma) \right) \quad . \end{aligned} \tag{7.9}$$

Here, the second term, for instance, covers the events where the ion is initially in the bright state, but measured to be in the dark state due to wrong photon counts and then transferred to the dark state. After that it decays during the second detection event into the bright state, where it is also measured to be in the bright state. Thus, the whole sequence yielded a detection of a dark ion, though it was initially bright.

In a similar way, the detection error for the dark state is determined. The corresponding decision tree is shown in Fig. 7.7. Again, summing over all branches that yield a measurement error, the total dark error probability reads

$$\begin{aligned} p_{\text{err}}^{D} = &\left(\int_0^\tau dt w(t) p(\xi_t > \sigma) \right) \cdot \left[\alpha \cdot p(\xi_\downarrow \le \sigma) + (1-\alpha) \cdot \left(\int_0^\tau dt w(t) p(\xi_t \le \sigma) \right.\right. \\ &\qquad\qquad\qquad\qquad \left.\left. + \int_\tau^\infty dt w(t) p(\xi_\uparrow \le \sigma) \right) \right] + \\ &\left(\int_\tau^\infty dt w(t) p(\xi_\uparrow > \sigma) \right) \cdot \left[(1-\alpha) \cdot p(\xi_\downarrow \le \sigma) + \alpha \cdot \left(\int_0^\tau dt w(t) p(\xi_t \le \sigma) \right.\right. \\ &\qquad\qquad\qquad\qquad \left.\left. + \int_\tau^\infty dt w(t) p(\xi_\uparrow \le \sigma) \right) \right] \quad . \end{aligned} \tag{7.10}$$

In Fig. 7.8, the bright (dark) errors $p_{\text{err}}^{B}(p_{\text{err}}^{D})$ are depicted in part (a) and (b) as a function of the detection time and the threshold. The (error) fidelity of the radio-frequency pulse was assumed to be $\alpha = 2\,\%$. While the detection error becomes arbitrarily small

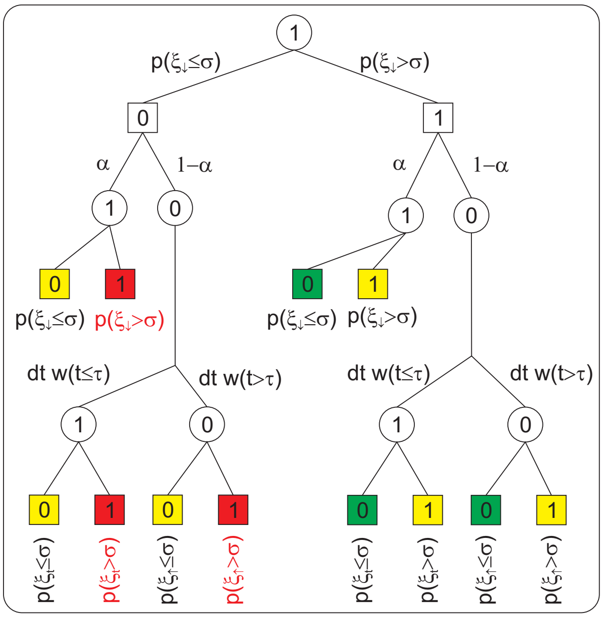

Figure 7.6: Decision tree for the π-detection technique for the bright state (1). Apart from detection errors resulting from a depumping of the dark state (0), an additional spin-flip error α for the RF π-pulse is introduced. All measurements that yield twice the same state, i.e. 00 or 11, are discarded (yellow boxes). A correct measurement (green box) in this case are all paths which yield a 10, whereas a 01 is a detection error (red boxes). In each step, circles represent the real state of the ion, whereas quadratic boxes represent the detected state.

when the detection time approaches zero, it should be noted that this is in principle true but not very helpful since it suffers from the fact that most of measurements are discarded by the algorithm. In part (c), a figure of merit which equally assesses the used statistics for both dark and bright is shown by plotting

$$p_{\text{stat}} = p(\xi_{\downarrow} > \sigma) \cdot p(\xi_{\uparrow} \leq \sigma) \quad . \tag{7.11}$$

If the threshold is, for instance, set to a very high value with respect to the average number of collected photons, i.e. $\sigma \gg \bar{\xi}_{\uparrow}$ and $\sigma \gg \bar{\xi}_{\downarrow}$, then the errors for the dark state become negligible and almost no bright state will be detected. That means that, while discarding all events that yield twice a dark state, the few remaining events where an actual bright state was measured, have a very low error probability. However, this situation is for practical reasons not desirable since the number of discarded events increases tremendously. For that reason the squared average error $\sqrt{(p^B_{\text{err}})^2 + (p^D_{\text{err}})^2}$, which is mainly governed by the dark state errors, has to be balanced with the number of discarded events (see part (d)). Though half of the events are discarded, an average error of $\sim 1\%$ is expected, which improves the state detection efficiency by a factor of

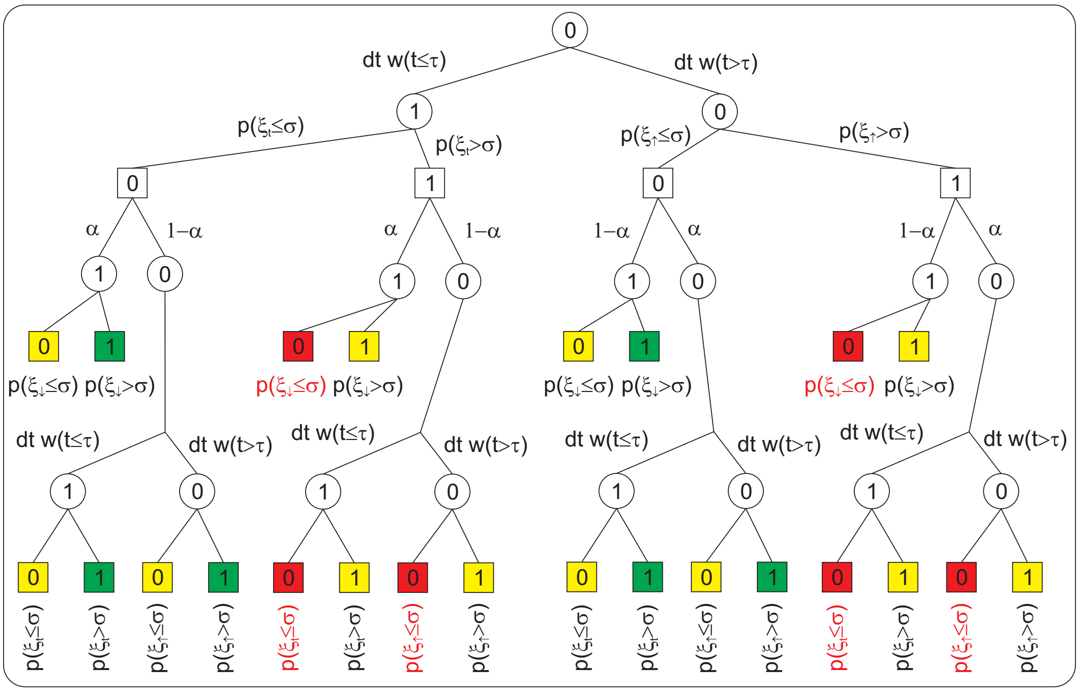
0
dt w(t≤τ)
dt w(t>τ)
1
0
p(ξt≤σ)
p(ξt>σ)
p(ξ↑≤σ)
p(ξ↑>σ)
0
1
0
1
α
1−α
α
1−α
1−α
α
1−α
α
1
0
1
0
1
0
1
0
0
1
0
1
0
1
0
1
p(ξ↓≤σ) p(ξ↓>σ)
p(ξ↓≤σ) p(ξ↓>σ)
p(ξ↓≤σ) p(ξ↓>σ)
p(ξ↓≤σ) p(ξ↓>σ)
dt w(t≤τ)
dt w(t>τ)
dt w(t≤τ)
dt w(t>τ)
dt w(t≤τ)
dt w(t>τ)
dt w(t≤τ)
dt w(t>τ)
1
0
1
0
1
0
1
0
0
1
0
1
0
1
0
1
0
1
0
1
0
1
0
1
p(ξt≤σ)
p(ξt>σ)
p(ξ↑≤σ)
p(ξ↑>σ)
p(ξt≤σ)
p(ξt>σ)
p(ξ↑≤σ)
p(ξ↑>σ)
p(ξt≤σ)
p(ξt>σ)
p(ξ↑≤σ)
p(ξ↑>σ)
p(ξt≤σ)
p(ξt>σ)
p(ξ↑≤σ)
p(ξ↑>σ)

Figure 7.7: Decision tree for the π-detection technique for the dark state (0). Color coding and description are the same as for the bright state shown in Fig. 7.6.

three compared to the distribution fit method.

7.5 Radio-Frequency Driven Rabi Flops

As an initial experiment radio-frequency driven Rabi oscillations between the $|\uparrow\rangle$ and $|\downarrow\rangle$ for a Doppler-cooled single ion were measured. The experimental sequence consists of a Doppler cooling pulse, a radio-frequency pulse and a detection pulse. In Fig. 7.9, the measured state population is shown as a function of the radio-frequency pulse length, where the distribution detection method has been used to obtain the state of the ion. The fit to a sinusoidal function $\rho = a\sin^2(\Omega t/2)$ yields a Rabi frequency of $\Omega = 2\pi \times 63.74(7)\,\mathrm{kHz}$ and a contrast of $2a = 97.8\pm1.4\%$. It should be mentioned that almost unity contrast with a single-frequency behaviour is observed here since the radio-frequency transition is not affected by the motion of the Doppler-cooled ion. This is a consequence of the negligible Lamb-Dicke parameter of $\eta \sim 10^{-7}$ for radio-frequency radiation with a wavelength of $\sim 16\,\mathrm{cm}$. In order to drive transitions which couple the motion of the ion to the internal degrees of freedom (sideband transitions) much higher-field gradients are required. This is only possible in different trap setups, where the field generating wires are much closer to the ion. In a recent experiment, radio-frequency driven sideband transition have been successfully implemented in a surface-electrode trap [86].

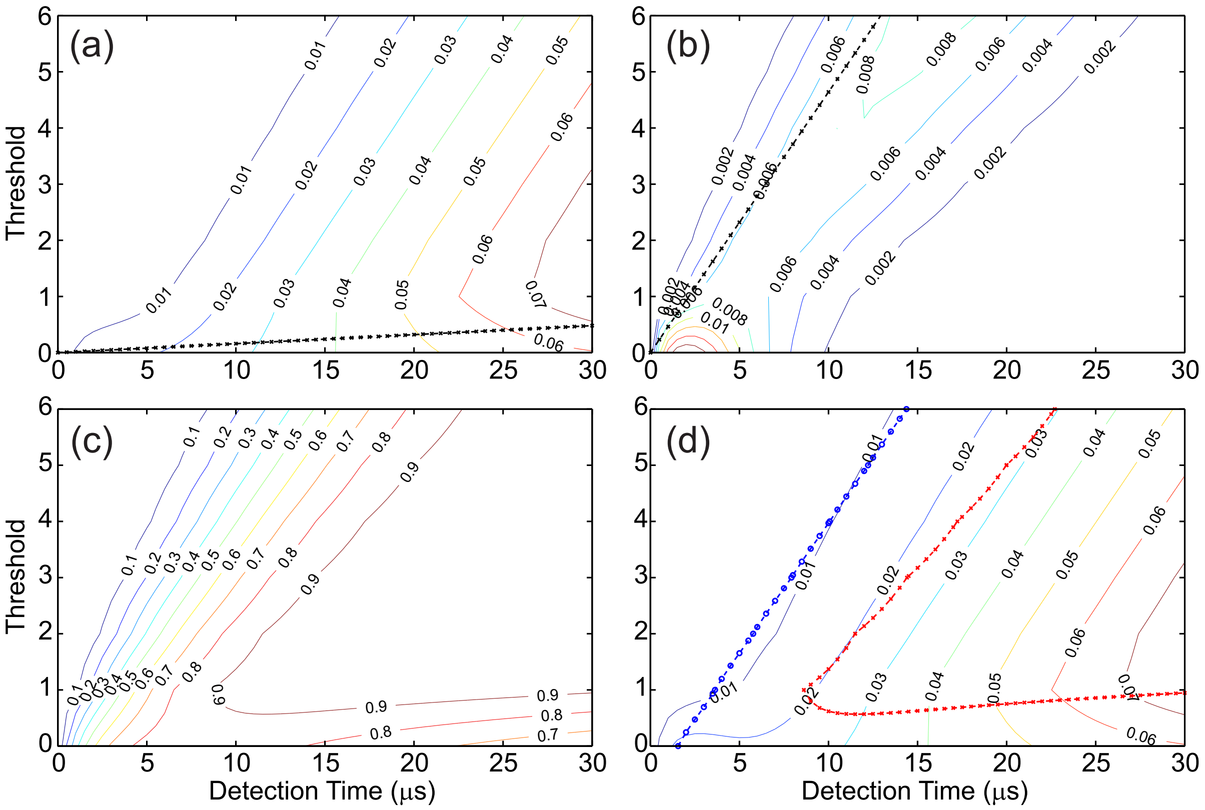

Figure 7.8: π-detection errors. The expected detection errors of the dark (a) and bright (b) state are shown as a function of the detection time and the chosen threshold. The dash-dotted lines correspond to the average number of photons. Part (c) shows the used combined statistics according to Eq. (7.11). The combined errors of bright and dark states are shown in part (d) along with the 90% (red) and the 50% (blue) line of the used statistics. While the error can be made arbitrarily small, the number of discarded measurements approaches 100%, which is, of course, undesirable from a practical point of view. The parameters for the scattering rates in this simulation were $\xi_{\downarrow}/\tau = 464\,\text{kHz}$ and $\xi_{\uparrow}/\tau = 16\,\text{kHz}$.

The simplicity of the radio-frequency induced Rabi flops makes them an ideal tool for several parameter checks prior to any experimental run. A major step worth mentioning is the following: The efficiency of the σ-repumper (see Fig. 8.3) along with its polarization can be checked. The ion is first prepared in the $|\uparrow\rangle$ state via a radio-frequency induced spin-flip. Then the σ-repumper laser is applied. After that, the contrast of the radio-frequency induced Rabi flops between the $|\uparrow\rangle$ and the $|\downarrow\rangle$ state is observed. A reduced contrast is an indication that a part of the population is repumped to states other than $|\downarrow\rangle$.

In the next section, such Rabi flops are used to characterize the different detection techniques and study their robustness.

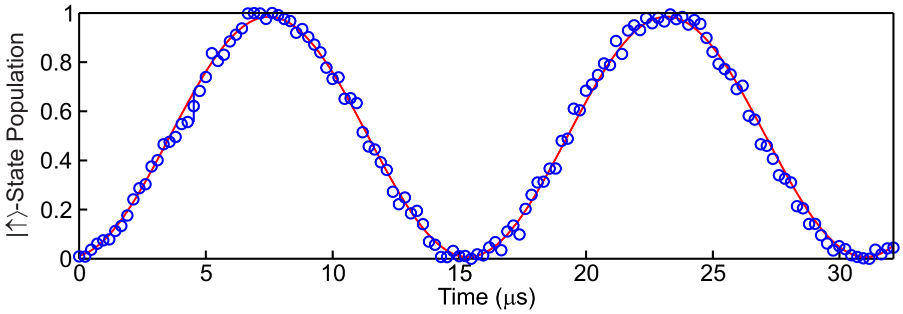

Figure 7.9: Rabi oscillation between the $|\downarrow\rangle$ and the $|\uparrow\rangle$ state driven by radio-frequency. The probability of finding the ion in the $|\uparrow\rangle$ is plotted as a function of the pulse length of the radio-frequency. A sinusoidal fit yields a Rabi frequency of $\Omega = 2\pi \times 63.74(7)$ kHz and a contrast of $97.8 \pm 1.4\%$. The statistical errors of each measurement, which has been repeated 3×100 times, are on the order of 3% and omitted for clarity.

7.6 Comparison and Robustness of Detection Methods

In order to compare the three different detection methods, a radio-frequency driven Rabi oscillation was measured as a function of radio-frequency pulse time whose result is shown in Fig. 7.10. A fit to the function $\rho = a\cos^2(\Omega t/2)$ yields the following parameters including their fitting errors for each individual method:

Method	Rabi Frequency $\Omega/2/\pi$ (kHz)	Contrast $2a$ (%)	Est. Error (%)
Threshold	64.22 ± 0.23	91.6 ± 1.1	$\sim 6-7\%$
Distribution Fit	64.30 ± 0.23	98.7 ± 1.1	$\sim 2-3\%$
π-pulse	64.13 ± 0.21	96.0 ± 1.0	$\sim 3\%$

While all detection methods result in the same Rabi frequency within the fitting errors, it is worth noting that no systematic deviations from the sinusoidal behaviour are observed in the residuals for neither of the techniques[3]. The major difference between the detection methods lies in the measured contrast. Here, the threshold technique is affected the most due to the finite overlap of each photon distribution.

While the graphs (a,b,c) in Fig. 7.10 are generated with a threshold of $\sigma = 1$, the dependence of the fitted contrast as a function of the chosen threshold is shown in part (d). Clearly, the results of the threshold technique (blue diamonds) suffer from an increased threshold since more and more events are assigned to the dark state. In

---

[3] That the detection methods behave like this, is not clear from the beginning. For instance, extending the threshold technique from a point to an interval to discard all events in the overlapping region of the histograms, results in asymmetries of the sinusoidal behavior since more events of one distribution are discarded than of the other and a bias for one of the states is introduced.

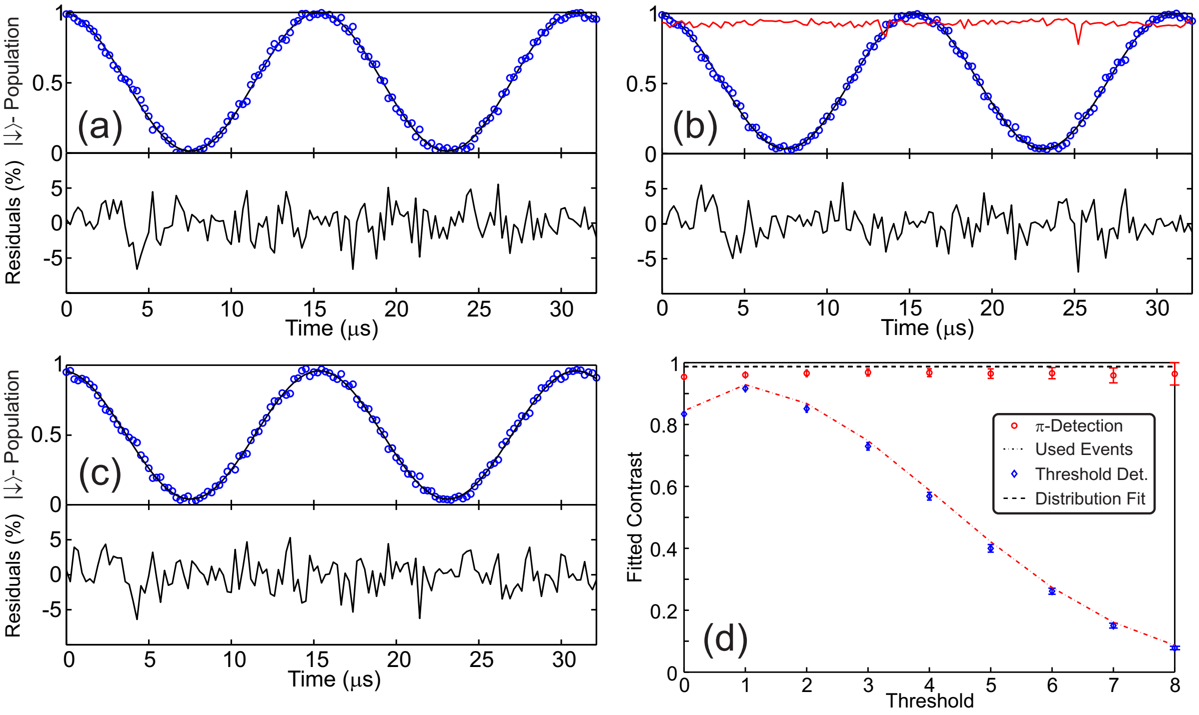

Figure 7.10: Comparison of detection methods. Radio-frequency driven Rabi oscillations are shown, which are analysed with (a) the threshold, (b) the π-pulse and (c) the distribution fit technique with a chosen threshold of $\sigma = 1$. All three methods show no significant deviation from the sinusoidal behavior, which is seen in the residuals below each part. In part (d), the fitted contrast is plotted as a function of the threshold. While the distribution fit method is independent of the threshold (black dashed line), the contrast resulting from the threshold technique various significantly (blue diamonds). The π-detection technique (red circles) also yields a threshold-independent contrast at the expense of the number of events which are taken into account (red dot-dashed line). The error corresponds to the fitting error and increases with less used statistics accordingly.

contrast to that, the π-pulse detection technique (red circles) filters out wrong events at higher thresholds while the contrast stays almost constant. The percentage of non-discarded events is depicted as well (red dashed line) and follows the fitted contrast of the threshold technique. This is explained by the fact that more events are assigned to the dark state with a higher threshold, while the π-detection method filters out exactly this fraction of events. At the same time, the fitting error increases due to the high number of discarded events. Furthermore, as a reference comparison - independent of the chosen threshold - the fitted contrast of the distribution fit method is plotted (black dashed line).

It should be noted that the expected detection error with respect to the measured contrast does not take any type of experimental imperfections such as power or frequency fluctuations and e.g. resonance frequency mismatches into account. Thus the expected

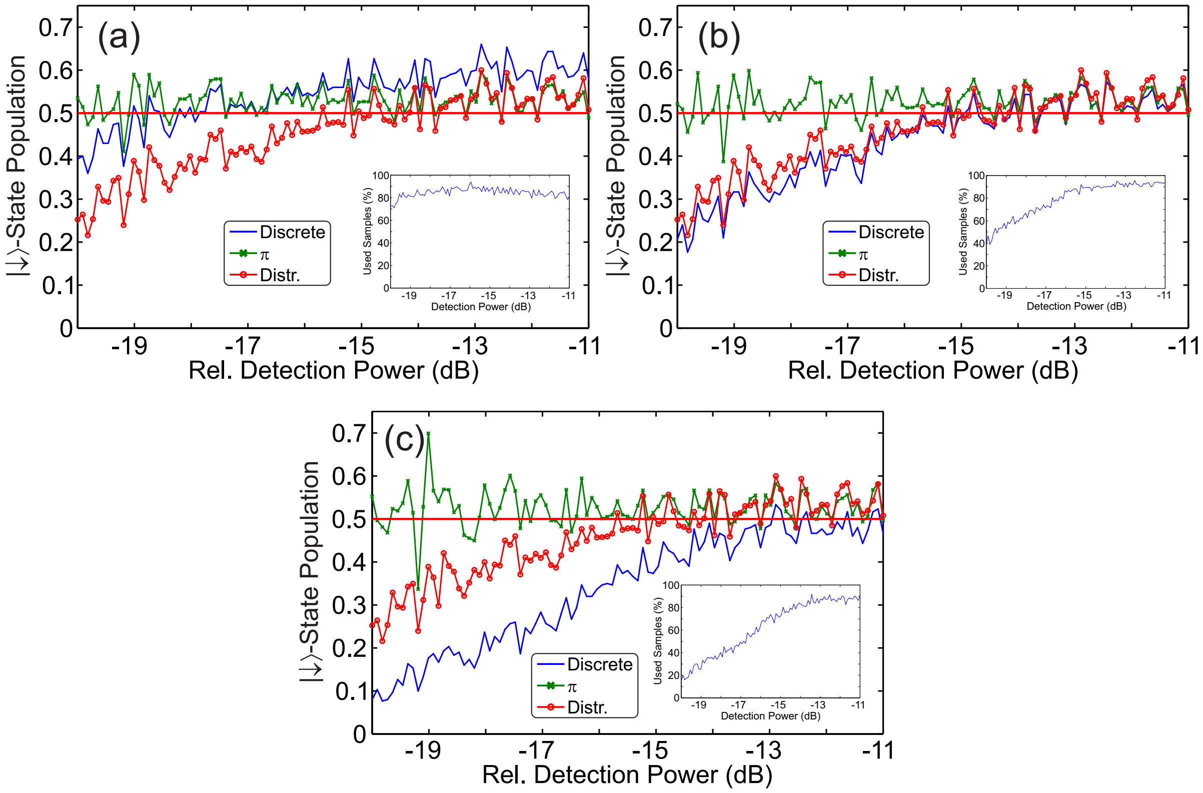

Figure 7.11: Robustness of detection methods. The result of the measured state detection for all three techniques is depicted as a function of the detection beam power. While both threshold and distribution fit technique suffer from power fluctuations and over- or underestimate the state of the ion, the π-detection technique corrects for that by discarding more statistics, as is shown in the insets. The parts vary in the chosen thresholds: (a) $\sigma = 0$ (b) $\sigma = 1$ and (c) $\sigma = 2$.

error slightly underestimates the measured deviation from unity contrast.

Judging only by the absolute contrast, the distribution fit technique seems to be the obvious method of choice. This conclusion is, however, misleading. This method in particular relies on stable experimental parameters, since fluctuations e.g. in the detection power, shift the observed photon distributions resulting in fitting errors. The threshold technique suffers from the same issue, in case the bright and dark state photon distributions are not sufficiently separated. In contrast, the π-detection method is more robust against fluctuations. In Fig. 7.11, the sensitivity to power fluctuations has been characterized by measuring the ion state as a function of the detection power. The analysis for different thresholds ($\sigma = 0$ in (a), $\sigma = 1$ in (b), $\sigma = 2$ in (c)) clearly shows that the ion, which is initially in the $\psi = \frac{1}{\sqrt{2}}\left(|\uparrow\rangle + |\downarrow\rangle\right)$ state, is biased towards the dark state $|\uparrow\rangle$ by the threshold and distribution technique for lower detection powers. At the same time, the π-pulse detection yields an almost constant value for the state population over the full power range, since it is not affected by shifts in the photon distributions.

Instead more events are discarded with lower detection powers, as can be seen in the insets. Thus, from a robustness point of view, the π-detection clearly outweighs both other techniques.

7.7 Coherence Time Measurements

Every measurement sequence is subject to various types of fluctuations among which there are magnetic field noise and background gas collisions. These contribute to internal state decoherence. The corresponding timescale is called coherence time T_{coh}[4] and can be measured using Ramsey experiments [132, 133].

In the applied Ramsey sequence, the ion is first brought into a superposition of the $|{\downarrow}\rangle$ and the $|{\uparrow}\rangle$ state by a resonant $\pi/2$ radio-frequency pulse. It is followed by a waiting time τ where the system evolves freely. A second $\pi/2$-pulse with phase ϕ_0 (relative to the first pulse) flips the spin from the $|{\downarrow}\rangle$ to the $|{\uparrow}\rangle$ state. In the presence of fluctuations, the frequency of the second radio-frequency pulse is detuned by δ from the resonance which introduces an additional phase evolution. For a single experiment, the probability to measure the ion in the $|{\uparrow}\rangle$ state is given by

$$\rho_{\uparrow} = \frac{1}{2} + \frac{1}{2}\cos(\phi_0 + \delta\cdot\tau) \quad . \tag{7.12}$$

Assuming symmetric fluctuations $P(\delta)$ in the detuning δ, an average over many experiments decreases the measured contrast as a function of the waiting time τ as follows

$$\begin{aligned}\langle\rho_{\uparrow}\rangle &= \frac{1}{2} + \frac{1}{4}\int_{-\infty}^{\infty} d\delta P(\delta)\left(e^{\mathrm{i}\phi_0+\mathrm{i}\delta\cdot\tau} + e^{-\mathrm{i}\phi_0-\mathrm{i}\delta\cdot\tau}\right)\\ &= \frac{1}{2} + \frac{1}{2}\cos(\phi_0)\int_{-\infty}^{\infty} d\delta P(\delta)\cos(\delta\cdot\tau) \quad .\end{aligned} \tag{7.13}$$

Assuming a Gaussian distribution for the fluctuations $P(\delta) = \frac{1}{\sigma\sqrt{2\pi}}e^{-\delta^2/2\sigma^2}$, the contrast reads

$$\langle\rho_{\uparrow}\rangle = \frac{1}{2} + \frac{1}{2}\cos(\phi_0)e^{-\sigma^2\tau^2/2} \quad . \tag{7.14}$$

The FWHM of these type of fluctuations is given by $\Delta\omega = \sqrt{16\ln(2)}\sigma$ and the coherence time is defined as the time where the contrast decreases to $1/e$, namely $\mathrm{T}_{\mathrm{coh}} = \sqrt{2}/\sigma$.

The result of the Ramsey experiment is shown in Fig. 7.12. One major source of fluctuations results from 50 Hz magnetic field noise[5]. The blue curve corresponds to a free-running experiment executed at different phases with respect to the line phase each time the experiment is run. The red curve shows the improvement in coherence time when the experiment is synchronized to the AC-line (line-triggered). The measurement was taken at different phases of the AC-line and averaged over. At each phase the frequency was adjusted to resonance. In the following table, the fitting results and the corresponding frequency and magnetic field fluctuations for a $^{25}\mathrm{Mg}^{+}$ ion are listed:

---

[4] This quantity is often called T_2 in nuclear-magnetic resonance experiments.

[5] For a full investigation of the decoherence effects, the complete Fourier spectrum of the fluctuations needs to be studied. High-frequency magnetic fields can e.g. result from the oscillating currents in the

line-triggered	$\mathrm{T}_{\mathrm{coh}}$ (μs)	$\Delta\omega$ (kHz)	ΔB (μT)
no	385(22)	$2\pi \times 1.38(0.08)$	0.059(0.003)
yes	1202(114)	$2\pi \times 0.44(0.04)$	0.019(0.002)

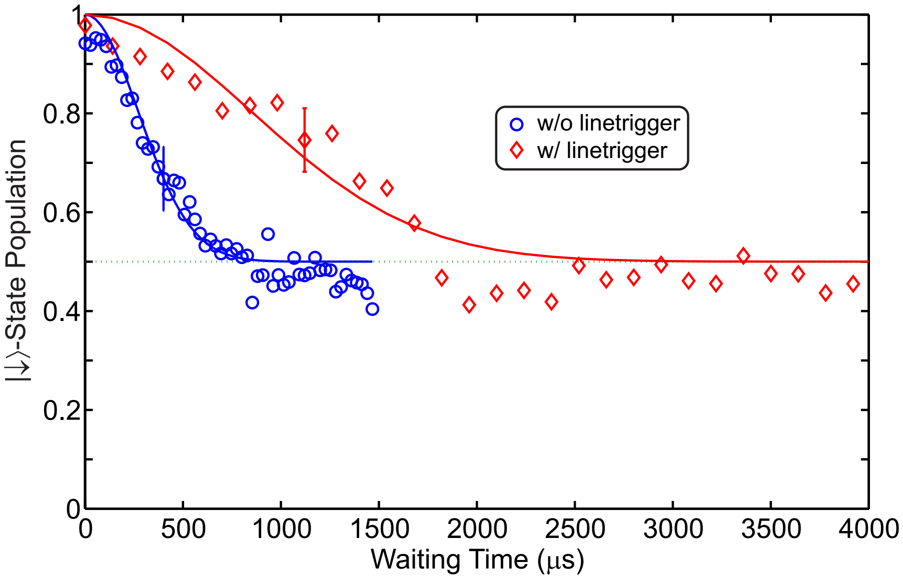

Figure 7.12: Coherence time measurement. The average contrast of multiple Ramsey experiments as a function of the waiting time τ is shown. Each experiment is comprised of two $\pi/2$ pulses with a relative phase of $\phi_0 = 0$. An improvement of the coherence time is observed if the experiment is synchronized to the AC-line (red diamonds). Assuming a Gaussian distribution for the fluctuations, a coherence time of $\sim 1200\,\mu$s is fitted (blue circles). Without line triggering only $\sim 385\,\mu$s are observed. The representative error in the graph corresponds to the standard deviation of the measurements.

Though the measured coherence time of $\sim 1\,$ms is sufficient for our experiments, it should be noted that sequences extended over several ms are subject to systematic frequency shifts due to the magnetic field oscillations. If one was to further increase the coherence time for future experiments, spin-echo techniques can be employed [134] or an

---

blades of the trap. Since such effects are negligible for the experiments presented here, the reader is referred to [65] for a detailed analysis.

active or passive field-stabilization including a μ-metal shielding can be incorporated. In general, the result is in good agreement with values observed in a similar type of trap in the group of R. Blatt. They measured a coherence time for a single $^{40}\mathrm{Ca}^+$ ion without any further active stabilization of $\mathrm{T}_{\mathrm{coh}} = 940(50)\,\mu\mathrm{s}$ [135].

Chapter 8

Experimental Results

Since the proposed photon-recoil spectroscopy relies on the detection of an increase in the motional quantum number of the ion after the spectroscopy probe laser has been applied, the best signal-to-noise ratio is achieved if the ion crystal is initially in the motional ground state of the trap. In this chapter, the cooling scheme of the motional states of the ion in the Paul trap is discussed and the results are presented. This is the first and basic step for the implementation of the recoil spectroscopy.

In the first part, the theoretically expected cooling limits, given by the available experimental parameters, are discussed for Doppler cooling as well as for a pulsed ground state cooling approach. After that, the main experimental results are presented and the achieved cooling performance and experimental limitations are investigated. It is worthwhile mentioning that all experiments in this chapter have been performed with only a single laser system (see Chapter 5). This rather economic approach has promising applications in other experiments that employ similar cooling schemes. The results of the scheme have been published in reference [136].

In the last part of this chapter, the ground state cooling scheme is employed to investigate heating rates of the ion. This is of relevance for the comb spectroscopy sequence, which will be implemented in the near future, since it imposes an experimental limitation on the spectroscopy pulse lengths and, thus, needs to be considered for the design of the exact spectroscopy protocol.

8.1 Limit for Laser Cooling of Trapped Ions

In this section, the limits of two common cooling methods are discussed: Doppler cooling [137] in the *weak binding regime* and resolved-sideband cooling [138] in the *strong binding regime*, where the narrow transition linewidth allows to spectroscopically resolve the motional sidebands, i.e. $\Gamma \ll \omega_{\mathrm{T}}$. While Doppler cooling usually acts as a pre-cooling stage, the absolute ground state of the harmonic oscillator is reached in the second stage by applying sideband cooling. The discussion on Doppler cooling is restricted to a free particle, since the results correspond to the case of a particle confined in a harmonic trap with $\Gamma \gg \omega_\mathrm{T}$. The interested reader is referred to reviews [63, 137, 139, 140, 141] for details and comparisons between the case of a confined and a free particle.

8.1.1 Doppler Cooling

Consider a two-level atom that interacts with a traveling electro-magnetic plane-wave. The polarization of the wave is given by the unit vector $\hat{\epsilon}$ and its wave vector by $\vec{k} = k\hat{k}$. In the non-relativistic limit of a particle of mass m at velocity $\vec{v}$, the change in energy to absorb and emit a photon is given by

$$\Delta E = \frac{1}{2} m \left(\vec{v}'^2 - \vec{v}^2 \right) \quad . \tag{8.1}$$

The primed variables designate the corresponding properties after the scattering process. The emission of the photon goes into a random direction. Using momentum conservation, the energy change in each dimension $(\alpha = x, y, z)$ is rewritten as

$$\begin{aligned} \Delta E_\alpha &= \frac{1}{2} m \left(\vec{v}'_\alpha - \vec{v}_\alpha \right) \left(\vec{v}'_\alpha - \vec{v}_\alpha + 2\vec{v}_\alpha \right) \\ &= \frac{\hbar}{2} \left(\vec{k}_\alpha - \vec{k}'_\alpha \right) \left(\frac{\hbar}{m} \left(\vec{k}_\alpha - \vec{k}'_\alpha \right) + 2\vec{v}_\alpha \right) \\ &= \frac{\hbar^2}{2m} \left(\vec{k}_\alpha - \vec{k}'_\alpha \right)^2 + \hbar \left(\vec{k}_\alpha - \vec{k}'_\alpha \right) \cdot \vec{v}_\alpha \\ &\approx \frac{\hbar^2 k^2}{2m} \left(\hat{k}_\alpha^2 - 2\hat{k}_\alpha \hat{k}'_\alpha + \hat{k}'^2_\alpha \right) + \hbar \left(\vec{k}_\alpha - \vec{k}'_\alpha \right) \cdot \vec{v}_\alpha \quad , \end{aligned} \tag{8.2}$$

where $|\vec{k}| \approx |\vec{k}'| \approx k$ is assumed in the last line.

After absorption, the photons are randomly emitted. The emission distribution depends on the particular transition. The random processes are taken into account by averaging over the complete solid angle for the scattered photons:

$$\langle \Delta E_\alpha \rangle_\Omega \;=\; \int d\Omega P(\hat{k}') \Delta E_\alpha = \int_0^{2\pi} d\phi \int_0^{\pi} d\theta \sin\theta P(\hat{k}') \Delta E_\alpha \quad , \tag{8.3}$$

where $P(\hat{k}')$ defines the emission pattern. It is determined by the normalized dipole operator and the polarization vector $\hat{\epsilon}_{1,2}$ as follows:

$$P(\hat{k}') d\Omega \;=\; \frac{3}{8\pi} \left(|\hat{d} \cdot \hat{\epsilon}_1(\hat{k}')|^2 + |\hat{d} \cdot \hat{\epsilon}_2(\hat{k}')|^2 \right) d\Omega \quad . \tag{8.4}$$

The pre-factor $3/8\pi$ is a result of normalization $\int d\Omega P(\hat{k}') = 1$. Since the emission process is not restricted to a certain polarization, the sum contains two perpendicular polarization vectors, where $\hat{\epsilon}_1 \cdot \hat{\epsilon}_2^* = 1$ and $\hat{k}' \cdot \hat{\epsilon}_{1,2} = 0$.

It follows for the energy change per scattering event

$$\begin{aligned} \langle \Delta E_\alpha \rangle_\Omega &= \frac{\hbar^2 k^2}{2m} \left(\hat{k}_\alpha^2 + f_\alpha \right) + \hbar \vec{k}_\alpha \vec{v}_\alpha \quad ; \\ f_\alpha &= \int d\Omega P(\hat{k}') \hat{k}_\alpha'^2 \quad . \end{aligned} \tag{8.5}$$

All terms linear in $\hat{k}'$ vanish due to the symmetry of the emission pattern $P(\hat{k}) = P(-\hat{k})$. Particular patterns are discussed in detail in Appendix B.

The cooling rate, which is equivalent to the energy change per time unit, is given by the product of the photon scattering rate $\Gamma/2$ and the change in energy per scattering event as follows

$$\frac{dE_\alpha}{dt} = \Gamma \cdot \frac{\Gamma^2 s_0/2}{\Gamma^2(1+s_0) + 4(\omega_0 - \omega_L + \vec{k}\vec{v})^2} \cdot \langle \Delta E_\alpha \rangle_\Omega \quad , \tag{8.6}$$

where $s_0 = I/I_{\text{sat}}$ represents the saturation parameter, I the laser intensity and $I_{\text{sat}} = \pi h c \Gamma / 3\lambda^3$ the saturation intensity, which depends on the wavelength λ of the particular transition.

Assuming that significant cooling has already occurred, the scattering probability can be expanded in the weak binding regime in terms of small velocities $\vec{k}\vec{v} \ll \omega_0 - \omega_L$ and $\vec{k}\vec{v} \ll \Gamma$ and averaged over all velocity components, designated by $\langle \cdot \rangle_v$. A symmetric velocity distribution is assumed, canceling all terms linear in $\vec{v}$. The steady-state is reached when the energy change equals zero, i.e.

$$\frac{d\langle E_\alpha \rangle_v}{dt} = 0 \quad , \tag{8.7}$$

with the steady-state energy

$$\langle E_{\alpha,\infty} \rangle_v \;=\; \frac{1}{2} m \langle v_\alpha^2 \rangle_v = \hbar (1 + f_\alpha) \frac{\Gamma^2(1+s_0) + 4(\omega_0 - \omega_L)^2}{32(\omega_0 - \omega_L)} \quad . \tag{8.8}$$

This energy is minimized by appropriately choosing the laser detuning, so that

$$\omega_0 - \omega_L = \frac{\Gamma}{2}\sqrt{1+s_0} \quad . \tag{8.9}$$

The final energy is often expressed in units of temperature as

$$\langle E_{\alpha,\infty} \rangle_v = \frac{1}{2} k_B T_D \quad \to \quad T_D = \frac{\hbar \Gamma}{4 k_B} (1 + f_\alpha) \sqrt{1+s_0} \quad . \tag{8.10}$$

This quantity is referred to as *Doppler temperature* in the literature. It represents the lowest achievable temperature with Doppler cooling. After the application of Doppler cooling to the ion, the motional states in the harmonic trap are distributed according to a thermal state distribution [142]. In Fig. 2.3, an example of such a distribution is shown for typical parameters in our experiments. Though a $^{25}\mathrm{Mg}^{+}$ ion can be cooled with this method to a low temperature of $\sim 1\,\mathrm{mK}$, a number of higher motional states are populated at this temperature. Since the discussed photon-recoil spectroscopy experiments depend on the fact that the ion is initially in the absolute motional ground state, a more sophisticated method, i.e. resolved-sideband cooling, must to be employed. In the following section, the theoretical limit of sideband cooling is discussed in more detail.

8.1.2 Pulsed Sideband Cooling

Similarly to the case of Doppler cooling, we consider a two-level system in a harmonic trap. Here, the excited state is assumed to have a long life time. In the regime where both the laser linewidth and the decay rate of the upper state are much smaller than the trap frequency $\Gamma \ll \omega_{\mathrm{T}}$, sometimes referred to as *strong binding regime*, resolved-sideband cooling is applicable [138]. In contrast to the case of Doppler cooling, the motional sideband transitions are spectroscopically resolved.

The principle of the cooling process is as follows: in a first step, a red sideband transition is coherently driven, coupling both electronic states and decreasing the motional quantum number of the ion. This step is followed by an (irreversible) spontaneous emission which takes entropy out of the system. Since the upper state is assumed to be a long-lived ground state, the emission process needs to be accelerated by resonant coupling of the excited state to an auxiliary state with high decay rate (*repumping process*). Ideally, neither the laser used for repumping nor the red sideband couple directly to the absolute ground state ($|{\downarrow}, n = 0\rangle$). Hence, the cooling process transfers and leaves the ion in the ground state. However, this ideal situation is compromised by off-resonant coupling of the laser fields and leads to a limitation on the lowest achievable ground state occupation.

In our experiment, sideband cooling is achieved by coupling the two hyperfine ground states ($|{\uparrow}\rangle$ and $|{\downarrow}\rangle$) of a harmonically confined $^{25}\mathrm{Mg}^{+}$ ion with a Raman transition. In the following, the lowest obtainable energy with this configuration is derived in a rate equation approach, where coherences are neglected. It is furthermore assumed that precooling has already taken place, so that the Lamb-Dicke criterion applies, i.e. only terms lower or equal to second order in η^2 are considered. In this case, it is sufficient to only take the lowest two trap levels into account. For a detailed discussion on cooling processes of ions or atoms outside the Lamb-Dicke regime the reader is referred to [143, 144]. In the discussion presented here, the focus is on the limitations of the sideband cooling given by the lowest obtainable energy.

Consider a four-level system, as depicted in Fig. 8.1, with the following parameter definitions: Ω_{eff} and Γ_{eff} are the Rabi frequency and decay rate of the $|{\downarrow}, n=1\rangle \rightarrow |{\uparrow}, n=0\rangle$ Raman transition; Γ_{re} is the decay rate of the (repumping) coupling to an auxiliary state. $s_{\text{re}} = I/I_{\text{sat}}$ corresponds to the saturation parameter of the repumper; η and $\tilde{\eta}$ are the Lamb-Dicke parameters for absorption and emission, respectively. These are different since the emission process takes place in the full solid angle; $\Delta_{\text{HF}} = 2\pi \times 1789\,\text{MHz}$ corresponds to the hyperfine splitting of the ground state in ${}^{25}\text{Mg}^{+}$.

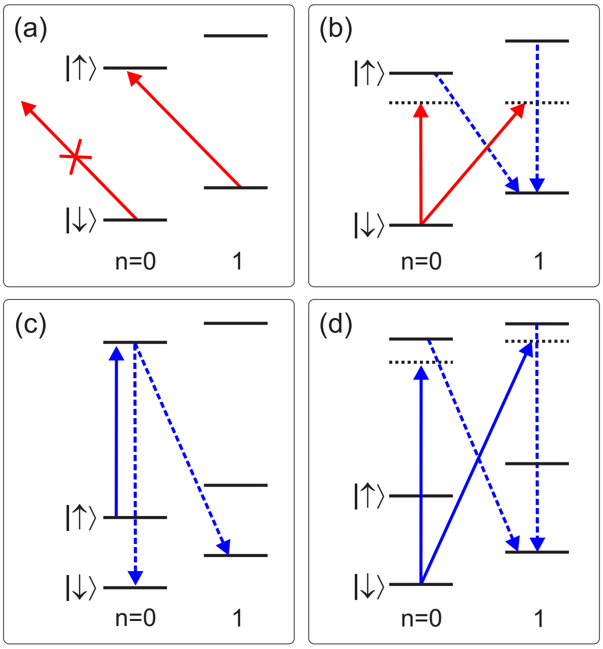

Figure 8.1: Heating and cooling processes in the pulsed sideband cooling scheme. (a) A red sideband cooling pulse transfers the population to the upper state while decreasing the vibrational quantum number by one. The ground state is a dark state for the red sideband. (b) Off-resonant excitation processes of the red sideband pulse on carrier and blue sideband. (c) Resonant repumping process with different decay channels. (d) Off-resonant coupling of the repumping pulse to the absolute ground state which leads to heating.

For typical experimental parameters, the quantities are related as

$$\underbrace{\Omega_{\text{eff}} \sim \Gamma_{\text{eff}}}_{<50\text{kHz}} \ll \underbrace{\omega_{\text{T}}}_{\sim 2\text{MHz}} \ll \underbrace{\Gamma_{\text{re}}}_{\sim 40\text{ MHz}} \ll \Delta_{\text{HF}} \quad . \tag{8.11}$$

In order to set up rate equations, the heating and cooling process rates need to be considered. In a pulsed strategy[1], the time evolution can be split into two separate steps: First, the coherent red sideband excitation and then the resonant repumping stage. As shown in Fig. 8.1, the considered effects to second order in η are:

- Cooling Process: The excitation pulse on the red sideband transfers all population from the $|\downarrow, n=1\rangle$ state to the $|\uparrow, n=0\rangle$ state. It is assumed that the only momentum transfer is given by the two-photon Raman process and that the π-time of the transition is exactly adjusted.

- Heating Processes:

  - The red sideband pulse excites a carrier transition off-resonantly and the ion decays on a sideband again, thus increasing the motional quantum number by one. This process is shown in Fig. 8.1 (b). The rate at which this process happens is given by

    $$h_1 = \left(\frac{\Omega_{\text{eff}}^2}{2\Omega_{\text{eff}}^2 + \Gamma_{\text{eff}}^2 + 4\omega_{\text{T}}^2}\right) \cdot \tilde{\eta}^2 \Gamma_{\text{eff}} \approx \left(\frac{\Omega_{\text{eff}}}{2\omega_{\text{T}}}\right)^2 \cdot \tilde{\eta}^2 \Gamma_{\text{eff}} \quad . \tag{8.12}$$

  - The red sideband pulse excites the first blue sideband transition off-resonantly and the ion decays on the carrier. This process is also shown in Fig. 8.1 (b). It occurs with a rate

    $$h_2 = \left(\frac{\eta\Omega_{\text{eff}}}{4\omega_{\text{T}}}\right)^2 \cdot \Gamma_{\text{eff}}(1 - 3\tilde{\eta}^2) = \left(\frac{\eta\Omega_{\text{eff}}}{4\omega_{\text{T}}}\right)^2 \cdot \Gamma_{\text{eff}} + O(\eta^4) \quad . \tag{8.13}$$

  - The repumper couples resonantly to the $|\uparrow\rangle$ state (part (c) in Fig. 8.1) and the ion decays on the first sideband or the carrier with the rate

    $$\begin{aligned} h_3 &= \left(\frac{s_{\text{re}}/2}{1+s_{\text{re}}}\right) \Gamma_{\text{re}} \tilde{\eta}^2 \quad , \\ h_4 &= \left(\frac{s_{\text{re}}/2}{1+s_{\text{re}}}\right) \Gamma_{\text{re}} \left(1 - \tilde{\eta}^2\right) + O(\tilde{\eta}^4) \quad . \end{aligned} \tag{8.14}$$

  - The repumper couples off-resonantly to the ground state and decays on the first sideband or it couples to the first sideband and decays on the carrier

---

[1] A similar treatment of continuous-wave sideband cooling is found in [64, 70].

(part (d) in Fig. 8.1). These processes occur with the rate

$$
\begin{aligned}
h_5 &= \left(\frac{s_{\mathrm{re}}/2}{1 + s_{\mathrm{re}} + \left(\frac{2\Delta_{\mathrm{HF}}}{\Gamma_{\mathrm{re}}(1-\tilde{\eta}^2/2)^2} \right)^2} \right) \tilde{\eta}^2 \Gamma_{\mathrm{re}} = \frac{\tilde{\eta}^2 \Gamma_{\mathrm{re}}^3 s_{\mathrm{re}}}{8\Delta_{\mathrm{HF}}^2} + O(\eta^4) \quad , \\
h_6 &= \left(\frac{\frac{s_{\mathrm{re}}}{2\tilde{\eta}^2}}{1 + \frac{s_{\mathrm{re}}}{\tilde{\eta}^2} + \left(\frac{2\Delta_{\mathrm{HF}}}{\Gamma_{\mathrm{re}}\tilde{\eta}^2} \right)^2} \right) \Gamma_{\mathrm{re}}(1 - 3\tilde{\eta}^2/2)^2 = \frac{\tilde{\eta}^2 \Gamma_{\mathrm{re}}^3 s_{\mathrm{re}}}{8\Delta_{\mathrm{HF}}^2} + O(\eta^4) \quad .
\end{aligned}
\tag{8.15}
$$

Comparing the magnitudes of the different scattering rates ($h_2 \sim 1\,\mathrm{Hz} \ll h_5 \sim 2\,\mathrm{kHz}$), it is clear that the repumping pulses dominate the dynamics limiting the lowest achievable average population. Thus, the off-resonant sideband excitations are neglected and the rate equations take the following form:

$$
\begin{aligned}
\dot{\rho}_0 &= -(h_5 + h_6)\rho_0 - h_4 \rho_{\mathrm{aux}} \quad ; \\
\dot{\rho}_1 &= (h_5 + h_6)\rho_0 + h_3 \rho_{\mathrm{aux}} \quad ; \\
\dot{\rho}_{\mathrm{aux}} &= -(h_3 + h_4)\dot{\rho}_{\mathrm{aux}} \quad ; \\
\rho_0 + \rho_1 + \rho_{\mathrm{aux}} &= 1 \quad ,
\end{aligned}
\tag{8.16}
$$

where $\rho_{0,1} := |\downarrow, n = 0, 1\rangle$ correspond to the population in the $n = 0, 1$ harmonic oscillator states, respectively, and ρ_{aux} corresponds to an auxiliary upper state (see also Fig. 8.1). These equations are trivially solved using a symbolic algebraic software, such as the open-source program Maxima [95].

In order to completely simulate the described sideband cooling process, an iterative procedure is followed. Starting with the ion in the $\rho_1^{(0)} = |\downarrow, n = 1\rangle$ state and applying a consecutive sideband and repumping pulses, the analytical steady-state solution reads

$$
\rho_1^{(k+1)} - \rho_1^{(k)} \approx 0 \quad \longrightarrow \quad \rho_1^{(\infty)} \approx \frac{t s_{\mathrm{re}} \Gamma_{\mathrm{re}}^3 \tilde{\eta}^2}{4\Delta_{\mathrm{HF}}^2} + O(\eta^4) \quad . \tag{8.17}
$$

Here, it is assumed that the repumping time t is long enough to completely empty the auxiliary state in each step. For shorter times, a numerical approach is taken including insufficient repumping. The average motional quantum number corresponds to the steady-state population in the first vibrational state, since

$$
\langle n \rangle_\infty \quad := \quad \bar{n} = \sum n \rho_n = \rho_1 \approx \rho_1^{(\infty)} \quad . \tag{8.18}
$$

In Fig. 8.2 the average motional quantum number is shown as a function of the repumping time t. The minimum population of $\langle n \rangle_\infty \sim 5 \times 10^{-5}$ is reached for a repumping time of $\sim 4.7\,\mathrm{ns}$. At shorter times, the repumping pulse does no longer efficiently empty the

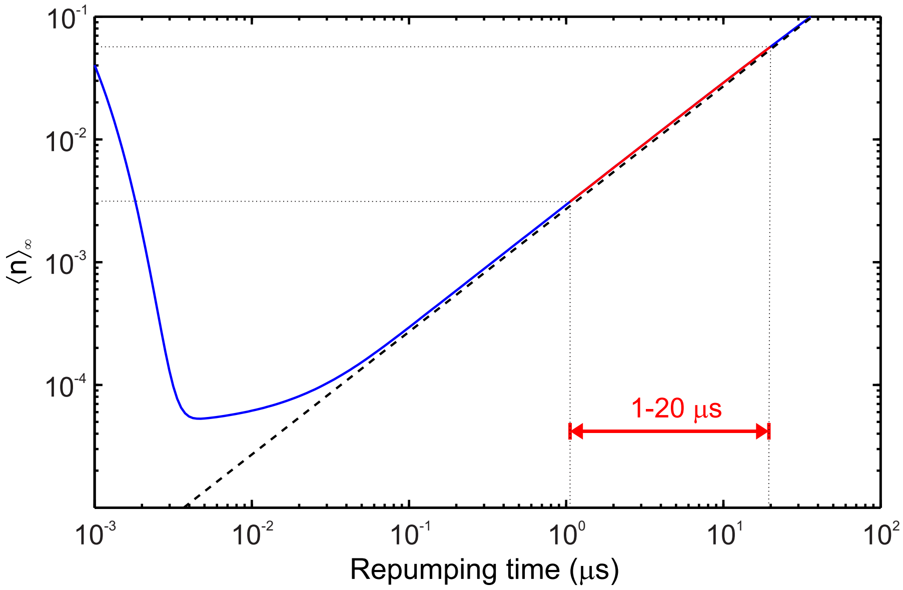

Figure 8.2: Limit on the achievable average population for pulsed sideband cooling. The theoretically expected average vibrational population is shown as a function of the repumping pulse time (solid blue line). The parameters for the plot were $\tilde{\eta} = 0.28; s_{\mathrm{re}} = 1; \Gamma_{\mathrm{re}} = 2\pi \times 41.3\,\mathrm{MHz}$ and $\Delta_{\mathrm{HF}} = 2\pi \times 1789\,\mathrm{MHz}$. When the repumping time is large compared to the decay rate, a linear analytical solution approximates the solution (black dashed line). For shorter times, the repumping becomes inefficient since the $|\uparrow\rangle$ state is not completely emptied after each pulse. Repumping times which are typically employed in our experiment are indicated in red.

upper state, so that the following sideband pulse transfers the population back to the $|\downarrow\rangle|n = 1\rangle$ state. However, these repumping times are not applicable in our experiment. Nevertheless, it is worth mentioning that theoretically the pulsed strategy for sideband cooling is comparable to the expectations for a continuous approach (see [70]).

A further limitation, not included in this simple model, originates from micromotion in the Paul trap. A detailed discussion including this effect is found in [68].

In the following section, the performance of resolved-sideband cooling is studied for a single $^{25}\mathrm{Mg}^+$ ion using the presented laser system and the main experimental results are presented.

8.2 Measurement Principle and Doppler Cooling

In the following sections, the basic elements of the experimental sequence to achieve ground state cooling of a single $^{25}\mathrm{Mg}^+$ ion are discussed. This represents the first step towards performing photon-recoil spectroscopy in the ion trap.

All measurements presented here follow a similar protocol: The ion is subject to

Doppler cooling for $< 1\,\mathrm{ms}$, then Raman-stimulated sideband cooling followed by a Raman spectroscopy pulse and after that a detection pulse of $\sim 10 - 15\,\mu\mathrm{s}$ which projects the ion into one of the $|\uparrow\rangle$ or $|\downarrow\rangle$ state. This procedure is repeated several hundred times at each point of the scanned parameter of interest to obtain sufficient statistics. The result of each measurement is the ratio between the number of times the ion was found in the $|\uparrow\rangle$ state compared to $|\downarrow\rangle$ state occurrences. For all measurements the distribution fitting technique has been used for quantum state detection (see Section 7).

As shown in Fig. 8.3, during the Doppler cooling step, two lasers cool the ion and prepare its initial state: the DC beam and the resonant σ-Raman beam (σ-repumper). The laser is tuned in such a way that both beams have one sideband resonant to the $\mathrm{P}_{3/2}$ level, if the EOM is switched on. While the DC beam optically pumps the population into the extremal magnetic sub-state, the repumper guarantees that no population remains in the $\mathrm{S}_{1/2}$ F=2 manifold.

It should be noted that the interdependent AOM configuration used in the experiment does not allow for switching off the π-Raman beam when the σ-Raman beam and the Doppler cooling beam is in use. If the σ-Raman beam was made resonant via the EOM, the π-Raman beam would simultaneously be resonant as well. Hence, the combination of Doppler cooler and repumper laser requires a pulsed operation mode, as shown in Fig. 8.3. In the experiment, no particular disadvantage has been observed for this way of Doppler cooling.

Prior to all measurements, the magnetic field alignment is adjusted by optimizing the σ-polarization of the Doppler cooling beam and the repumper. Furthermore, the Doppler cooling beam is detuned by half the linewidth to the slope of the transition and its power is calibrated to the saturation intensity $s_0 \sim 1$ for optimal performance. For the state detection pulse, the Doppler cooling beam has been tuned to the resonance to increase the number of detected photons.

It is worthwhile mentioning that all measurements presented here have been performed using a laser which is blue-detuned with respect to the $\mathrm{P}_{3/2}$ level. The main reason for this configuration was the fact that the LBO cavities could not be stabilized due to resonances in the transmission spectrum that lead to strong asymmetries in the error signal possibly originating from molecular resonances in air. After covering the whole laser setup and preventing air flow, these resonances were significantly suppressed and locking the laser in a red-detuned way was possible. Since the latter configuration has lead to a much stabler ion crystal if more than a single ion has been loaded, it has been kept henceforth. In particular, in the case of simultaneously loading different species, much longer lifetimes were observed with the red-detuned configuration.

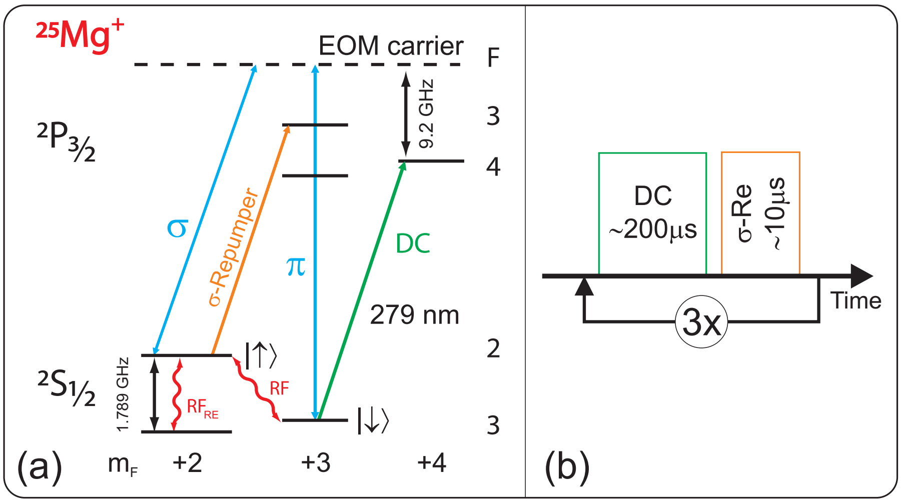

Figure 8.3: Cooling and manipulation of $^{25}\mathrm{Mg}^+$. (a) Laser beams used for resonant Doppler cooling (DC + repumper) and Raman stimulated coherent manipulation (σ and π) are shown. While the laser is tuned 9.2 GHz off-resonant to the $\mathrm{P}_{3/2}$ level, one of the sidebands of the EOM is resonant. Additionally shown is the coherent manipulation via radio-frequency radiation. (b) The Doppler cooling sequence for $^{25}\mathrm{Mg}^+$ consists of a Doppler cooling pulse followed by a repumping pulse to repump any population from the $\mathrm{S}_{1/2}$ F=2 manifold. The sequence is typically repeated up to three times yielding a total Doppler cooling length of $\sim$1 ms.

8.3 Ground State Cooling of a Single Magnesium Ion

The initial step of the cooling process, namely Doppler cooling, prepares the ions motion in a thermal state [142]. At optimum laser parameters for the Doppler cooling beam, i.e. saturation intensity and a detuning of $\Gamma/2$, the motional degrees of freedom are ideally at the Doppler cooling temperature of 1 mK (see Eq. (8.10)). In addition to that, the Doppler cooling beam, including the σ-repumper, optically pumps the ion to the $|\downarrow\rangle$. Thus, the expected population distribution is given by

$$\rho \;=\; |\downarrow\rangle \otimes \sum_{n=0}^{\infty} p_n\,|n\rangle \quad , \tag{8.19}$$

where p_n follows the Bose-Einstein distribution

$$p_n = \left(1 - e^{-\hbar\omega_z/k_B T}\right) e^{-n\hbar\omega_z/k_B T} \quad . \tag{8.20}$$

This distribution is depicted in Fig. 2.3 at the Doppler cooling limit for a single $^{25}\mathrm{Mg}^+$ ion in a 1D-confinement with a trapping frequency $\omega_T = 2\pi \times 2\,\mathrm{MHz}$ and a Lamb-Dicke parameter $\eta = 0.28$. In this case, the average population number is approximately $\bar{n} \sim 10$ with the given trap frequency. In order to reduce $\bar{n}$ further and cool the ion to the absolute ground state, resolved-sideband cooling is employed to the axial motional degree of freedom. While the radial degrees of freedom stay in a thermal state at the Doppler cooling temperature, the axial mode is in a Fock state after the cooling process. In order to cool all degrees of freedom, additional Raman beams addressing the other two directions are required.

An overview of the sideband cooling sequence is shown in Fig. 8.4. After Doppler cooling, a red sideband is driven by adjusting the Raman lasers resonant to the red sideband transition frequency and irradiating the ion for a time t_n. The pulse length t_n is adjusted to match the π-time for a red sideband transition of the nth trap level. This pulse transfers the population from the $|\downarrow\rangle|n\rangle$ state into the $|\uparrow\rangle|n-1\rangle$ state. After that, the ion is reinitialized into the $|\downarrow\rangle|n-1\rangle$ by applying a short ($\sim 10\,\mu$s) resonant σ-Raman repumping pulse. This is achieved by simultaneously switching on the EOM during the excitation. However, due to a finite branching ratio between the excited $\mathrm{P}_{3/2}\,|3,3\rangle$ and the $\mathrm{S}_{1/2}\,|3,2\rangle$ states, a second repumping step is required. It is achieved by transferring the complete population from $\mathrm{S}_{1/2}\,|3,2\rangle$ to $|\uparrow\rangle$ by a radio-frequency π-pulse ($\mathrm{RF}_{\mathrm{Re}}$ in Fig. 8.3), followed by another optical σ-repumping pulse. Typically 2 to 3 repetitions guarantee the reinitialization to the $|\downarrow\rangle|n-1\rangle$ state. It should be noted that higher-order and off-resonant processes lead to population in the $|\downarrow\rangle|n \pm 1, 2, \ldots\rangle$ states. This effectively imposes a lower limit on the achievable average population number (see Section 8.1.2).

Both, first and second order sideband pulses are used in the cooling sequence. The 2nd order sideband pulses are introduced to optimize the population transfer of the states beyond the zero-crossing of the Rabi frequency of the 1st order sideband. Furthermore, this method decreases the total time of the cooling sequence by $\sim 20\%$ due to the higher Rabi frequencies of the 2nd order red sideband at higher trap levels (see Fig. 2.3).

The whole ground state cooling sequence comprises of two major steps: First, typically 25× 2nd order red sideband pulses are applied, starting at a high trap level of $n \sim 40$ down to $n \sim 15$. The pulse times t_n are adjusted correspondingly for each sideband pulse to act as individual π-pulses. When the point of $n \sim 15$ is reached, the remaining steps are covered by 1st order red sideband pulses. Since the trap state at $n = 0$ is a dark state for the sidebands and not affected by the repumping steps, the ion is cooled to the ground state and remains there.

Each part of the sequence is repeated several times to improve the cooling performance. The total length of the sequence depends on the corresponding overall Rabi frequency which is determined by the laser power and is typically on the order of 10 – 15 ms, including all repetitions. The intermediate σ- and RF-repumping steps are each on the order of 10 μs.

It is worth mentioning that the AOMs are left switched on between experimental repetitions to reduce thermal effects.

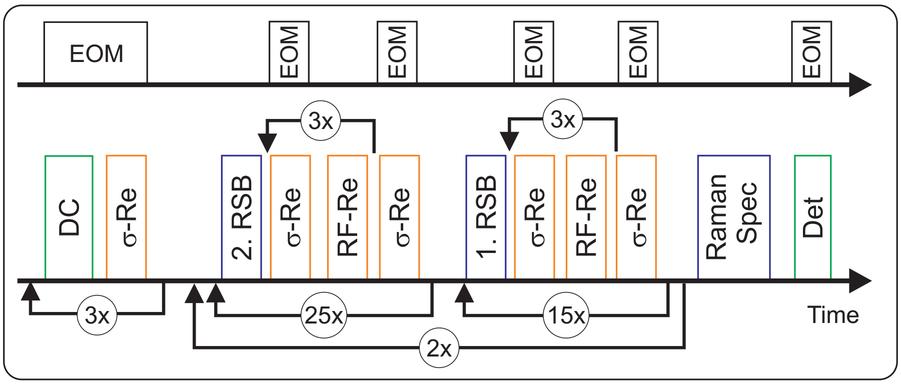

Figure 8.4: Experimental sideband cooling sequence. The complete sequence to implement and investigate ground state cooling of a single ^{25}Mg^{+} is shown. The four major steps are: Doppler cooling, sideband cooling, Raman spectroscopy and state detection. Not shown are auxiliary pulses for intensity stabilization. In the upper line, the EOM switching times are shown. They correspond to the times when resonant transitions are driven.

8.3.1 Sideband Cooling Results

The performance of the sideband cooling scheme is analysed by means of Raman spectroscopy. In Fig. 8.5, the result of a frequency scan over the carrier, the red and blue sideband is shown for a (a) Doppler-cooled and a respective (b) sideband-cooled ion.

The first major difference is the missing excitation on the red sideband after sideband cooling. This is due to the fact that the ground state is a dark state for the red sideband. Secondly, the excitation of the carrier and the 1st blue sideband increase compared to the case of a Doppler-cooled ion. This is best understood in the scope of Rabi oscillations of the different transitions.

In the case of a Doppler-cooled ion, many different motional trap levels are populated, ideally following a thermal state distribution as described. Driving a Raman transition between the $|\downarrow\rangle\,|n\rangle$ and the $|\uparrow\rangle\,|n'\rangle$ states, will excite all different trap levels at the same time since the transitions are degenerate in frequency. Consequently, an overlap of many Rabi oscillations is expected. Since the Rabi frequencies of the different types of transitions, i.e. carrier and sideband transitions, depend on the trap level, the π-times for each level are different (see Fig. 2.3). This reflects itself in an average of many sinusoidals with different frequencies in the population of the $|\downarrow\rangle$ and the $|\uparrow\rangle$ states and results in a reduced amplitude. In contrast to that, a ground state cooled ion resides in a Fock state. Thus, only a single-frequency oscillation with full amplitude is expected there. Furthermore, while the red sideband is a dark state for a ground state cooled ion, the blue sideband and the carrier differ in their Rabi frequencies by a factor of the Lamb-Dicke parameter η (see Eq. (2.27)). This comparison can be used to experimentally determine the Lamb-Dicke parameter.

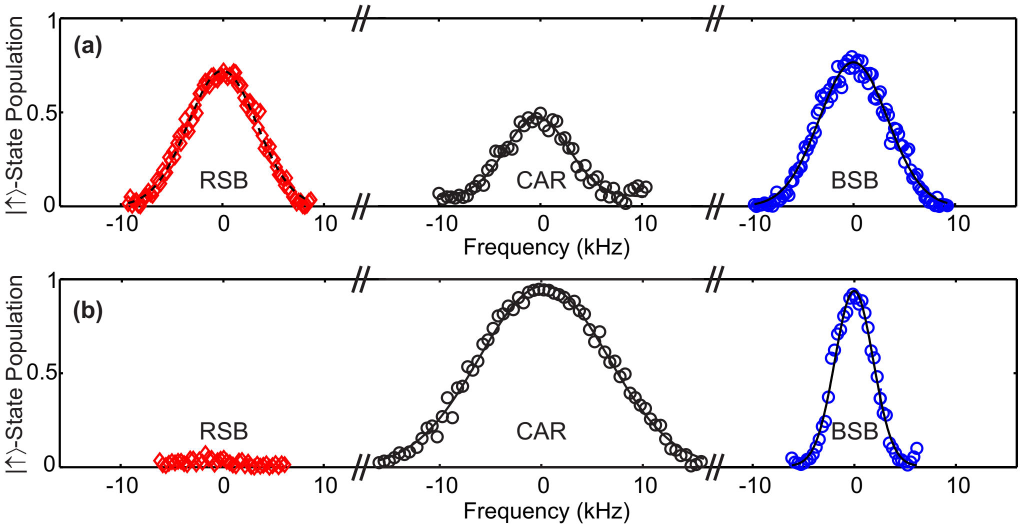

Figure 8.5: Sideband spectroscopy of a single $^{25}\mathrm{Mg}^{+}$ ion. (a) Frequency scans over the carrier transition (CAR) and the 1st red and blue sideband (RSB and BSB) for a Doppler-cooled ion are shown. The frequencies are shifted for clarity. In the corresponding scans for a sideband-cooled ion (b), the almost unity excitation on the carrier and the blue sideband and the missing excitation on the red sideband clearly indicates a high ground state occupation. Each point corresponds to 3 × 100 measurements and the average fitting error is on the order of 3%, omitted for clarity. The solid lines correspond to Gaussian fits. The excitation pulse has a length of 25 μs in (a) and 45 μs in (b) for the sidebands, respectively, and 14 μs in (a) and 25 μs in (b) for the carrier.

In Fig. 8.6, Raman-driven Rabi oscillations on the carrier and the sideband transitions for a Doppler- and a sideband-cooled single $^{25}\mathrm{Mg}^{+}$ ion are shown. While the excitation on the red sideband almost vanishes as expected, the oscillation on the blue sideband becomes more single-frequency like. This effect is even stronger when it comes to the carrier transition. Here, the Doppler-cooled ion shows no oscillation at all since an average over many sinusoidals with different Rabi frequencies is given. In contrast to that, as described, the ion is approximately in the Fock state $|\downarrow\rangle\,|0\rangle$ after sideband cooling and the carrier, as well as the blue sideband transition, exhibit a clear single-frequency behavior.

In order to quantify the performance of the sideband cooling processes, the temperature defined by the motional state distribution in the harmonic trap needs to be determined. There are several methods to infer this temperature from properties easily accessible in the setup. An overview of these methods can be found in [63]. Here, a comparison of the red and the blue sideband excitation is employed to determine the temperature.

Assuming that the motional state of the ion is given by a thermal distribution, the ratio of the excitation probabilities on the rth order red and blue sidebands is given by [145]

$$Q := \frac{\rho_r^{\mathrm{rsb}}(t)}{\rho_r^{\mathrm{bsb}}(t)} = \left(\frac{\bar{n}}{1+\bar{n}}\right)^r \quad . \tag{8.21}$$

Re-arranging terms yields a simple formula for the average population number

$$\bar{n} = \frac{Q^{1/r}}{1-Q^{1/r}} \quad . \tag{8.22}$$

This way, the temperature of the ion is determined as

$$k_B T = \hbar\omega_T \frac{1}{\log\left(1+1/\bar{n}\right)} \quad , \tag{8.23}$$

where ω_T is the harmonic trapping frequency. A more detailed calculation is given in Appendix C.

It should be noted that the ratio in Eq. (8.21) is time-independent. This is a result of the assumed thermal population distribution. In other situations, where the population follows e.g. a Gaussian distribution, Eq. (8.21) is no longer applicable.

Comparing in total nine individual measurements at the maximum of the first sideband oscillation yields $\bar{n} = 0.03 \pm 0.01$ as an upper limit for the average vibrational population number. The measured value corresponds to a population in $\sim 97\%$ of the harmonic oscillator ground state and a temperature of $T = 30\,\mu$K. Given the repumping time of $\sim 10\,\mu$s used in the sequence, this is in excellent agreement with the expected achievable values from Section 8.1.2.

In addition to the analysis of the vibrational population in the ground state, the theoretically expected Rabi oscillations for the red and blue sideband transitions are plotted for the Doppler-cooled ion in Fig. 8.6 in form of a weighted sum over sinusoidal functions with Rabi frequencies corresponding to a thermal state with $\bar{n} = 16 \pm 5$. Within this range, the curves resemble the observed behavior reasonably well. The result indicates that the ion is cooled closely to the expected Doppler cooling limit of $\bar{n} \sim 10$.

In a similar approach, where acousto-optic modulators instead of an electro-optic modulator were used to bridge the frequency splitting between the two hyperfine ground states, an average population of $\bar{n} = 0.34 \pm 0.08$ was achieved [146]. Among other issues,

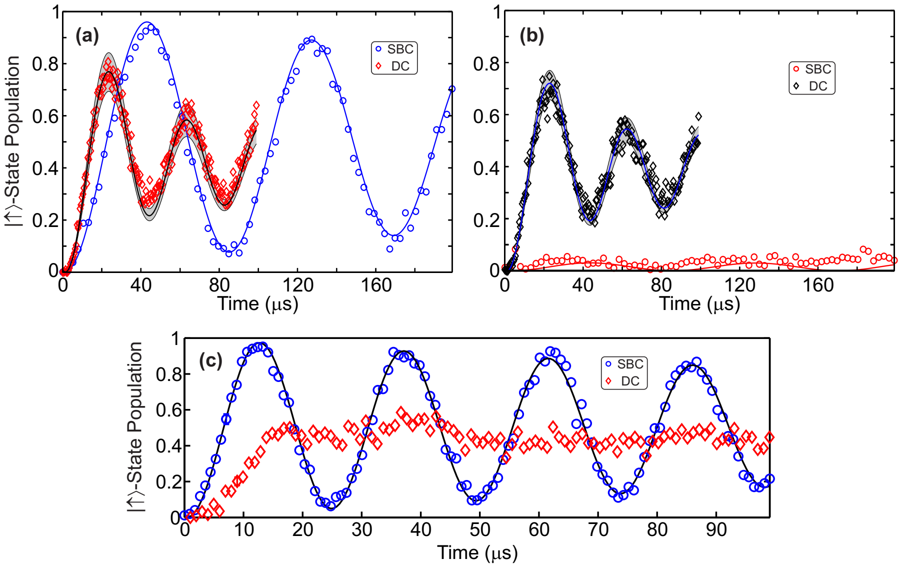

Figure 8.6: Rabi oscillations of a single $^{25}\mathrm{Mg}^{+}$ ion. Rabi oscillations of a single Doppler-cooled (DC) and sideband-cooled (SBC) $^{25}\mathrm{Mg}^{+}$ ion on the (a) blue sideband, (b) red sideband and (c) the carrier transition are shown. Each point corresponds to 3×100 measurements and the average error of 3% is omitted for clarity. The measurements were taken at a trap frequency of $\omega_z \sim 2.2\,\mathrm{MHz}$. The fit of the sideband-cooled data of the carrier and blue sideband with an exponentially decaying sinusoidal yields a Lamb-Dicke parameter of $\eta = 0.282 \pm 0.004$. The solid curves surrounded by the gray area for the Doppler-cooled ion are no fits, instead they correspond to a weighted sum over sinusoidal functions with Rabi frequencies corresponding to a thermal state of $\bar{n} = 16 \pm 5$, which resembles the measured behavior reasonably well.

off-resonant incoherent photon scattering due to a small detuning of the Raman laser beams of 900 MHz from the excited state imposed a lower limit on the lowest achievable $\bar{n}$ [147]. However, in our case, this effect is reduced due to the higher EOM detuning, but imparts a loss of contrast in the observed Rabi oscillations. This is discussed in more detail in the next section.

8.3.2 Off-Resonant Depumping

The observed decay in the oscillations in Fig. 8.6 for a ground state cooled ion can be caused by at least three different reasons: i) remaining population in upper trap levels ($n > 0$) results in a dephasing; ii) residual fluctuations in the laser intensity and the magnetic field leads to frequency shifts and readout errors; iii) loss of contrast due to off-resonant scattering events of the Raman laser beams [126, 147, 148].

Due to the finite detuning of 9.2 GHz of both Raman laser beams from the $P_{3/2}$ state, an unavoidable amount of scattering events occurs during each spectroscopy pulse. These events lead to depumping of the internal states as shown in Fig. 8.7. To demonstrate this effect, the ion is first initialized in the $|\downarrow\rangle$ state and a Raman pulse, which is detuned from the carrier transition by half the trap level spacing, irradiates the ion. The blue circles depict the state population as a function of the Raman pulse length. Assuming a linear decay, the fit yields a depumping to other states by $\gamma_1 \sim 0.02 \pm 0.01\%/\mu\mathrm{s}$. The red circles depict the same experiment with the difference that the ion has been initially prepared in the $|\uparrow\rangle$ state. Here, a stronger decoherence is observed and a linear fit yields a rate of $\gamma_2 \sim 0.06 \pm 0.01\%/\mu\mathrm{s}$.

Taking both rates into account by correcting the population excitation in Fig. 8.6 according to

$$\rho'_\downarrow = \rho_\downarrow + (\gamma_1 t)\,\rho_\downarrow - (\gamma_2 t)\,(1-\rho_\downarrow) \tag{8.24}$$

and performing the same analysis, yields an average population number of $\bar{n} = 0.02 \pm 0.01$.

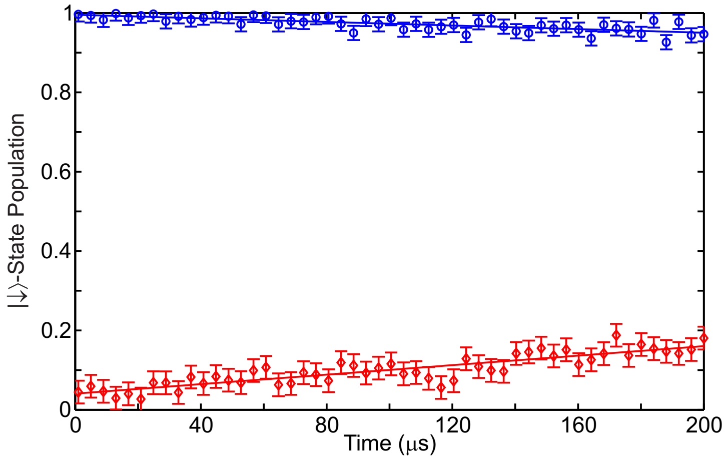

Figure 8.7: Off-resonant excitation by the Raman Lasers. The measured state population is plotted as a function of excitation pulse length. The Raman beams are detuned by half the trap frequency. The off-resonant excitation differs between the initial states: the bright state is de-excited with a fitted rate $\gamma_1 \sim 0.02 \pm 0.01\%/\mu\mathrm{s}$, whereas the dark state experiences a rate $\gamma_2 \sim 0.06 \pm 0.01\%/\mu\mathrm{s}$.

It is worth mentioning that the amount of off-resonant excitation in the experiment restricts the implementation of sequences that require high-fidelity operations, as e.g. gate operations. A change of the EOM resonance frequency to higher values as well as the use of the second order sideband instead of the first with a laser detuned by 18.4 GHz with respect to the $P_{3/2}$ level, would be one way to overcome this limitation. However, since high-fidelity operations are not required in the proposed spectroscopy experiments here, this issue is not further discussed.

8.3.3 Heating Rates

The fact that the temperature of the ion is accessible by comparing the excitation on the blue and the red sidebands can be used to study heating rates of the trap setup. These are of relevance to the design of the photon-recoil spectroscopy scheme since the heating rates introduce a background which reduces the expected signal to noise ratio.

After the ion is cooled to the absolute ground state of the harmonic confinement all cooling and spectroscopy lasers are switched off for a certain time. During this time, the ion is subject to environmental fluctuations and it experiences an excitation to higher motional states. Measuring the average vibrational population number as a function of the waiting time yields the desired heating rate. In Fig. 8.8, such a measurement is shown and heating rates for different axial trap frequencies. For the measurement, the micromotion of the ion was compensated in all three directions by re-directing one of the Raman beams and performing resolved sideband spectroscopy to compensate for the micromotion in all directions. It should be noted that the rather large error bars are a result of laser intensity and pointing fluctuations since no stabilization scheme can be employed during the waiting.

Unfortunately, the observed heating rates of ~ 1 phonon per 10 ms are rather high compared to similar setups (e.g. 1 phonon in 390(20) ms in [71]). There are different sources which can be the reason for such high heating rates. A possible explanation are remaining electrical forces on the ion at the trap frequency. These can be induced in different ways. A prominent candidate is found to be fluctuations of parameters of the trap confinement [149]. This effect originates for instance in the remaining noise of the output of the precision voltage supplies. In addition to that, the occurrence of patch potentials on the blade electrodes is found [65, 145]. This second effect might be even more critical for motional heating. The patch potentials have various origins. In our case, during the initial stage of the experiment, an electron emitter was used for photoionization of neutral magnesium atoms. The impact or absorption of the electrons by the blade electrodes charges the blades leading to unwanted additional electric stray fields. This effect resulted in a macroscopic change of the necessary micromotion compensation voltages for operating the trap. For the same reason, a macroscopic change in the ion position is observed if the blade electrodes are irradiated with the UV light at 280 nm. In addition to directly charging the trap electrodes, a deposition of oven materials, like magnesium or calcium, onto the electrodes also induces patch potentials. In our case, even though no macroscopic deposition is observed from outside the vacuum chamber, the activation and the first tests with the calcium oven made it necessary to change one of the compensation voltages by several hundred volt.

At present, the previously described capacitive shunting is installed in the DC voltage lines and no further electronic filtering is employed. Though the voltage supply shows a rms noise of only ∼1.6 mV, additional low-pass filters to further reduce the noise at the trap frequencies are currently under construction to further reduce the heating rates of the ion in the Paul trap.

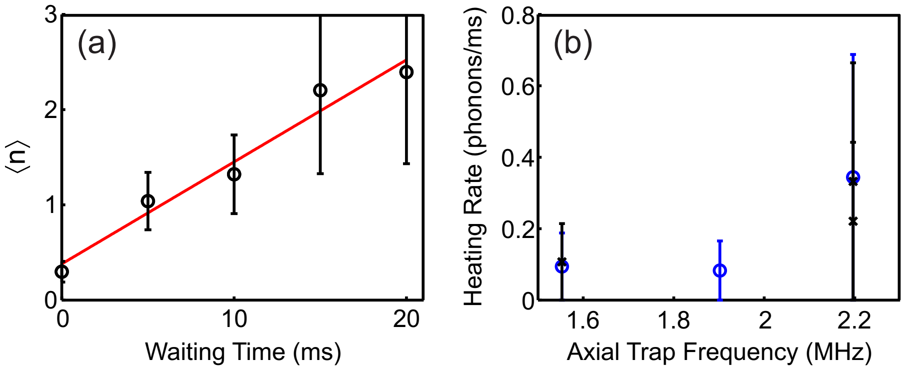

Figure 8.8: Heating rates of a single ^{25}Mg$^+$ ion. (a) The average motional quantum number is plotted as a function of the waiting time after ground state cooling. The measurement has been carried out for an axial trap frequency of $\omega_{\mathrm{ax}} \sim 2\pi \times 1.55\,\mathrm{MHz}$. A linear fit yields a heating rate of ∼0.1 phonon per ms. (b) The heating rates are plotted for different axial trap frequencies. The black crosses correspond to measurements where only the axial micromotion was compensated for, whereas the blue circles represent situations if the micromotion was compensated in all three directions by resolved sideband spectroscopy. No significant difference is observed between both cases.

Chapter 9

Summary and Outlook

In the scope of this thesis, a versatile experimental setup that allows for precision spectroscopy of single ions stored in a linear Paul trap using an optical frequency comb has been designed and characterized. The major motivation of its development is to provide more accurate data for various complex species such as Ca^+, Ti^+ and Fe^+ with a special focus on the determination of their isotope shifts, as an input to the ongoing analysis of quasar absorption spectra in view of a search for a possible variation of the fine-structure constant [9]. Such ions have resisted laser spectroscopy due to both missing cycling transitions and the necessity for a broad-band laser source with a narrow linewidth. At present, mainly Fourier transform spectroscopy using hollow-cathode lamps has been implemented with such types of ions. It is worth mentioning that even though a very good accuracy of $< 10^{-5}$ nm due to a high signal-to-noise ratio is achieved in these experiments, they do not resolve the isotope shifts of the different elements, owing to the Doppler-broadened line profiles. It is therefore desirable to confirm the acquired results and extend the spectroscopy data with the isotope shifts with an independent method.

The principle of the spectroscopy scheme presented in this thesis is to sympathetically cool the ion of interest to the absolute motional ground state via a simultaneously confined $^{25}Mg^+$ ion and employ a phase-stabilized optical frequency comb as a spectroscopy source. While the investigation of the Ca^+ ion mainly serves the purpose of a calibration leading to a better understanding of the systematics of the spectroscopy scheme, the long-term goal of the experiment is to investigate the desired transitions in Ti^+ and Fe^+.

The theoretical calculations on the expected spectroscopy signal using semi-classical optical Bloch equations have been discussed and presented in detail. In this context, different strategies to perform spectroscopy on all individual transitions among the S, P and D states in a $^{40}Ca^+$ ion have been studied. A very sensitive type of spectroscopy, which measures the photon recoil induced by a few resonant scattering events of the spectroscopy source, is proposed. The expected transition lineshapes are distorted due to the presence of the sideband transitions which need to be taken into account when carrying out the experiment. The approach discussed within this thesis promises an accuracy at least on the level of the natural linewidth of the considered elements, which is on the order of 10 MHz or larger. This is in contrast to other heating spectroscopy techniques, were only Doppler-cooled ions are used [59].

With the presented strategies, all electronic excitations between the lowest five energy levels in Ca^+ are accessible and can be measured. It is worth mentioning that, though not of astrophysical relevance, the repumping transitions between the D-P levels have so far to our best knowledge not been subject to precision spectroscopy. As a further application, it has been shown that, with correctly tuned parameters, the comb spectrum can be engineered at will and drive e.g. a Raman transition between different Ca^+ levels, which provide a means to study of coherence properties of the comb spectrum.

The first necessary step of the spectroscopy schemes is cooling a $^{25}Mg^+$ ion to the absolute ground state. In the experiments presented here, this has been successfully implemented using a single solid-state laser system. The novelty of the setup is the incorporation of an electro-optic modulator which allows for switching between an off-resonant coherent manipulation and a resonant repumping and detection configuration. This is an enormous simplification to other setups where several laser systems are often required for the same purposes [58, 65].

The efficiency of the setup has been quantified by its cooling performance. With the applied schemes, an average vibrational population number of $\bar{n} = 0.03 \pm 0.01$ has been inferred. In a similar approach, using acousto- instead of electro-optic modulators, a population of $\bar{n} = 0.34 \pm 0.08$ was measured [146]. The major limitation in these approaches arises from the finite detuning to intermediate states, leading to off-resonant scattering events. In future experiments, we envision to use either higher order sidebands or an electro-optic modulator with a higher resonance frequency to access a regime where the realization of high-fidelity quantum gates becomes feasible. However, in the near future, the performance of the implemented pulsed cooling schemes will be compared to a continuous-wave approach by studying cooling rates and the achievable ground state occupation.

Since the spectroscopy signal is to be obtained by acquiring the vibrational state information of the 2-ion crystal, the internal state discrimination plays a crucial role in our experiments. While the finite splitting between the qubit states limits the interaction time due to off-resonant depumping effects, the photon distributions of both states are not unambiguously defined. For that reason, different detection schemes have been investigated, along with their detection error limits and sensitivity towards experimental fluctuations. Among the different techniques, the *π-pulse detection*, that makes use of the statistically gathered information and correlation between detection events by combining resonant laser pulses and radio-frequency induced spin-flips, is a very promising candidate due to its simplicity for application in other experimental setups which also utilize hyperfine ground states for state discrimination. In a next step, a further detection method which is based on Bayesian analysis of the detected photons will be studied and compared to the previously used ones. This method, in combination with the mapping to an optical qubit, yielded in a different experiment a net readout fidelity of 99.77(3)% of a hyperfine qubit [129, 130].

The direct frequency comb spectroscopy source will be a passively mode-locked pulsed Ti:Saph laser. The electronics for phase-stabilizing and scanning both the offset frequency and repetition rate is currently being set up and tested. After that, a calcium ion simultaneously confined with a magnesium ion will be cooled to the ground state and the spectroscopy will be carried out. One necessary step in the analysis of the first spectroscopy signals will be to adapt the pulse shape of the frequency comb used in the simulations to the true output of the laser. Especially the inclusion of pulse broadening and chirping, which result from the employed micro-structured fibre to provide an octave-spanning spectrum, is a formidable challenge to be taken into account in the simulations.

After the calcium electronic level structure is mapped out, Ti^+ and Fe^+ transitions in the ultra-violet will be studied in the same setup. Since the necessary atomic sources are already built into the vacuum chamber, only a photo-ionization laser system for each individual element is needed. We plan to implement two different strategies for these elements. In a first approach, in a similar way as in the case of $^{40}\mathrm{Ca}^+$ ion, direct frequency comb spectroscopy with a comb that is upconverted to the ultra-violet will be employed. The second approach employs quantum logic spectroscopy with a cw dye laser as a spectroscopy source while using a frequency comb in combination with an ultra-violet lamp for repumping.

At present, certain dipole transitions in the spectrum of Ti^+ have been investigated, experimentally and theoretically, by means of high-resolution Fourier transform spectroscopy [150], as well as several isotope shifts in a beam or vapor configurations [151, 152, 153]. It is worth mentioning that apart from dipole transitions, also forbidden lines are of astrophysical interest and are currently being studied by other groups [154, 155].

Fe^+ has transition lines which are extremely sensitive to a change in the fine-structure constant and are thus even more interesting for astrophysical analyses. At present, spectroscopy of Fe^+ has only been accomplished using hollow-cathode lamps and ion clouds [156, 157, 158]. Various theoretical predictions on the corresponding isotope shifts are available [159, 160]. However, no independent verification of the Fourier transform spectroscopy results or isotopically resolves spectroscopy has been performed to our best knowledge.

As a further future prospect, the cooling of molecular ions should be mentioned. In the last years, there has been an enormous progress in this field [23, 161]. We plan to employ methods similar to the cooling schemes presented in this thesis to cool molecular ions, such as MgH^+ and CaH^+, to the ro-vibrational ground states and subsequently subject them to precision spectroscopy. The results of such measurements are of interest both from a pure spectroscopic point of view as well as for astrophysical studies of the variation of the electron to proton mass ratio [162, 163].

Appendix

Appendix A

Wigner Symbols and Normalizations

An detailed overview of the Wigner symbols and their relation to the Clebsch-Gordan coefficients can be found in [164]. Here, only the relations used in this thesis are summarized. For a further discussion on different normalizations, the reader is referred to [165, 166].

The Wigner-$3j$ and the Wigner-$6j$ symbol follow the orthogonality relations

$$(2j+1)\sum_{m_1,m_2}\begin{pmatrix} j_1 & j_2 & j \\ m_1 & m_2 & m \end{pmatrix}_{3j}^2 = \sum_{j,m}(2j+1)\begin{pmatrix} j_1 & j_2 & j \\ m_1 & m_2 & m \end{pmatrix}_{3j}^2 = 1 \quad ,$$

$$\sum_{j_3}(2j_3+1)\begin{Bmatrix} j_1 & j_2 & j_3 \\ j_4 & j_5 & j_6 \end{Bmatrix}_{6j}^2 = \frac{1}{2j_6+1} \quad .$$

These relations can be used to calculate sums over the magnetic quantum numbers m_{F} and q

$$\sum_{m_F,m'_F,q}\begin{pmatrix} F & F' & J_{\mathrm{ph}} \\ m_F & -m_{F'} & q \end{pmatrix}_{3j}^2 = \sum_q \frac{1}{2J_{\mathrm{ph}}+1} = 1 \quad ,$$

$$\sum_{m_F,q}\begin{pmatrix} F & J_{\mathrm{ph}} & F' \\ m_F & q & -m_{F'} \end{pmatrix}_{3j}^2 = \frac{1}{2F'+1} \quad .$$

The normalization of the reduced matrix elements is also of importance. As mentioned in Section 2.2.3, the reduced matrix element can be further simplified as

$$\langle JIF||d||J'IF'\rangle = (-1)^{J+I+F'+1}\sqrt{(2J+1)(2F'+1)}\begin{Bmatrix} J & F & I \\ F' & J' & 1 \end{Bmatrix}_{6j}\langle J||d||J'\rangle \quad .$$

Again, using the orthogonality relation above, the sums over different quantum numbers can be calculated using the symmetry under permutations[1]

$$\begin{aligned}\sum_{F'}|\langle JIF||d||J'IF'\rangle|^2 &= (2J+1)\sum_{F'}(2F'+1)\begin{Bmatrix} I & J' & F' \\ 1 & F & J \end{Bmatrix}^2_{6j}|\,\langle J||d||J'\rangle\,|^2 \\ &= |\,\langle J||d||J'\rangle\,|^2 \quad .\end{aligned}$$

Using these relations, the full matrix element reads

$$\begin{aligned}&|\langle JFm_F|d|J'F'm_{F'}\rangle|^2 \qquad\qquad (A.1)\\ =\;&\underbrace{(2F+1)(2F'+1)(2J+1)\begin{Bmatrix} J & F & I \\ F' & J' & 1 \end{Bmatrix}^2_{6j}\begin{pmatrix} F' & J_{\text{ph}} & F \\ m_{F'} & q & -m_F \end{pmatrix}^2_{3j}}_{=:\kappa^2}|\,\langle J||d||J'\rangle\,|^2 \quad .\end{aligned}$$

It is normalized in the following ways

$$\begin{aligned}\sum_{F',m_{F'},q}|\langle JFm_F|d|J'F'm_{F'}\rangle|^2 &= |\,\langle J||d||J'\rangle\,|^2 \quad , \\ \sum_{F,m_F,q}|\langle JFm_F|d|J'F'm_{F'}\rangle|^2 &= \left(\frac{2J+1}{2J'+1}\right)|\,\langle J||d||J'\rangle\,|^2 \quad .\end{aligned}$$

---

[1] It should be noted that for quadrupole transitions the term 1 in the Wigner-6j symbol is to be replaced with 2.

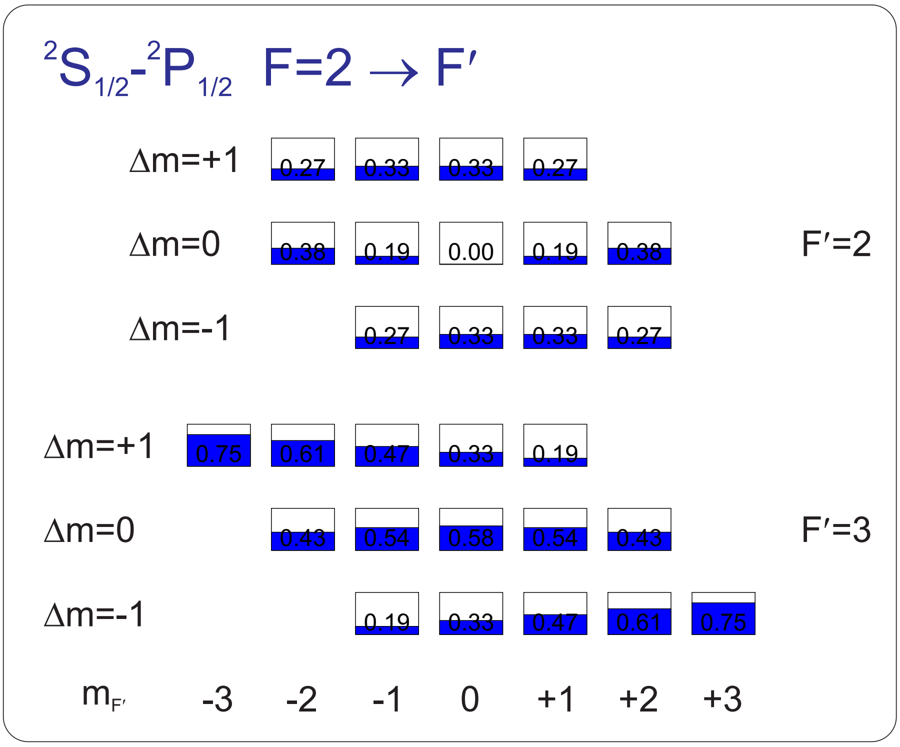

Figure A.1: Transition strengths $|\kappa|\sqrt{2J'+1}/\sqrt{2J+1}$ (see Eq. (A.1)) of the $S_{1/2}(F=2, m_F) \rightarrow P_{1/2}(F', m_{F'})$ in $^{25}\mathrm{Mg}^+$ are shown. The difference $\Delta m = m_F - m_{F'}$ represents the kind of transition, i.e. $\Delta m = \pm 1$ corresponds to a $\sigma^\pm$-transition, whereas $\Delta m = 0$ corresponds to a π-transition.

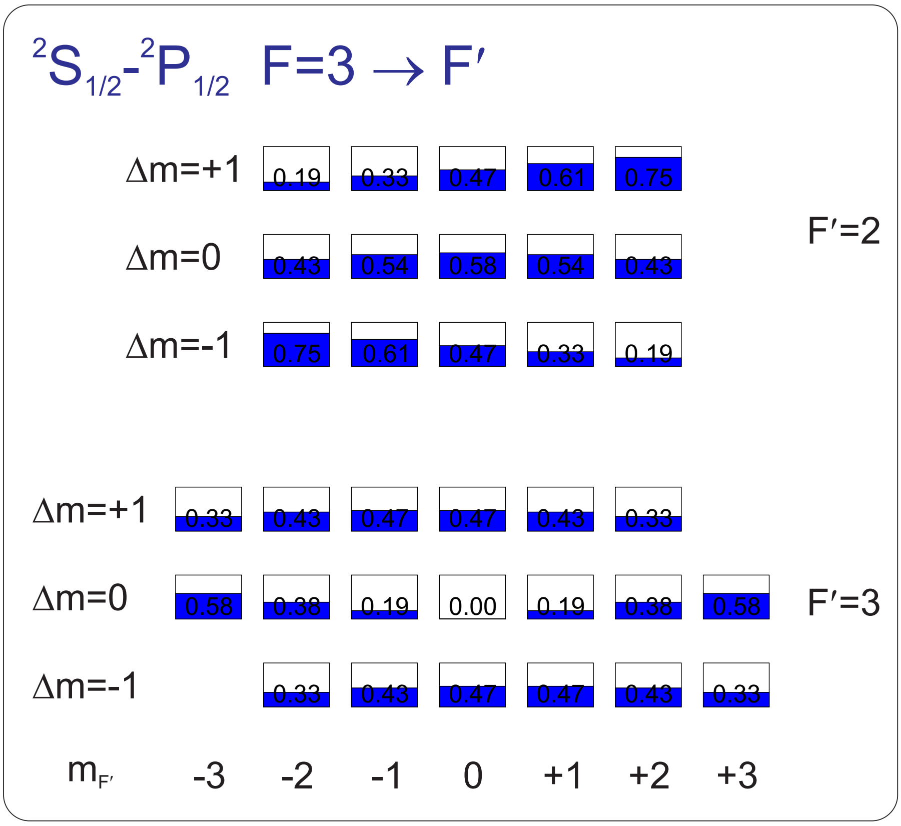

Figure A.2: Transition strengths $|\kappa|\sqrt{2J'+1}/\sqrt{2J+1}$ (see Eq. (A.1)) of the $S_{1/2}(F=3, m_F) \rightarrow P_{1/2}(F', m_{F'})$ in $^{25}\mathrm{Mg}^+$ are shown. The difference $\Delta m = m_F - m_{F'}$ represents the kind of transition, i.e. $\Delta m = \pm 1$ corresponds to a $\sigma^\pm$-transition, whereas $\Delta m = 0$ corresponds to a π-transition.

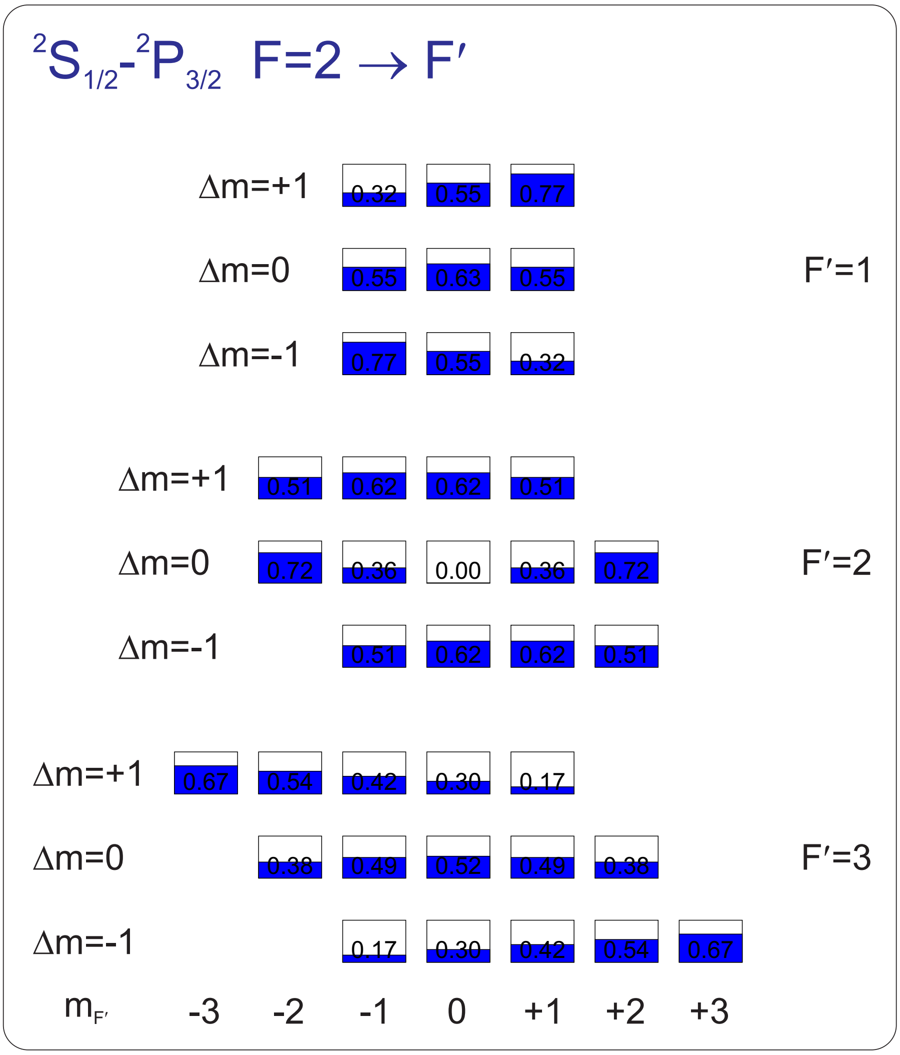

Figure A.3: Transition strengths $|\kappa|\sqrt{2J'+1}/\sqrt{2J+1}$ (see Eq. (A.1)) of the $S_{1/2}(F=2, m_F) \rightarrow P_{3/2}(F', m_{F'})$ in $^{25}\mathrm{Mg}^+$ are shown. The difference $\Delta m = m_F - m_{F'}$ represents the kind of transition, i.e. $\Delta m = \pm 1$ corresponds to a $\sigma^\pm$-transition, whereas $\Delta m = 0$ corresponds to a π-transition.

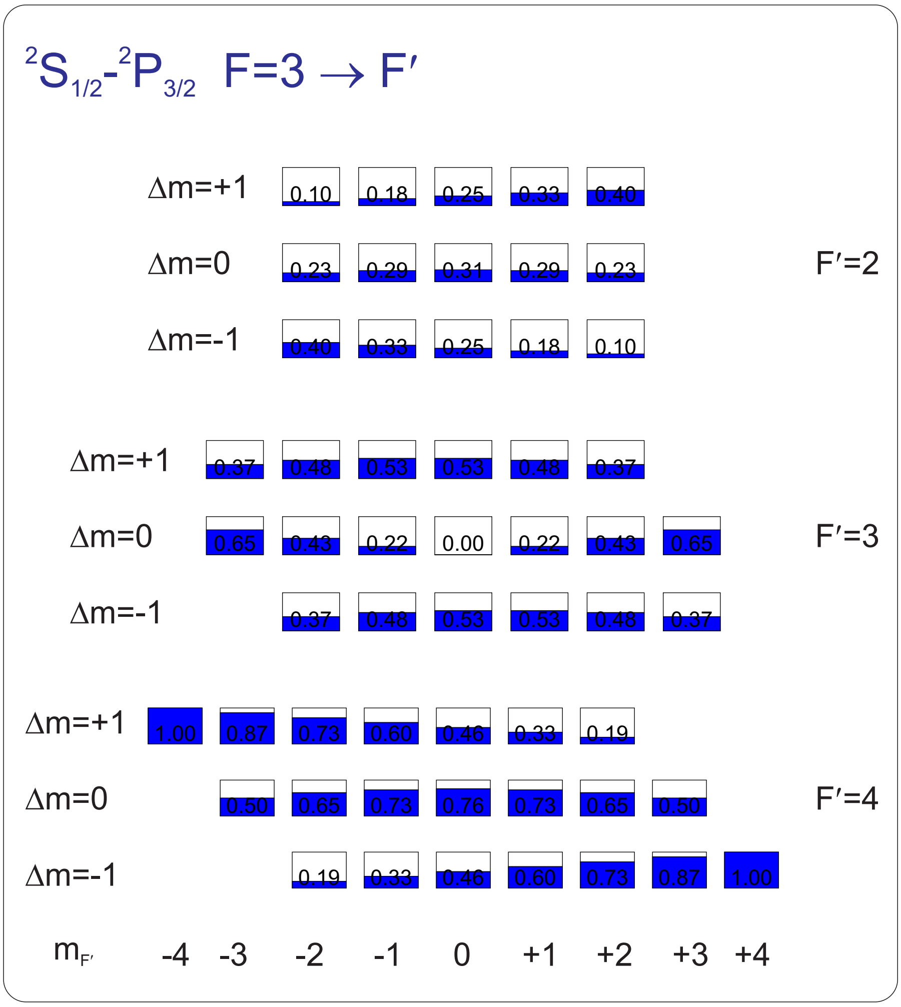
$^2S_{1/2}$-$^2P_{3/2}$ F=3 → F′
Δm=+1 0.10 0.18 0.25 0.33 0.40
Δm=0 0.23 0.29 0.31 0.29 0.23
F′=2
Δm=-1 0.40 0.33 0.25 0.18 0.10
Δm=+1 0.37 0.48 0.53 0.53 0.48 0.37
Δm=0 0.65 0.43 0.22 0.00 0.22 0.43 0.65
F′=3
Δm=-1 0.37 0.48 0.53 0.53 0.48 0.37
Δm=+1 1.00 0.87 0.73 0.60 0.46 0.33 0.19
Δm=0 0.50 0.65 0.73 0.76 0.73 0.65 0.50
F′=4
Δm=-1 0.19 0.33 0.46 0.60 0.73 0.87 1.00
$m_{F'}$ -4 -3 -2 -1 0 +1 +2 +3 +4

Figure A.4: Transition strengths $|\kappa|\sqrt{2J'+1}/\sqrt{2J+1}$ (see Eq. (A.1)) of the $S_{1/2}(F = 3, m_F) \rightarrow P_{3/2}(F', m_{F'})$ in $^{25}\mathrm{Mg}^+$ are shown. The difference $\Delta m = m_F - m_{F'}$ represents the kind of transition, i.e. $\Delta m = \pm 1$ corresponds to a $\sigma^\pm$-transition, whereas $\Delta m = 0$ corresponds to a π-transition.

Appendix B

Polarization and Radiation Pattern

In this section, some general considerations on the basis transformation to spherical harmonics are given. After that, the radiation pattern for different transition types is calculated. The calculations closely follow the quantum mechanics script of Prof. Peter S. Riseborough [167].

Spherical Harmonics

The vector $\vec{a}_{\mathrm{C}} = (x, y, z)$ in cartesian coordinates can be expressed in a basis of spherical harmonics as

$$\vec{a}_{\mathrm{S}} = \begin{pmatrix} \frac{1}{\sqrt{2}}(-x - \mathrm{i}y) \\ \frac{1}{\sqrt{2}}(x - \mathrm{i}y) \\ z \end{pmatrix} = r\sqrt{\frac{4\pi}{3}} \begin{pmatrix} Y_{1,1} \\ Y_{1,-1} \\ Y_{1,0} \end{pmatrix} \quad .$$

The spherical harmonics have the following definition

$$\begin{aligned} Y_{1,0} &= \sqrt{\frac{3}{4\pi}} \cos\theta \quad ; \\ Y_{1,1} &= -\sqrt{\frac{3}{8\pi}} \sin\theta e^{\mathrm{i}\phi} \quad ; \\ Y_{1,-1} &= \sqrt{\frac{3}{8\pi}} \sin\theta e^{-\mathrm{i}\phi} \quad . \end{aligned}$$

The scalar product of two vectors $\vec{a}_S$ and $\vec{b}_S$ stays unchanged under this orthogonal transformation

$$\vec{a}_S \cdot \vec{b}_S = \vec{a}_C \cdot \vec{b}_C = \sum_k a_k^* b_k \quad .$$

Vectors in this basis are useful to determine selection rules for dipolar transitions, for instance.

Polarization Vector and Emission Pattern

Consider a planar wave with a unit k-vector in spherical coordinates

$$\hat{k} = \begin{pmatrix} \sin\theta\cos\phi \\ \sin\theta\sin\phi \\ \cos\theta \end{pmatrix} \quad .$$

Here, the quantization axis is chosen to be in the z-direction, $\hat{B}\cdot\hat{k} = \cos\theta$. The corresponding unit polarization vectors are perpendicular to the k-vector perpendicular with respect to each other

$$\begin{aligned} \hat{\epsilon}_k \cdot \hat{\epsilon}_l &= \delta_{kl} \quad ; \\ \hat{k}\cdot\hat{\epsilon}_k &= 0 \quad . \end{aligned}$$

They can be expressed as

$$\hat{\epsilon}_1 = \begin{pmatrix} \cos\theta\cos\phi \\ \cos\theta\sin\phi \\ -\sin\theta \end{pmatrix} \quad ; \quad \hat{\epsilon}_2 = \begin{pmatrix} -\sin\phi \\ \cos\phi \\ 0 \end{pmatrix} \quad .$$

The radiation pattern is determined by the product of the dipole operator $\vec{r} = (x, y, z)$ and the unit polarization vector. It can be expressed in spherical harmonics as follows:

$$\begin{aligned} \langle\psi'|\hat{\epsilon}_1\cdot\vec{r}|\psi\rangle &= -\sin\theta\,\langle\psi'|z|\psi\rangle + \frac{1}{2}\cos\theta e^{\mathrm{i}\phi}\,\langle\psi'|x-\mathrm{i}y|\psi\rangle - \frac{1}{2}\cos\theta e^{-\mathrm{i}\phi}\,\langle\psi'|-x-\mathrm{i}y|\psi\rangle \quad ; \\ \langle\psi'|\hat{\epsilon}_2\cdot\vec{r}|\psi\rangle &= \mathrm{i}\frac{e^{\mathrm{i}\phi}}{2}\,\langle\psi'|x-\mathrm{i}y|\psi\rangle - \mathrm{i}\frac{e^{-\mathrm{i}\phi}}{2}\,\langle\psi'|-x-\mathrm{i}y|\psi\rangle \quad . \end{aligned}$$

The angular dependence of the dipolar decay is found by summing over all possible polarizations

$$\begin{aligned} &|\,\langle\psi'|\hat{\epsilon}_1\cdot\vec{r}|\psi\rangle\,|^2 + |\,\langle\psi'|\hat{\epsilon}_2\cdot\vec{r}|\psi\rangle\,|^2 \\ =\; &\underbrace{\sin^2\theta|\,\langle\psi'|z|\psi\rangle\,|^2}_{\pi-\text{transition}} + \underbrace{\frac{1}{4}(1+\cos^2\theta)|\,\langle\psi'|x-\mathrm{i}y|\psi\rangle\,|^2}_{\sigma^- -\text{transition}} + \underbrace{\frac{1}{4}(1+\cos^2\theta)|\,\langle\psi'|-x-\mathrm{i}y|\psi\rangle\,|^2}_{\sigma^+ -\text{transition}} \quad . \end{aligned}$$

Including this result, the emission pattern distribution for different types of transitions are

$P(\hat{k})$	Transition/Emission Type	f_α
$\frac{3}{8\pi}\sin^2\theta$	$\pi-$ transition	$\frac{1}{5}\cdot(2,2,1)$
$\frac{3}{16\pi}(1+\cos^2\theta)$	$\sigma^- -$ transition	$\frac{1}{10}\cdot(3,3,4)$
$\frac{3}{16\pi}(1+\cos^2\theta)$	$\sigma^+ -$ transition	$\frac{1}{10}\cdot(3,3,4)$
$\frac{1}{2}(\delta(\theta-\frac{\pi}{2})\delta(\phi)+\delta(\theta-\frac{\pi}{2})\delta(\phi-\pi))$	Parallel to k-vector $(\theta,\phi)=(\pi/2,0)$	$(1,0,0)$
$\frac{1}{4\pi}$	Isotropic	$\frac{1}{3}\cdot(1,1,1)$

The distributions are chosen such that the normalization condition $\int d\Omega P=1$ is fulfilled.

In the Doppler cooling model (see Section 8.1.1), the distribution weighted with the wave vector of the emitted photon

$$f_\alpha=\int d\Omega P(\hat{k})\hat{k}_\alpha^2$$

needs to be calculated. The corresponding values are listed in the table above.

Appendix C

Population Distribution and Sideband Ratios

In a thermal state, the probability population distribution of the nth state of the harmonic oscillator is given by the expectation value of the density operator in the grand canonical ensemble

$$\begin{aligned} \rho &= \frac{1}{Z} e^{-H/k_B T} \quad \text{where} \quad Z = \mathrm{tr}\left(e^{-H/k_B T}\right) \quad ; \\ p_n &= \langle n|\, \rho\, |n\rangle = \left[1 - e^{-\hbar\omega_z/k_B T}\right] e^{-n\hbar\omega_z/k_B T} \quad . \end{aligned}$$

With the definition of the average vibrational number

$$\bar{n} \equiv \langle n\rangle \quad := \quad \sum_n n p_n = \frac{1}{e^{\hbar\omega_z/k_B T} - 1} \quad ,$$

the population distribution can be simplified as

$$p_n = \frac{\bar{n}^n}{(1+\bar{n})^{n+1}} \quad .$$

In order to get an estimate for the average population $\bar{n}$ after doppler cooling, the population in the bright and dark state of the red and blue sideband. The temporal evolution of the population on the rth red sideband is given as the sum over Rabi oscillations with n-dependent frequencies as

$$\begin{aligned}
\rho_r^{\mathrm{rsb}} &= \sum_{n=r}^{\infty} p_n \cdot \sin^2\left(\Omega_{n-r,n} \cdot t\right) \\
&= \sum_{n=r}^{\infty} \frac{\bar{n}^n}{(1+\bar{n})^{n+1}} \cdot \sin^2\left(\Omega_{n-r,n} \cdot t\right) \\
&= \sum_{n'=0}^{\infty} \frac{\bar{n}^{n'+r}}{(1+\bar{n})^{n'+r+1}} \cdot \sin^2\left(\Omega_{n',n'+r} \cdot t\right) \\
&= \left(\frac{\bar{n}}{1+\bar{n}}\right)^r \sum_{n'=0}^{\infty} \frac{\bar{n}^{n'}}{(1+\bar{n})^{n'+1}} \cdot \sin^2\left(\Omega_{n'+r,n'} \cdot t\right) \\
&= \left(\frac{\bar{n}}{1+\bar{n}}\right)^r \sum_{n'=0}^{\infty} p_{n'} \cdot \sin^2\left(\Omega_{n'+r,n'} \cdot t\right) \\
&= \left(\frac{\bar{n}}{1+\bar{n}}\right)^r \rho_r^{\mathrm{bsb}} \quad .
\end{aligned}$$

Here, the symmetry in the red and blue sidebands was used. Re-arranging terms yields

$$\bar{n} = \frac{\sqrt[r]{Q}}{1-\sqrt[r]{Q}} \quad \text{where} \quad Q = \frac{\rho_r^{\mathrm{rsb}}}{\rho_r^{\mathrm{bsb}}} \quad .$$

Thus, the comparison of the rth red and rth blue sideband excitation yields the average population $\bar{n}$, assuming a thermal distribution. Given $\bar{n}$, the ground state population can be calculated

$$p_0 = \frac{1}{1+\bar{n}} = 1 - \sqrt[r]{Q} \quad .$$

Assuming that the ion is well enough in the absolute ground state, the Lamb-Dicke parameter is related to the Rabi frequencies of the carrier transition $\Omega_{0,0}$ and the first blue sideband transitions $\Omega_{1,0}$ as follows:

$$\left.\begin{aligned}
\Omega_{0,0} &= \Omega \cdot e^{-\eta^2/2} \\
\Omega_{1,0} &= \Omega \cdot e^{-\eta^2/2} \cdot \eta
\end{aligned}\right\} \rightarrow \eta = \frac{\Omega_{1,0}}{\Omega_{0,0}} \quad .$$

Thus, by comparison of the carrier and blue sideband excitations, the Lamb-Dicke parameter can be determined.

Appendix D

Comb Structure and Unitary Phase Transformation

D.1 Comb Structure

The sum appearing in the Fourier transformation of the comb spectrum (see Eq. (3.5))

$$\sum_{k=0}^{p} e^{-\mathrm{i}(\omega-\omega_0)k\tau_R}$$

corresponds to a geometric sum which can be simplified as

$$S_p \;=\; \sum_{k=0}^{p} e^{\mathrm{i}\alpha k} = \frac{1-e^{\mathrm{i}\alpha(p+1)}}{1-e^{\mathrm{i}\alpha}} = \frac{\sin\left(\frac{\alpha(p+1)}{2}\right)}{\sin\left(\frac{\alpha}{2}\right)} \cdot e^{\mathrm{i}\frac{\alpha p}{2}} \qquad ,$$

where $\alpha = (\omega - \omega_0)\tau_R$. Taking the square yields

$$|S_p|^2 \;=\; \frac{\cos(\alpha(p+1))-1}{\cos(\alpha)-1} \qquad .$$

D.2 Unitary Transformation for the Phase Dependence

In the following, three examples of the unitary transformation to remove the phase dependence of the time propagation operator are shown. The Hamiltonian and the time propagation operator are transformed in the following way

$$\begin{aligned} U_I(t,\varphi) &= K(\varphi)\cdot U_I(t)\cdot K^\dagger(\varphi) \quad ; \\ H^I_{\text{int}}(t,\varphi) &= K(\varphi)\cdot H^I_{\text{int}}(t)\cdot K^\dagger(\varphi) \quad ; \\ K(\varphi)\cdot K^\dagger(\varphi) &= 1 \quad . \end{aligned}$$

2-Level System This is an example for a generic two-level system. For clarity, the time arguments are omitted.

$$\begin{aligned} K &= \begin{pmatrix} e^{\mathrm{i}\varphi} & 0 \\ 0 & 1 \end{pmatrix} \quad ; \quad H^I_{\text{int}} = \begin{pmatrix} 0 & h_{12} \\ h_{21} & 0 \end{pmatrix} \quad ; \\ H^I_{\text{int}}(\varphi) &= K H^I_{\text{int}} K^\dagger = \begin{pmatrix} 0 & h_{12}e^{\mathrm{i}\varphi} \\ h_{21}e^{-\mathrm{i}\varphi} & 0 \end{pmatrix} \quad ; \\ U_I(\varphi) &= K \begin{pmatrix} u_{11} & u_{12} \\ u_{21} & u_{22} \end{pmatrix} K^\dagger = \begin{pmatrix} u_{11} & u_{12}e^{\mathrm{i}\varphi} \\ u_{21}e^{-\mathrm{i}\varphi} & u_{22} \end{pmatrix} \end{aligned}$$

3-Level System Regarding the three-level system, there are two possibilities. In the first example, two-photon transitions are allowed from the first, via the second, to the third level.

$$\begin{aligned} K &= \begin{pmatrix} 1 & 0 & 0 \\ 0 & e^{\mathrm{i}\varphi} & 0 \\ 0 & 0 & e^{2\mathrm{i}\varphi} \end{pmatrix} \quad ; \quad H^I_{\text{int}} = \begin{pmatrix} 0 & h_{12} & 0 \\ h_{21} & 0 & h_{23} \\ 0 & h_{32} & 0 \end{pmatrix} \quad ; \\ H^I_{\text{int}}(\varphi) &= \begin{pmatrix} 0 & h_{12}e^{\mathrm{i}\varphi} & 0 \\ h_{21}e^{-\mathrm{i}\varphi} & 0 & h_{23}e^{\mathrm{i}\varphi} \\ 0 & h_{32}e^{-\mathrm{i}\varphi} & 0 \end{pmatrix} \quad ; \\ U_I(\varphi) &= \begin{pmatrix} u_{11} & u_{12}e^{\mathrm{i}\varphi} & u_{13}e^{2\mathrm{i}\varphi} \\ u_{21}e^{-\mathrm{i}\varphi} & u_{22} & u_{23}e^{\mathrm{i}\varphi} \\ u_{31}e^{-2\mathrm{i}\varphi} & u_{32}e^{-\mathrm{i}\varphi} & u_{33} \end{pmatrix} \end{aligned}$$

The second example describes a V-type level system where only single-photon transitions from the ground state are allowed.

$$
\begin{aligned}
K &= \begin{pmatrix} 1 & 0 & 0 \\ 0 & e^{-\mathrm{i}\varphi} & 0 \\ 0 & 0 & e^{-\mathrm{i}\varphi} \end{pmatrix} \quad ; \quad H^I_{\text{int}} = \begin{pmatrix} 0 & h_{12} & h_{13} \\ h_{21} & 0 & 0 \\ h_{31} & 0 & 0 \end{pmatrix} \quad ; \\
H^I_{\text{int}}(\varphi) &= \begin{pmatrix} 0 & h_{12}e^{\mathrm{i}\varphi} & h_{13}e^{\mathrm{i}\varphi} \\ h_{21}e^{-\mathrm{i}\varphi} & 0 & 0 \\ h_{31}e^{-\mathrm{i}\varphi} & 0 & 0 \end{pmatrix} \quad ; \\
U_I(\varphi) &= \begin{pmatrix} u_{11} & u_{12}e^{\mathrm{i}\varphi} & u_{13}e^{\mathrm{i}\varphi} \\ u_{21}e^{-\mathrm{i}\varphi} & u_{22} & u_{23} \\ u_{31}e^{-\mathrm{i}\varphi} & u_{32} & u_{33} \end{pmatrix}
\end{aligned}
$$

The 5-Level Calcium System The calcium ion consists of five energy levels (see Fig. 4.2) with the following definitions for the electronic levels: $\mathrm{S}_{1/2} \leftrightarrow |1\rangle$, $\mathrm{D}_{3/2} \leftrightarrow |2\rangle$, $\mathrm{D}_{5/2} \leftrightarrow |3\rangle$, $\mathrm{P}_{1/2} \leftrightarrow |4\rangle$ and $\mathrm{P}_{3/2} \leftrightarrow |5\rangle$. In the presented simulations, the following Hamiltonian and transformation matrix was used:

$$
\begin{aligned}
K &= \begin{pmatrix} 1 & 0 & 0 & 0 & 0 \\ 0 & e^{\mathrm{i}\epsilon_2 t_k - \mathrm{i}\phi_k} & 0 & 0 & 0 \\ 0 & 0 & e^{\mathrm{i}\epsilon_3 t_k - \mathrm{i}\phi_k} & 0 & 0 \\ 0 & 0 & 0 & e^{\mathrm{i}\epsilon_4 t_k - 2\mathrm{i}\phi_k} & 0 \\ 0 & 0 & 0 & 0 & e^{\mathrm{i}\epsilon_5 t_k - 2\mathrm{i}\phi_k} \end{pmatrix} \quad ; \\
H^I_{\text{int}}(t' + k\tau_R) &= \begin{pmatrix} 0 & 0 & 0 & \mu_{14}\sigma_2(t')e^{-\mathrm{i}(\omega_{14}-2\omega_L)t'} & \mu_{15}\sigma_2(t')e^{-\mathrm{i}(\omega_{15}-2\omega_L)t'} \\ \cdot & 0 & 0 & \mu_{24}\sigma(t')e^{-\mathrm{i}(\omega_{24}-\omega_L)t'} & \mu_{25}\sigma(t')e^{-\mathrm{i}(\omega_{25}-\omega_L)t'} \\ \cdot & \cdot & 0 & 0 & \mu_{35}\sigma(t')e^{-\mathrm{i}(\omega_{35}-\omega_L)t'} \\ \cdot & \cdot & \cdot & 0 & 0 \\ \cdot & \cdot & \cdot & \cdot & 0 \end{pmatrix} \quad ;
\end{aligned}
$$

$$H^I_{\mathrm{int}}(t' + k\tau_R, \phi_k) =$$
$$\begin{pmatrix} 0 & 0 & 0 & \mu_{14}\sigma_2(t')e^{-\mathrm{i}(\omega_{14}-2\omega_L)t'+\mathrm{i}(2\phi_k-\omega_{14}t_k)} & \mu_{15}\sigma_2(t')e^{-\mathrm{i}(\omega_{15}-2\omega_L)t'+\mathrm{i}(2\phi_k-\omega_{15}t_k)} \\ \cdot & 0 & 0 & \mu_{24}\sigma(t')e^{-\mathrm{i}(\omega_{24}-\omega_L)t'+\mathrm{i}(\phi_k-\omega_{24}t_k)} & \mu_{25}\sigma(t')e^{-\mathrm{i}(\omega_{25}-\omega_L)t'+\mathrm{i}(\phi_k-\omega_{25}t_k)} \\ \cdot & \cdot & 0 & 0 & \mu_{35}\sigma(t')e^{-\mathrm{i}(\omega_{35}-\omega_L)t'+\mathrm{i}(\phi_k-\omega_{35}t_k)} \\ \cdot & \cdot & \cdot & 0 & 0 \\ \cdot & \cdot & \cdot & \cdot & 0 \end{pmatrix} ;$$

$$U_I(\phi_k) =$$
$$\begin{pmatrix} u_{11} & u_{12}e^{-\mathrm{i}\omega_{12}t_k+\mathrm{i}\phi_k} & u_{13}e^{-\mathrm{i}\omega_{13}t_k+\mathrm{i}\phi_k} & u_{14}e^{-\mathrm{i}\omega_{14}t_k+\mathrm{i}2\phi_k} & u_{15}e^{-\mathrm{i}\omega_{15}t_k+\mathrm{i}2\phi_k} \\ u_{21}e^{\mathrm{i}\omega_{12}t_k-\mathrm{i}\phi_k} & u_{22} & u_{23}e^{-\mathrm{i}\omega_{23}t_k} & u_{24}e^{-\mathrm{i}\omega_{24}t_k+\mathrm{i}\phi_k} & u_{25}e^{-\mathrm{i}\omega_{25}t_k+\mathrm{i}\phi_k} \\ u_{31}e^{\mathrm{i}\omega_{13}t_k-\mathrm{i}\phi_k} & u_{32}e^{\mathrm{i}\omega_{32}t_k} & u_{33} & u_{34}e^{-\mathrm{i}\omega_{34}t_k+\mathrm{i}\phi_k} & u_{35}e^{-\mathrm{i}\omega_{35}t_k+\mathrm{i}\phi_k} \\ u_{41}e^{\mathrm{i}\omega_{14}t_k-\mathrm{i}2\phi_k} & u_{42}e^{\mathrm{i}\omega_{24}t_k-\mathrm{i}\phi_k} & u_{43}e^{\mathrm{i}\omega_{34}t_k-\mathrm{i}\phi_k} & u_{44} & u_{45}e^{-\mathrm{i}\omega_{45}t_k} \\ u_{51}e^{\mathrm{i}\omega_{15}t_k-\mathrm{i}2\phi_k} & u_{52}e^{\mathrm{i}\omega_{25}t_k-\mathrm{i}\phi_k} & u_{53}e^{\mathrm{i}\omega_{35}t_k-\mathrm{i}\phi_k} & u_{54}e^{\mathrm{i}\omega_{45}t_k} & u_{55} \end{pmatrix}$$

Appendix E

UV objective

The objective used in the setup is an extension of the one presented in [116]. Since no high resolution was aimed for, the optimal design was approximated by commericially available lenses for economic reasons.

The complete imaging setup comprises of two steps: First, the five-lens UV-objective images the ion onto an iris with a 150 μm diameter to minimize stray light. The iris is then imaged with a separate two-lens objective onto the CCD camera or the PMT. The complete optical setup is defined in the following listing of the optical surfaces (all values are given in units of mm):

No	Curvature	Distance	Focal Length	Thorlabs Item #
1	-135.3	7.8	150	LE 4125
2	-46.5	0.5	-	
3	-193.4	6.6	200	LE 4560
4	-63	0.5	-	
5	∞	5.4	300	LA 4855
6	-138	0.5	-	
7	67	12.5	75	LB 4553
8	-67	8.91	-	
9	-46	4	-100	LC 4743
10	∞	295.44	-	
11	-	77.6	-	Intermediate Picture
12	∞	10.6	100	LA 4545
13	-46	0.5	-	
14	46	10.6	100	LA 4545
15	∞	95.7	-	
16	-	0	-	Image

In Fig. E.1 an image of a precision test target[1] with the objective is shown. The analysis yields a conservative upper limit for the resolution of 4.4μm. This is sufficient for the experiment since all quantitative readout is done by integrating over the complete image using the photo-multiplier tube. The main reason for this rather low resolution is the replacement of the optimal lenses by ones which approximate the ideal surface curvatures and the fact that the lenses are tilted with respect to each other when being put into the objective mount.

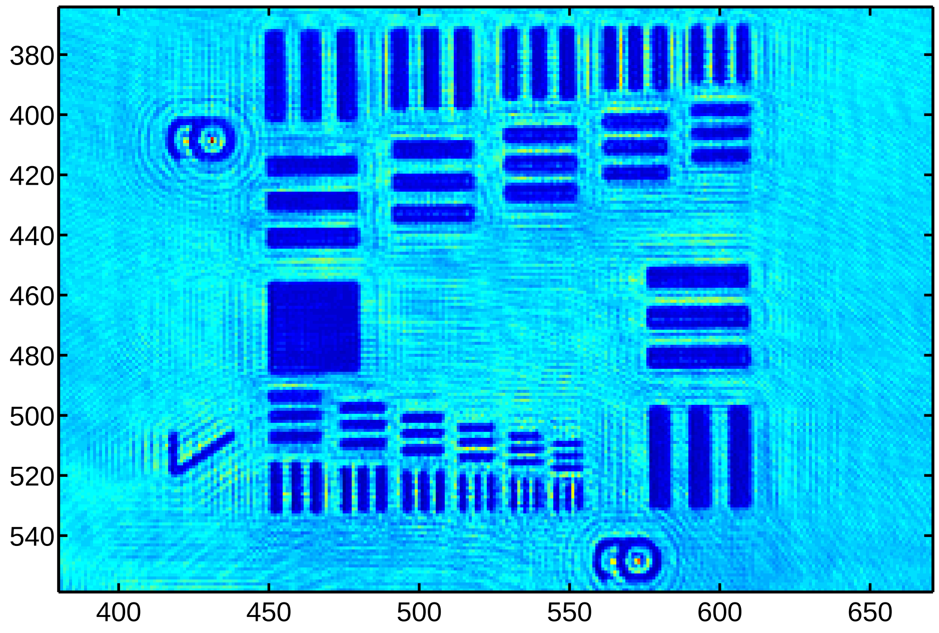

Figure E.1: A Thorlabs USAF 1951 test target is used to estimate the resolution of the objective. The contrast of ∼60% of the smallest line pair on the target yields an upper limit of 4.4μm.

---

[1] Thorlabs USAF 1951

Bibliography

[1] P. J. Mohr, B. N. Taylor, and D. B. Newell, *CODATA recommended values of the fundamental physical constants: 2006*, Rev. Mod. Phys. **80**, 633 (2008). Cited in Page(s) viii.

[2] S. G. Karshenboim, *Fundamental physical constants: looking from different angles*, Can. J. Phys. **83**, 767 (2005). Cited in Page(s) 1.

[3] P. A. M. Dirac, *The cosmological constants*, Nature **139**, 323 (1937). Cited in Page(s) 1.

[4] W. J. Marciano, *Time Variation of the Fundamental "Constants" and Kaluza-Klein Theories*, Phys. Rev. Lett. **52**, 489 (1984). Cited in Page(s) 1.

[5] A. A. Michelson and E. W. Morely, *On the Relative Motion of the Earth and the Luminiferous Ether*, Am. J. of Sci. **34**, 333 (1887). Cited in Page(s) 2.

[6] J.-P. Uzan, *The fundamental constants and their variation: observational and theoretical status*, Rev. Mod. Phys. **75**, 403 (2003). Cited in Page(s) 2.

[7] J.-P. Uzan, *Varying Constants, Gravitation and Cosmology*, Living Reviews in Relativity **14**, 2 (2011). Cited in Page(s) 2.

[8] V. A. Dzuba, V. V. Flambaum, and M. G. Kozlov, *Combination of the many-body perturbation theory with the configuration-interaction method*, Phys. Rev. A **54**, 3948 (1996). Cited in Page(s) 2.

[9] V. A. Dzuba, V. V. Flambaum, and J. K. Webb, *Space-Time Variation of Physical Constants and Relativistic Corrections in Atoms*, Phys. Rev. Lett. **82**, 888 (1999). Cited in Page(s) 2, 3, 117.

[10] V. A. Dzuba, V. V. Flambaum, and J. K. Webb, *Calculations of the relativistic effects in many-electron atoms and space-time variation of fundamental constants*, Phys. Rev. A **59**, 230 (1999). Cited in Page(s) 2, 3.

[11] J. K. Webb, M. T. Murphy, V. V. Flambaum, V. A. Dzuba, J. D. Barrow, C. W. Churchill, J. X. Prochaska, and A. M. Wolfe, *Further Evidence for Cosmological Evolution of the Fine Structure Constant*, Phys. Rev. Lett. **87**, 091301 (2001). Cited in Page(s) 2, 3.

[12] T. Rosenband, D. B. Hume, P. O. Schmidt, C. W. Chou, A. Brusch, L. Lorini, W. H. Oskay, R. E. Drullinger, T. M. Fortier, J. E. Stalnaker, S. A. Diddams, W. C. Swann, N. R. Newbury, W. M. Itano, D. J. Wineland, and J. C. Bergquist, *Frequency Ratio of Al*$^+$ *and Hg*$^+$ *Single-Ion Optical Clocks; Metrology at the 17th Decimal Place*, Science **319**, 1808 (2008). Cited in Page(s) 2.

[13] T. M. Fortier, N. Ashby, J. C. Bergquist, M. J. Delaney, S. A. Diddams, T. P. Heavner, L. Hollberg, W. M. Itano, S. R. Jefferts, K. Kim, F. Levi, L. Lorini, W. H. Oskay, T. E. Parker, J. Shirley, and J. E. Stalnaker, *Precision Atomic Spectroscopy for Improved Limits on Variation of the Fine Structure Constant and Local Position Invariance*, Phys. Rev. Lett. **98**, 070801 (2007). Cited in Page(s) 2.

[14] E. Peik, B. Lipphardt, H. Schnatz, T. Schneider, C. Tamm, and S. G. Karshenboim, *Limit on the Present Temporal Variation of the Fine Structure Constant*, Phys. Rev. Lett. **93**, 170801 (2004). Cited in Page(s) 2.

[15] E. Peik, B. Lipphardt, H. Schnatz, C. Tamm, S. Weyers, and R. Wynands, *Laboratory Limits on Temporal Variations of Fundamental Constants: An Update*, ArXiv **physics/0611088 [physics.atom-ph]** (2006). Cited in Page(s) 2.

[16] S. G. Porsev, V. V. Flambaum, and J. R. Torgerson, *Transition frequency shifts with fine-structure constant variation for Yb II*, Phys. Rev. A **80**, 042503 (2009). Cited in Page(s) 2.

[17] S. Bize, P. Laurent, M. Abgrall, H. Marion, I. Maksimovic, L. Cacciapuoti, J. Grnert, C. Vian, F. P. dos Santos, P. Rosenbusch, P. Lemonde, G. Santarelli, P. Wolf, A. Clairon, A. Luiten, M. Tobar, and C. Salomon, *Cold atom clocks and applications*, Journal of Physics B: Atomic, Molecular and Optical Physics **38**, S449 (2005). Cited in Page(s) 2.

[18] M. Fischer, N. Kolachevsky, M. Zimmermann, R. Holzwarth, T. Udem, T. W. Hänsch, M. Abgrall, J. Grünert, I. Maksimovic, S. Bize, H. Marion, F. P. D. Santos, P. Lemonde, G. Santarelli, P. Laurent, A. Clairon, C. Salomon, M. Haas, U. D. Jentschura, and C. H. Keitel, *New Limits on the Drift of Fundamental Constants from Laboratory Measurements*, Phys. Rev. Lett. **92**, 230802 (2004). Cited in Page(s) 2.

[19] S. Blatt, A. D. Ludlow, G. K. Campbell, J. W. Thomsen, T. Zelevinsky, M. M. Boyd, J. Ye, X. Baillard, M. Fouché, R. Le Targat, A. Brusch, P. Lemonde, M. Takamoto, F.-L. Hong, H. Katori, and V. V. Flambaum, *New Limits on Coupling of Fundamental Constants to Gravity Using* ^{87}Sr *Optical Lattice Clocks*, Phys. Rev. Lett. **100**, 140801 (2008). Cited in Page(s) 2.

[20] A. T. Nguyen, D. Budker, S. K. Lamoreaux, and J. R. Torgerson, *Towards a sensitive search for variation of the fine-structure constant using radio-frequency* $E1$ *transitions in atomic dysprosium*, Phys. Rev. A **69**, 022105 (2004). Cited in Page(s) 2.

[21] V. V. Flambaum, *Enhanced effect of temporal variation of the fine-structure constant in diatomic molecules*, Phys. Rev. A **73**, 034101 (2006). Cited in Page(s) 3.

[22] V. V. Flambaum and M. G. Kozlov, *Enhanced Sensitivity to the Time Variation of the Fine-Structure Constant and* m_p/m_e *in Diatomic Molecules*, Phys. Rev. Lett. **99**, 150801 (2007). Cited in Page(s) 3.

[23] T. Schneider, B. Roth, H. Duncker, I. Ernsting, and S. Schiller, *All-optical preparation of molecular ions in the rovibrational ground state*, Nature Physics **6**, 275 (2010). Cited in Page(s) 3, 120.

[24] J. C. Berengut, V. A. Dzuba, and V. V. Flambaum, *Enhanced Laboratory Sensitivity to Variation of the Fine-Structure Constant using Highly Charged Ions*, Phys. Rev. Lett. **105**, 120801 (2010). Cited in Page(s) 3.

[25] V. V. Flambaum, *Enhanced Effect of Temporal Variation of the Fine Structure Constant and the Strong Interaction in* ^{229}Th, Phys. Rev. Lett. **97**, 092502 (2006). Cited in Page(s) 3.

[26] A. Hayes and J. Friar, *Sensitivity of nuclear transition frequencies to temporal variation of the fine structure constant or the strong interaction*, Physics Letters B **650**, 229 (2007). Cited in Page(s) 3.

[27] J. C. Berengut, V. A. Dzuba, V. V. Flambaum, and S. G. Porsev, *Proposed Experimental Method to Determine* α *Sensitivity of Splitting between Ground and 7.6* eV *Isomeric States in* ^{229}Th, Phys. Rev. Lett. **102**, 210801 (2009). Cited in Page(s) 3.

[28] R. Srianand, H. Chand, P. Petitjean, and B. Aracil, *Limits on the Time Variation of the Electromagnetic Fine-Structure Constant in the Low Energy Limit from Absorption Lines in the Spectra of Distant Quasars*, Phys. Rev. Lett. **92**, 121302 (2004). Cited in Page(s) 3.

[29] M. Murphy, J. Webb, V. Flambaum, C. Churchill, and J. Prochaska, *Possible evidence for a variable fine-structure constant from QSO absorption lines: systematic errors*, Monthly Notices of the Royal Astronomical Society **327**, 1223 (2001). Cited in Page(s) 3.

[30] M. Murphy, J. Webb, V. Flambaum, and S. Curran, *Does the fine structure constant vary? A detailed investigation into systematic effects*, Astrophysics and Space Science **283**, 577 (2003). Cited in Page(s) 3.

[31] J. K. Webb, J. A. King, M. T. Murphy, V. V. Flambaum, R. F. Carswell, and M. B. Bainbridge, *Evidence for spatial variation of the fine structure constant*, ArXiv **1008.3907 [astro-ph.CO]** (2010). Cited in Page(s) 3.

[32] J. K. Webb, V. V. Flambaum, C. W. Churchill, M. J. Drinkwater, and J. D. Barrow, *Search for Time Variation of the Fine Structure Constant*, Phys. Rev. Lett. **82**, 884 (1999). Cited in Page(s) 3.

[33] M. T. Murphy, P. Tzanavaris, J. K. Webb, and C. Lovis, *Selection of ThAr lines for wavelength calibration of echelle spectra and implications for variations in the fine-structure constant*, Monthly Notices of the Royal Astronomical Society **378**, 221 (2007). Cited in Page(s) 3.

[34] M. T. Murphy, T. Udem, R. Holzwarth, A. Sizmann, L. Pasquini, C. Araujo-Hauck, H. Dekker, S. D'Odorico, M. Fischer, T. W. Hänsch, and A. Manescau, *High-precision wavelength calibration of astronomical spectrographs with laser frequency combs*, Monthly Notices of the Royal Astronomical Society **380**, 839 (2007). Cited in Page(s) 3.

[35] C.-H. Li, A. J. Benedick, P. Fendel, A. G. Glenday, F. X. Kaertner, D. F. Phillips, D. Sasselov, A. Szentgyorgyi, and R. L. Walsworth, *A laser frequency comb that enables radial velocity measurements with a precision of 1 cm* s^{-1}, Nature **452**, 610 (2008). Cited in Page(s) 3.

[36] J. C. Berengut, V. A. Dzuba, V. V. Flambaum, J. A. King, M. G. Kozlov, M. T. Murphy, and J. K. Webb, *Atomic transition frequencies, isotope shifts, and sensitivity to variation of the fine structure constant for studies of quasar absorption spectra*, ArXiv **1011.4136 [astro-ph.CO]** (2010). Cited in Page(s) 3, 4.

[37] J. Sullivan and A. Walsh, *High intensity hollow-cathode lamps*, Spectrochimica Acta **21**, 721 (1965). Cited in Page(s) 3.

[38] D. C. Morton, *Atomic data for resonance absorption lines. I - Wavelengths longward of the Lyman limit*, Astr. J. Supp. S. **77**, 119 (1991). Cited in Page(s) 3.

[39] D. C. Morton, *Atomic Data for Resonance Absorption Lines. II. Wavelengths Longward of the Lyman Limit for Heavy Elements*, Astr. J. Supp. S. **130**, 403 (2000). Cited in Page(s) 3.

[40] D. C. Morton, *Atomic Data for Resonance Absorption Lines. III. Wavelengths Longward of the Lyman Limit for the Elements Hydrogen to Gallium*, Astr. J. Supp. S. **149**, 205 (2003). Cited in Page(s) 3.

[41] M. Aldenius, *Laboratory wavelengths for cosmological constraints on varying fundamental constants*, Physica Scripta **2009**, 014008 (2009). Cited in Page(s) 3.

[42] M. G. Kozlov, V. A. Korol, J. C. Berengut, V. A. Dzuba, and V. V. Flambaum, *Space-time variation of the fine-structure constant and evolution of isotope abundances*, Phys. Rev. A **70**, 062108 (2004). Cited in Page(s) 3.

[43] T. Ashenfelter, G. J. Mathews, and K. A. Olive, *Chemical Evolution of Mg Isotopes versus the Time Variation of the Fine Structure Constant*, Phys. Rev. Lett. **92**, 041102 (2004). Cited in Page(s) 3.

[44] D. J. Larson, J. C. Bergquist, J. J. Bollinger, W. M. Itano, and D. J. Wineland, *Sympathetic cooling of trapped ions: A laser-cooled two-species nonneutral ion plasma*, Phys. Rev. Lett. **57**, 70 (1986). Cited in Page(s) 4.

[45] P. O. Schmidt, T. Rosenband, C. Langer, W. M. Itano, J. C. Bergquist, and D. J. Wineland, *Spectroscopy Using Quantum Logic*, Science **309**, 749 (2005). Cited in Page(s) 4, 43.

[46] S. T. Cundiff, J. Ye, and J. L. Hall, *Optical frequency synthesis based on mode-locked lasers*, Rev. Sci. Instrum. **72**, 3749 (2001). Cited in Page(s) 4.

[47] S. T. Cundiff and J. Ye, *Colloquium: Femtosecond optical frequency combs*, Rev. Mod. Phys. **75**, 325 (2003). Cited in Page(s) 4, 24.

[48] M. C. Stowe, M. J. Thorpe, A. Pe'er, J. Ye, J. E. Stalnaker, V. Gerginov, and S. A. Diddams, *Direct frequency comb spectroscopy*, Advances In Atomic, Molecular, and Optical Physics **55**, 1 (2008). Cited in Page(s) 5.

[49] A. Marian, M. C. Stowe, J. R. Lawall, D. Felinto, and J. Ye, *United Time-Frequency Spectroscopy for Dynamics and Global Structure*, Science **306**, 2063 (2004). Cited in Page(s) 5.

[50] A. Marian, M. C. Stowe, D. Felinto, and J. Ye, *Direct Frequency Comb Measurements of Absolute Optical Frequencies and Population Transfer Dynamics*, Phys. Rev. Lett. **95**, 023001 (2005). Cited in Page(s) 5.

[51] A. L. Wolf, S. A. van den Berg, W. Ubachs, and K. S. E. Eikema, *Direct Frequency Comb Spectroscopy of Trapped Ions*, Phys. Rev. Lett. **102**, 223901 (2009). Cited in Page(s) 5, 39.

[52] A. L. Wolf, S. v. Berg, C. Gohle, E. J. Salumbides, W. Ubachs, and K. S. E. Eikema, *Frequency comb spectroscopy on calcium ions in a linear Paul trap*, Springer Series in Chemical Physics **92**, 852 (2009). Cited in Page(s) 5.

[53] A. L. Wolf, J. Morgenweg, J. C. J. Koelemeij, S. A. van den Berg, W. Ubachs, and K. S. E. Eikema, *Direct frequency-comb spectroscopy of a dipole-forbidden clock transition in trapped* $^{40}Ca^{+}$ *ions*, Opt. Lett. **36**, 49 (2011). Cited in Page(s) 5, 39.

[54] W. Paul, *Electromagnetic Traps for Charged and Neutral Particles*, Review of Modern Physics **62**, 531 (1990). Cited in Page(s) 5, 7, 8.

[55] R. Gerritsma, G. Kirchmair, F. Zähringer, J. Benhelm, R. Blatt, and C. F. Roos, *Precision measurement of the branching fractions of the* $4p\,^2P_{3/2}$ *decay of Ca II*, Eur. Phys. J. D **50**, 13 (2008). Cited in Page(s) 5, 39.

[56] M. Chwalla, J. Benhelm, K. Kim, G. Kirchmair, T. Monz, M. Riebe, P. Schindler, A. S. Villar, W. Hänsel, C. F. Roos, R. Blatt, M. Abgrall, G. Santarelli, G. D. Rovera, and P. Laurent, *Absolute Frequency Measurement of the* $^{40}Ca^{+}$ $4s\,^2S_{1/2} - 3d\,^2D_{5/2}$ *Clock Transition*, Phys. Rev. Lett. **102**, 023002 (2009). Cited in Page(s) 5, 39.

[57] A. L. Wolf, S. A. van den Berg, C. Gohle, E. J. Salumbides, W. Ubachs, and K. S. E. Eikema, *Frequency metrology on the* $4s^2S_{1/2}$-$4p^2P_{1/2}$ *transition in* $^{40}Ca^{+}$ *for a comparison with quasar data*, Phys. Rev. A **78**, 032511 (2008). Cited in Page(s) 5, 39.

[58] A. Friedenauer, F. Markert, H. Schmitz, L. Petersen, S. Kahra, M. Herrmann, T. Udem, T. Hänsch, and T. Schätz, *High power all solid state laser system near 280nm*, Applied Physics B: Lasers and Optics **84**, 371 (2006). Cited in Page(s) 5, 55, 59, 118.

[59] C. R. Clark, J. E. Goeders, Y. K. Dodia, C. R. Viteri, and K. R. Brown, *Detection of single-ion spectra by Coulomb-crystal heating*, Phys. Rev. A **81**, 043428 (2010). Cited in Page(s) 6, 47, 118.

[60] H. Häffner, C. Roos, and R. Blatt, *Quantum computing with trapped ions*, Physics Reports **469**, 155 (2008). Cited in Page(s) 7.

[61] R. Blatt and D. Wineland, *Entangled states of trapped atomic ions*, Nature **453**, 1008 (2008). Cited in Page(s) 7.

[62] P. K. Gosh, *Ion Traps* (Clarendon Press, 1995). Cited in Page(s) 7, 8.

[63] F. G. Major, V. N. Gheorghe, and G. Werth, *Charged Particle Traps Physics and Techniques of Charged Particle Field Confinement* (Springer Series on Atomic Optical and Plasma Physics, Germany, 2004). Cited in Page(s) 7, 8, 10, 15, 100, 112.

[64] D. Leibfried, R. Blatt, C. Monroe, and D. Wineland, *Quantum dynamics of single trapped ions*, Rev. Mod. Phys. **75**, 281 (2003). Cited in Page(s) 8, 15, 104.

[65] D. J. Wineland, C. Monroe, W. M. Itano, D. Leibfried, B. E. King, and D. M. Meekhof, *Experimental issues in coherent quantum-state manipulation of trapped atomic ions*, J. Res. Natl. Inst. Stand. Tech. **103**, 259 (1998). Cited in Page(s) 8, 15, 17, 97, 115, 118.

[66] R. J. Cook, D. G. Shankland, and A. L. Wells, *Quantum theory of particle motion in a rapidly oscillating field*, Phys. Rev. A **31**, 564 (1985). Cited in Page(s) 9.

[67] D. J. Berkeland, J. D. Miller, J. C. Bergquist, W. M. Itano, and D. J. Wineland, *Minimization of ion micromotion in a Paul trap*, Journal of Applied Physics **83**, 5025 (1998). Cited in Page(s) 11, 76, 77, 78, 79.

[68] J. I. Cirac, L. J. Garay, R. Blatt, A. S. Parkins, and P. Zoller, *Laser cooling of trapped ions: The influence of micromotion*, Physical Review A **49**, 421 (1994). Cited in Page(s) 11, 76, 106.

[69] E. Peik, J. Abel, T. Becker, J. von Zanthier, and H. Walther, *Sideband cooling of ions in radio-frequency traps*, Phys. Rev. A **60**, 439 (1999). Cited in Page(s) 11, 76.

[70] C. Roos, *Controlling the Quantum State of Trapped Ions*, Ph.D. thesis, Universität Innsbruck, Austria, (2000). Cited in Page(s) 12, 80, 81, 84, 104, 106.

[71] J. Benhelm, *Precision Spectroscopy and Quantum Information Processing with Trapped Calcium Ions*, Ph.D. thesis, Universität Innsbruck, Austria, (2008). Cited in Page(s) 12, 115.

[72] M. Herrmann, V. Batteiger, S. Knünz, G. Saathoff, T. Udem, and T. W. Hänsch, *Frequency Metrology on Single Trapped Ions in the Weak Binding Limit: The* $3s_{1/2} - 3p_{3/2}$ *Transition in* $^{24}Mg^{+}$, Phys. Rev. Lett. **102**, 013006 (2009). Cited in Page(s) 12.

[73] V. Batteiger, S. Knünz, M. Herrmann, G. Saathoff, H. A. Schüssler, B. Bernhardt, T. Wilken, R. Holzwarth, T. W. Hänsch, and T. Udem, *Precision spectroscopy of the* $3s-3p$ *fine-structure doublet in* Mg^{+}, Phys. Rev. A **80**, 022503 (2009). Cited in Page(s) 12.

[74] C. Schwartz, *Theory of Hyperfine Structure*, Phys. Rev. **97**, 380 (1955). Cited in Page(s) 12.

[75] I. I. Sobelman, *Atomic Spectra and Radiative Transitions* (Springer-Verlag, 1996). Cited in Page(s) 12.

[76] W. M. Itano and D. J. Wineland, *Precision measurement of the ground-state hyperfine constant of* $^{25}Mg^{+}$, Phys. Rev. A **24**, 1364 (1981). Cited in Page(s) 13.

[77] C. Sur, B. K. Sahoo, R. K. Chaudhuri, B. P. Das, and D. Mukherjee, *Comparative studies of the magnetic dipole and electric quadrupole hyperfine constants for the ground and low lying excited states of* $^{25}Mg^{+}$, European Physical Journal D **32**, 25 (2005). Cited in Page(s) 13.

[78] L. D. Landau and E. M. Lifshitz, *Quantum Mechanics. Nonrelativistic theory* (Akademie Verlag, 1974). Cited in Page(s) 13, 20.

[79] T. Beier, *The* g_j *factor of a bound electron and the hyperfine structure splitting in hydrogenlike ions*, Physics Reports **339**, 79 (2000). Cited in Page(s) 14.

[80] R. H. Garstang, *Radiative Hyperfine Transitions*, The Astrophysical Journal **447**, 962 (1995). Cited in Page(s) 14.

[81] J. I. Cirac and P. Zoller, *Quantum Computations with Cold Trapped Ions*, Phys. Rev. Lett. **74**, 4091 (1995). Cited in Page(s) 15.

[82] D. J. Wineland, M. Barrett, J. Britton, and et al., *Quantum information processing with trapped ions*, Royal Society of London Philosophical Transactions Series A **361**, 1349 (2003). Cited in Page(s) 19, 22.

[83] C. J. Foot, *Atomic Physics* (Oxford University Press, 2005). Cited in Page(s) 19, 21.

[84] C. Cohen-Tannoudji, B. Diu, and F. Laloe, *Quantum Mechanics* (Wiley-Interscience, 2006). Cited in Page(s) 19.

[85] D. A. Steck, *Rubidium 87 D line data* (http://steck.us/alkalidata, 2002). Cited in Page(s) 20.

[86] C. Ospelkaus, U. Warring, Y. Colombe, K. R. Brown, J. M. Amini, D. Leibfried, and D. J. Wineland, *Microwave quantum logic gates for trapped ions*, ArXiv **1104.3573 [quant-ph]** (2011). Cited in Page(s) 22, 91.

[87] N. V. Vitanov and P. L. Knight, *Coherent excitation of a two-state system by a train of short pulses*, Phys. Rev. A **52**, 2245 (1995). Cited in Page(s) 26.

[88] D. Felinto, C. A. C. Bosco, L. H. Acioli, and S. S. Vianna, *Coherent accumulation in two-level atoms excited by a train of ultrashort pulses*, Optics Communications **215**, 69 (2003). Cited in Page(s) 27.

[89] D. Felinto, L. H. Acioli, and S. S. Vianna, *Accumulative effects in the coherence of three-level atoms excited by femtosecond-laser frequency combs*, Phys. Rev. A **70**, 043403 (2004). Cited in Page(s) 27.

[90] D. Felinto and C. E. E. López, *Theory for direct frequency-comb spectroscopy*, Phys. Rev. A **80**, 013419 (2009). Cited in Page(s) 27.

[91] A. Marian, *Direct Frequency Comb Spectroscopy for Optical Frequency Metrology and Coherent Interactions*, Ph.D. thesis, University of Colorado, USA, (2005). Cited in Page(s) 27, 33.

[92] R. Loudon, *The Quantum Theory of Light* (Oxford University Press, 1973). Cited in Page(s) 30, 83.

[93] V. Roudnev and B. D. Esry, *General Theory of Carrier-Envelope Phase Effects*, Phys. Rev. Lett. **99**, 220406 (2007). Cited in Page(s) 33.

[94] MATLAB, *version 7.8.0 (R2009a)* (The MathWorks Inc., 2009). Cited in Page(s) 33, 35.

[95] Maxima, *version 5.21.1* (http://maxima.sourceforge.net/, 2010). Cited in Page(s) 35, 105.

[96] Y. Ralchenko, A. Kramida, J. Reader, and N. A. Team, *NIST Atomic Spectra Database (version 4.0), [Online]. Available: http://physics.nist.gov/asd3 [Tuesday, 08-Mar-2011 14:01:17 EST]*, National Institute of Standards and Technology, Gaithersburg, MD (2008). Cited in Page(s) 38, 39.

[97] R. Yamazaki, H. Sawamura, K. Toyoda, and S. Urabe, *Stimulated Raman spectroscopy and the determination of the D-fine-structure level separation in* $^{40}Ca^+$, Phys. Rev. A **77**, 012508 (2008). Cited in Page(s) 39.

[98] H. Wang and A. M. Weiner, *Efficiency of short-pulse type-I second-harmonic generation with simultaneous spatial walk-off, temporal walk-off, and pump depletion*, IEEE Journal of Quantum Electronics **39**, 1600 (2003). Cited in Page(s) 42.

[99] M. C. Stowe, *Direct Frequency Comb Spectroscopy and High-Resolution Coherent Control*, Ph.D. thesis, University of Colorado, USA, (2008). Cited in Page(s) 49.

[100] N. Kjaergaard, L. Hornekaer, A. Thommesen, Z. Videsen, and M. Drewsen, *Isotope selective loading of an ion trap using resonance-enhanced two-photon ionization*, Applied Physics B: Lasers and Optics **71**, 207 (2000). Cited in Page(s) 54.

[101] R. W. P. Drever, J. L. Hall, F. V. Kowalski, J. Hough, G. M. Ford, A. J. Munley, and H. Ward, *Laser phase and frequency stabilization using an optical resonator*, Applied Physics B: Lasers and Optics **31**, 97 (1983). Cited in Page(s) 55.

[102] D. Nigg, *Aufbau eines Frequenz-vervierfachten Diodenlasers für die Photoionisation von Magnesium*, Diploma thesis, Universität Innsbruck, Austria, (2009). Cited in Page(s) 55, 56, 69, 75.

[103] T. Hänsch and B. Couillaud, *Laser frequency stabilization by polarization spectroscopy of a reflecting reference cavity*, Optics Communications **35**, 441 (1980). Cited in Page(s) 56.

[104] L. An der Lan, *Aufbau eines frequenzvervierfachten Lasersystems zum Coulomb-Kühlen von Magnesium-Ionen*, Diploma thesis, Universität Innsbruck, Austria, (2008). Cited in Page(s) 56.

[105] W. Demtröder, *Laser spectroscopy: Basic concepts and instrumentation* (Springer-Verlag, 1981). Cited in Page(s) 57.

[106] P. J. Lee, B. B. Blinov, K. Brickman, L. Deslauriers, M. J. Madsen, R. Miller, D. L. Moehring, D. Stick, and C. Monroe, *Atomic qubit manipulations with an electro-optic modulator*, Opt. Lett. **28**, 1582 (2003). Cited in Page(s) 58.

[107] B. E. A. S. Saleh and M. C. Teich, *Fundamentals of Photonics* (Wiley Series in Pure and Applied Optics, 1991). Cited in Page(s) 58.

[108] R. P. Smith, P. A. Roos, J. K. Wahlstrand, J. A. Pipis, M. B. Rivas, and S. T. Cundiff, *Optical Frequency Metrology of an Iodine-Stabilized He-Ne Laser Using the Frequency Comb of a Quantum-Interference-Stabilized Mode-Locked Laser*, J. Res. Natl. Inst. Stand. Technol. **112**, 289 (2007). Cited in Page(s) 60.

[109] W. R. C. Rowley and A. J. Wallard, *Wavelength values of the 633 nm laser, stabilized with 127 I 2 saturated absorption*, Journal of Physics E: Scientific Instruments **6**, 647 (1973). Cited in Page(s) 60.

[110] P. Cerez, A. Brillet, and F. Hartmann, *Metrological Properties of the R(127) Line of Iodine Studied by Laser Saturated Absorption*, Instrumentation and Measurement, IEEE Transactions on **23**, 526 (1974). Cited in Page(s) 60.

[111] C.-H. Chang, R. K. Heilmann, M. L. Schattenburg, and P. Glenn, *Design of a double-pass shear mode acousto-optic modulator*, Review of Scientific Instruments **79**, 033104 (2008). Cited in Page(s) 62.

[112] E. A. Donley, T. P. Heavner, F. Levi, M. O. Tataw, and S. R. Jefferts, *Design of a double-pass shear mode acousto-optic modulator*, Review of Scientific Instruments **79**, 033104 (2008). Cited in Page(s) 62.

[113] R. A. Negres, M. A. Norton, D. A. Cross, and C. W. Carr, *Growth behavior of laser-induced damage on fused silica optics under UV, ns laser irradiation*, Opt. Express **18**, 19966 (2010). Cited in Page(s) 62.

[114] R. C. Weast, *Handbook of Chemistry and Physics* (Chemical Rubber, Cleveland, 1974). Cited in Page(s) 68.

[115] W. Macalpine and R. Schildknecht, *Coaxial Resonators with Helical Inner Conductor*, Proceedings of the IRE **47**, 2099 (1959). Cited in Page(s) 68.

[116] W. Alt, *An objective lens for efficient fluorescence detection of single atoms*, Optik-International Journal for Light and Electron Optics **113**, 142 (2002). Cited in Page(s) 70, 137.

[117] Zemax, (http://www.zemax.com/). Cited in Page(s) 70.

[118] F. Gérôme, R. Jamier, J.-L. Auguste, G. Humbert, and J.-M. Blondy, *Simplified hollow-core photonic crystal fiber*, Opt. Lett. **35**, 1157 (2010). Cited in Page(s) 72.

[119] P. Pham, A general-purpose pulse sequencer for quantum computing, Master's thesis, Massachusetts Institute of Technology, USA, (2005). Cited in Page(s) 73.

[120] Sourceforge project: Pulse programmer, http://sourceforge.net/projects/pulse-sequencer/. Cited in Page(s) 73.

[121] P. Schindler, *Frequency synthesis and pulse shaping for quantum information processing with trapped ions*, Diploma thesis, Universität Innsbruck, Austria, (2008). Cited in Page(s) 73.

[122] R. G. DeVoe, J. Hoffnagle, and R. G. Brewer, *Role of laser damping in trapped ion crystals*, Phys. Rev. A **39**, 4362 (1989). Cited in Page(s) 78.

[123] M. Chwalla, *Precision spectroscopy with* $^{40}Ca^{+}$ *ions in a Paul trap*, Ph.D. thesis, Universität Innsbruck, Austria, (2009). Cited in Page(s) 79.

[124] H. Dehmelt, *Proposed* 10^{14} $\Delta\nu < \nu$ *Laser Fluorescence Spectroscopy on Tl+ Mono-Ion Oscillator II (spontaneous quantum jumps)*, Bull. Am. Phys. Soc. **20**, 60 (1975). Cited in Page(s) 81.

[125] M. Acton, K. . Brickman, P. C. Haljan, P. J. Lee, L. Deslauriers, and C. Monroe, *Near-Perfect Simultaneous Measurement of a Qubit Register*, ArXiv **quant-ph/0511257** (2005). Cited in Page(s) 81.

[126] C. E. Langer, *High Fidelity Quantum Information Processing with Trapped Ions*, Ph.D. thesis, University of Colorado, USA, (2000). Cited in Page(s) 81, 86, 113.

[127] B. E. King, *Quantum state engineering and information processing*, Ph.D. thesis, University of Colorado, USA, (1999). Cited in Page(s) 81.

[128] A. Keselman, Y. Glickman, N. Akerman, S. Kotler, and R. Ozeri, *High-fidelity state detection and tomography of a single ion Zeeman qubit*, ArXiv **1103.5253 [quant-ph]** (2011). Cited in Page(s) 81.

[129] A. H. Myerson, D. J. Szwer, S. C. Webster, D. T. C. Allcock, M. J. Curtis, G. Imreh, J. A. Sherman, D. N. Stacey, A. M. Steane, and D. M. Lucas, *High-Fidelity Readout of Trapped-Ion Qubits*, Phys. Rev. Lett. **100**, 200502 (2008). Cited in Page(s) 82, 119.

[130] A. H. Burrell, D. J. Szwer, S. C. Webster, and D. M. Lucas, *Scalable simultaneous multiqubit readout with* 99.99% *single-shot fidelity*, Phys. Rev. A **81**, 040302 (2010). Cited in Page(s) 82, 119.

[131] T. Schaetz, M. D. Barrett, D. Leibfried, J. Britton, J. Chiaverini, W. M. Itano, J. D. Jost, E. Knill, C. Langer, and D. J. Wineland, *Enhanced Quantum State Detection Efficiency through Quantum Information Processing*, Phys. Rev. Lett. **94**, 010501 (2005). Cited in Page(s) 84.

[132] N. F. Ramsey, *A New Molecular Beam Resonance Method*, Phys. Rev. **76**, 996 (1949). Cited in Page(s) 96.

[133] N. F. Ramsey, *A Molecular Beam Resonance Method with Separated Oscillating Fields*, Phys. Rev. **78**, 695 (1950). Cited in Page(s) 96.

[134] E. L. Hahn, *Spin Echoes*, Phys. Rev. **80**, 580 (1950). Cited in Page(s) 97.

[135] F. Schmidt-Kaler, S. Gulde, M. Riebe, T. Deuschle, A. Kreuter, G. Lancaster, C. Becher, J. Eschner, H. Häffner, and R. Blatt, *The coherence of qubits based on single Ca^+ ions*, Journal of Physics B: Atomic, Molecular and Optical Physics **36**, 623 (2003). Cited in Page(s) 98.

[136] B. Hemmerling, F. Gebert, Y. Wan, D. Nigg, I. Sherstov, and P. Schmidt, *A single laser system for ground-state cooling of $^{25}Mg^+$*, Applied Physics B: Lasers and Optics, DOI: 10.1007/s00340-011-4444-0 (2011). Cited in Page(s) 99.

[137] W. M. Itano and D. J. Wineland, *Laser cooling of ions stored in harmonic and Penning traps*, Physical Review A **25**, 35 (1982). Cited in Page(s) 99, 100.

[138] C. Monroe, D. M. Meekhof, B. E. King, S. R. Jefferts, W. M. Itano, D. J. Wineland, and P. Gould, *Resolved-Sideband Raman Cooling of a Bound Atom to the 3D Zero-Point Energy*, Phys. Rev. Lett. **75**, 4011 (1995). Cited in Page(s) 99, 102.

[139] J. Javanainen and S. Stenholm, *Laser cooling of trapped particles. I - The heavy particle limit*, Applied Physics **21**, 283 (1980). Cited in Page(s) 100.

[140] J. Javanainen and S. Stenholm, *Laser cooling of trapped particles. II - The fast particle limit*, Applied Physics **24**, 71 (1981). Cited in Page(s) 100.

[141] J. Javanainen and S. Stenholm, *Laser cooling of trapped particles. III - The Lamb-Dicke limit*, Applied Physics **24**, 151 (1981). Cited in Page(s) 100.

[142] S. Stenholm, *The semiclassical theory of laser cooling*, Rev. Mod. Phys. **58**, 699 (1986). Cited in Page(s) 102, 108.

[143] G. Morigi, J. I. Cirac, M. Lewenstein, and P. Zoller, *Ground-state laser cooling beyond the Lamb-Dicke limit*, Europhysics Letters **39**, 13 (1997). Cited in Page(s) 103.

[144] L. Santos and M. Lewenstein, *Dynamical cooling of trapped gases: One-atom problem*, Phys. Rev. A **59**, 613 (1999). Cited in Page(s) 103.

[145] Q. A. Turchette, D. Kielpinski, B. E. King, D. Leibfried, D. M. Meekhof, C. J. Myatt, M. A. Rowe, C. A. Sackett, C. S. Wood, W. M. Itano, C. Monroe, and D. J. Wineland, *Heating of trapped ions from the quantum ground state*, Phys. Rev. A **61**, 063418 (2000). Cited in Page(s) 112, 115.

[146] R. J. Epstein, S. Seidelin, D. Leibfried, J. H. Wesenberg, J. J. Bollinger, J. M. Amini, R. B. Blakestad, J. Britton, J. P. Home, W. M. Itano, J. D. Jost, E. Knill, C. Langer, R. Ozeri, N. Shiga, and D. J. Wineland, *Simplified motional heating rate measurements of trapped ions*, Phys. Rev. A **76**, 033411 (2007). Cited in Page(s) 112, 118.

[147] R. Ozeri, C. Langer, J. D. Jost, B. DeMarco, A. Ben-Kish, B. R. Blakestad, J. Britton, J. Chiaverini, W. M. Itano, D. B. Hume, D. Leibfried, T. Rosenband, P. O. Schmidt, and D. J. Wineland, *Hyperfine Coherence in the Presence of Spontaneous Photon Scattering*, Phys. Rev. Lett. **95**, 030403 (2005). Cited in Page(s) 113.

[148] H. Uys, M. J. Biercuk, A. P. VanDevender, C. Ospelkaus, D. Meiser, R. Ozeri, and J. J. Bollinger, *Decoherence due to Elastic Rayleigh Scattering*, Phys. Rev. Lett. **105**, 200401 (2010). Cited in Page(s) 113.

[149] D. Wineland, C. Monroe, W. Itano, B. King, D. Leibfried, D. Meekhof, C. Myatt, and C. Wood, *Experimental Primer on the Trapped Ion Quantum Computer*, Fortschr. Phys. **46**, 363 (1998). Cited in Page(s) 115.

[150] M. P. Ruffoni and J. C. Pickering, *Accurate Laboratory Wavelengths of the 1910 Ti II Resonance Transitions Relevant to Studies of Possible Variations of the Fine-structure Constant*, The Astrophysical Journal **725**, 424 (2010). Cited in Page(s) 119.

[151] L. Gianfrani, O. Monda, A. Sasso, M. Schisano, G. Tino, and M. Inguscio, *Visible and ultraviolet high resolution spectroscopy of Ti I and Ti II*, Optics Communications **83**, 300 (1991). Cited in Page(s) 119.

[152] J. C. Berengut, V. V. Flambaum, and M. G. Kozlov, *Isotope shift calculations in Ti II*, Journal of Physics B: Atomic, Molecular and Optical Physics **41**, 235702 (2008). Cited in Page(s) 119.

[153] Z. Nouri, S. D. Rosner, R. Li, T. J. Scholl, and R. A. Holt, *Measurements of isotope shifts and hyperfine structure in Ti II*, Physica Scripta **81**, 065301 (2010). Cited in Page(s) 119.

[154] M. Aldenius and S. Johansson, *Accurate Ritz wavelengths of parity-forbidden [FeII], [TiII], and [CrII] infrared lines of astrophysical interest*, A&A **467**, 753 (2007). Cited in Page(s) 119.

[155] N. C. Deb, A. Hibbert, Z. Felfli, and A. Z. Msezane, *[Ti II] lines observed in η Carinae Sr-filament and lifetimes of the metastable states of Ti$^+$*, Journal of

Physics B: Atomic, Molecular and Optical Physics **42**, 015701 (2009). Cited in Page(s) 119.

[156] G. Nave, R. C. M. Learner, A. P. Thorne, and C. J. Harris, *Precision Fe I and Fe II wavelengths in the ultraviolet spectrum of the iron–neon hollow-cathode lamp*, J. Opt. Soc. Am. B **8**, 2028 (1991). Cited in Page(s) 119.

[157] M. Aldenius, S. Johansson, and M. T. Murphy, *Accurate laboratory ultraviolet wavelengths for quasar absorption-line constraints on varying fundamental constants*, Monthly Notices of the Royal Astronomical Society **370**, 444 (2006). Cited in Page(s) 119.

[158] M. Ascoli, E. E. Eyler, D. Kawall, and D. DeMille, *High-resolution saturation spectroscopy of singly-ionized iron with a pulsed UV laser*, Measurement Science and Technology **19**, 045602 (2008). Cited in Page(s) 119.

[159] S. G. Porsev, K. V. Koshelev, I. I. Tupitsyn, M. G. Kozlov, D. Reimers, and S. A. Levshakov, *Transition frequency shifts with fine-structure constant variation for Fe II: Breit and core-valence correlation corrections*, Phys. Rev. A **76**, 052507 (2007). Cited in Page(s) 119.

[160] S. G. Porsev, M. G. Kozlov, and D. Reimers, *Transition frequency shifts with fine-structure constant variation for Fe I and isotope-shift calculations in Fe I and Fe II*, Phys. Rev. A **79**, 032519 (2009). Cited in Page(s) 119.

[161] P. F. Staanum, K. Hjbjerre, P. S. Skyt, A. K. Hansen, and M. Drewsen, *Rotational laser cooling of vibrationally and translationally cold molecular ions*, Nature Physics **6**, 271 (2010). Cited in Page(s) 120.

[162] V. V. Flambaum and M. G. Kozlov, *Studying variation of fundamental constants with molecules*, ArXiv **0711.4536 [physics.atom-ph]** (2007). Cited in Page(s) 120.

[163] V. V. Flambaum and V. A. Dzuba, *Search for variation of the fundamental constants in atomic, molecular and nuclear spectra*, Canadian Journal of Physics **87**, 25 (2009). Cited in Page(s) 120.

[164] A. R. Edmonds, *Angular Momentum in Quantum Mechanics* (Princeton University Press, 1957). Cited in Page(s) 122.

[165] B. King, *Angular Momentum Coupling and Rabi Frequencies for Simple Atomic Transitions*, ArXiv **0804.4528 [atom-ph]** (2008). Cited in Page(s) 122.

[166] P. M. Farrell and W. R. MacGillivray, *On the consistency of Rabi frequency calculations*, Journal of Physics A: Mathematical and General **28**, 209 (1995). Cited in Page(s) 122.

[167] P. S. Riseborough, *Advanced Quantum Mechanics*, Lecture Script (2010). Cited in Page(s) 128.

Acknowledgements

This thesis wouldn't have been possible without the support of many people, to whom I owe my deepest gratitude. At this point, I would like to thank these people.

Firstly, I sincerely offer my gratitude to my supervisor Prof. Piet Schmidt, who supported me throughout this thesis. Seldomly have I met someone with such passion for physics. I cannot express how indebted I am for his investing time in discussing ideas and in helping to search for solutions. His knowledge and guidance made him the perfect mentor one could wish for, while letting me develop my own ideas at the same time. Thank you for the most enjoyable and instructive time!

I would also like to sincerely acknowledge Prof. Rainer Blatt, who gave me the great opportunity to start my Ph.D. thesis in his group and in this fascinating field of physics. I could benefit from his experience and knowledge in the field in countless ways. The building of our laboratory wouldn't have been possible without his support, especially when we moved to the PTB in Braunschweig.

I would like to thank Prof. Christian Ospelkaus und Prof. Manfred Lein for agreeing to co-referee this work.

I thank Prof. Steven Cundiff for interesting and helpful discussions on our frequency comb setup.

Many thanks go to my former colleagues from the Innsbruck Difcos team, namely Lukas An der Lan, Birgit Brandstätter and especially Daniel Nigg, who helped me to move the Difcos lab. Another special thanks goes to Max Harlander, who has been a very good friend and one of the funniest colleagues I ever had, always providing a joyful atmosphere in the lab. I would also like to acknowledge him as a co-founder of the 'Weißwurst-Kochgruppe'! Furthermore, I would like to thank Philipp Schindler for his help with Paul's Box and Michael Chwalla for introducing me to the intricate world of frequency combs.

I thank my co-workers Florian Gebert and Yong Wan, who will both take over the experiment after me. I had a very enjoyable time sharing a lab with you and I believe the setup is more than in good hands with you. I wish you the best results in the future.

I would also like to thank the members of the Iqloc team: Olaf Mandel, for many helpful discussions related to our project and also for a lot of help and insight in the world of Linux. Long live the Penguin! Sana Amairi and Jannes Wuebbena, for being very nice office companions and for providing the lasers for calcium.

I would like to thank the team of Tanja Mehlstäubler with Karsten Pyka, Jonas Keller and Norbert Herschbach for all the interesting discussions and the nice evenings with 'grandma's crusty potato pancakes' we had.

Setting up this experiment wouldn't have been possible without the help of the electronic and the machine workshops. I thank Stefan Haslwanter, Andreas Strasser, Anton Schönherr and Helmut Jordan for building the ion trap and many other things needed in the setup. Very special thanks go to Peter-Christian Carstens. You fixed so many small and large problems we had in the experiment and I have learned so much about electronics from you, that I can only express my deepest gratitude. I hope future group members will benefit from your knowledge as much as I did. At the same time, I would like to thank Christopher Bleuel and Sven Klitzing. I hope Sven and Karsten will maintain the coffee premium user culture in the future and be a guide for others who think they know anything about coffee.

No experiment is possible without a tremendous administrative support. At this point, I would like to thank Patricia Moser, Karin Köhle, Sandra Ludwig and Wolfgang Jahns for all their help.

Timo Ottenstein, Christian and Helena Braun, who are the best friends one could wish for. I thank you for all your support, help, understanding and, especially, fun in the last years.

Com grande alegria, à Clarice, minha querida mulher, eu especialmente agradeço. Sempre me apoiado, você tem, durante esta tese, em bons e complicados momentos. Nenhuma palavra, e especialmente não estas poucas aqui escritas, pode explicar quanta felicidade à minha vida você trouxe. Não somente pelas suas virtudes, minha alma gêmea em você encontrei. De mim, desistiu, você nunca, mesmo que em lugares distantes tenhamos vivido. Mas agora uma toalha eu pego, e caminhando para você, eu irei, meu amor.

Vera e Domingos, muito obrigado pela calorosa acolhida em sua família. Vocês agora são parte integral da minha vida e é impossível imaginá-la sem vocês. E é claro, um muito obrigado especial para o Avô e a Avó, por todos os papinhos que batemos e pela netinha que ajudaram a criar, com quem eu me honro de estar casado.

Finally, I would like to thank my parents and the rest of my family for their support in a number of ways. I wouldn't have achieved all these things without your help.

Curriculum Vitae

Börge Hemmerling

Personal Information	Born 15.04.1981 German citizen
Contact Information	QUEST Institute of Experimental Quantum Metrology Physikalisch-Technische Bundesanstalt Bundesallee 100 D-38116 Braunschweig, Germany email: boerge.hemmerling@quantummetrology.de web: www.quantummetrology.de

---

Education

03/2009-07/2011 **Physikalisch-Technische Bundesanstalt & Leibniz University of Hannover**, Germany

Graduate student in the group of Prof. Piet O. Schmidt at the QUEST Institute for Experimental Quantum Metrology
Ph.D. thesis defense on July 1st, 2011

08/2006-03/2009 **University of Innsbruck**, Austria

Graduate student in the group of Prof. Rainer Blatt in the scope of the START award of Prof. Piet O. Schmidt at the Institute for Experimental Physics
Thesis topic: *Towards Direct Frequency Comb Spectroscopy Using Quantum Logic*

08/2000-03/2006 **University of Heidelberg**, Germany

Diploma student in the group of Prof. Markus K. Oberthaler at the Kirchhoff Institute of Physics
Diploma thesis title: *Thermally Induced Fluctuations in a Bosonic Josephson Junction*

06/2000 **Max-Planck Gymnasium Saarlouis**, Germany

Abitur

Publications

[1] Börge Hemmerling, Florian Gebert, Yong Wan, Daniel Nigg, Ivan V. Sherstov and Piet O. Schmidt, *A Single Laser System for Ground State Cooling of* $^{25}Mg^{+}$, Applied Physics B (*accepted*), doi: 10.1007/s00340-011-4444-0 (2010)

[2] Piet O. Schmidt, Börge Hemmerling, Birgit Brandstätter, Lukas An der Lan and Daniel Nigg, *Quantum Logic for Precision Spectroscopy*, PTB-Mitteilungen (Special Issue) **119**, 54-59 (2009)

[3] Rudolf Gati, Börge Hemmerling, Jonas Fölling, Michael Albiez and Markus K. Oberthaler, *Noise Thermometry with Two Weakly Coupled Bose-Einstein Condensates*, Physical Review Letters **96**, 130404 (2006)

[4] Rudolf Gati, Jerome Esteve, Börge Hemmerling, Timo B. Ottenstein, Jens Appmeier, Andreas Weller and Markus K. Oberthaler, *A Primary Noise Thermometer for Ultracold Bose Gases*, New Journal of Physics **8**, 189 (2006)

[5] Rudolf Gati, Michael Albiez, Jonas Fölling, Börge Hemmerling and Markus K. Oberthaler, *Realization of a Single Josephson Junction for Bose-Einstein Condensates*, Applied Physics B **82**, 207 (2006)